MANIPULATION OF MAGNETIC MOMENT USING THE SPIN CURRENT FROM MAGNETIC AND NON-MAGNETIC MATERIALS

A Dissertation

Presented to the Faculty of the Graduate School

of Cornell University

In Partial Fulfillment of the Requirements for the Degree of

Doctor of Philosophy

by

Luqiao Liu

August 2012

MANIPULATION OF MAGNETIC MOMENT USING THE SPIN CURRENT FROM MAGNETIC AND NON-MAGNETIC MATERIALS

Luqiao Liu, Ph. D.

Cornell University 2012

This thesis summarizes my studies on the effect of spin transfer torque on metallic ferromagnets. The spin current for generating the spin torque is either from ferromagnetic electrode through the spin filtering effect, or from nonmagnetic material through the spin Hall effect (SHE). In the experiment using the spin filtering effect, the current flows vertically through the nanoscale spin valve geometries. I will describe the fabrication process that I used to make the nanopillar structure and the strategy that I developed to reduce the critical current.

In the experiment utilizing the SHE, the current flows within the film plane and the spin current is injected transversely from the non-magnetic (NM) film into the adjacent ferromagnetic (FM) layer. I will present five studies that I made to characterize the properties of the SHE and its influence on the magnetic moment.

In the first study, I employed the spin torque ferromagnetic resonance (FMR) technique to determine the spin Hall angle. In this experiment, radio frequency current was applied onto the NM/FM bilayer and FMR was induced by the resultant oscillating spin current. By looking into the amplitude of the FMR signal, I was able to get the value of the spin Hall angle.

In the second and third studies, I demonstrated that the SHE could be utilized to switch magnetic moment of both perpendicularly and in-plane magnetized FM films. For the perpendicular case, the spins injected into the FM film exert a torque that is

perpendicular to the equilibrium position of the moment and it fights against the restoring anisotropy field and induces switching. For the in-plane case, the spins cause switching through the anti-damping mechanism.

In the fourth study, I showed that the SHE could induce persistent magnetic oscillations. DC spin current reduces the magnetic damping to zero and the moment undergoes precession around the applied magnetic field.

In the final study, I demonstrated that the SHE switching current can be modulated by the electric field applied across the FM/oxide barrier. The electric field modifies the anisotropy of the free FM layer and alters the critical current correspondingly.

BIOGRAPHICAL SKETCH

Luqiao Liu was born on October 8th, 1983, in Feicheng, Shandong, a small town in East China. In 2002 Luqiao got admitted by Peking University, so he left his hometown and started to receive the systematic training of physics in the following four years. In his junior year, he joined the group of Prof. Dapeng Yu, whose research mainly focuses on the properties of semiconductor nanostructures. Luqiao's major work in Prof. Yu's lab had been to grow and characterize magnetic semiconductors. It was the interesting experiment he did in Prof. Yu's lab that made him determined to continue his study on magnetics as a graduate student. The other important achievement that he made in his college was that he met with Ying Xu, the girl who later on became his bride.

In 2006 Luqiao enrolled at Cornell University in the field of applied physics. Upon arrival at Cornell, Luqiao was lucky to be able to join Bob Buhrman's group, where he was allowed to further develop his interest in magnetics and spintronics. Luqiao passed his qualifying exam in December of 2006, received his MS in 2010 and his PhD in 2012. After graduating from Cornell, Luqiao will continue the practical research of magnetic memories at IBM Watson research center in Yorktown, NY.

To my parents and my wife.

ACKNOWLEDGMENTS

I wish to thank my advisor Bob Buhrman for the continuous supports and the patient instructions he has given to me over the past six years. I learned a lot from him about how to become a good scientist as well as how to be a great human being. His hands-off style gives me large freedom to investigate the topics that I am interested in. In the meantime, his rich knowledge and good guidance ensure that my research stays on the right track. All of these allow me to develop the abilities that are needed for an independent researcher.

I would also like to acknowledge Dan Ralph, who has given me invaluable help during my study. With his insistence on the truth and his strict attitude about research, he has set up an example of a real physicist for me. He is so intelligent, having gifted intuitions on physics problems, but meanwhile he is also extremely diligent in scientific research. All of these impressed and benefited me greatly.

I am also grateful to Bruce van Dover for serving in my special committee and teaching me the course of *Magnetic Materials.* The knowledge that I learned from this class proved to be extremely beneficial in my research and I believe that it will continue to nurture my future work.

I also wish to thank my labmates and collaborators in both Buhrman's and Ralph's groups. It has been a nice experience to work together with those talented individuals and they have made my life colorful.

As my mentors, John Read and Pat Braganca taught me a lot about vacuum systems, film growth as well as nanofabrication. When I first joined the group, I knew almost nothing about those areas and it was the training that I got from them that led me into this wonderful world. Takahiro Moriyama worked as a post-doc at Cornell for three years. During his stay, he taught me a lot in film growth and high frequency

measurement. Discussions with him have enriched my knowledge and stimulated many insightful ideas. Oukjae Lee, Praveen Gowtham and Hsin-wei Tseng joined the Buhrman's group at about the same time with me. Chat with them has always been enjoyable. They were so generous in sharing their knowledge. Yun Li and Chen Wang were my classmates since we were in college. It has been almost ten years since we first knew each other. This long friendship has been a great treasure to me and has benefited me both inside and outside the labs. As my colleagues and my friends, Yongtao Cui, Sufei Shi, Lin Xue and Wan Li have given me countless valuable suggestions on my experiments and on my life. I would also like to acknowledge all of the other students in Buhrman's and Ralph's groups for making the Clark Hall basement such a lovely place: Ozhan Ozatay, Greg Fuchs, Vlad Pribiag, Eric Ryan, Zhipan Li, Chi-Feng Pai, Junbo Park, Kiran Thadani, Eugenia Tam, Ted Gudmundsen, Allex Mellnik, Colin Heikes and Luis Vilela-Leao.

I also owe debt of gratitude to many former members of Buhrman's and Ralph's groups: Nathan Emley, Jack Sankey, Ilya Krivorotov and so on. Although I don't have overlap time with them at Cornell, their papers, thesis as well as the softwares that they previously written have been a good resource for me to refer to.

I want to thank the excellent support that I got from Jon Shu and Steve Kriske at CNS, Nate Ellis at the machine shop and all of the staff members at CNF. Undoubtedly, I could not have finished my experiments without their precious help.

Finally, I should especially thank my parents and my wife, who have given me support and love unconditionally. The process of research is always much more difficult than it looks to be. There are so many unexpected problems. There are so many more unworking experiments compared with the ones that finally work out. It was their trust which gave me the courage to face those challenges. And I know that I was never fighting alone.

TABLE OF CONTENTS

LIST OF FIGURES

LIST OF TABLES

CHAPTER1

INTRODUCTION

Spin based electronics, or spintronics is a research field which has attracted huge amount of interest over the past one or two decades [1]. In conventional electronic devices, only the charge degree of freedom of electrons is employed. The idea of utilizing both the charge and spin degree of freedom of electrons opens up possibilities for new devices which can have lower power consumption, faster speed as well as non-volatility. By integrating the electron charge with its spin, people can now both alter the electronic transport properties using spins, and in the reverse way, manipulate spins with electron charges. And those processes usually happen in the nanometer scale or even in the single spin level, which makes the potential devices highly scalable, compatible with nowadays' electronic industry. As a study of the interplay between the electron charge and spin, the start of the research in spintronics can date back to the 1980s, when the important discoveries like the injection of spin polarized current from ferromagnetic metal to normal metal [2] and giant magnetoresistance [3-4] were made.

1.1 Giant magnetoresistance and tunneling magnetoresistance

In a sandwich structure composed of ferromagnetic (FM)/non-magnetic (NM)/ferromagnetic (FM) multilayer thin films, the resistance of the stack varies depending on the relative orientation of the two ferromagnetic layers. When the two layers are parallel (P) with each other, the system has a lower resistance and when the two layers are antiparallel (AP), it exhibits a higher resistance. This effect can be realized in two different types of systems. Depending upon the nature of the material used as the non-magnetic spacer, the corresponding magnetoresistance can be

categorized into giant magnetoresistance (GMR) when the spacer is a normal metal, or tunneling magnetoresistance (TMR) when the spacer is an insulator. Because of the distinct difference between the types of spacers, the mechanism for the magnetoresistance usually has different origins in those two systems.

For the GMR effect, electron transport in FM/NM/FM stack happens in the diffusive regime. So the different resistances for the AP and P states come from the fact that the spin polarized electrons have different scattering rates both in the FM electrodes and at the FM/NM interface. Usually, when the conduction electrons have the same spin orientation with the electrode magnet, the electrons will experience less scattering. Therefore, if the two FM electrodes have parallel magnetic orientation, the majority electrons can travel through both of those two layers with very little scattering and the system exhibits a lower resistance. In the meantime, both the up and down spins will be scattered heavily in either of the two electrodes when the two FM layers are in the AP state, hence exhibiting the high resistance states. The GMR effect was first discovered in the current-in-plane configuration [3-4], and later explored in the current perpendicular to plane geometry via the spin valve structures [5]. As the start of spintronic research, the discovery of the GMR effect does not only have significant influences on the scientific exploration in the field of magnetics, but also generates broad impact on practical applications. One good example has been the use of the GMR effect in the hard disk read head. Since its application in the hard disk drive, people have seen several orders of magnitude increase in the storage capacity.

For the TMR effect, electron transport across the tunnel barrier happens in the tunneling regime. In a magnetic tunnel junction (MTJ), the oxide barrier is usually made thin enough such that the conduction electrons can tunnel through it. The

tunneling probability for the electrons is proportional to the density of states in both of the two electrodes, which is spin-dependent. And this is the reason that the P and AP states can have different tunneling resistance. The dependence of the tunneling resistance on the magnetic orientation was discovered as early as in 1975 [6], earlier than the GMR, probably because it is relatively easier to observe the large tunneling resistance compared with the small absolute resistance in the all metallic system. And the latter one usually requires nanoscale fabrication technique or superconducting electrodes for the observation [5]. Another great advantage associated with MTJ is that the TMR is usually higher than GMR. Inside the MTJ, most of the resistance comes from the tunneling barrier and the contribution from the metallic electrode is negligible. In contrast, for spin valves, the resistance of the FM/NM/FM structure is in series with the resistance from the leads, which is usually in the same order of magnitude with the sandwich structure or even higher. So in most cases the final resistance change for spin valves is only a few percent of the overall resistance (This is usually true if only one repeat of FM/NM/FM exists and normal metal leads instead of superconducting leads are utilized). Aluminum oxide (AlO_x) was extensively studied as the material for the tunnel barrier because of the ease with which high quality barriers are made. Amorphous AlO_x can be formed by natural or plasma assisted oxidation from metallic Aluminum films and TMR higher than 10% can be readily obtained [7-8].

In 2001, theorists predicted that much higher TMR can be obtained in crystallized MgO based MTJs [9-10]. Because of the symmetry matches between the MgO band and the band of the Fe electrode, the tunneling barrier plays the role as a spin filter, and greatly enhances the TMR value. Experimentally, TMR value around 200% was reported in MgO based MTJs by the Parkin group [11] and the Yuasa group

[12] in 2004. The large TMR value made it promising to utilize MTJ as the memory cell for random access memory (RAM). Compared with its counterparts based upon semicondutors, magnetic RAM (MRAM) has the advantage of non-volatility and potentially higher storage density. So far, field switched MRAM up to 16Mb is commercially available on the market and great efforts are being made for the development of spin torque switched MRAM.

1.2 Spin transfer torque

So far we have seen that the transport properties of GMR and TMR devices can be influenced by the magnetic orientation of the FM electrodes. It is natural to ask whether the reverse effect can happen, i.e., whether the transport of the conduction electrons will exert any influence on the polarization of the local magnetic momentum. This kind of reverse effect was first studied theoretically in 1996, when two theorists independently predicted the existence of spin transfer torque [13-14]. For conduction electrons, when they pass through one layer of FM electrode, their spins will be aligned along the orientation of the local magnetic moment. When they enter the second FM layer, the transverse component of the transmitted or reflected electrons will be absorbed by the local momentum of the second FM electrode, with the result that the conduction electrons will be aligned collinearly with the FM momentum within a few monolayers. Because of the conservation of the angular momentum, the loss of the transverse component of the conduction electron spins should be equal to the gain of the magnetic moment of the local atoms. That's why we say the spin momentum is "transferred" from the conduction electrons onto the local FM electrode. Since the change of angular momentum per unit time $d\vec{L}/dt$ has the same unit with torque $\vec{\tau}$, the net effect of transfer of the spin momentum is equivalent to a current induced torque, the Slonczewski torque. The behavior of the magnetic momentum can

then well be described by incorporating this spin torque term in to the equation of motion for magnetic moment, the LLG equation. It can be shown using this equation that the orientation of the magnetic momentum can be reversed given that the injected spin current is large enough.

The effect of the spin torque was experimentally verified at Cornell, first in multidomain magnetic stacks with point contact [15] and then in a nanopillar geometry [16]. In the latter geometry, the FM/NM/FM stack films were patterned into elliptical shapes with the dimension lower than 200 nm. Therefore, the influence of the spin torque can begin to dominate over other accompanying effects (like the Oersted field or the Joule heating) and the behavior of the magnetic free layer can be readily modeled using a quasi single domain picture. The geometry of the nanopillar structure has attracted huge amount of interest since its discovery because of the rich physics that can be carried out in this system and the important potential application as a unit cell for magnetic memory. Besides switching, another important regime that was predicted from the LLG equation is the persistent oscillation of the magnetic moment. When the external field applied onto the free layer is larger than the coercive field and the spin current is large enough, the magnetic moment of the free layer can undergo spontaneous precession under the influence of spin torque. Direct evidence for magnetic dynamics caused by DC current was first observed by Kiselev *et al.* [17] in a spin valve system and by Rippard *et. al.* [18] in point-contact geometry.

The first experimental demonstrations of the spin torque induced switching and oscillation happened in the metallic spin valve system. With the development of the MTJ, especially the discovery of high TMR in MgO-MTJ, it is natural to study the spin torque effect in the MTJ system, where higher polarization can lead to more

efficient switching and large TMR signal can be used to provide stronger signal for various types of applications. However, the biggest technical difficulty associated with the spin torque in MTJ was to get a large enough tunneling current, which therefore requires a very thin tunnel barrier and low RA product. Spin torque switching in MTJs was first demonstrated by Huai *et al.*[19] and Fuchs *et al.* in AlO_x based MTJs [20]. Later, switching was observed in MTJs with MgO as the tunnel barrier [21-22]. DC dynamics were also studied in AlO_x [20] and MgO [23] based tunnel junction, separately. Compared with spin valves, magnetic oscillators based on MTJ can provide much larger resistance change, therefore can provide higher output power.

Besides using a large DC current, magnetic moment precession can also be excited using an RF current. When the frequency of the applied current satisfies the resonance condition, magnetic moment will undergo precession. Just like in conventional field driven ferromagnetic resonance, the spin torque driven ferromagnetic resonance (ST-FMR) can be used for probing the properties of the ferromagnetic layer, such as the damping coefficient, anisotropy as well as the micromagnetic modes. Since ST-FMR is generally carried out in spin valve or MTJs, the precession of the magnetic moment will result in the oscillation of magnetoresistance, which will further be mixed with the injected RF charge current and form a detectable DC voltage. Therefore, instead of detecting the power absorption or power reflection like in the conventional FMR experiment, ST-FMR measurement relies on the resistance oscillation and can be much more sensitive and can be used to measure magnet in the nanometer scale. ST-FMR measurement was used to study the spin torques in both the spin valves [24] and the MTJs [25-27].

1.3 Outline of the dissertation

The experimental realization of spin transfer torque benefits from the progress in nanofabrication techniques. Only when the size of the devices is reduced below a certain dimension (around 200 nanometers), the effect of the spin torque, instead of the accompanying current induced Oersted field will begin to dominate. Therefore, it is critical to be able to make the magnetoelectronic devices, which are usually in the nanopillar form, in a reliable and quick way. Previously developed nanopillar fabrication recipes at Cornell, while being very successful in terms of allowing the study of many interesting physics, could be very time consuming and usually the yield was not satisfactory. The typical fabrication period is usually three weeks to one month. And the long hours' work in the cleanroom sometimes makes the fabrication not a very enjoyable process. So it is necessary to develop a new fabrication method which can both simplify the steps and improve the device yield. In Chapter 2, I will describe a new recipe that I developed for nanopillar fabrication, which employs Hydrogen silsesquioxane (HSQ) as the e-beam and ion milling mask. Unlike the previous recipe, in this new process, the HSQ capping layer and the insulating oxide situated above can be easily removed by soaking the sample in chemicals. So, it is now very easy to make the top contact and the yield associated with this process can also be much higher than the previous carbon based recipe.

The physics associated with spin transfer torque both in the spin valve and magnetic tunnel junction systems have been basically understood after years of extensive study. But on the other hand, to be used as practical non-volatile magnetic memories, there are still many realistic technical diffculties in the field of spin transfer torque that need to be solved. Lowering the critical current is one of those important problems. Different approaches have been developed in order to get a low critical current. In Chapter 3, I will describe a strategy that I studied to achieve this goal. It

can reduce the critical current by more than 5 times and at the same time keep the thermal stability. In this study, interfacial perpendicular anisotropy was introduced into the free magnetic layer intentionally by using ferromagnetic multilayers. The perpendicular anisotropy cancels part of the demagnetization field and hence reduces the critical current. Meanwhile, since the demag field does not contribute to the energy barrier, the decrease in demag field does not harm the thermal stability.

Besides the spin transfer torque, another interesting topic that has been studied in the past few years is the phenomenon called spin Hall effect. The spin Hall effect (SHE) was both discovered in the semiconductor [28] and metals [29] in the mid-2000s. Unlike in spin valves or MTJs, where the spin current is generated due to the filtering effect of the FM electrode on the conduction electrons. In materials with the SHE, spin current can be generated out of non-magnetic materials. So, it will have a promising potential to be used as the non-magnetic source for spin current. Therefore, considerable amount of attentions have been paid to the study of SHE, to learn the origins of this effect, to measure its magnitude as well as to utilize this effect to manipulate magnet. In Chapter 4, I will give a brief review on the studies of the SHE in metallic system, especially on the experiments that are used to determined the magnitude of the SHE. Different techniques that are used for measureing the SHE will be compared and possible artifacts and errors associated with these experiments will be discussed.

In the study of spin transfer torque, different techniques have been developed in order to determine the nature of the spin torque and the properties of the nanomagnet. For example, when the spin current is large, the effect of the spin torque can be exhibited through the switching or the persistent oscillations of the free

magnetic layer. When the spin current is small, the spin torque can still be studied, through the use of spin torque ferromagnetic resonance (ST-FMR) measurment. Just like in ordinary FMR experiment, where a small oscillating field is utilitzed to cause precession in the magnetic moment of the FM layer, an oscillating spin current can also lead to resonance because of the spin torque effect. Since the spin current needed for the observation of the resonance is small, this provides a way to study the SHE, where the spin current can be much weaker compared that in conventional spin valves or MTJs. From the amplitude of the ferromagentic resonance, we can extract the information about the magntidue as well as the direction of the spin current due to the SHE. In Chapter 5, I will discuss the details of the SHE induced ST-FMR measurement on different materials of Pt and Ta.

After knowing the magnitude of the SHE, it is natural to ask whether the spin current from the SHE can be utilized to manipulate the magnet in the same way as in a spin valve or MTJ: to switch the magnetic moment or to induce DC dynamics. Two different types of SHE induced switching were observed experimentally, one for perpendicular magnetized FM films and the other for in-plane magnetized FM films. In both of the two cases, the injected spins are orientated in the film plane. Therefore, two different types of switching mechanism are involved here, precessional switching and anti-damping switching. In Chapter 6 and Chapter 7, I will talk about the experiment and theory about those two switchings, seperately. For perpendicularly magnetized films, experimental results obtained from Hall bar geometries will be presented both for Pt system and Ta based system. And for in-plane magnetized film, a three terminal device which combines the SHE and the MTJ is utilized for the demonstration.

In Chapter 8, persistent oscillation caused by the SHE will be discussed. Just like in a spin valve or MTJ, DC current can also lead to spontaneous oscillations in the FM layer using SHE as the spin current source. The three terminal magnetic device is utilized again. And DC spin current is injected into the FM free layer from the SHE while the microwave power is detected from the MTJ terminals.

In the past few years, people have been ethusiastically pursued another goal in the field of spintronics: to manipulate the magnet with electric field. Different from the spin torque approach, where a charge current is required, the electric field can be used to control the magnet in the absence of charge current (or with very small current), and hence is very economic in terms of power consumption. Recently, people discovered that by applying a electric field at the ferromagnet/oxide interface, the anisotropy of the magnet can be greatly modified. In Chapter 9, I will show that by utilizing this effect in the three terminal device, the critical current for the SHE switching can be modulated greatly. The capability of tuning the critical current using the electric gate voltage can lead to new architecture for magnetic memories and new spin logic operations.

REFERENCES

1. S. A. Wolf, D. D. Awschalom, R. A. Buhrman, J. M. Daughton, S. von Molnar, M. L. Roukes, A. Y. Chtchelkanova and D. M. Treger, Spintronics: A spin-based electronics vision for the future, *Science* **294**, 1488 (2001).
2. M. Johnson and R. H. Silsbee, Interfacial Charge-Spin Coupling - Injection and Detection of Spin Magnetization in Metals, *Phys. Rev. Lett.* **55**, 1790 (1985).
3. G. Binasch, P. Grunberg, F. Saurenbach and W. Zinn, Enhanced Magnetoresistance in Layered Magnetic-Structures with Antiferromagnetic Interlayer Exchange, *Phys. Rev. B* **39**, 4828 (1989).
4. M. N. Baibich, J. M. Broto, A. Fert, F. N. Vandau, F. Petroff, P. Eitenne, G. Creuzet, A. Friederich and J. Chazelas, Giant Magnetoresistance of (001)Fe/(001) Cr Magnetic Superlattices, *Phys. Rev. Lett.* **61**, 2472 (1988).
5. W. P. Pratt, S. F. Lee, J. M. Slaughter, R. Loloee, P. A. Schroeder and J. Bass, Perpendicular Giant Magnetoresistances of Ag/Co Multilayers, *Phys. Rev. Lett.* **66**, 3060 (1991).
6. M. Julliere, Tunneling between Ferromagnetic-Films, *Phys. Lett. A* **54**, 225 (1975).
7. J. S. Moodera, L. R. Kinder, T. M. Wong and R. Meservey, Large Magnetoresistance at Room-Temperature in Ferromagnetic Thin-Film Tunnel-Junctions, *Phys. Rev. Lett.* **74**, 3273 (1995).
8. T. Miyazaki and N. Tezuka, Giant Magnetic Tunneling Effect in Fe/Al2O3/Fe Junction, *J. Magn. Magn. Mater.* **139**, L231 (1995).
9. W. H. Butler, X. G. Zhang, T. C. Schulthess and J. M. MacLaren, Spin-dependent tunneling conductance of Fe vertical bar MgO vertical bar Fe sandwiches, *Phys. Rev. B* **63**, 054416 (2001).
10. J. Mathon and A. Umerski, Theory of tunneling magnetoresistance of an epitaxial Fe/MgO/Fe(001) junction, *Phys. Rev. B* **63**, 220403 (2001).
11. S. S. P. Parkin, C. Kaiser, A. Panchula, P. M. Rice, B. Hughes, M. Samant and S. H. Yang, Giant tunnelling magnetoresistance at room temperature with MgO (100) tunnel barriers, *Nature Mat.* **3**, 862 (2004).
12. S. Yuasa, T. Nagahama, A. Fukushima, Y. Suzuki and K. Ando, Giant room-temperature magnetoresistance in single-crystal Fe/MgO/Fe magnetic tunnel junctions, *Nature Mat.* **3**, 868 (2004).
13. J. C. Slonczewski, Current-driven excitation of magnetic multilayers, *J. Magn. Magn. Mater.* **159**, L1 (1996).
14. L. Berger, Emission of spin waves by a magnetic multilayer traversed by a current, *Phys. Rev. B* **54**, 9353 (1996).
15. E. B. Myers, D. C. Ralph, J. A. Katine, R. N. Louie and R. A. Buhrman, Current-induced switching of domains in magnetic multilayer devices, *Science* **285**, 867 (1999).
16. J. A. Katine, F. J. Albert, R. A. Buhrman, E. B. Myers and D. C. Ralph, Current-driven magnetization reversal and spin-wave excitations in Co/Cu/Co pillars, *Phys. Rev. Lett.* **84**, 3149 (2000).

17. S. I. Kiselev, J. C. Sankey, I. N. Krivorotov, N. C. Emley, R. J. Schoelkopf, R. A. Buhrman and D. C. Ralph, Microwave oscillations of a nanomagnet driven by a spin-polarized current, *Nature* **425**, 380 (2003).
18. W. H. Rippard, M. R. Pufall, S. Kaka, S. E. Russek and T. J. Silva, Direct-current induced dynamics in Co90Fe10/Ni80Fe20 point contacts, *Phys. Rev. Lett.* **92**, 027201 (2004).
19. Y. M. Huai, F. Albert, P. Nguyen, M. Pakala and T. Valet, Observation of spin-transfer switching in deep submicron-sized and low-resistance magnetic tunnel junctions, *Appl. Phys. Lett.* **84**, 3118 (2004).
20. G. D. Fuchs, et al., Spin-transfer effects in nanoscale magnetic tunnel junctions, *Appl. Phys. Lett.* **85**, 1205 (2004).
21. H. Kubota, et al., Magnetization switching by spin-polarized current in low-resistance magnetic tunnel junction with MgO (001) barrier, *IEEE Transaction Magn.* **41**, 2633 (2005).
22. Z. Diao, D. Apalkov, M. Pakala, Y. F. Ding, A. Panchula and Y. M. Huai, Spin transfer switching and spin polarization in magnetic tunnel junctions with MgO and AlOx barriers, *Appl. Phys. Lett.* **87**, 232502 (2005).
23. A. M. Deac, et al., Bias-driven high-power microwave emission from MgO-based tunnel magnetoresistance devices, *Nature Phys.* **4**, 803 (2008).
24. J. C. Sankey, P. M. Braganca, A. G. F. Garcia, I. N. Krivorotov, R. A. Buhrman and D. C. Ralph, Spin-transfer-driven ferromagnetic resonance of individual nanomagnets, *Phys. Rev. Lett.* **96**, 227601 (2006).
25. A. A. Tulapurkar, Y. Suzuki, A. Fukushima, H. Kubota, H. Maehara, K. Tsunekawa, D. D. Djayaprawira, N. Watanabe and S. Yuasa, Spin-torque diode effect in magnetic tunnel junctions, *Nature* **438**, 339 (2005).
26. J. C. Sankey, Y. T. Cui, J. Z. Sun, J. C. Slonczewski, R. A. Buhrman and D. C. Ralph, Measurement of the spin-transfer-torque vector in magnetic tunnel junctions, *Nature Phys.* **4**, 67 (2008).
27. H. Kubota, et al., Quantitative measurement of voltage dependence of spin-transfer torque in MgO-based magnetic tunnel junctions, *Nature Phys.* **4**, 37 (2008).
28. Y. K. Kato, R. C. Myers, A. C. Gossard and D. D. Awschalom, Observation of the spin hall effect in semiconductors, *Science* **306**, 1910 (2004).
29. S. O. Valenzuela and M. Tinkham, Direct electronic measurement of the spin Hall effect, *Nature* **442**, 176 (2006).

CHAPTER 2

HSQ BASED NANOPILLAR FABRICATION

2.1 Introduction

The fundamental structure for the study of spin torque in both spin valve and MTJ is the FM/NM/FM sandwich nanopillar. In nanopillars, both the free FM layer and fixed FM layer are patterned into elliptical/circular shapes with the dimension of a few tens to a few hundred nanometers. Usually the procedure for making nanopillars consists of first patterning the whole stack into a nanopillar with extended bottom leads and then making the contact between the top electrode of the nanopillar and the top leads. In this process, several factors are important for the success of the fabrication. First of all, advanced lithography techniques are needed for the definition of the pillar. In order to define shapes with lateral dimensions below 200 nms, either electron beam lithography or deep ultraviolet photolithography (or related immersion lithography) techniques have to be utilized. In the meantime, we should also be able to transfer the pattern defined by lithography into the metallic stacks through some etching technique. So this requires that the lithography resist need to have a high etching selectivity. Secondly, there should be good insulation between the top and bottom leads. Since the top and bottom leads are actually overlapping with each other, it is important to separate those two layers electrically to avoid shunting. Thirdly, good electrical contact needs to be made between the top of the nanopillar and top leads. Therefore, the current should flow nowhere except through the nanopillar. Different from most of the other nanostructures people used to make, the nanopillar structure is actually 3 dimensional in nature, and raises very strict requirments for fabrication.

2.2 Carbon based nanopillar fabrication

Fortunately, previous researchers at Cornell developed relatively mature recipes, which make it possible to fabricate nanopillars with very small dimensions. The standard recipe for nanopillar fabrication at Cornell is a carbon based process. Basically, it utilizes PMMA as the e-beam lithography resist and then transfers the mask onto evaporated carbon layers [1]. As is described in Fig. 2.1, the major steps associated with the carbon based recipes are as flowing:

(a) grow metallic stack and evaporate carbon film on top of the stack,

(b) electron beam lithography which defines the shape of the nanopillar, bilayer PMMA resist were utilized which give rise to the undercut,

(c) evaporation of Cr thin film,

(d) strip of the PMMA resist and etch the carbon film using oxygen plasma, the elliptical shape is transferred from PMMA to carbon film,

(e) Ion milling to etch the metallic multilayer,

(f) deposition of oxide for insulation,

(g) low angle ion milling to planarize the oxide,

(h) Ion milling to open the window above the nanopillar,

(i) Oxygen plasma etching to remove the residual of carbon mask on top of the pillar,

(j) top electrode deposition to make the contact.

As one of the most popular e-beam resists, PMMA has very high resolution. Meanwhile, PMMA is a positive tone resist meaning that the portion of resist exposed by electron beam will be dissolvable by the developer. So PMMA is widely employed in fabrication processes where lift-off is utilized. However, for the fabrication of nanopillar, where a milling mask is needed, PMMA is not the ideal resist. This is both because of the tone of the resist and also the low etching selectivity. This is the reason

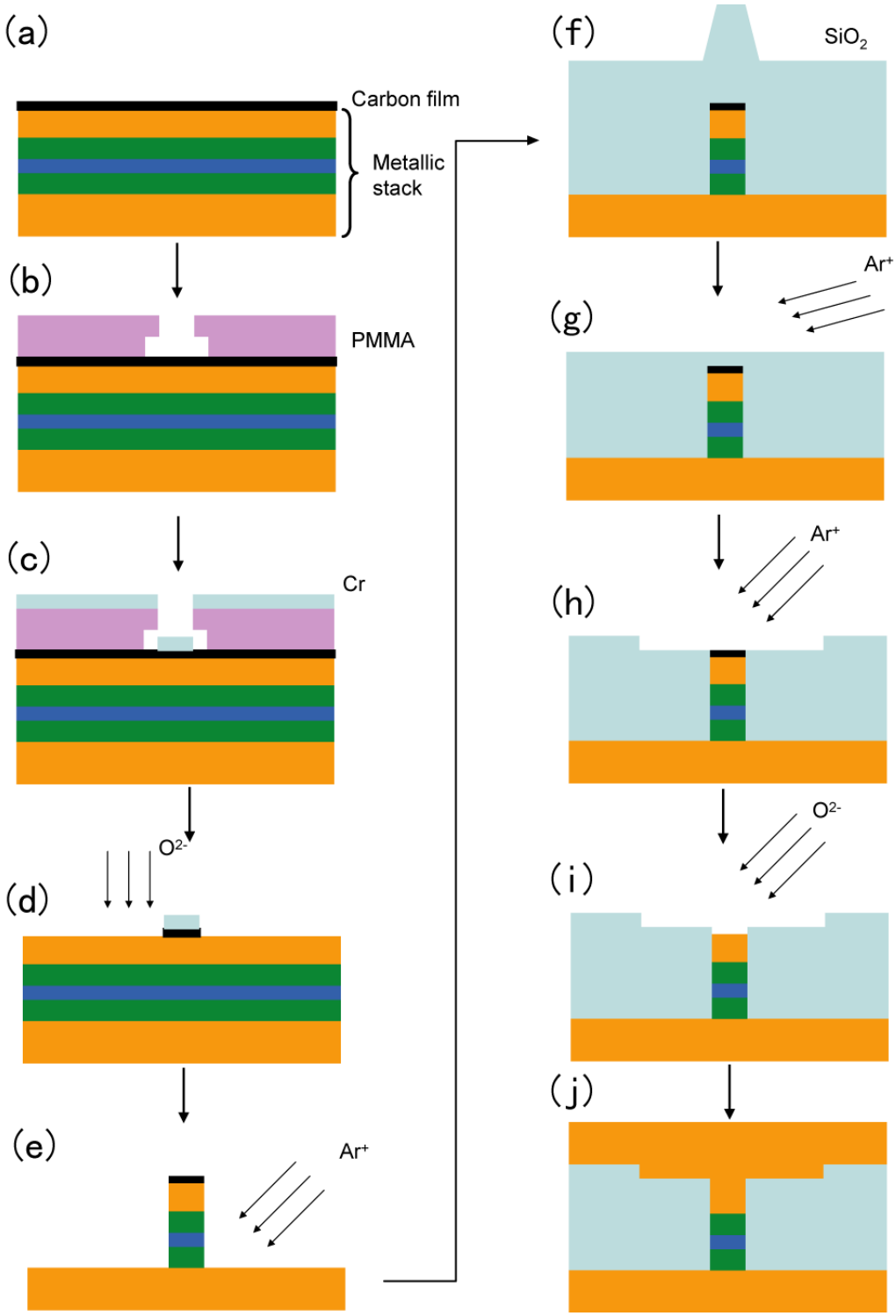

Figure 2.1 Nanopillar fabrication with carbon mask. The patterns only reprent a schematic illustration and the structures are not drawn to scale. So the thickness of the layers looks to be thicker than they really are.

why we have to evaporate a thin layer of carbon as the mask material, and then use Cr to transfer the pattern from PMMA to carbon. The major difficulty in the nanopillar fabrication is in step (g) and (h). In step (g), low angle ion milling is needed which can flatten the surface of silicon dioxide. And in the following step the silicon dioxide is further milled to expose the top electrode of the nanopillar. This is the most critical step in the whole process because both under-etching and over-etching in this step will destroy the device. What's more, unlike other ion milling steps where end point detector can be used to determine the milling time, there is no obvious signal in these two steps which can be used. Therefore, it requires very precise calibration on the etching rate of SiO_2 and sometimes it relies on trial and errors. (In reality, people had to cut the whole wafer into multiple pieces and try different milling time for this step.)

2.3 HSQ based nanopillar fabrication

2.3.1 Overview

Hydrogen silsesquioxane, or HSQ is a new type of e-beam resist, which is negative in tone and has a resolution comparable to PMMA. After exposure, HSQ is transformed into a compound composed of silicon and oxide [2], and therefore has an etching rate similar to normal metal and oxide. Both of these features make HSQ an ideal e-beam resist for nanopillar fabrication. By replacing PMMA with HSQ, we can skip the steps shown as (a)~(d) in Fig. 2.1 and greatly simplify the fabrication process. But since HSQ is converted into silicon oxide compound after exposure, it is still very difficult to strip it after patterning the metallic stack into the nanopillar geometry. Several previous group members have tried different strategies to overcome this difficulty and have achieved successes to a certain extent.

First of all, similar to step (g) and (i) in Fig. 2.1, low angle ion milling can still be utilized to expose the top part of the nanopillar. Now the whole process is to replace PMMA with HSQ but still using the same procedure to planerize the oxide above the nanopillar. This is tested and verified by Braganca at Cornell [3]. The disadvantage with this process is also obvious because the major difficulty of fabrication still exists and the complexity is not significantly reduced.

Another approach is to use chemical mechanical polishing (CMP) to remove the oxide and residual of the HSQ resist above the nanopillar. Since CMP has some selectivity on SiO_2 over metals, it should be more efficient compared with low angle ion-milling which is non-selective on materials. What's more, it was also suggested that some buffer layer could be used between the HSQ resist and metallic stack to reduce the adhesion. So it was expected that with a simple polishing, the HSQ resist residual as well as the oxide above would be torn off and the top of the nanopillar could be exposed. This approach was suggested by Emley [1] and later tested by Braganca and myself. The major issue associated with this process is that tearing-off the resist is not as easy as expected. As is proposed, PMMA is used as the adhesion layer between the metallic layer and HSQ resist. But it turned out it was very difficult to remove this bilayer resist during the polishing. Therefore, so far the polishing process is still not a working recipe at Cornell.

In the process of testing and developing the polishing based nanopillar fabrication recipes, I developed an even simpler process which utilized an omnicoat/PMMA/HSQ trilayer resist for e-beam exposure and ion-milling. The use of omnicoat as the adhesion layer between PMMA/HSQ and the metallic stack greatly simplified the fabricaiton process since now it is possible to remove the resist and

oxide above by simply soaking the sample inside chemicals and doing a quick sonication. So, now neither polishing nor low angle ion milling is necessary to open the window on top of the nanopillar and the yield is significantly enhanced.

2.3.2 Fabrication process

As the key element for the success of this recipe, omnicoat is a chemical developed by Microchem to be used together with resists such as SU-8 and SU-2000. Once exposed, SU-8 and SU-2000 will be cross-linked, and it is known that it will be extremely difficult to remove those resists with solvent or ordinary etching technique. But omnicoat can be used as the release layer for SU-8 or SU-2000. By spinning a thin layer of omnicoat between the wafer and SU-8 or SU-2000, these resists can be easily stripped after exposure and development. So, thanks to omnicoat, it is possible to do lift-off with SU-8(SU-2000). Because of this unique capability, omnicoat is chosen to be used as the release layer between HSQ and the wafer. But one problem associated with omnicoat/HSQ bilayer resist is that omnicoat is dissolvable in the developer for HSQ. This is the reason that additional PMMA layer is inserted between HSQ and omnicoat to protect omnicoat layer from being dissolved during the development of HSQ.

The major steps associated with the HSQ based fabrication recipe are shown in Fig. 2.2, and it can be seen that compared with the carbon based recipe (Fig. 2.1), the process is greatly simplified. The following is the description of the fabrication steps:

(a) spin omnicoat/PMMA/HSQ trilayer e-beam resist,

(b) E-beam lithography to define the nanopillar,

(c) O_2 plasma etching to remove omnicoat/PMMA,

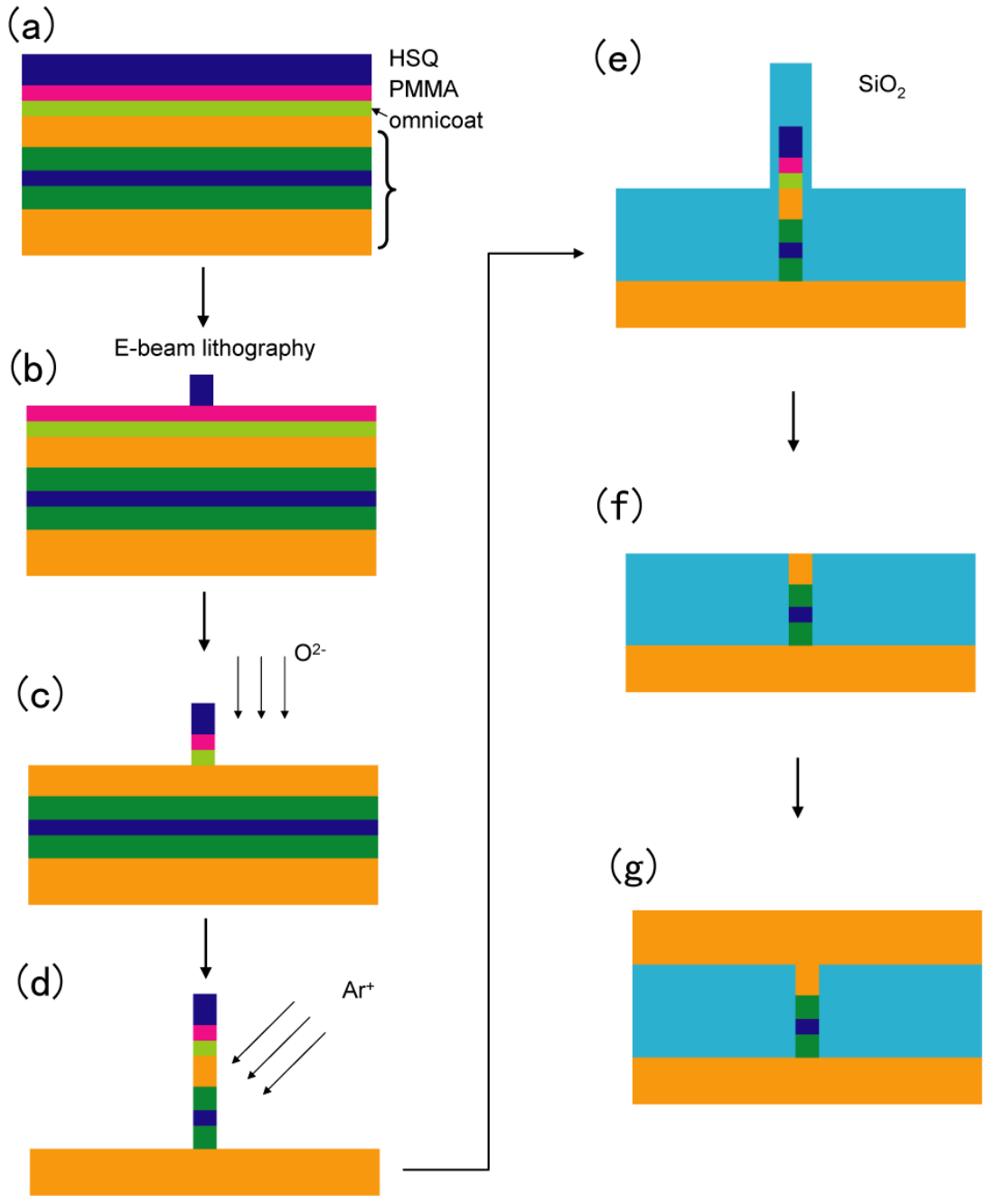

Figure 2.2 Nanopillar fabrication with HSQ resist.

(d) Ion mill to define the pillar,

(e) Evaporation of SiO_2 to protect the nanopillar,

(f) Soak in chemicals, strip the resist and the oxide above the pillar,

(g) Deposition of the top contact.

Because of the fact that the omnicoat/PMMA/HSQ trilayer resist can be stripped by the developer for photolithography (the developers for photolithography and for HSQ are the same), we cannot do any photolithography between step (c) and (d). This means that unlike in the carbon based recipe, where we do the e-beam lithography at the beginning of the whole fabrication procedure, we need to isolate the device and define the pad first using photolithography, and then do the e-beam lithography. Therefore, instead of aligning the photolithography pattern onto the e-beam pattern, here, we do the opposite, aligning the e-beam to photolithography. This means that we need to do aligned e-beam lithography. This adjustment on the sequence of the fabrication steps brings in a little bit extra work, but it is still acceptable considering the advantage that we can gain by using HSQ. A set of alignment marks which contain the marks both for e-beam lithography and photolithography should be made before any of the other lithography steps. And all of the following patterns should be aligned onto those marks. The alignment marks can be made either using photolithography or e-beam lithography, depending upon the requirement of the accuracy. Since for most of the fabrications, the e-beam defined pattern – the nanopillar is finally aligned onto the photolithography defined leads, the final alignment accuracy is determined by photolithography anyway. So there is no need to use e-beam lithography for defining these alignment marks. Fig. 2.3 gives the illustration on the design of the mask that I used to define the alignment marks. Here, the star like alignment marks are for photolithography and the center square is for the

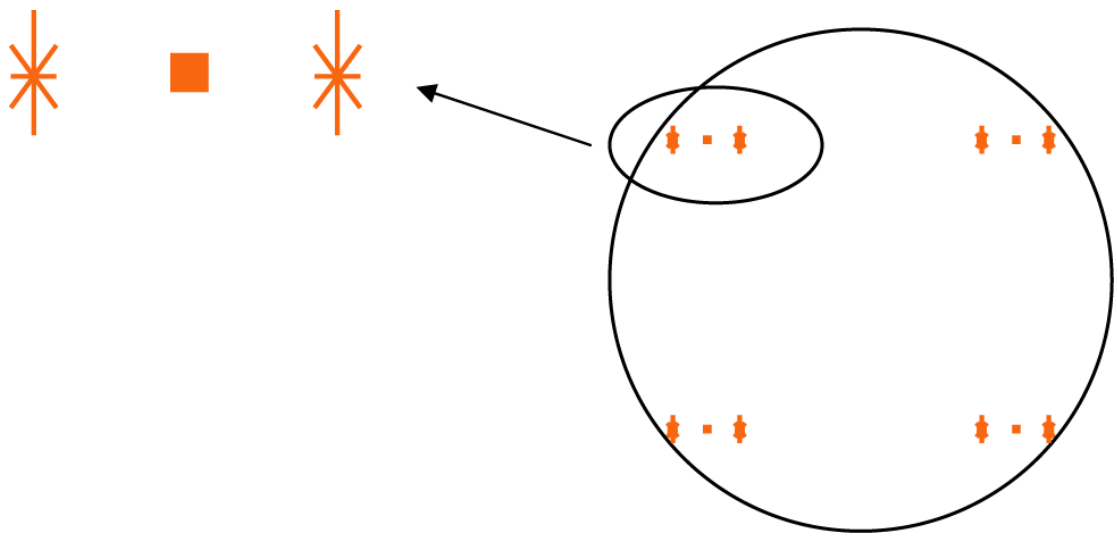

Figure 2.3 Photolithography mask for defining the alignment marks. The big circle on the right represent the wafer and four dies are exposed for this step. Within each die (left), alignment marks for both the photolithography and e-beam lithography are defined in the same step.

e-beam lithography (Actually the square alignment marks are for the old e-beam tool VB-6 made by Leica, where four alignment marks are needed for the aligned e-beam lithography. For the new e-beam machine made by JEOL, a pair of cross-like alignment marks are needed.) There are also cases where more than one layer of aligned e-beam lithography is needed for the fabrication. The three terminal device that I will show in Chapter 7 gives a good example on this. In this kind of situation, better accuracy is needed for the alignment between different layers of e-beam lithography. So it is necessary to use e-beam lithography to define the alignment marks described above. All of the features shown in Fig. 2.3 should be written with e-beam lithography but the mark design scheme remains the same.

The alignment marks can be formed either by etching into the wafer or depositing some heavy metal films. Both of those two approaches have been verified in my experiments. For aligned e-beam lithography, the e-beam machine finds the alignment marks from the secondary electrons contrast (that is, similar to scanning

electron microscope). This is the reason why films with large Z atom numbers are required if the metallic film alignment mark is used. I have tried both Au and Pt for this purpose, and 100nm of either metal should give enough contrast. Another important requirement on the alignment marks is that they need to have sharp edges so that they can be distinguished by the e-beam tool. So, for deposition of the metallic films, either lift-off resist (LOR, for photolithography) or bilayer PMMA (for e-beam lithography) needs to be used to get a clean edge. To make the alignment marks using the etching method, trenches of a few hundreds of nanometers deep on silicon wafers are needed. Therefore, a long time ion milling (1.5 hours) is used in previous experiments.

2.3.3 Step parameters

I will describe the detailed fabrication procedure in this section, with the hope of giving an executable, step by step recipe. Parameters for the steps that are different from the previous Carbon based processes will be given. For steps that are the same with or similar to the Carbon based process, please refer to the 3rd chapter of ref. [1] for detailed discussions. All of the discussion below is for the fabrication of a simple two terminal nanopillar device. For the fabrication details of more complicated structures, please see section 7.2 of this dissertation.

Step 0: growth of metallic stacks

I should mention here that the material used as the capping is very important for the success of this recipe. I have tested Pt, Ru and Ta as the capping layer. It turned out that only Ru works. Omnicoat does not stick well onto Pt or Ta and the whole resist will peel off during development after the e-beam lithography. The exact reason is unknown but the use of Ru is necessary at this moment.

Step 1: Defining the alignment marks using photolithography and ion milling.

Table 2.1. Parameters for the alignment mark definition. The following recipe applies to the case where the marks are defined by photolithography and ion milling.

Step 1.1: spining photoresist	S1813, 2000rpm, 115°C bake
1.2: photolithography	5X, 1s expose
1.3: development	MIF 300, 60s
1.4: Ion milling	Beam voltage: 150 V Accelerating voltage: 150 V Beam current = neutralizing current = 35 mA Milling angle: 165° Time: 90 min
1.5: strip resist	overnight soaking in Remover PG + heated to 90°C Sonication

The design on the patterns of the alignment marks have been discussed in the previous section. The parameters for this step is given in Table 2.1.

Step 2: Isolating the device and defining the pads.

This step is similar to the carbon based recipe. During the ion milling, it is not necessary to mill all the way down to the SiO_2 substrate because the parts that are milled in this step will be further etched in the step of defining the pillar.

Step 3: E-Beam lithography and defining the pillar.

The parameters for the e-beam lithography part are given in Table 2.2.

Step 4: Evaporation of SiO_2 to cover the pillar

This step is similar to Carbon based process. The only difference is that in the carbon recipe, usually the oxide is grown using plasma enhanced physical vapor deposition (PECVD) method to get a conformal covering. But here the oxide layer can only be grown using evaporation otherwise the oxide cannot be stripped afterwards. The thickness of the SiO_2 is also critical here, and it cannot be too thick. Ideally, SiO_2 is designed to have the same thickness with the nanopillar [step (e) in Fig. 2.2.].

Step 5: Stripping the omnicoat/PMMA/HSQ resist

Table 2.2. Parameters for e-beam lithography.

Step 3.1: spinning omnicoat	1000 rpm, 170 °C bake; spinning the resist twice, the total thickness is ~ 30 nm
3.2: spinning PMMA	495K 2%, 4000 rpm, 170 °C bake 15 min, thickness ~ 50 nm
3.3: spining HSQ	XR1541, 1000 rpm, 170 °C bake 2 min, thickness ~ 100 nm
3.4: e-beam exposure	Dose: ~1000 to 10000 $\mu C/cm^2$
3.5: developing	MIF 300, 4 min
3.6: etching PMMA and omnicoat	O_2 plasma etching, 2 min.

Table 2.3. Parameters for stripping the resist

Step 5.1: soaking in Remover PG	Time: a few hours (overnight if possible) Temperature: heat the beaker to 90°C
5.2: sonication	Time: above 10 mins Sometimes it helps to scrach the surface of the wafer with clean room style cotton stick
5.3: rinsing	IPA → DI water → IPA
5.4: blow dry	

This is the most important step in the whole process. Whether the resist and the oxide can be removed or not in this step determines the final yield. The parameters are shown in Table 2.3.

Step 6: Short protection

Optional, similar to the old recipe.

Step 7: Opening the window above the pads

Similar to old recipe. Do not use HF wet etching because the top surface of the pads is now Cu instead of Pt or Ru after the previous milling. It is known that Cu can

be etched by HF solvent. Use ion milling or plasma etching for this step. It is found that CF_4 plasma etching works best.

Step 8: Making top contacts

Similar to old recipe. The difference is that in old recipes, the top surface of the contact pads are still Pt(Ru) after all the previous steps. But here, the top surface is usually Cu or Ta, which cannot provide a very good contact for wire bonding or probes. So, it is necessary to deposit the pads again in this step. A specially designed mask needs to be used.

2.3.4 Sample images

In this section, I will give some sample SEM or AFM images that I took during the development of this process, to illustrate how the HSQ based recipe works.

Fig. 2.4 shows the pattern after the e-beam exposure. The omnicoat/PMMA bilayer has been etched using O_2 plasma. Fig. 2.5 gives an image of the nanopillars after the resist is stripped. The pillars are already defined by e-beam lithography + ion milling and they are also surrounded by SiO_2. Fig. 2.5 (a) illustrates a matrix of nanopillars. It can be clearly seen that some of the pillars have different contrast compared with the rest. It turned out that the brighter ones represent the ones where the resist has been successfully removed [Fig. 2.5(c)]. And for the darker ones, they are the pillars that still have the resist and oxide on top [Fig. 2.5(b)]. It can be seen that relatively high yield can be obtained using this recipe. In Fig. 2.6, structures with even smaller sizes are shown. Fig 2.6 (a) represents elliptical nanopillars of 60 nm × 180 nm and Fig 2.6 (b) represents circular pillars of 100 nm × 100 nm. The different rows in the figures represent different e-beam exposure time. The dose increases from the top to the bottom. It can be seen from Fig. 2.6 (b) that below a certain dose (around

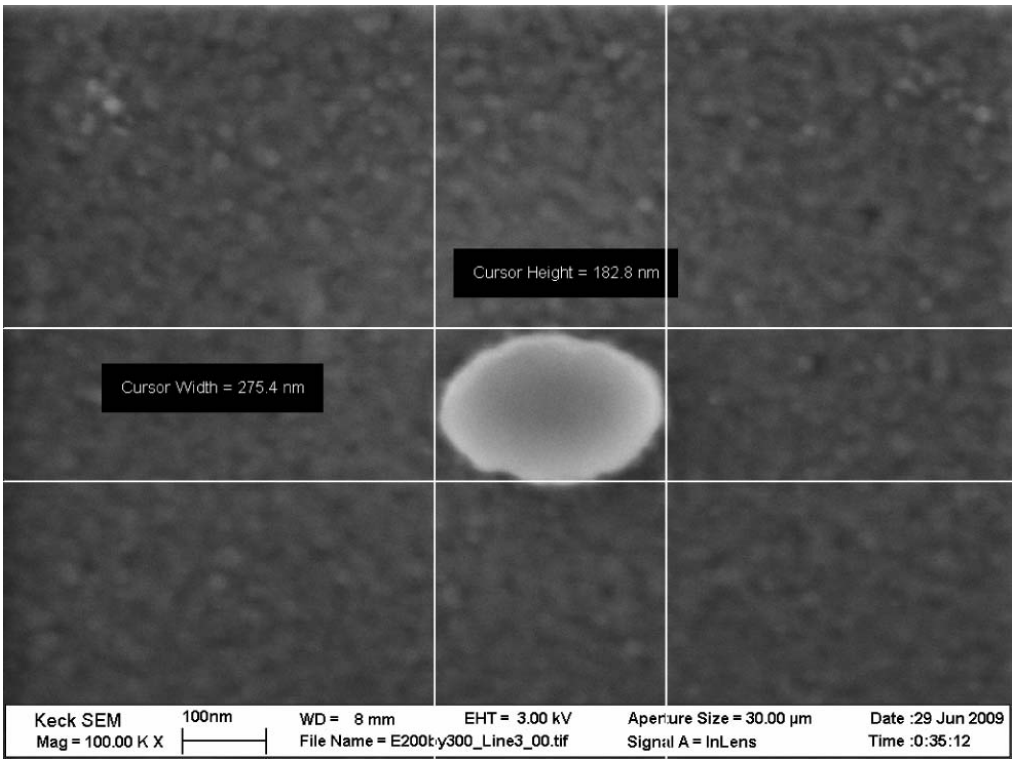

Figure 2.4 SEM image of a nanopillar after e-beam exposure. The pattern is around 180 nm × 275 nm.

1000 μC/cm^2), the resist cannot be stripped. So, it is helpful to use a relatively large dose during the e-beam lithography step. Fig. 2.7 gives an AFM image of the nanopillars. Fig. 2.7 (a) corresponds to the case before the resist is stripped. And we can see that there are large steps associated with these pillars. These shapes do not reflect the real dimension of the pillar. The artifact is due to the large height difference between the pillar and the other parts of the wafer. Fig. 2.7 (b) shows the situation after the resist is stripped. We can see that the top parts of the pillars are exposed. And this is even clearer in Fig. 2.7 (c), where a single device is scanned. From the cross section [Fig. 2.7 (d)], we can see that height of the pillar is basically the same with the surrounding SiO_2 except close to the edge of the pillar, where the SiO_2 is higher than

other parts because of the tapering shape of the pillar [4]. Fig. 2.8 shows a group of larger nanopillars with the dimension of 1 μm × 300 nm. We can clearly see that the height of the center of the pillars is lower because the resist is removed.

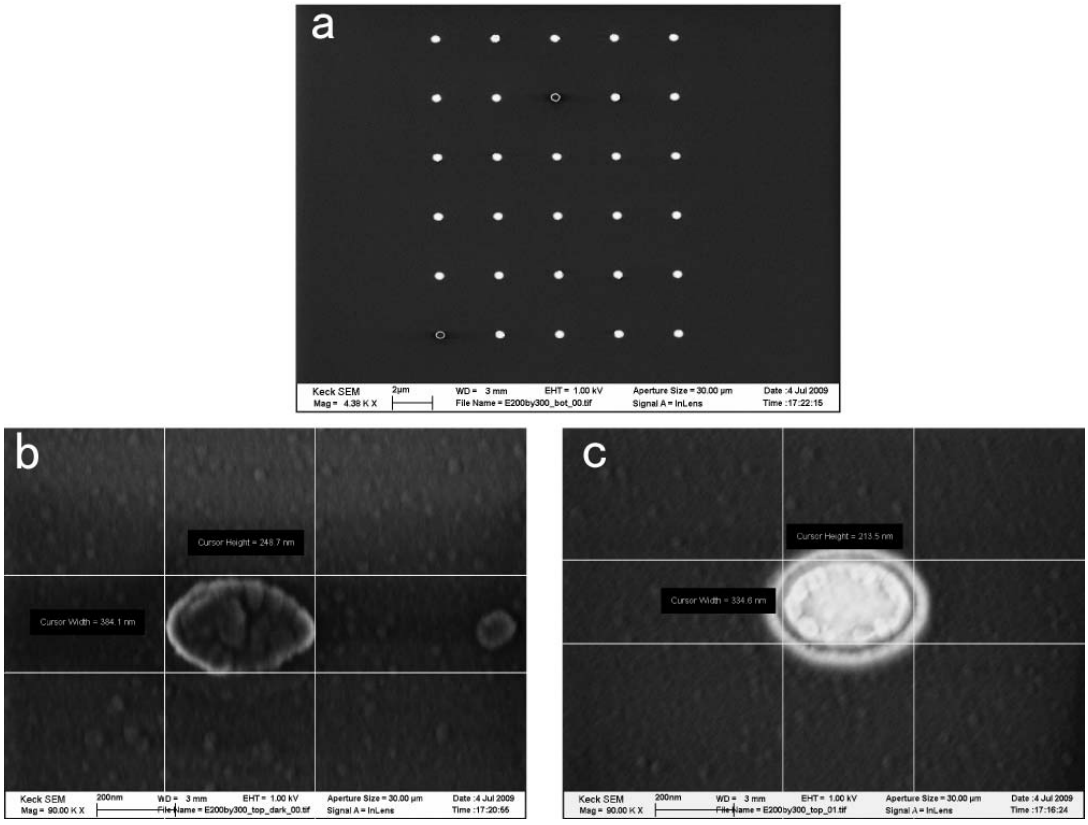

Figure 2.5 SEM images of nanopillars after the resist is stripped. (a) an array of 180 nm× 270 nm nanopillars. (b) SEM image of a darker nanopillar in (a) where the resist is not stripped (c) SEM image of a bright nanopillar in (a), the resist is already removed.

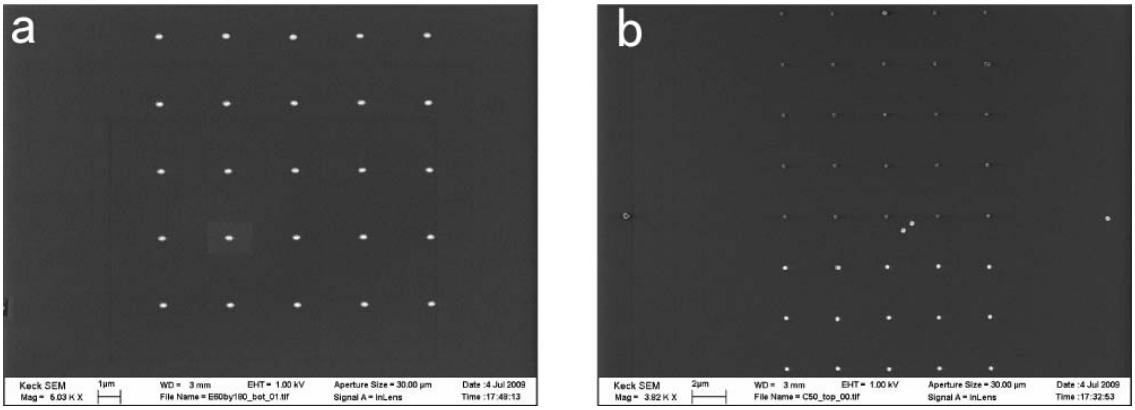

Figure 2.6 SEM images of nanopillars after the resist is stripped. (a) 180 nm× 60 nm elliptical nanopillars. (b) 100 nm× 100 nm circular nanopillars. The darker ones on the top are those that still have the resist.

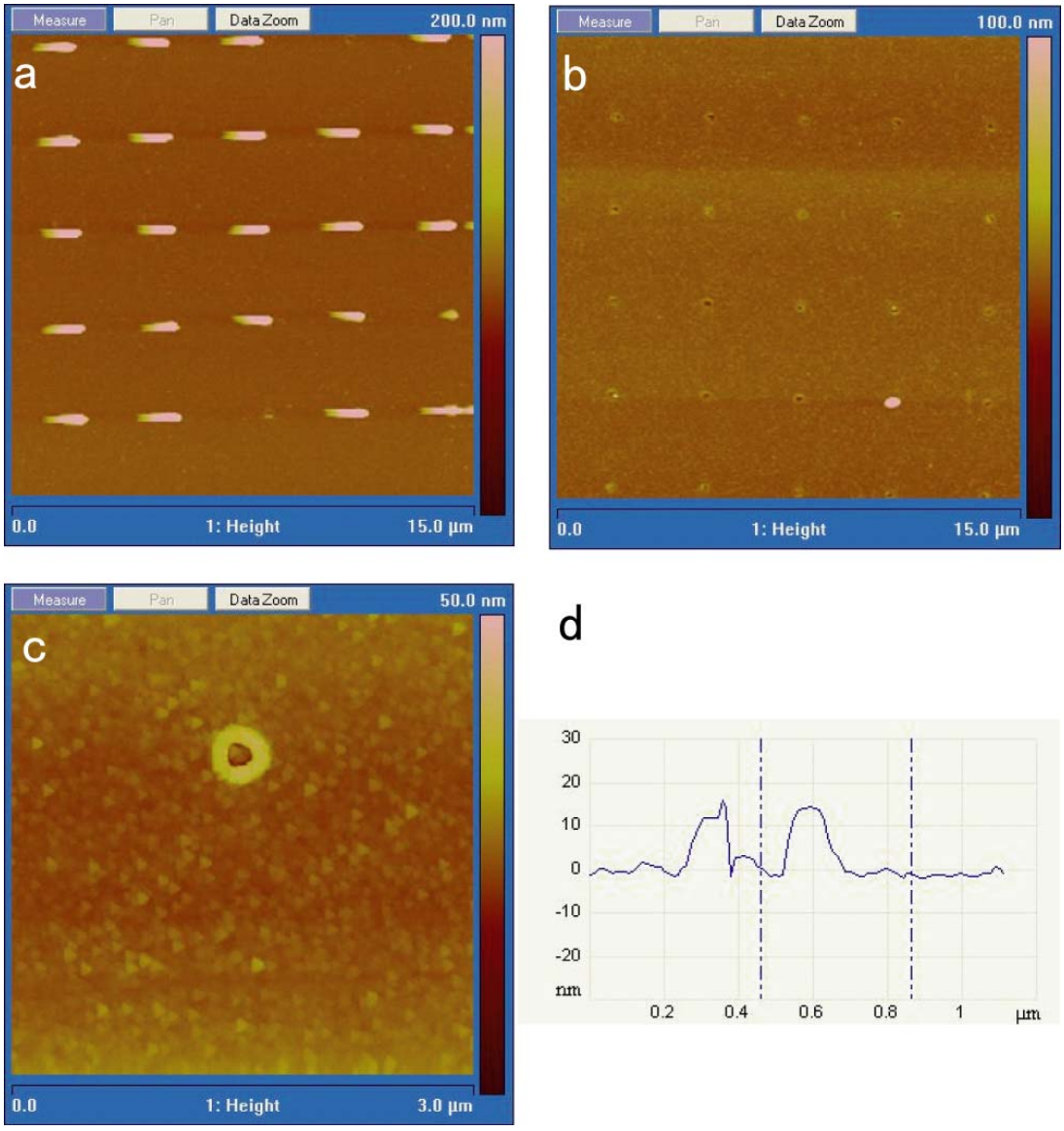

Figure 2.7 AFM images of nanopillars before and after the resists are stripped. (a) An array of 100 nm× 100 nm nanopillars before stripping the resist. (b) AFM image of the same nanopillars in (a) after the resist was stripped. (c) a single nanopillar in (b). (d) cross section scan of the nanopillar shown in (c).

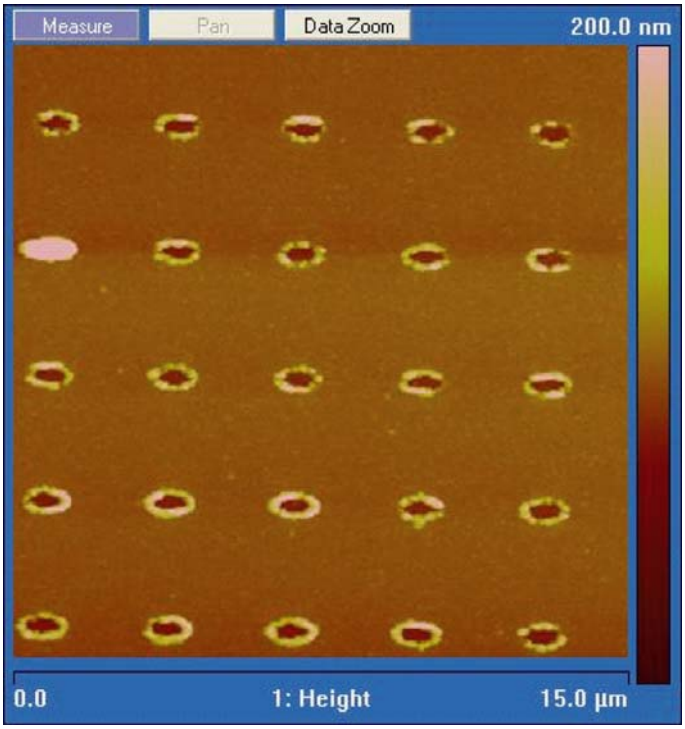

Figure 2.8 AFM image of 1 µm × 300 nm nanopillars after the resist is stripped.

REFERENCES

1. N. C. Emley, Ph.D. thesis, *Cornell University* (2006).
2. Dow Corning Corporation, Midland, Michigan 48686-0994, FOx (R) *Flowable Oxide Baseline Processing Overview.*
3. P. M. Braganca, PhD thesis, *Cornell University* (2010).
4. P. M. Braganca, O. Ozatay, A. G. F. Garcia, O. J. Lee, D. C. Ralph and R. A. Buhrman, Enhancement in spin-torque efficiency by nonuniform spin current generated within a tapered nanopillar spin valve, *Phys. Rev. B* **77**, 144423 (2008).

CHAPTER 3

REDUCTION OF THE SPIN-TORQUE CRITICAL CURRENT BY PARTIALLY CANCELING THE FREE LAYER DEMAGNETIZATION FIELD

3.1 Introduction

A large amount of attention has been paid to the study of spin transfer torque since its discovery [1-4] both because of the rich underlying physics and also the important application in magnetic memory [5-6]. While the physics associated with the spin transfer torque, both in the spin valve and magnetic tunnel junction systems, have been basically understood, there are still many technical difficulties for applications. For example, in order to be competitive with existing semiconductor based memory techniques, the spin torque MRAM needs to have very high density, low cost, high speed and low power consumption. Moreover, the fabrication process and the spin torque switching current density also need to be compatible with the CMOS technology. This is because that the one of the most promising architectures for spin torque MRAM would be one transistor one MTJ, meaning that for each of the storage cell of MTJ, there needs to be a transistor in series with the MTJ to switch it ON and OFF. Since the area of each transistor needs to be small to satisfy the requirement of high storage density, the writing current that can be provided by each transistor is very limited. Therefore, it is critical to reduce the spin torque switching current and at the same time keep the device thermally stable.

Many different strategies have been developed in order to lower the critical current for spin torque switching. First of all, the discovery of high TMR MTJ may represent one important step towards increasing the spin torque efficiency [7-8]. Compared with spin valves, where the spin polarization is in most cases 20 ~30 %,

spin polarizations higher than 70% can be easily obtained in MgO based MTJ. The increase in spin polarization makes it possible to get a lower critical current. Secondly, magnetic films with perpendicular magnetic anisotropy (PMA) have been utilized in order to get a lower critical current and higher thermal stability [9-13]. In FM films with PMA, the critical current and the thermal stability have the same dependence on the coercive field of the free layer magnet, and therefore will have a lower limit for critical current under the prerequisite of being thermally-stable (explained below). Moreover, several other methods have also been developed in order to reduce the critical current, like the use of tapered structures [14] or synthetic antiferromagnetic/ferromagnetic free layers [15].

For in-plane magnetized nanomagnets the critical current I_c is dominated by the out-of-plane demagnetization field H_d [4, 16]:

$$I_{c0} \approx \frac{2e}{\hbar}\frac{\alpha\mu_0 M_S V}{P}(H_c + \frac{1}{2}H_d) \tag{3.1}$$

where α and M_S are the Gilbert damping coefficient and saturation magnetization of the film, P represents the spin polarization, V is the magnetic volume of the nanomagnet, H_C is the coercive field and $H_d = M_{eff}$ is the demagnetization field. For most in-plane magnetized spin valves or MTJs, H_C of the free layer is usually a few hundred Oersted while H_d can be above 5000 Oe. The large demagnetization field comes from the shape anisotropy of the nanomaget. Generally, the shape anisotropy of a thin film magnet is represented by the demagnetization factor N_x, N_y and N_z. For a nanomagnet shown as in Fig. 3.1 (a), if the condition $t << w, l$ is satisfied, we have approximately $N_x \approx 2t/\pi w$, $N_y \approx 2t/\pi l$ and $N_z \approx 1$ [17]. The demagnetization field in the z direction is therefore given by $H_d^z = M_S N_Z \approx M_S$. And the in-plane coercive field can be calculated as $H_C = H_d^y - H_d^x = M_S(N_y - N_x)$. Take permalloy as an

example, M_S for the thin film permalloy is about 6.4×10^5 A/m [18]. For a typical FM free layer we have $t = 4$ nm, $w = 50$ nm and $l = 100$ nm, this leads to a demagnetization field of 8000 Oe and in-plane coercive field of 200 Oe. Therefore, I_{C0} in Equation 3.1 can be approximated as $I_{c0} \approx \frac{e}{\hbar}\frac{\alpha\mu_0 M_S V}{P} H_d$. In the meantime, this strong effective demagnetization field, unfortunately, does not contribute to the nanomagnet's thermal stability. The thermal stability of the free FM layer is determined by the in-plane coercive field H_C given that $H_C << H_d$. The energy barrier that the magnetic moment needs to overcome in the process of switching is given by $E = 0.5H_C M_y V + 0.5H_d M_z V$, where M_y and M_z satisfy $M_y^2 + M_z^2 = 1$. As is shown in Fig. 3.1 (b), the energy barrier reaches the maximum when $M_y = 0$ and $M_z = \pm 1$ and reaches the minimum when $M_z = 0$ and $M_y = \pm 1$. Therefore, thermally induced switching can be realized when the magnetic moment flips over the in-plane hard axis.

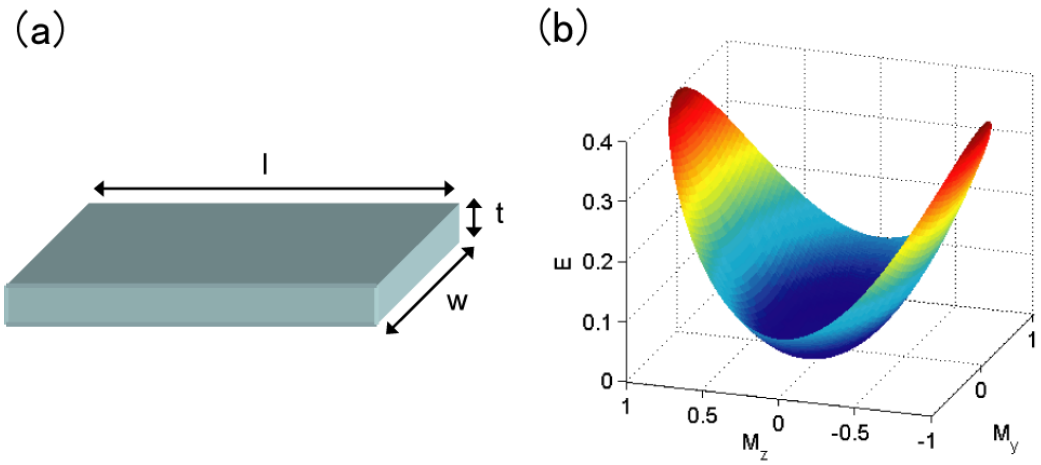

Figure 3.1 Demagnetization energy in the thin film limit. (a) schematic illustration of a thin film nanomagnet with the thickness t, length l and width w. (b) the energy barrier against switching for different (M_y, M_z) values.

In contrast, for perpendicularly magnetized FM films, in the single domain limit the critical current and the energy barrier have the same dependence on the anisotropy field. The critical current can be written as:

$$I_{c0} \approx \frac{e}{\hbar}\frac{\alpha\mu_0 M_S V}{P} H_{an} \tag{3.2}$$

where H_{an} is the effective perpendicular anisotropy field. The perpendicular anisotropy field can originate from the intrinsic crystalline anisotropy of the FM films [12-13] or from the interfacial anisotropy of specially engineered stacks [9]. The energy barrier in this case is also proportional to H_{an}: $E = 0.5\mu_0 H_{an} M_S V$. Therefore, under this condition the critical current is directly related to the energy barrier $I_{c0} = \frac{2e}{\hbar}\frac{\alpha}{P}E$. Under the requirement of 10 years of retention $E = 40k_B T$, this gives the theoretical minimum for the critical current of spin torque driven switching [16].

In principle, utilizing materials with a high PMA should be a very effective strategy for reducing I_c. However, at the early stage of the development of PMA spin torque devices, the reduction in I_{c0} is not significant in comparison with the I_{c0} of in-plane magnetized devices. This is likely due to either a low spin polarization [9, 19] or a large damping [13] in the PMA materials that have been employed. Another disadvantage associated with the PMA approach is the large dipole field that the fixed layer exerts on the free layer [9, 19], an effect that can be eliminated for the in-plane magnetized case with the use of properly balanced synthetic antiferromagnetic (SAF) fixed layers. A continuous fixed layer could possibly address this dipole field problem for the out-of-plane case, but it is likely that this will greatly limit the integration density of ST-MRAM. The use of PMA fixed layer material with a low net saturation magnetization (M_s) could also address this problem but that approach faces a number of materials challenges before it can be fully realized.

Instead of making the magnetic moment of the FM layers fully out of plane, the reduction of critical current can also be realized by simply reducing the demagnetization field of the free magnetic layer. Rather than employing a material with a very large $H_{K\perp}$ that dominates H_d of the free layer, we can only partially cancel H_d with a moderate $H_{K\perp}$. Since I_c is expected to scale with the H_d, so a reduction of an order of magnitude can be achieved if H_d is decreased from the normal value to close to H_C. At the same time, the fact that the free layer magnetic moment still lies in plane provides a large freedom in the choice of the fixed layer materials and structures, making this approach highly flexible.

3.2 Experiment

3.2.1 Reducing the demagnetization field in ferromagnetic films

In a system where both the demagnetization energy and perpendicular crystalline/interfacical anisotropy energy exist, the total energy of the system is:

$$E_{tot} = E_{K\perp} + E_{demag} = K\cos^2\theta + \frac{1}{2}N_D M_S^2 \sin^2\theta = (K - 0.5N_D M_S^2)\cos^2\theta + const. \quad (3.3)$$

Here K is the coefficient for crystalline anisotropy, N_D is the demagnetization factor, θ is the angle between the magnetic moment and the film plane. So the mixed anisotropy is still uniaxial, and the magnetic moment will end up being either in the film plane (when $K < 0.5N_D M_S^2$) or perpendicular to the film plane (when $K > 0.5N_D M_S^2$). No intermediate angles are allowed within this first order approximation for $E_{K\perp}$. Therefore, our goal here was to obtain a K that satisfies $K < 0.5N_D M_S^2$ while ensuring that $0.5N_D M_S^2 - K$ was small.

As is shown in Fig. 3.2, as early as in 1990s, Daalderop *et al.* [20] showed that by varying the thickness of each layer in a Co/Ni multilayer and/or the number of

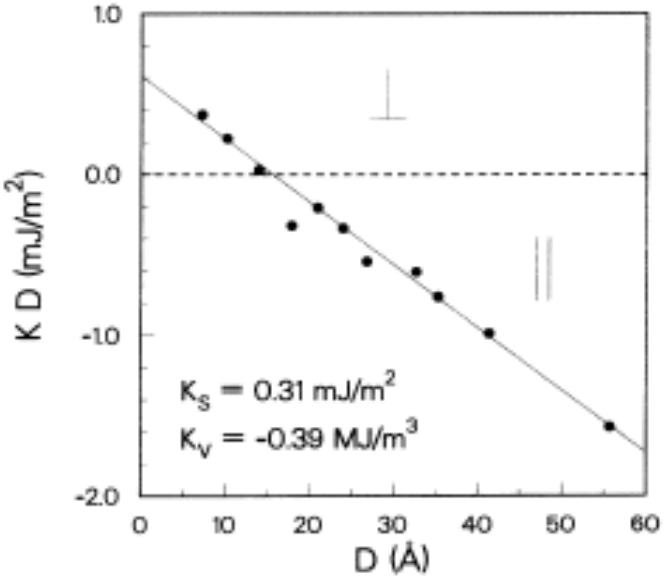

Figure 3.2 Change of effective anisotropy energy with the variation in the thickness of Co/Ni bilayer. The anisotropy energy is measured from $[Co/Ni]_N$ multilayers but normalized with the number of repeats N. The ratio between the thickness of Co and Ni layers is kept constant at 2.2:1. The figure is taken from [20].

repeats, the perpendicular anisotropy field can be continuously tuned within a wide range, from the in-plane magnetized regime to the perpendicular regime. Even where the interfacial anisotropy energy K and the demagnetization energy $0.5N_D M_S^2$ are close to each other (E_{tot} is close to zero), the contribution from the 2nd order term of the anisotropy energy is not obvious. So from equation 3.3, the system can be well described by an effective demagnetization field $H_d^{eff} = H_d^{in} - H_{an} = M_S - 2K / M_S$, where the intrinsic demagnetization field is $H_d = M_S$ in the thin film limit ($N_D = 1$).

In our experiment, Co/Ni multilayers were deposited using a DC sputtering system with a base pressure less than 5 x 10^{-9} torr. A $[Ta(5)/CuN_x(20)]_3/Ta(5)/Cu(3)$ (thickness in nm) seeding layer was used to provide a smooth base layer with [111] texture, as verified by x-ray diffraction. The growth rate was controlled to be low (<

0.05 nm/s) to increase the crystalline texturing. A control experiment was carried out in which a single layer of Cu was used as the bottom layer, but no strong perpendicular anisotropy was observed, suggesting that the seed layer is important for PMA. Co/Ni multilayers with different thicknesses and repeats were tested, and it turned out that $[Co(0.4)/Ni(1)]_2/Co(0.4)$ multilayers have a low H_d. Typical perpendicular-to-plane *M-H* curves, as measured by a vibrating sample magnetometer (VSM), of continuous film samples of this low demagnetization field (LD) material are as shown in Fig. 3.3. For comparison, we also made a control sample composed of Ni(2)/Co(1.2) which has the same total thickness for both Co and Ni as the LD sample, but which exhibits high demagnetization field (HD). And the *M-H* response for the HD sample is represented by the blue dots in Fig. 3.3. From the perpendicular *M-H* curves, we can easily see that the demagnetization field of the LD sample was reduced from ~7000 Oe to ~ 600 Oe due to the presence of the perpendicular anisotropy arising from the multiple Co/Ni interfaces. The in-plane *M-H* curve for the LD sample shows that the in-plane remnant magnetization is ~0.9 M_S, indicating a good easy-plane anisotropy.

3.2.2 Spin valve device with reduced demag field

With the free layer composition determined above, full stacks composed of seeding layer/free layer/Cu(8nm)/permalloy(20nm)/capping layer were deposited for spin valve devices. The stacks were then patterned into elliptical nanopillars with the cross section ~90 nm × 190 nm through the combination of e-beam lithography and ion-beam etching. HD control samples of the same device size were also made with the same stack composition, except with the free layer being replaced with a simple Ni(2)/Co(1.2) structure. At least three devices of the same nominal size of each type of sample were measured in detail. Similar results were obtained for the devices of each

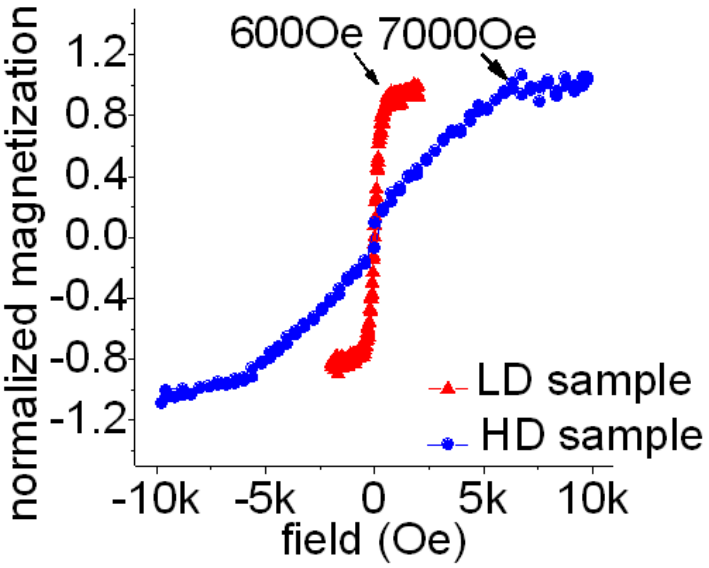

Figure 3.3 Perpendiculr to plane M-H curves for Co/Ni films. The red triangles correspond to [Co(0.4)/Ni(1)]2/Co(0.4) (units in nm) film, while the blue circles represent Ni(2)/Co(1.2) thin film.

type. All of the following data are from one typical device of the two different types.

The minor magnetoresistance loop of a typical LD device, as taken at room temperature, is shown in Fig. 3.4 (a). Its coercive field H_c is ~43 Oe and the magnetoresistance is ~40 mΩ. The current scan was taken with the dipole field (H_{dip}) from the simple permalloy fixed layer cancelled by an applied external field (H_{app}) [Fig. 3.4 (b)], and the switching currents were determined to be ~0.14 mA for both the antiparallel to parallel (AP to P) switching and the parallel to antiparallel (P to AP) switching. For comparison, the corresponding minor loop and spin transfer loop for the HD sample are represented by the blue curve in Fig. 3.4(a) and (b), respectively, with H_c ~ 52Oe and ΔR ~ 60mΩ, and the switching currents were: $I_{AP\text{-}P}$ = 0.81mA and $I_{P\text{-}AP}$ = 1.24mA. It can be noted from these two different devices that ΔR of the HD sample is about 1.5 times larger than that of the LD sample. This difference may be due to different spin polarization values in the Co/Ni films. Although both the LD and

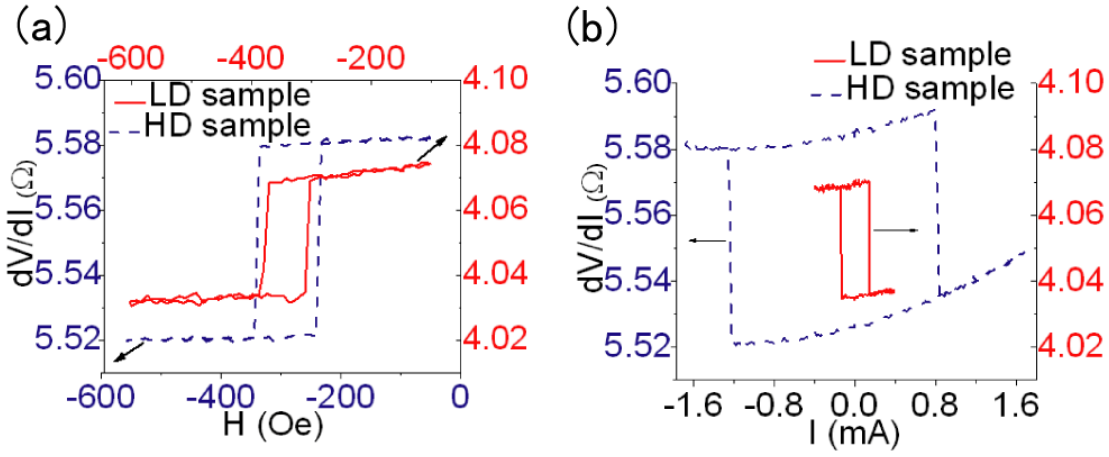

Figure 3.4 Comparisons of the magnetic and spin transfer behaviors between the HD and LD samples. (a) Magnetoresistance minor loop for the LD sample (red solid) and HD sample (blue dash), respectively. (b) Spin transfer loop for the LD sample (red solid) and HD sample (blue dash), respectively. All of the data are taken at room temperature.

the HD free layers are terminated with Co, the thicknesses of that terminating Co layer are different. For the LD sample it is 0.4 nm, while it is 1.2 nm for the HD sample. Previous experiments have shown that a Co thickness of order ~1nm is needed to fully achieve the maximum spin filtering effect [21].

3.2.3 Ramp rate measurement and pulse measurement

To determine the energy barrier E against thermally activated magnetic reversal and the zero-thermal-fluctuation critical current I_{c0}, a ramp rate measurement was carried out for both the LD sample and the HD sample. The results are shown in Fig. 3.5 (a) and (b). In the thermally activated switching regime, the switching current $<I_c>$ and ramp rate $\dot{I}$ have the following relation [22-23]:

$$< I_c >= I_{c0}[1-\frac{k_B T}{E}\ln(\frac{k_B T}{E}\frac{I_{c0}/\tau_0}{\dot{I}})], \qquad (3.4)$$

where τ_0 is the fluctuation attempt rate, which is assumed to be 1 ns. For each point, we obtained $<I_c>$ by averaging over 25 scans. For the LD sample we obtained: $U_{AP\text{-}P}$ =

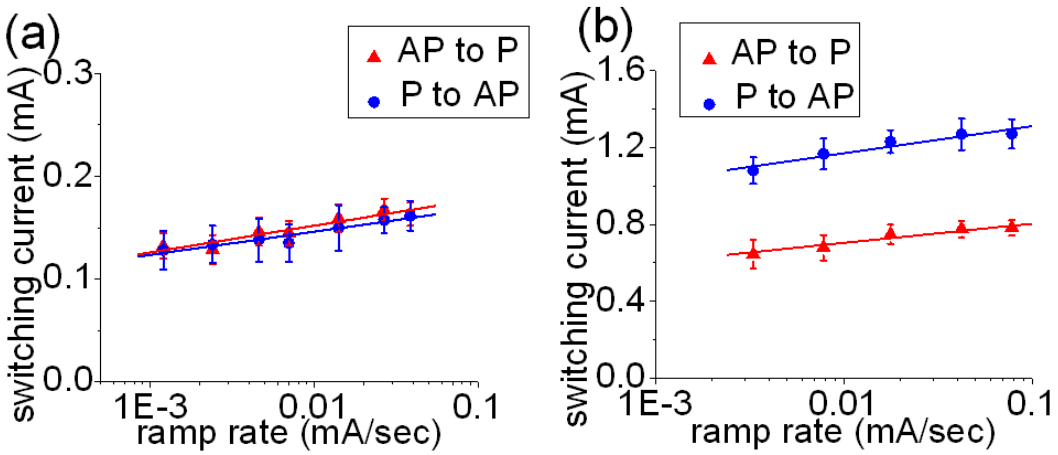

Figure 3.5 Switching currents of spin valves as a function of the ramp rate. (a) ramp rate measurement from LD sample. (b) ramp rate measurement from HD sample. The red triangles stand for AP to P switching and the blue circles for P to AP switching.

0.88 eV, $U_{P\text{-}AP}$ = 0.92 eV and $I_{c0,AP\text{-}P}$ = 0.39 mA, $I_{c0,P\text{-}AP}$ = 0.35 mA. Corresponding parameters for the HD sample were extracted in the same way: $U_{AP\text{-}P}$ = 0.996 eV, $U_{P\text{-}AP}$ = 1.08 eV and $I_{c0,AP\text{-}P}$ = 1.66 mA, $I_{c0,P\text{-}AP}$ = 2.54 mA. By comparing the two groups of data, we can easily see that the critical current is reduced by a factor of ~5 for both directions, while the thermal stability is compromised by less than 20%. As is discussed in the previous section, the non-thermal-assisted critical current I_{c0} is proportional to the effective demagnetization field H_d given that $H_d >> H_C$. The decrease of critical current (~ 5x) agrees reasonably well with the reduction in H_d (~ 11x) after taking the change in spin polarization (~ 1.5x) into account. The deviation from the expected value may come from the fact that for H_d ~ 600 Oe, the relationship $\frac{1}{2}H_d \gg H_c$ does not hold precisely. (Note H_c here should be the non-thermal fluctuation value). So the relationship of $I_{c0} \propto H_d$ should be replaced with $I_{c0} \propto (0.5H_d + H_C)$ in this regime. The decrease in thermal stability is in good agreement with the measured H_c value.

A practical ST-MRAM element should work at the ns timescale so pulse measurements with pulse width varying from 1ns to 10ns were made to study the switching behavior in this regime. The results are summarized in Fig. 3.6 (a) and (b). According to the spin transfer theory, within the macrospin approximation, in the intrinsic ST-switching regime a linear relationship should exist between the switching speed τ^{-1} and the amplitude of the applied current pulse I [16]:

$$\tau^{-1} = \frac{P(\mu_B / e)}{M_s V \ln(\pi / 2\theta_0)}(I - I_{c0}), \quad \tau^{-1} = \zeta \cdot (I - I_{c0}) \quad (I > I_{c0}) \tag{3.5}$$

where θ_0 is the initial angle between the free layer magnetic moment and its equilibrium position. The deviation from a linear relationship in the high current regime, where τ = 1ns, is observed for both types of samples as has been reported elsewhere [14, 24] and is perhaps due to non-uniform effects in the high speed reversal. So the 1 ns points were ignored in the linear fits. The values of I_{c0} are:, $I_{c0,AP\text{-}P}$ = 0.28 mA, $I_{c0,P\text{-}AP}$ = 0.36 mA for the LD sample, and for the HD sample, $I_{c0,AP\text{-}P}$ = 1.74 mA, $I_{c0,P\text{-}AP}$ = 1.79 mA. These numbers agree reasonably well with the values obtained from the ramp rate measurement given the differences in the reversal process in the two cases. According to equation 3.5, the slopes of the ST switching curves ζ are determined by the spin polarization P and the initial angle θ_0 when the magnetic moment of the free layer is fixed. Since P_{HD} is about 1.5 times larger than P_{LD}, we should expect that the slopes scale the same way. However for AP to P switching, we find $\zeta_{HD} / \zeta_{LD} \approx 1$, and $\zeta_{HD} / \zeta_{LD} \approx 1.8$ for P to AP switching. This difference can be qualitatively explained by the difference in micromagnetic configurations in the two cases [25]. As is shown in the insets in Fig. 3.6, the free layer magnetization of the LD device curls or cants significantly out of plane near its edges to minimize the magnetostatic energy in response to the non-uniform dipole field arising from the cant of magnetization in the fixed layer due to its taper [14]. But for the HD sample,

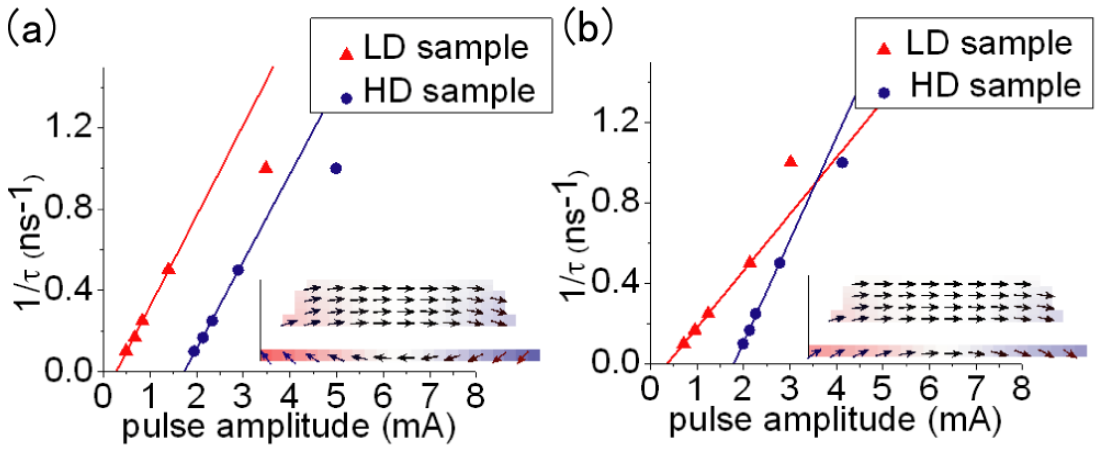

Figure 3.6 Pulse measurement of the switching currents. (a) The inverse of pulse width as a function of the pulse amplitude for AP to P switching with the red triangles for LD sample and the blue circles for HD sample. (b) The inverse of pulse width as a function of the pulse amplitude for P to AP switching. Inset: Micromagnetic simulations showing the cants in both the fixed layer and the free layer magnetization. Only the LD samples are shown here since there are no significant cants associated with the HD sample.

no significant curling is observed for the free layer in the micromagnetic simulation due to its higher anisotropy. For the LD sample, in the AP (P) state, the fixed layer and the free layer will curl in the opposite (same) direction, hence resulting in a large (small) initial angle θ_0. This difference in the initial angle affects the switching speed in these two configurations [14]. The cants observed in the LD sample can also account for the reduction in the coercive field and in the thermal stability as well.

A further demonstration that the reduction of I_c is due to the decreased H_d rather than other factors, such as a change in magnetic moment, comes from results obtained with a Co/Ni sample with four repeats, i.e., the free layer being composed of $[Co(0.4)/Ni(1)]_4/Co(0.4)$. VSM determined that $H_d \sim 1000$ Oe for this material. As is shown in Fig. 3.7, ramp rate and pulse measurement on a device with this free layer yielded: $I_{c0,AP\text{-}P} \approx 0.95$ mA, $I_{c0,P\text{-}AP} \approx 0.62$mA (ramp rate) and $I_{c0,AP\text{-}P} \approx 0.6$mA and $I_{c0,P\text{-}}$

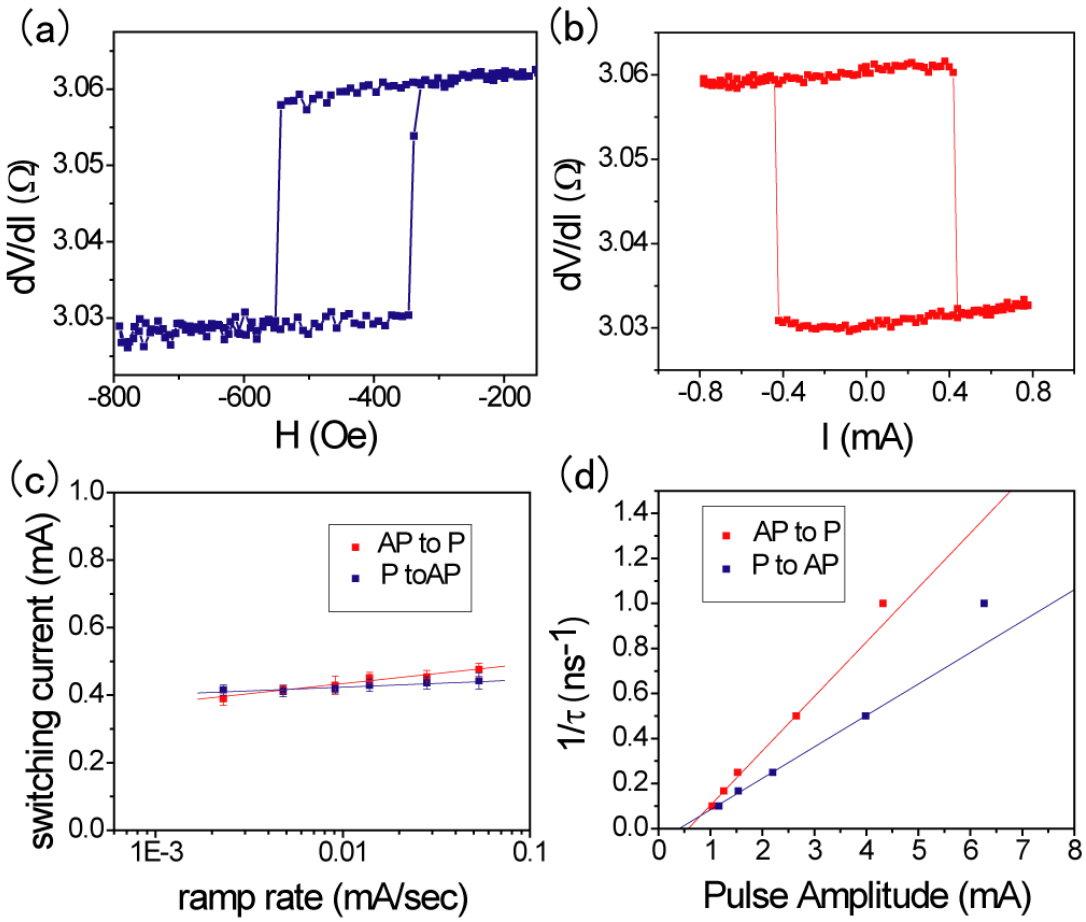

Figure 3.7 Switching behaviors of a sample with four repeats. (a) Magnetoresistance minor loop for the sample with four repeats of Co/Ni bilayer. (b) Spin transfer loop of the sample. Ramp rate (c) and short pulse (d) measurement for the same sample. The red points are for AP to P switching and the blue points are for P to AP switching.

$_{AP}$≈ 0.4mA (pulse). These numbers agree well with the Co/Ni bilayer sample, considering that its magnetic moment is roughly twice that of LD sample and HD sample.

3.3 Outlook

The work of reducing the critical current by introducing interfacial perpendicular anisotropy and partially canceling the demagnetization field was carried out around 2008. Since then, there has been significant progress in the area of utilizing

the PMA of magnetic thin films. Here I will give a brief review of this more recent research

3.3.1 Recent progress in spin torque devices with perpendicular anisotropy

First of all, after the demonstration of feasibility of reducing the critical current by decreasing H_d, naturally the next step would be to verify this approach in the MTJ system since for the real MRAM device, an MTJ instead of a spin valve should be utilized to achieve a large TMR ratio. Also compared with spin vavles, MTJs generally have a higher spin polarization, therefore lead to even smaller critical current. One of the major difficulties in reducing the demagnetization field in a MTJ lies in the mismatch of the crystalline structure between different layers. Since high quality MTJs are mostly obtained from MgO based systems which use amorphous CoFeB (before annealing) as the FM electrode, it is necessary to combine the CoFeB electrode into the FM stacks which can have the low H_d at the same time. This was demonstrated by T. Moriyama *et al* at Cornell in 2010 [26]. By inserting a thin CoFeB layer (1.1 nm) between the Co/Ni stack and the MgO barrier, one could achieve a TMR around 50%. At the same time, due to the exchange interaction between the Co/Ni stack and CoFeB layer, the demagnetization field of the free layer as a whole can be reduced from its bulk value of 1.3 Tesla to ~ 0.2 Tesla. The critical current also decreases correspondingly. Everspin is now working to commercialize this approach of utilizing MTJs with free layers that have reduced demagnetization field for magnetic memories.

Meanwhile, major advances have also been made in the study of MTJs with fully perpendicularly magnetized films. First of all, S. Ikeda *et al* showed that strong PMA can be achieved by using the intrinsic interfacial magnetic anisotropy associated

with the CoFeB/MgO interface and this PMA will dominate over the demagnetization field of the CoFeB free layer when its thickness is below 1.3 nm [27]. This represents a major step towards the practical utilization of PMA in spin torque MRAM because it avoids the use of additional materials or structures, which usually have high damping coefficient and low spin polarization, as is mentioned in the introduction section of this chapter. And this discovery also greatly reduces the critical current for spin torque switching from sub mA region to below 50 μA, which is very promising for applications. Secondly, the other problem associated with perpendicularly magnetized spin torque device is also resolved through technical progresses: an SAF fixed layer with perpendicular anisotropy was successfully demonstrated in 2010 [28]. Now the large dipole field associated with PMA materials is addressed and both the P and AP states can be accessible under no external biasing field. Companies like IBM and others are now working to commercialize magnetic memories utilizing MTJs with perpendicular magnetized layers.

3.3.2 Possible applications of devices with reduced demagnetization field

As is discussed in the introduction section, the advantage with perpendicularly magnetized films lies in that it is possible to get a higher storage density because the coercive field in the perpendicularly magnetized samples is usually larger than that obtained from in-plane magnetized samples, whose H_C originates from the shape anisotropy. Therefore, it is commonly believed that in order to be competitive with semiconductor memories, perpendicular magnetized films need to be utilized. The same concept has already been verified in the hard disk media, where the prevailing material used as the media in today's hard disk drives is PMA FM layers. Although it is quite likely that the mainstream MRAM will use magnetic materials with PMA, MTJs with in-plane magnetized free and fixed layers may still be useful in several

areas. For example, besides standalone memory, there are other needs for non-volatile memories where the storage density is not the highest priority. For example, for embedded memories that are designed to be used inside logic devices, the area of the MTJ cell may not be critical because usually there will be more than one transistors in each cell and the density is no longer determined by the area of the MTJ. In this kind of situation, in-plane magnetized MTJs with the dimension around 100 nm can still be competitive because of the compatibility in fabrication process with CMOS technology and because of the ease for film growth. So the strategy of utilizing a reduced demag field can be still useful in these areas. Another advantage associated with in-plane magnetized FM layer is that it is possible to realize ultra-fast switching using the in-plane free layer and out-of plane polarizer layer. Experimentally, it is demonstrated that sub-ns switching could be realized using this kind of geometry [29]. What's more, in-plane magnetized FM free layer can be used in conditions where the perpendicularly polarized spin current is unavailable, for example, in the spin Hall effect case. This point will become clearer in Chapter 7 and Chapter 9.

REFERENCE

1. J. C. Slonczewski, Current-driven excitation of magnetic multilayers, *J. Magn. Magn. Mater.* **159**, L1 (1996).
2. L. Berger, Emission of spin waves by a magnetic multilayer traversed by a current, *Phys. Rev. B* **54**, 9353 (1996).
3. E. B. Myers, D. C. Ralph, J. A. Katine, R. N. Louie and R. A. Buhrman, Current-induced switching of domains in magnetic multilayer devices, *Science* **285**, 867 (1999).
4. J. A. Katine, F. J. Albert, R. A. Buhrman, E. B. Myers and D. C. Ralph, Current-driven magnetization reversal and spin-wave excitations in Co/Cu/Co pillars, *Phys. Rev. Lett.* **84**, 3149 (2000).
5. J. A. Katine and E. E. Fullerton, Device implications of spin-transfer torques, *J. Magn. Magn. Mater.* **320**, 1217 (2008).
6. D. C. Ralph and J. Z. Sun, Magnetoresistance and spin-transfer torque in magnetic tunnel junctions, *J. Magn. Magn. Mater.* **320**, 1227 (2008).
7. S. S. P. Parkin, C. Kaiser, A. Panchula, P. M. Rice, B. Hughes, M. Samant and S. H. Yang, Giant tunnelling magnetoresistance at room temperature with MgO (100) tunnel barriers, *Nature Mat.* **3**, 862 (2004).
8. S. Yuasa, T. Nagahama, A. Fukushima, Y. Suzuki and K. Ando, Giant room-temperature magnetoresistance in single-crystal Fe/MgO/Fe magnetic tunnel junctions, *Nature Mat.* **3**, 868 (2004).
9. S. Mangin, D. Ravelosona, J. A. Katine, M. J. Carey, B. D. Terris and E. E. Fullerton, Current-induced magnetization reversal in nanopillars with perpendicular anisotropy, *Nature Mat.* **5**, 210 (2006).
10. D. Ravelosona, S. Mangin, Y. Lemaho, J. A. Katine, B. D. Terris and E. E. Fullerton, Domain wall creation in nanostructures driven by a spin-polarized current, *Phys. Rev. Lett.* **96**, 186604 (2006).
11. H. Meng and J. P. Wang, Spin transfer in nanomagnetic devices with perpendicular anisotropy, *Appl. Phys. Lett.* **88**, 172506 (2006).
12. T. Seki, S. Mitani and K. Takanashi, Nucleation-type magnetization reversal by spin-polarized current in perpendicularly magnetized FePt layers, *Phys. Rev. B* **77**, 214414 (2008).
13. M. Nakayama, et al., Spin transfer switching in TbCoFe/CoFeB/MgO/CoFeB/TbCoFe magnetic tunnel junctions with perpendicular magnetic anisotropy, *J. Appl. Phys.* **103**, 07a710 (2008).
14. P. M. Braganca, O. Ozatay, A. G. F. Garcia, O. J. Lee, D. C. Ralph and R. A. Buhrman, Enhancement in spin-torque efficiency by nonuniform spin current generated within a tapered nanopillar spin valve, *Phys. Rev. B* **77**, 144423 (2008).
15. J. Hayakawa, S. Ikeda, Y. M. Lee, R. Sasaki, T. Meguro, F. Matsukura, H. Takahashi and H. Ohno, Current-induced magnetization switching in MgO barrier based magnetic tunnel junctions with CoFeB/Ru/CoFeB synthetic ferrimagnetic free layer, *Jpn J Appl Phys 2* **45**, L1057 (2006).

16. J. Z. Sun, Spin-current interaction with a monodomain magnetic body: A model study, *Phys. Rev. B* **62**, 570 (2000).
17. R. C. O'Handley, *Modern Magnetic Materials : Principles and Applications*. (Wiley, New York, 2000).
18. I. N. Krivorotov, N. C. Emley, J. C. Sankey, S. I. Kiselev, D. C. Ralph and R. A. Buhrman, Time-domain measurements of nanomagnet dynamics driven by spin-transfer torques, *Science* **307**, 228 (2005).
19. S. Mangin, Y. Henry, D. Ravelosona, J. A. Katine and E. E. Fullerton, Reducing the critical current for spin-transfer switching of perpendicularly magnetized nanomagnets, *Appl. Phys. Lett.* **94**, 012502 (2009).
20. G. H. O. Daalderop, P. J. Kelly and F. J. A. Denbroeder, Prediction and Confirmation of Perpendicular Magnetic-Anisotropy in Co/Ni Multilayers, *Phys. Rev. Lett.* **68**, 682 (1992).
21. S. K. Upadhyay, R. N. Louie and R. A. Buhrman, Spin filtering by ultrathin ferromagnetic films, *Appl. Phys. Lett.* **74**, 3881 (1999).
22. F. J. Albert, N. C. Emley, E. B. Myers, D. C. Ralph and R. A. Buhrman, Quantitative study of magnetization reversal by spin-polarized current in magnetic multilayer nanopillars, *Phys. Rev. Lett.* **89**, 226802 (2002).
23. J. Kurkijar, Intrinsic Fluctuations in a Superconducting Ring Closed with a Josephson Junction, *Phys. Rev. B* **6**, 832 (1972).
24. S. Kaka, M. R. Pufall, W. H. Rippard, T. J. Silva, S. E. Russek, J. A. Katine and M. Carey, Spin transfer switching of spin valve nanopillars using nanosecond pulsed currents, *J. Magn. Magn. Mater.* **286**, 375 (2005).
25. M. J. Donahue and D. G. Porter, OOMMF User's Guide, Version 1.0, National Institute of Standards and Technology Technical Report No. NISTIR 6376, (1999).
26. T. Moriyama, T. J. Gudmundsen, P. Y. Huang, L. Q. Liu, D. A. Muller, D. C. Ralph and R. A. Buhrman, Tunnel magnetoresistance and spin torque switching in MgO-based magnetic tunnel junctions with a Co/Ni multilayer electrode, *Appl. Phys. Lett.* **97**, 072513 (2010).
27. S. Ikeda, et al., A perpendicular-anisotropy CoFeB-MgO magnetic tunnel junction, *Nature Mat.* **9**, 721 (2010).
28. I. Tudosa, J. A. Katine, S. Mangin and E. E. Fullerton, Perpendicular spin-torque switching with a synthetic antiferromagnetic reference layer, *Appl. Phys. Lett.* **96**, 212504 (2010).
29. O. J. Lee, V. S. Pribiag, P. M. Braganca, P. G. Gowtham, D. C. Ralph and R. A. Buhrman, Ultrafast switching of a nanomagnet by a combined out-of-plane and in-plane polarized spin current pulse, *Appl. Phys. Lett.* **95**, 012506 (2009).

CHAPTER 4

SPIN HALL EFFECT IN METALS

The spin Hall effect (SHE) was first predicted theoretically about 40 years ago [1]. Because of the existence of spin orbit coupling, it was proposed that electrons with different spin orientations would be spatially separated by the impurity scattering when a charge current was applied onto a semiconductor. Therefore, pure spin current and spin accumulation were expected to be formed within a non-magnetic material. Unlike the ordinary Hall effect or the anomalous Hall effect (AHE), where the phenomena can be easily detected through the transverse electric voltage, the SHE corresponds to an imbalance in electrons spins instead of electron charges and therefore it was difficult to verify the concept experimentally. It was not until about 2000 that people re-examined the idea and proposed ways to experimentally detect this effect [2-3]. Meanwhile, thanks to the development of the theories in anomalous Hall effect [4], people realized that the SHE could be treated as an analogue of the AHE in non-magnetic materials and previous knowledge about the interaction between spin and current could be directly borrowed from AHE. The prediction of the existence of the SHE is no longer limited to semiconductor systems but also extended to metals. Besides the extrinsic impurity scattering mechanism, intrinsic effects which come from the band structure of the material were also proposed as a possible source for the spin current [5-6]. The magnitude of the spin Hall effect is described by the spin Hall angle θ_{SH}, which is defined using the ratio between the transverse-flowing spin current density $(\hbar/2)J_S/e$ and the applied charge current density J_e: $\theta_{SH} = J_S/J_e$. Theoretically it was predicted that an inverse effect could also exist, where a pure spin current can be converted into a charge current by the same spin orbit scattering

mechanism. And it is known that the efficiency of this inverse spin Hall effect (ISHE) was given by the same spin Hall angle, $J_e = \theta_{SH} J_S$ [2].

The SHE was first discovered experimentally in 2004 by Kato *et al*. [7] in semiconductor systems using magneto-optical Kerr effect. In their experiment, a charge current was applied through the GaAs thin film, and out of equilibrium spins were accumulated at opposite sides of the GaAs channel due to the SHE, which further induced changes in the signal of Kerr rotation. Instead of employing an optical technique, SHE in metallic system was first verified using an all electric measurement technique [8]. As proposed in ref. [3], ferromagnetic probes were employed to detect the spin current by the SHE. Fig. 4.1 shows the samples used to study the SHE in metals, where spin current was injected from the ferromagnetic electrode into the SHE material and the voltage generated by the ISHE was read out from a Hall cross.

Following the initial discoveries of the SHE, many different techniques have been developed for the determination of the spin Hall angle, both in the DC and RF regime. Especially large spin Hall angles were discovered in metals [9-10], making SHE a promising way to generate or detect spin current. In the rest of this chapter, I will focus my discussion on the SHE in metallic systems. In section 4.1 ~ 4.3, I will review experiments that are used to determine the spin Hall angle. In section 4.3 I will talk about experiments that utilize SHE to manipulate the magnetic moment. And in section 4.4 I will discuss another utilization of the SHE, i.e., to use the ISHE to detect spin current.

4.1 Measurement of the SHE using non-local spin valves

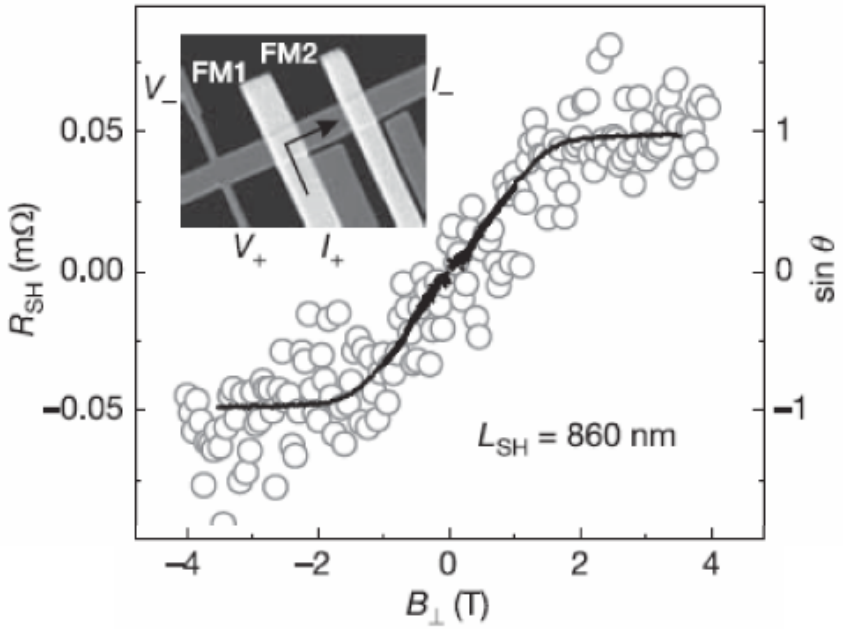

Figure 4.1 ISHE in a non-local spin valve. Left *y* axis shows the measured spin Hall resistance and the right axis represents the out of plane angle of the injected spins converted from R_{SH}. The field was applied perpendicular to the plane. Inset: SEM image of the device used to detect the voltage generated by the ISHE. Current was injected from I+ end through the FM1 electrode (CoFe 400 nm) into I- end of the Al strip. The voltage was measured through the V_+/V_- ends of the Hall bar patterned on the Al strip. Figures reproduced from ref. [8].

4.1.1 Review of the experiments

As we mentioned above, the SHE was first electrically measured in metals using geometries of non-local spin valves [8]. The structures of non-local spin valves were first developed in the 1980s to study spin injection and accumulation in normal metals [11]. Since the spin current is not accompanied with a net charge current inside these geometries, the large intrinsic resistance of the metals won't make a contribution. Therefore, spin accumulation can be measured with very high signal to noise ratio. So the non-local spin valve also makes an ideal geometry for the study of SHE. As is shown in inset of Fig. 4.1, an aluminum film was patterned into a Hall bar and two FM

electrodes were deposited onto the Al film. Current was injected from FM1 and flowed towards to the right, away from the Hall cross. So, there was no net charge current at the cross point but only spin current. Because of the ISHE, the non-local spin current was converted into a measurable voltage that can be detected from the two ends of the Hall cross V_+ and V_-. Because of the large easy plane anisotropy of the CoFe electrode, the equilibrium position of the magnetic moment lies in the film plane. Under a large perpendicular magnetic field $B_\perp$, the magnetic moment m begins to tilt out of plane and the orientation of the injected spins σ should also be aligned along m. Since the charge current density generated by the ISHE is given by $\vec{J}_e = \theta_{SH}\vec{\sigma} \times \vec{J}_S$, it is easy to check that the Hall voltage gets its maximum when the injected spins are aligned fully out of plane. The spin Hall angle was determined to be ~1- 3 × 10^{-4} for Al by fitting the $R_{SH} \sim B_\perp$ curve with the drift diffusion model.

Kimura *et al.* from the Otani group continued this effort, but worked on a different system made of Pt [9]. Pt was studied because theoretically the spin Hall effect should be larger in heavy metals due to the stronger spin orbit coupling. In their work, both the SHE and ISHE were measured and it was shown that the spin Hall angle determined from these two approaches were equivalent. As is shown in Fig. 4.2, the Py electrode was connected to the Pt strip through a Cu bridge. In the ISHE case [Fig. 4.2 (a)], similar to the Al case, current flowed from the permalloy electrode into the copper layer and a non-local spin current was injected into the copper layer and diffused into the Pt wire. The transverse voltage generated across the Pt due to the inverse spin Hall effect was measured. In the SHE experiment, charge current was applied along the Pt wire and the spin current was injected from Pt into the Cu wire due to the SHE [Fig. 4.2 (b)]. The resulting spin accumulation at the Cu/permalloy interface was detected electrically. The generated voltage was due to the imbalance of

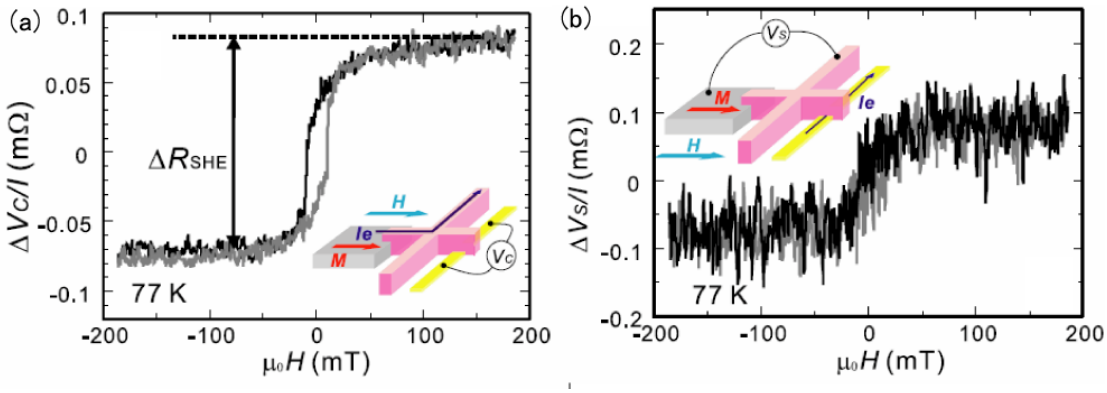

Figure 4.2 DSHE and ISHE measurement for Pt. (a) The change of the spin Hall resistance versus the applied in-plane field. The spin current was injected from the FM electrode and a DC voltage V_c due to the ISHE in Pt was measured. (b) Spin accumulation signal due to the spin current generated by the DSHE. The charge current was applied in the Pt strip and the spin current was injected from the Pt into the Cu bridge, the voltage V_S is formed due to the spin accumulation at the Cu/FM interface. Both experiments were carried out at 77 K and the field was applied along the in-plane easy axis. Figures are reproduced from ref. [9].

the spin dependent electrochemical potentials on the opposite sides of the interface. Unlike the previous experiment where the spin current flows in the film plane, in the Py/Cu/Pt structure, the spin current is injected into or extracted from Pt vertically. Therefore, in-plane fields instead of out of plane fields were needed to modulate the spin orientation. As is shown in the Fig. 4.2, the spin Hall resistances measured in both of the two configurations are the same, which is consistent with the Onsager reciprocal relations. The spin Hall angle was determined to be 0.0037.

This work on Pt was pioneering in that it was the first experiment to demonstrate the direct spin Hall effect in a metal, and it also showed that the spin Hall conductivity in Pt is much larger than in semiconductors and aluminum. However, the initial results were not quantitatively correct because of several reasons: (i) The spin diffusion length of Pt λ_{sf} was not accounted for in this first effort. It was assumed implicitly in the paper that the spin current was injected into the Pt without any decay

and there was also no spin accumulation at the Pt/substrate interface. This is not correct because the SHE or the ISHE will only be significant within the range of λ_{sf} at the Pt/Cu interface. When the thickness of Pt d is larger than λ_{sf}, the bottom part of the Pt film will not contribute to the SHE or ISHE signal. If d is smaller than λ_{sf} then the spin accumulation at the Pt/substrate interface will cause a backflow spin current which can also reduce the real spin current. (ii) The amount of spin current injected into the Pt is not accurate. In this experiment, the spin current density injected into Pt was calculated using the spin polarization of Py after considering the spin diffusion length of Cu bridge, but the real spin current injected into Pt can be heavily influenced by the transparency of the Py/Cu and Cu/Pt interfaces. (iii) The original analysis of the data did not take into account the fact that the Cu wire in contact with Pt will shunt the current flowing inside Pt. At the cross point of the Cu/Pt interface, the current distribution is non-uniform while this paper assumes that all of the current flows inside Pt. This can greatly influence the final result because compared with Pt, Cu is much more conductive and the shunting effect could result in a large underestimation in the spin Hall angle.

The first two effects that I mentioned above were taken into account in their following works. In ref. [12] and [13], the effect of the finite spin diffusion length was accounted for by considering the non-uniform spin current distribution along the injection direction, although there may still be some inaccuracy in the value of the spin diffusion length that they assumed. And in order to get a better estimate on the spin current injected into Pt, they also modified the geometry used in ref. [9]. In the new structures, the Pt nanowire is put between two FM electrodes, and the spin current injected into Pt was estimated from the reduction of the non-local spin valve signal. As for the third problem, after some initial communications [14], in 2011 the authors

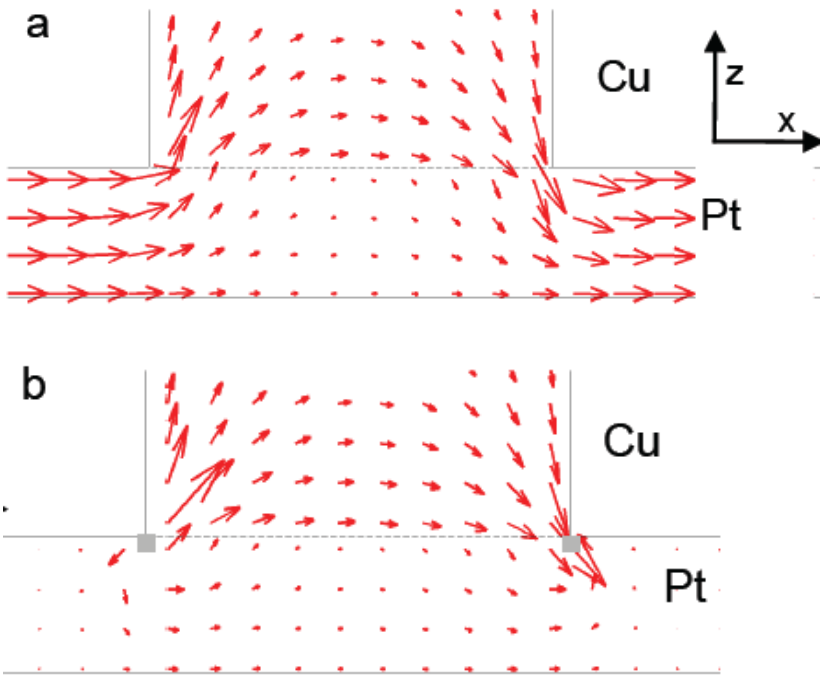

Figure 4.3. Current distribution at the cross point of a Pt/Cu bridge. (a) Calculated charge current distribution in a Cu/Pt device in the SHE experiment, the current is shunted by a Cu overlayer above a Pt wire when current flow is generated by application of a voltage between the ends of the Pt wire. Only a part of the Cu overlayer is shown. (b) Calculated backflow charge current distribution generated by the inverse spin Hall effect when the spin diffusion length is 2 nm. In both panels, each arrow represents the value of the charge current density at the position of the arrow's base, not its midpoint. We assume that the Pt layer is 20 nm thick and the Cu overlayer is 100 nm long and 100 nm thick. The shaded regions in (b) show approximately where the source term $\nabla \bullet J_{ISHE}$ is nonzero. We use $\sigma_{Pt}/\sigma_{Cu} = 0.13$.

began to apply a correction within their analyses to account for the shunting (see the supplemental material for ref. [15] and ref. [13]). After taking all of the effects above into account, their updated values for the spin Hall angle in Pt (measured at 10 K) was $\theta_{SH} \approx 0.021$ [13].

4.1.2 Analysis on the current distribution

In this section, I will focus on the shunting effect caused by the copper wire at the Cu/Pt interface. We will see that there are still some inaccuracies in the correction procedure used in ref. [13] and ref. [15]. The discussion on the shunting effect should also apply to other types of SHE experiments where the spin Hall effect material is in contact with a FM or NM metal, for example, the ISHE experiment based upon spin pumping that we will talk about in section 4.2.

The current distributions in the SHE and ISHE experiments at the cross point of the Pt/Cu bridge are given in Fig. 4.3 (a) and (b), in which the arrows indicate the direction and relative magnitude of the local charge density near a Cu/Pt interface. In the SHE configuration [Fig. 4.3 (a)], since Cu has a larger electrical conductivity than Pt (ref. [13] gives $\sigma_{Cu} = 48 \times 10^6$ $(\Omega\text{m})^{-1}$ compared to $\sigma_{Pt} = 6.4 \times 10^6$ $(\Omega\text{m})^{-1}$) and the Cu wire is also much thicker than the Pt, a majority of the charge current will be shunted through the Cu, and the charge current density in the Pt near the Cu interface will be greatly reduced. This decrease in the charge current flowing in the Pt will reduce the spin accumulation in Cu arising from the spin Hall effect by a factor x_S (relative to the value under the assumption that all the charge current flows within the Pt) and will therefore cause an underestimate of θ_{SH} by the same factor. In the ISHE [Fig. 4.3 (b)], the Cu overlayer will affect the final result similarly. The spin current injected from the Cu into the Pt gives rise to a transverse charge current flowing in the Pt. The experiment of Kimura *et al.* [9] measured the voltage generated across the Pt wire under an open circuit condition that no net charge current flowed to the external circuit. The measured voltage in this case is therefore determined by the condition that a backward-flowing current associated with the voltage cancels the forward-flowing current generated by the inverse spin Hall effect. In the original analysis performed by Kimura *et al.*, it was assumed that the backward-flowing current arising from the

voltage would flow only within Pt wire. However, for the device geometry studied, the voltage will actually drive backflow charge current in both the Pt and the Cu overlayer, which means that much less voltage is required to cancel the forward-going ISHE current than would be the case if no charge current flowed within the Cu. (The need to correct for this shunting effect in inverse spin Hall experiments was pointed out by references [16] and [17]). A quantitative analysis shows that the shunting decreases the inverse spin Hall signal by the same factor x_S as for the direct spin Hall effect experiment, leading to the same underestimate of θ_{SH} in the inverse spin Hall effect measurement as for the direct spin Hall effect measurement.

The correction procedure introduced in references [13, 15] by the Otani group determines the fraction of the lateral component of the charge current that flows in the spin Hall metal compared to the total current through the bilayer device when a voltage is applied between the two ends of the Pt wire. (To determine the correction factor, the lateral component of the charge current in the spin Hall metal is averaged over the lateral direction and summed over the full film thickness in the vertical direction.) This correction factor of x was used to account for the reduction of the spin Hall signal due to the shunting effect. But we will see that the shunting factor x determined here is not the same as the factor that should be used to describe the reduction in the spin Hall signal x_S. The relation of $x = x_S$ holds only in the limit that the spin diffusion length is much greater than the film thickness of the spin Hall metal, so that the entire thickness of the spin Hall film contributes equally to the direct spin Hall or inverse spin Hall signal. However, if the thickness of the spin Hall metal layer is greater than the spin diffusion length λ_{sf} (as is the case for all of the materials studied in ref. [13]), the assumption of $x = x_S$ actually underestimates the shunting effect and therefore result in a smaller value for the spin Hall angle.

4.1.2.1 Correction for the shunting effect in SHE

It is easy to understand why we have $x \neq x_S$ for the SHE case in general. In the SHE configuration, the current distribution near the Cu interface looks like the schematic illustration in Fig. 4.3 (a). Note that this current distribution varies with position both in the lateral and vertical directions. In the vertical direction, because of shunting by Cu the current density in the spin Hall metal near the Cu interface can be significantly smaller than the charge current density averaged over the full thickness of the spin-Hall-metal film. When computing the strength of the spin current that will be injected into the Cu by the spin Hall effect, only the lateral charge current density flowing in the spin Hall metal within a distance of approximately the spin diffusion length from the Cu will contribute; the charge current density flowing near the bottom of the spin Hall metal wire will be immaterial. Consequently, when λ_{sf} is short the reduction in the strength of the spin Hall signal is more severe than indicated by the shunting-induced correction factor *x* that describes the reduction in the total current averaged over the full thickness of the spin-Hall-metal wire, *i.e.* $x_s < x$ when $\lambda_{sf} < t_{SHM}$. In Fig. 4.4 we plot calculations of the lateral component of the charge current density in the spin Hall metal, averaged over lateral positions within the shunting region, as a function of vertical position in the spin Hall metal, for the cases corresponding to the resistivities of Pt and Ta (Ta is discussed here because Ta represents a type of SHE material which has even lower conductivity, so more severe shunting effect could exist). (We use $\sigma_{Pt} / \sigma_{Cu} = 0.13$ and $\sigma_{Ta} / \sigma_{Cu} = 0.005$, corresponding to the values in ref. [13].) These results suggest that the local charge current density near the Cu interface in the case of Pt/Cu is about 50% of the current density averaged over the full thickness of the Pt wire and in the case of Ta/Cu it is approximately only 10% of the full-thickness averaged charge current density (the

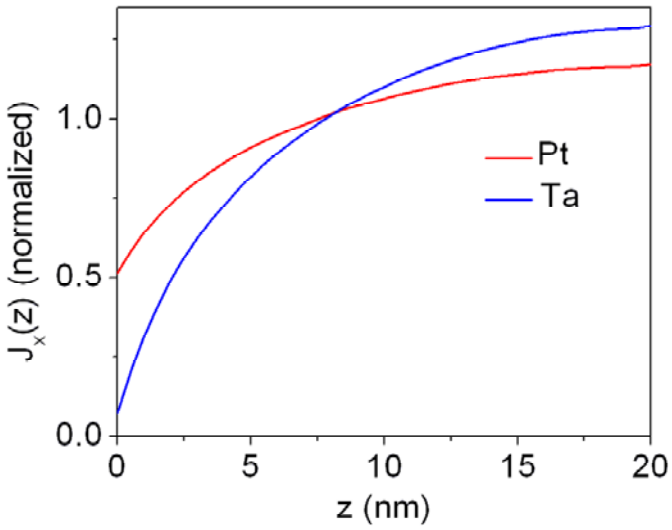

Figure 4.4. Distribution of the current density J_x in the spin Hall metal. The *x* component of the current density was averaged over the *x* direction and plotted as a function of the vertical distance z from the interface with Cu ($z = 0$ is the interface position). The values are normalized relative to the average value $\langle J_x(z) \rangle$ over the whole thickness of the spin Hall metal film for each material.

difference between materials being due to the much lower conductivity of Ta). If the spin diffusion length is on the scale of 1 nm for both Pt and Ta, it is the charge current density very close to the Cu interface that contributes to the direct spin Hall effect, not the value averaged over the full film thickness.

4.1.2.2 Correction for the shunting effect in ISHE

By the Onsager reciprocity principle, the correction factors should be the same for both the spin Hall and inverse spin Hall experimental configurations, so the correction factor obtained in section 4.1.2.1 should also be applicable to the ISHE case. However, it will be helpful to analyze ISHE independently to get a more intuitive picture.

In the case of an inverse spin Hall effect configuration, the proper correction procedure should be to (i) calculate the ISHE charge current density J_{ISHE} generated by the injected spin current. (ii) under the current continuity requirement, $\nabla \cdot (J_{ISHE} + J_{\varphi}) = 0$, calculate the back flow charge current density J_{φ}. (iii) integrate J_{φ} in the NM and Cu bridge separately and get the final correction factor.

In the system as is shown in Fig. 4.3 (b), the current continuity equation should hold to give a reasonable steady state solution, otherwise charge accumulation would be formed inside the system and grow with time. To calculate the shunting correction factor, one can perform a finite-element calculation for the electric potential φ that maintains consistency with the continuity equation:

$$\nabla \cdot (\vec{J}_{\varphi} + \vec{J}_{ISHE}) = 0 = \nabla \cdot (-\sigma \nabla \varphi + \vec{J}_{ISHE}) \quad , \tag{4.1}$$

and

$$\nabla^2 \varphi = \nabla \cdot \vec{J}_{ISHE} / \sigma \, . \tag{4.2}$$

By using equation (4.1) and (4.2), we can get the actual distribution of the backflow charge current density J_{φ} in Pt as is plotted in Fig 4.3 (b). Here, we assumed that the spin diffusion length of Pt is λ_{sf} = 2 nm and J_{ISHE} is generated uniformly within the distance of λ_{sf} from the Pt/Cu interface.

Instead of using the correction procedure described above, ref. [13, 15] used a different approach to account for the shunting effect in the ISHE. In their analysis, they (i) calculated the total charge current generated in the spin-Hall-metal wire by the inverse spin Hall effect, taking into account that this may be nonuniform in the vertical direction because of the finite spin diffusion length and (ii) calculated how much voltage must be applied between the ends of the spin-Hall-metal wire to produce a

backflow current in the total bilayer that cancels (globally) the current generated by the inverse spin Hall effect, so that the overall net current leaving the device is zero. That is, this procedure assumes that the backflow current distribution may be calculated *independently* of the spatial distribution of the current density arising from the inverse spin Hall effect. This assumption is, however, incorrect because the two portions of the charge current density J_{ISHE} and $J_{\varphi} = -\sigma\nabla\varphi$ are not independent; the steady-state equation of continuity for the total charge current density $\nabla \cdot (J_{ISHE} + J_{\varphi}) = 0$ must hold locally everywhere within the sample. The charge current distributions determined in references [13] and [15] do not satisfy the continuity equation because the solutions for J_{φ} are based on the assumption that $\nabla \cdot J_{\varphi} = 0$ everywhere within the sample volume, despite the fact that $\nabla \cdot J_{ISHE}$ is explicitly nonzero in the regions of the spin Hall metal directly under the edges of the Cu overlayer where the inverse spin Hall charge current originates and ends. The way to calculate the current density in ref. [13, 15] is actually equivalent to Fig. 4.3 (a), where the charge current density J_{φ} due to the applied voltage V at the wire ends is determined. It can be seen that this distribution is significantly different than the backflow charge current density pattern calculated by the correct procedure in Fig. 4.3 (b), particularly in the lower half of the spin Hall metal wire.

4.2 Experiments based upon spin pumping

4.2.1 Magnetic field provided by microwave cavities

Besides the DC electrical measurement, there is another category of experiments that were widely used for the study of SHE, or more accurately the ISHE. In this type of experiments, spin pumping was employed to inject spin current into a nonmagnetic metal and DC charge current was generated through the ISHE. As is

shown in Fig. 4.5 (a), Permalloy/Pt bilayer film was put inside a microwave cavity and RF magnetic field was applied onto the sample. Ferromagnetic resonance will take place when the frequency of the RF magnetic field and the amplitude of the applied DC magnetic field satisfy the resonance condition. When the magnetic moment of the FM layer undergoes precession around its equilibrium position, pure spin current can be injected into the adjacent NM film due to the spin pumping [18-19]. The spin current extracted from the FMR has the form of $J_S\vec{\sigma} \propto \vec{m} \times \partial\vec{m}/\partial t$ and can be absorbed by materials that act like a good spin sink, such as Pt or Pd. The damping coefficient is therefore increased.

The absorption coefficient of microwave power by a Permalloy/Pt bilayer sample was measured as a function of the applied DC magnetic field in Fig. 4.5 (b) [20]. The linewidth of the resonance peak is proportional to the effective Gilbert coefficient of the FM layer. It can be seen that compared with the resonant peak of single layer of Permalloy film, the linewidth of the Permalloy/Pt bilayer film is significantly higher, reflecting the spin pumping mechanism. The spin current injected into the Pt layer is converted into a charge current due to the ISHE and a DC voltage *V* can be measured under the open circuit condition [Fig. 4.5 (c)]. The measured *dV/dI* curve is very similar to lineshape of the absorption of the microwave power, indicating that origins of the observed signal are due to the spin pumping and ISHE. What's more, the signal can only be observed when the orientation of the injected spins has a component perpendicular to the measured electric field, consistent with the equation of the ISHE $\vec{J}_e = \theta_{SH}\vec{\sigma} \times \vec{J}_S$.

In this initial effort, the ISHE signal was qualitatively illustrated, but no value of the spin Hall angle was obtained. This is probably partly due to the difficulty in

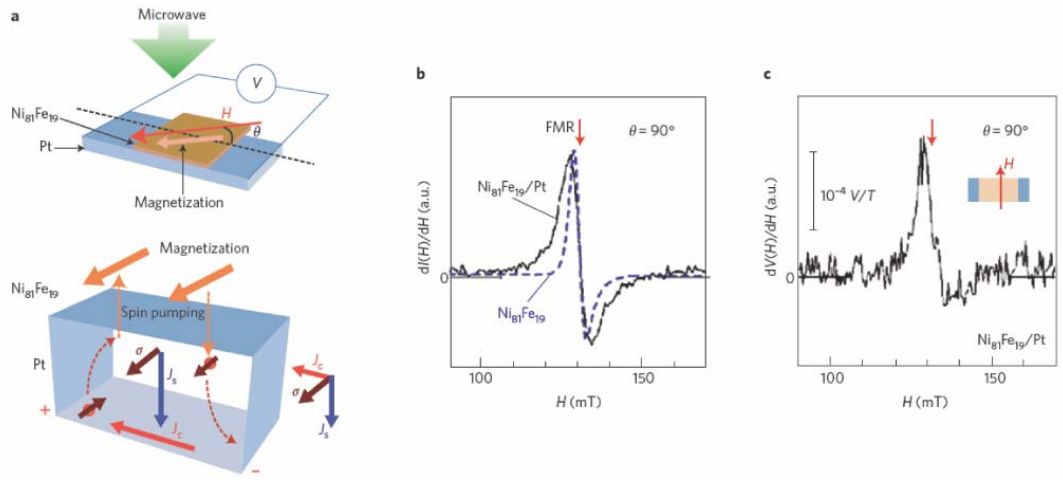

Figure 4.5 Measurement on ISHE using ferromagnetic resonance spin pumping. (a) Schematic of the permalloy/Pt sample used in the study. Microwaves were used to drive the ferromagnetic resonance of the permalloy layer. J_S represents the spin current injected from permalloy into Pt due to the spin pumping and J_c is the charge current generated from the ISHE. (b) Magnetic field dependence of the FMR signal for the Permalloy/Pt bilayer film and a pure Permalloy sample. I is the intensity of the absorbed microwave. (c) Magnetic field dependence of dV/dH for the Permalloy/Pt sample. V is the voltage due to the ISHE. Figure reproduced from ref. [20].

determining the amplitude of the RF magnetic field in the microwave cavity. Another factor that influenced the experiment was the existence of the anisotropic magnetoresistance (AMR) effect. Besides the ISHE, the AMR can also contribute to the final DC voltage measured in the experiment [21]. As is known, the AMR in FM films has the form of $R = R_0 + \Delta R \cos^2 \theta$, where θ represents the angle between the current flowing direction and the magnetic moment orientation. In resonance, the oscillation of the magnetic moment will naturally induce an oscillation in the resistance of the sample δR. Inside the microwave cavity, the RF magnetic field (H_{RF}) is generally accompanied by an RF electric field (E_{RF}), which further induces an oscillating current I_{RF}. The I_{RF} and δR can be mixed together and result in a measurable DC voltage. Similar to the ISHE signal, the DC voltage generated from the

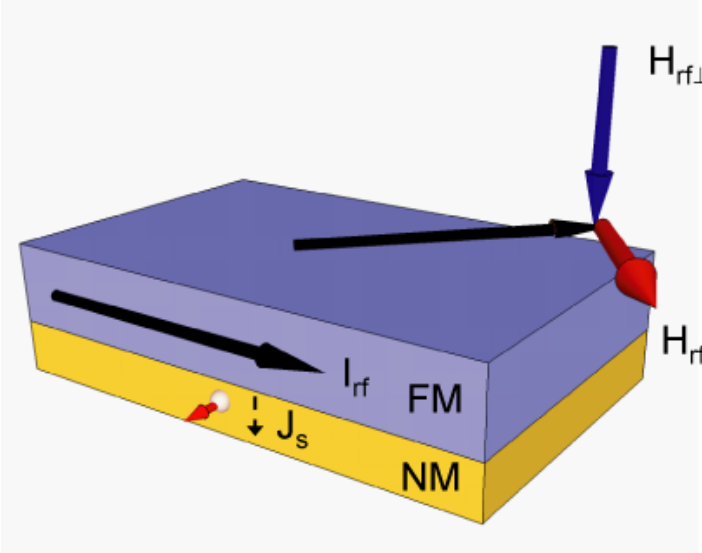

Figure 4.6 Schematic illustration of the direction of the rf magnetic field. $H_{rf//}$ and $H_{rf\perp}$ represent the RF magnetic field parallel to the sample film and perpendicular to the film, separately. I_{rf} is the electric current induced by the RF electric field. J_S stands for the spin current injected into the NM due to the spin pumping.

AMR effect also has a Lorentzian lineshape when the DC magnetic field is swept and generally it is difficult to separate those two effects apart.

As is shown in Fig 4.6, in the most general case, the RF magnetic field can be decomposed into three components: the component perpendicular to the sample plane $H_{rf\perp}$, the component in the film plane but perpendicular to the magnetic moment $H_{rf//}$ and the component completely parallel with the magnetic moment. It is easy to check that the component parallel with the magnetic moment will not contribute to the magnetic dynamics of the FM layer and therefore can be neglected. The torques generated by the two field components $\tau = m \times H_{rf//(\perp)}$ will be in the perpendicular and in-plane direction, separately. In the meanwhile, an rf charge current I_{rf} can be induced by the RF electric field existing in the microwave cavity. If H_{rf} and I_{rf} have the same phase, it can be checked mathematically that in resonance the torque perpendicular to

the plane will give rise to an anti-symmetric Lorentzian lineshape and the torque parallel to the film plane can give rise to a symmetric Lorentzian in the V versus H curves (For the mathematical derivation, see section 5.2). Since the signal due to the ISHE also has a form of symmetric Lorentzian lineshape, the final measured voltage will be a mixture of these three effects. Note that here we make the assumption that H_{rf} and I_{rf} are in-phase, which may not always hold because the phase of the induced I_{rf} is generally dependent upon the capacitance and inductance of the effective circuit that contains the sample and the leads. If there is any difference between the phases of H_{rf} and I_{rf}, the lineshapes due to $H_{rf//}$ and $H_{rf\perp}$ will be both a mixture of symmetric and antisymmetric Lorentzian, and are even more difficult to tell apart.

To exclude the contribution from the AMR effect, Azevedo *et al.* [22] carried out a measurement where they studied the angle dependence of the measured DC voltage signal. In this experiment, the AMR and ISHE contributions to the resulting dc voltage were separated by analyzing the signal as a function of rotation angle between the sample and the cavity. The direction of the applied DC magnetic field was kept fixed relative to the orientation of the cavity. By extracting the ISHE signal from the measured total signal, they finally obtained a value for the spin Hall angle γ_H = 0.08 ± 0.01. However, the analysis of Azevedo *et al.* does not account properly for the shunting of the ISHE signal by the permalloy layer as explained in section 4.1.2.2, which can result in an underestimate for γ_H.

Recently, the microwave-cavity based techniques have been improved by placing the sample in a position along the axis of a cylindrical cavity so that by the symmetries of the electromagnetic fields no oscillating current is induced within the Pt/ferromagnet bilayer and hence no AMR contribution is present [23-25]. Another

signal that might arise in large-area samples from the anomalous Hall effect is also absent by virtue of the absence of any induced oscillatory current. Therefore the dc voltage outputs of these experiments are due entirely to the spin-pumping/ISHE effect, and the analysis of the signals is simplified. Ando *et al.* [25] analyzed the signals from Pt/permalloy films and took into account the shunting effect as is discussed in section 4.1.2.2 and finally obtained the spin Hall angle of $\theta_{SH} = 0.04$.

4.2.2 Magnetic field provided by coplanar waveguides

Besides using a microwave cavity, FMR can also be excited by RF magnetic fields generated from a coplanar waveguide (CPW). Compared to a microwave cavity, the CPW can have some advantages, *e.g.*, various frequencies instead of a single fixed frequency can be used to drive the FMR. And it is also believed that it is easier to estimate the amplitude of the RF magnetic field in the CPW structure.

A quantitative measurement of the ISHE using a CPW was performed by Mosendz *et al.* at the Argonne National Laboratory [26]. They used the magnetic field from an oscillating current in an Au coplanar waveguide situated above (and electrically insulated from) a Pt/permalloy bilayer wire to drive magnetic resonance in the permalloy, and measured a DC voltage signal along the Pt/permalloy bilayer [Fig. 4.7]. As we discussed above, the DC voltage was generated by a combination of two effects: (a) spin pumping together with the inverse spin Hall effect (ISHE) and (b) an anisotropic magnetoresistance (AMR) signal. In their analysis they argued that the spin-pumping/ISHE signal should be strictly a symmetric function of applied field relative to the midpoint of the resonance peak, while the AMR signal should be strictly antisymmetric. In an initial analysis [26] they determined that $\theta_{SH} = 0.0067$ for their

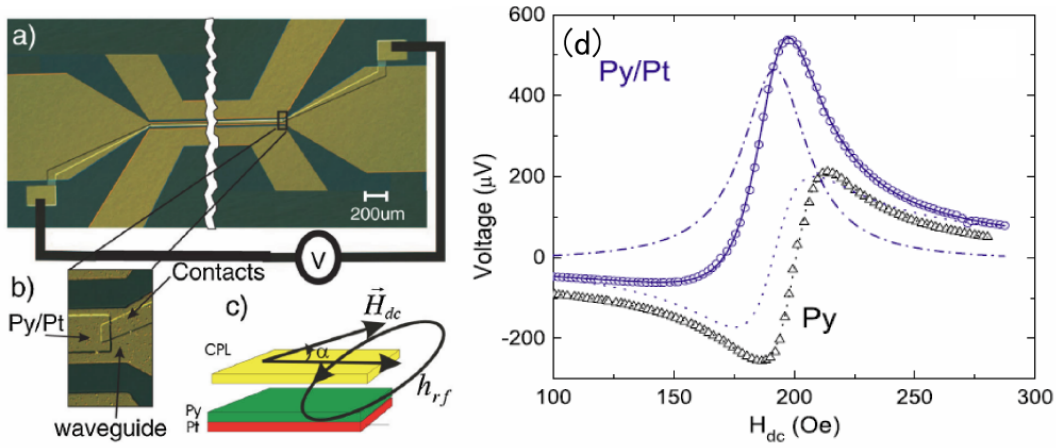

Figure 4.7 ISHE experiment based upon CPW. (a) and (b) microscope images for the experimental setup. (c) Schematic illustration of the locations of the signal line of the CPW and the Pt/Py sample, as well as the orientation of the rf magnetic field h_{rf} and the DC magnetic field H_{dc}. (d) DC voltage generated by the ISHE and AMR effect. Samples of Py/Pt bilayers and Py single layer are compared. Figures are reproduced from ref. [26].

Pt at room temperature, and their analysis was later refined by accounting for the ellipticity of magnetic precession to give $\theta_{SH} = 0.013 \pm 0.002$ [17].

Several factors can influence the accuracy of the spin Hall angle determined in this experiment. First of all, as we discussed above, the AMR component of the signal need not be a strictly antisymmetric function of applied field relative to the center of the resonance because the in-plane rf magnetic field and the induced current need not be exactly in phase at resonance as argued by Mosendz *et al.*, and therefore a more complicated analysis is required to separate the AMR and spin-pumping/ISHE contributions to the experimental signal. Both Azevedo *et al.*[22] and Harder *et al.* [21] show experimental evidence from FMR measurements on ferromagnet/nonmagnetic-metal bilayer devices that the phase between the current and the magnetization oscillations at resonance can be different than 90° and can change depending on the microwave frequency. Secondly, the choice of the spin diffusion length of Pt can also influence the value of the spin Hall angle. So far spin diffusion length for Pt has been

determined in several experiments and the obtained numbers are quite different from each other [12, 22, 27-28]. In all of the ISHE experiments that we discussed, the spin Hall angle depends upon the spin diffusion length through: $\theta_{SH} \propto V_{ISHE} / [\tanh(t_{NM} / 2\lambda_{sf})\lambda_{sf}]$ [17]. So, given the same measured DC voltage V_{ISHE}, different choices of λ_{sf} could result in totally different θ_{SH}. Since the spin diffusion length is closely related to the scattering that electrons experience inside the material, a self-consistent measurement on the spin diffusion length is highly desirable for each experiment, to account for the possible differences in film quality. So in conclusion, a more detailed analysis which takes into account the possible phase difference in H_{rf} and I_{rf} and uses the correct spin diffusion length is required to get the correct spin Hall angle from the experiments of ref. [17, 26].

4.3 Spin torque generated by the SHE

Most of the experiments that we talked about above actually studied the inverse spin Hall effect, where the spin current was injected into the non-magnetic material and DC charge current or voltage was measured. The ISHE experiment provides a convenient way for detecting the effect since the final signal is simply a voltage, which can be easily measured. In the meanwhile, the direct spin Hall effect, the conversion of a charge current into a spin current, also attracts quite a lot of interest because of the potential to be used as a source for spin current. Now since the result of the effect is no longer an electrically detectable quantity, we need to rely on the interaction between the spin current and a magnetic moment to determine the existence and magnitude of this effect. In this section, I will review the experiments that employed the spin current generated from the SHE for magnetic moment manipulation.

4.3.1 Tuning the damping coefficient

The first experiment that showed that the spin Hall effect can be used to modulate the magnetic properties of ferromagnetic films was carried out by Ando *et al.* of the Saitoh group [10]. Similar to the microwave-cavity-based ISHE experiment, Ando *et al.* excited FMR by placing the Pt/permalloy bilayer sample inside a cavity. Instead of measuring the generated DC voltage, they applied a DC current onto the bilayer sample. And it turned out that the linewidth of the FMR peaks could be modified by the applied DC current. This is because the spin current could be generated inside Pt from the applied charge current due to the SHE. This spin current was further injected into the adjacent permalloy layer and resulted in a spin transfer torque at the interface. As is known, a dc spin transfer torque acts like an effective magnetic damping on the FM film [29] and will either increase or decrease the net damping coefficient, depending on whether the injected spins are parallel or antiparallel with the magnetic moment. In this experiment, Ando *et al.* not only demonstrated that the SHE can be used to modulate damping coefficient through the spin torque mechanism, but also determined the spin Hall angle to be $\theta_{SH} \approx 0.08$ by measuring the current dependence of the effective magnetic damping.

4.3.2 Exciting magnetic dynamics

Persistent magnetic dynamics can be excited by dc spin current when the effective magnetic damping is reduced to zero, as is demonstrated in spin valves [30] and MTJs [31-32]. Naturally it is expected that similar oscillations could be induced by the spin current generated from the SHE. Generally this is not an easy task because of the following reasons. First, the efficiency of generating spin current densities using the SHE is weaker than in a spin valve or MTJ. Take the most studied material Pt as an example: the spin Hall angle in Pt was measured to be 0.01 ~ 0.08, much lower

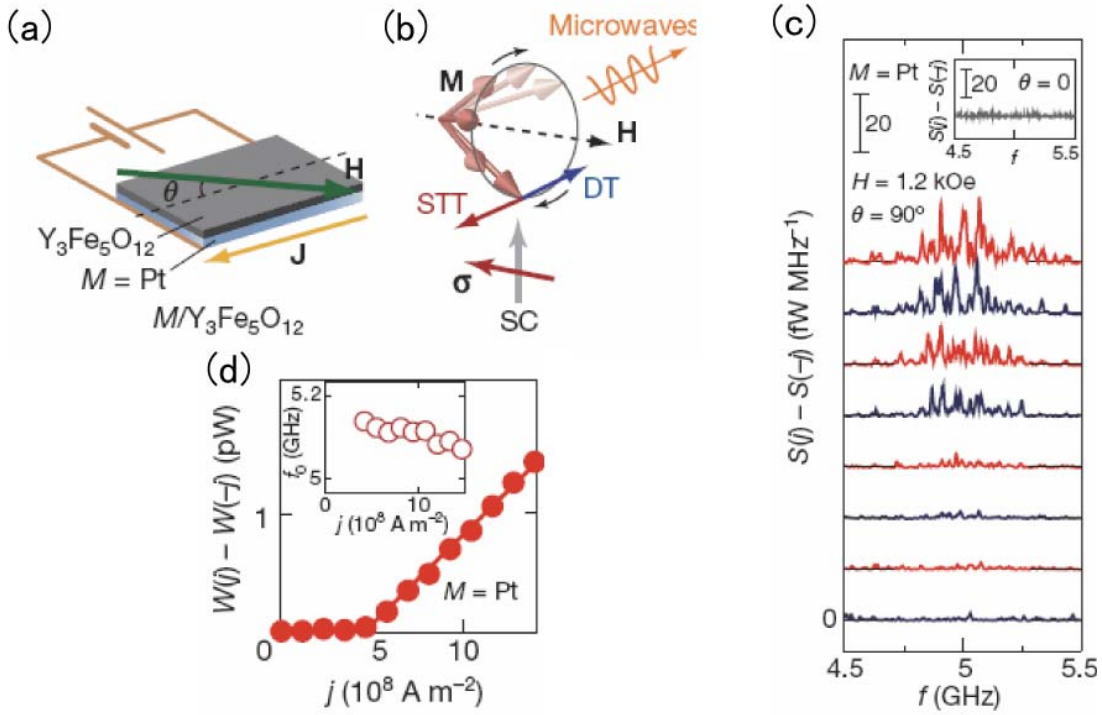

Figure 4.8 Magnetic oscillation induced by SHE in Pt/YIG. (a) Schematic illustration of the measurement setup. DC current J was applied in the Pt film. DC magnetic field H was applied in the YIG film plane. θ denotes the angle between H and current flowing direction. (b) Schematic illustration of the direction of the spin transfer torque (STT) and damping torque (DT). σ represents the spin orientation of the injected spin current (SC). Microwave was emitted from the system when the DT was cancelled by the STT. (c) Power spectrum density as measured from spectrum analyzer for θ = 90° case. S(J) and S(-J) represents the power under the applied current of ± J. Inset: no microwave power emission was observed when θ = 0°. (d) values of the integrated power for the microwave spectrum for different applied current in (c). Figures reproduced from ref. [33].

than the spin polarization in conventional spin valves or MTJs, which is generally believed to be larger than 0.3. Secondly, SHE materials usually bring in an extra magnetic damping through the spin pumping mechanism. Since magnetic oscillations can only happen when the effective damping reduces to zero, this extra damping will require an even higher critical current. Finally, unlike in spin valve or MTJs, where the magnetic dynamics can be electrically detected through the oscillation of the GMR or

TMR, the dynamics excited inside a ferromagnetic film through the SHE can be more challenging for detection.

In order to realize the SHE induced magnetic dynamics, Kajiwara *et al.* utilized $Y_3Fe_5O_{12}$ (YIG) as the magnetic material [33]. As a ferrimagnetic insulator, YIG exhibits a small saturation magnetization ($M_S \sim 150$ emu/cm^3 according ref. [33]) and an ultra-low magnetic damping (damping coefficient $\alpha \sim 7 \times 10^{-5}$). Both of those two features make it an ideal candidate for the magnetic dynamics study. By applying a dc current through the Pt/YIG bilayer film [Fig. 4.8 (a)], Kajiwara demonstrated that spontaneous magnetic oscillations could be excited. As is shown in Fig. 4.8 (b), when the orientations of spins injected into YIG were antiparallel with the equilibrium position of the magnetic moment ($\theta = 90°$), the damping torque could be cancelled by the spin transfer torque and persistent oscillations would be excited. When the injected spins were orthogonal to the magnetic moment, no magnetic oscillation would happen. These two cases are shown in the main panel and the inset of Fig. 4.8 (c), seperately. The integrated microwave power is summarized in Fig. 4.8 (d).

4.4 ISHE as a tool for detecting spin currents

Although there are still debates on the origins and magnitude of the spin Hall effect, the ISHE has been widely utilized as a way to detect spin currents. Originally, the spin current was a quantity that was difficult to measure electrically. And the only way to detect the spin current or the spin accumulation was to use a non-local spin valve. After the discovery of ISHE, the spin current could be converted into a charge current and could be easily detected by measuring the open circuit voltage. This is especially useful in spin caloritronics, where pure spin current can be generated from a temperature gradient.

A spin current can be injected into a nonmagnetic material from a ferromagnetic material either by a voltage bias, as is the case in most spintronic experiments or by a temperature bias, as is the case in the spin Seebeck effect. As we know, in ferromagnetic metals, electrons in different spin channels have different electrical conductivity $\sigma_\uparrow$ and $\sigma_\downarrow$. So by applying a voltage bias, spin current can be generated: $J_\uparrow - J_\downarrow = -[\sigma_\uparrow - \sigma_\downarrow]\partial V / \partial x$. Similarly, the capability of electrons to transfer heat is also different, depending upon their spin orientation. And this will naturally result in a thermally induced spin current: $J_\uparrow - J_\downarrow = -[\sigma_\uparrow - \sigma_\downarrow]S\partial T / \partial x$, where S is the Seebeck coefficient and $\partial T / \partial x$ is the temperature gradient. Therefore, any thermal current between a FM and NM should be accompanied by a spin current. This discussion applies to the case where the FM electrode is made of metal since the electrons are the main carriers for heat in metals. As for the ferromagnetic insulators, heat is no longer transferred through the conduction electrons, but instead through the energy exchange between the phonons and magnons. In the following we will see that a spin current can still be formed at ferromagnetic insulator/normal metal interface.

In Section 4.2.1 we have already seen that spin current can be pumped into the adjacent normal metal when the ferromagnetic moment undergoes precession under the driven rf magnetic field. Similarly, the ferromagnet can also be thermally excited, resulting in a thermal ferromagnetic resonance. And a net spin pump current can be formed between the ferromagnet and the normal metal. The pump current is given by the same form as in the field driven FMR case: $J_S\vec{\sigma} \propto \vec{m} \times \partial\vec{m} / \partial t$ [19]. Therefore, when the temperature of the FM insulator is higher than the NM metal, thermal current will flow from the FM to the NM, and meanwhile the magnons will be transferred into the NM in the form of the spin pumping current. If the temperature of the FM insulator is lower than the NM metal, thermal current would flow in the opposite way, from the

NM into the FM insulator. In this process, the oscillation angle of the magnetic moment will be increased, meaning that spins are transferred from the NM into the FM insulator and increased the population of the magnons [34]. So no matter whether the FM is a metal or insulator, a net spin current will always exist in the presence of a temperature gradient across the NM/FM interface.

The spin Seebeck effect was first experimentally discovered in permalloy [35] and then in ferromagnetic insulator [36-37], magnetic semiconductor [38] and Heusler alloys [39]. In all of those experiments, the ISHE in Pt was used for the detection of the spin current. In the following I will take the ferromagnetic insulator case as an example and explain the experiment ideas. As is shown in Fig. 4.9 (a), Pt thin film was deposited on top of a YIG slab. The temperature at the top surface of the Pt film was kept at 300K while the bottom of the YIG slab was in contact with a heat bath with temperature of 300K + ΔT. So under the temperature gradient, spin current was injected from the YIG into the Pt film and DC voltage was measured at the two ends of the Pt film [Fig. 4.9 (b)]. An external magnetic field was applied in the film plane and formed an angle of θ with respect to the measured electric field direction. From Fig. 4.9 (b), we can see that an ISHE voltage was detected, which is proportional to the temperature difference ΔT. And the ISHE signal was only observed when the injected spin are perpendicular to the measured electric field direction, i.e., $\theta = 90°$. No voltage was detected for the $\theta = 0°$ case, consistent with the ISHE mechanism.

4.5 Conclusion

In summary, various experiments have been carried out in the field of SHE and ISHE, which clearly demonstrated that the spin current and charge current can be converted into each other due to the spin orbit coupling mechanism. The spin Hall

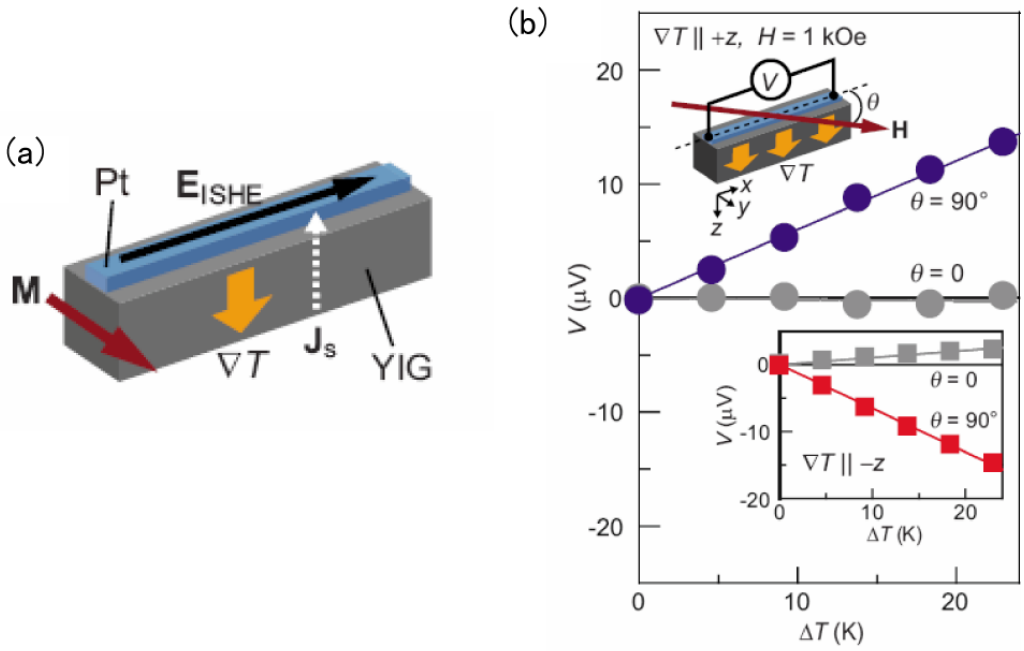

Figure 4.9 Spin Seebeck effect measured using ISHE in Pt. (a) Schematic illustration of the sample used for the measurement. Pt film was deposited on top of YIG. ∇T represents the temperature gradient while J_S denotes the spin current injected into Pt. (b) Voltage of the ISHE as a function of the temperature difference. Experimental data for both θ = 90° and 0° are shown. The main panel represents a positive temperature bias case ($\nabla T > 0$) while the inset shows $\nabla T < 0$ case. Figures reproduced from ref. [37].

angle was determined using different techniques. Although there are still discrepancies on the values of the spin Hall angle obtained from different measurement techniques, people have already began to utilize both the SHE and ISHE for different applications. Especially, the spin current generated by the SHE was employed to manipulate magnetic moment and the ISHE was used as a technique to detect spin currents. In the following chapters, I will describe the efforts that I made to utilize the SHE to modulate the magnetic properties, to induce magnetic switching and to excite magnetic moment oscillations. In the meantime, for the various types of applications with the SHE and ISHE, it is always advantageous to be able to obtain a material which has a larger spin Hall angle, and this is another theme for the rest of this thesis.

REFERENCE

1. M. I. Dyakonov and V. I. Perel, Current-Induced Spin Orientation of Electrons in Semiconductors, *Phys. Lett. A* **35**, 459 (1971).
2. J. E. Hirsch, Spin Hall effect, *Phys. Rev. Lett.* **83**, 1834 (1999).
3. S. F. Zhang, Spin Hall effect in the presence of spin diffusion, *Phys. Rev. Lett.* **85**, 393 (2000).
4. N. Nagaosa, J. Sinova, S. Onoda, A. H. MacDonald and N. P. Ong, Anomalous Hall effect, *Reviews of Modern Physics* **82**, 1539 (2010).
5. J. Sinova, D. Culcer, Q. Niu, N. A. Sinitsyn, T. Jungwirth and A. H. MacDonald, Universal intrinsic spin Hall effect, *Phys. Rev. Lett.* **92**, 126603 (2004).
6. S. Murakami, N. Nagaosa and S. C. Zhang, Dissipationless quantum spin current at room temperature, *Science* **301**, 1348 (2003).
7. Y. K. Kato, R. C. Myers, A. C. Gossard and D. D. Awschalom, Observation of the spin hall effect in semiconductors, *Science* **306**, 1910 (2004).
8. S. O. Valenzuela and M. Tinkham, Direct electronic measurement of the spin Hall effect, *Nature* **442**, 176 (2006).
9. T. Kimura, Y. Otani, T. Sato, S. Takahashi and S. Maekawa, Room-temperature reversible spin Hall effect, *Phys. Rev. Lett.* **98**, 156601 (2007).
10. K. Ando, S. Takahashi, K. Harii, K. Sasage, J. Ieda, S. Maekawa and E. Saitoh, Electric manipulation of spin relaxation using the spin Hall effect, *Phys. Rev. Lett.* **101**, 036601 (2008).
11. M. Johnson and R. H. Silsbee, Interfacial Charge-Spin Coupling - Injection and Detection of Spin Magnetization in Metals, *Phys. Rev. Lett.* **55**, 1790 (1985).
12. L. Vila, T. Kimura and Y. Otani, Evolution of the spin hall effect in Pt nanowires: Size and temperature effects, *Phys. Rev. Lett.* **99**, 226604 (2007).
13. M. Morota, Y. Niimi, K. Ohnishi, D. H. Wei, T. Tanaka, H. Kontani, T. Kimura and Y. Otani, Indication of intrinsic spin Hall effect in 4d and 5d transition metals, *Phys. Rev. B* **83**, 174405 (2011).
14. Y. Niimi, private communication, (2010).
15. Y. Niimi, M. Morota, D. H. Wei, C. Deranlot, M. Basletic, A. Hamzic, A. Fert and Y. Otani, Extrinsic Spin Hall Effect Induced by Iridium Impurities in Copper, *Phys. Rev. Lett.* **106**, 126601 (2011).
16. H. Nakayama, K. Ando, K. Harii, Y. Kajiwara, T. Yoshino, K. Uchida and E. Saitoh, Inverse Spin-Hall Effect Induced by Spin Pumping in Different Thickness Pt Films, *IEEE Transaction Magn.* **46**, 2202 (2010).
17. O. Mosendz, V. Vlaminck, J. E. Pearson, F. Y. Fradin, G. E. W. Bauer, Bader and H. A., Detection and quantification of inverse spin Hall effect from spin pumping in permalloy/normal metal bilayers, *Phys. Rev. B* **82**, 214403 (2010).

18. S. Mizukami, Y. Ando and T. Miyazaki, Ferromagnetic resonance linewidth for NM/80NiFe/NM films (NM = Cu, Ta, Pd and Pt), *J. Magn. Magn. Mater.* **226**, 1640 (2001).
19. Y. Tserkovnyak, A. Brataas and G. E. W. Bauer, Spin pumping and magnetization dynamics in metallic multilayers, *Phys. Rev. B* **66**, 224403 (2002).
20. E. Saitoh, M. Ueda, H. Miyajima and G. Tatara, Conversion of spin current into charge current at room temperature: Inverse spin-Hall effect, *Appl. Phys. Lett.* **88**, 182509 (2006).
21. M. Harder, Z. X. Cao, Y. S. Gui, X. L. Fan and C. M. Hu, Analysis of the line shape of electrically detected ferromagnetic resonance, *Phys. Rev. B* **84**, 054423 (2011).
22. A. Azevedo, L. H. Vilela-Leao, R. L. Rodriguez-Suarez, A. F. L. Santos and S. M. Rezende, Spin pumping and anisotropic magnetoresistance voltages in magnetic bilayers: Theory and experiment, *Phys. Rev. B* **83**, 144402 (2011).
23. H. Y. Inoue, K. Harii, K. Ando, K. Sasage and E. Saitoh, Detection of pure inverse spin-Hall effect induced by spin pumping at various excitation, *J. Appl. Phys.* **102**, 083915 (2007).
24. F. D. Czeschka, et al., Scaling Behavior of the Spin Pumping Effect in Ferromagnet-Platinum Bilayers, *Phys. Rev. Lett.* **107**, 046601 (2011).
25. K. Ando, et al., Inverse spin-Hall effect induced by spin pumping in metallic system, *J. Appl. Phys.* **109**, 103913 (2011).
26. O. Mosendz, J. E. Pearson, F. Y. Fradin, G. E. W. Bauer, S. D. Bader and A. Hoffmann, Quantifying Spin Hall Angles from Spin Pumping: Experiments and Theory, *Phys. Rev. Lett.* **104**, 046601 (2010).
27. H. Kurt, R. Loloee, K. Eid, W. P. Pratt and J. Bass, Spin-memory loss at 4.2 K in sputtered Pd and Pt and at Pd/Cu and Pt/Cu interfaces, *Appl. Phys. Lett.* **81**, 4787 (2002).
28. H. Nakayama, K. Ando, K. Harii, T. Yoshino, R. Takahashi, Y. Kajiwara, K. Uchida, Y. Fujikawa and E. Saitoh, Geometry dependence on inverse spin Hall effect induced by spin pumping in Ni81Fe19/Pt films, *Phys. Rev. B* **85**, 144408 (2012).
29. J. C. Slonczewski, Current-driven excitation of magnetic multilayers, *J. Magn. Magn. Mater.* **159**, L1 (1996).
30. S. I. Kiselev, J. C. Sankey, I. N. Krivorotov, N. C. Emley, R. J. Schoelkopf, R. A. Buhrman and D. C. Ralph, Microwave oscillations of a nanomagnet driven by a spin-polarized current, *Nature* **425**, 380 (2003).
31. S. Petit, C. Baraduc, C. Thirion, U. Ebels, Y. Liu, M. Li, P. Wang and B. Dieny, Spin-torque influence on the high-frequency magnetization fluctuations in magnetic tunnel junctions, *Phys. Rev. Lett.* **98**, 077203 (2007).
32. A. M. Deac, et al., Bias-driven high-power microwave emission from MgO-based tunnel magnetoresistance devices, *Nature Phys.* **4**, 803 (2008).
33. Y. Kajiwara, et al., Transmission of electrical signals by spin-wave interconversion in a magnetic insulator, *Nature* **464**, 262 (2010).

34. J. Xiao, G. E. W. Bauer, K. Uchida, E. Saitoh and S. Maekawa, Theory of magnon-driven spin Seebeck effect, *Phys. Rev. B* **81**, 214418 (2010).
35. K. Uchida, S. Takahashi, K. Harii, J. Ieda, W. Koshibae, K. Ando, S. Maekawa and E. Saitoh, Observation of the spin Seebeck effect, *Nature* **455**, 778 (2008).
36. K. Uchida, et al., Spin Seebeck insulator, *Nature Mat.* **9**, 894 (2010).
37. K. Uchida, H. Adachi, T. Ota, H. Nakayama, S. Maekawa and E. Saitoh, Observation of longitudinal spin-Seebeck effect in magnetic insulators, *Appl. Phys. Lett.* **97**, 172505 (2010).
38. C. M. Jaworski, J. Yang, S. Mack, D. D. Awschalom, J. P. Heremans and R. C. Myers, Observation of the spin-Seebeck effect in a ferromagnetic semiconductor, *Nature Mat.* **9**, 898 (2010).
39. S. Bosu, Y. Sakuraba, K. Uchida, K. Saito, T. Ota, E. Saitoh and K. Takanashi, Spin Seebeck effect in thin films of the Heusler compound Co2MnSi, *Phys. Rev. B* **83**, 224401 (2011).

CHAPTER 5

SPIN TORQUE FERROMAGNETIC RESONANCE INDUCED BY THE SPIN HALL EFFECT

5.1 Introduction

As is described in the previous chapter, the spin Hall effect (SHE) can convert a longitudinal charge current density J_C into a transverse spin current density $J_S\hbar/2e$, through spin-orbit scattering [1-6]. Therefore the SHE attracts great interest because it provides the possibility to manipulate a ferromagnetic moment with a pure spin current that is generated from a non-magnetic source. Before the SHE can be efficiently utilized, one important question needs to be answered. That is, what is the magnitude of the SHE in different materials? Several techniques [6-8] have been developed to determine the magnitude of the SHE in metals, which is generally characterized by the spin Hall angle, $\theta_{SH} = J_S/J_C$. For thin-film Pt, estimates of θ_{SH} obtained using different approaches differ by more than an order of magnitude [8-10]. In this chapter I will show that the spin torque from the SHE can be used to excite rf magnetic dynamics in an ordinary metallic ferromagnet. And the ferromagnetic resonance driven by the SHE also allows a quantitative determination of the SHE strength with small experimental uncertainties.

As a classical analysis method, ferromagnetic resonance (FMR) has long been used in the study of magnetic materials. The most standard way to carry out an FMR experiment has been to utilize an oscillating magnetic field to induce the magnetic precession. To do the field driven FMR measurement, one needs to use either a microwave cavity or a coplanar waveguide to provide the radio frequency (RF)

magnetic field. The resonance signal is obtained by monitoring the change in the absorbed microwave power. There will be a peak (or valley) in the transmission coefficient/ reflection coefficient of the microwave power when the resonance condition is satisfied. Using the FMR technique, many properties of the magnetic materials like the damping coefficient, the saturation magnetization, the anisotropy as well as the spin wave modes can be extracted. The disadvantage of this technique is also obvious. Because the signal relies on the change of the absorption of the microwave power, large enough samples are needed for the observation of FMR. Usually, the sample dimension needs to be at least in the sub-millimeter regime.

Compared with the field driven FMR, spin torque driven FMR (ST-FMR)[11-14] can have much higher sensitivity and can be used to study the properties of a nanomagnet. Instead of using an RF magnetic field, in ST-FMR current induced spin torque is employed. The oscillating spin torque can excite the magnetic dynamics when the driving frequency and the applied DC magnetic field satisfy the resonance condition. Usually the spin torque FMR is studied in spin valves or MTJs, where the precession of magnetic moment can lead to the oscillation of the resistance. Therefore, the dynamics of the magnetic moment can be observed electrically. There are several ways to detect the resistance change. The simplest method is to detect the mixed DC voltage. The RF current $\tilde{I} = I_{RF}\sin(\omega t)$ and the oscillating resistance $\tilde{R} = \Delta R\sin(\omega t + \varphi)$ have the same frequency, therefore their product $\tilde{I} \bullet \tilde{R}$ will exhibit a DC component -- the mixed voltage. Other methods of detecting the ST induced FMR consist of using a high frequency oscilloscope to detect the RF voltage $\tilde{V} = I_{DC}\tilde{R}$ directly [15], or using imaging techniques like time-resolved x ray magnetic circular dichroism to map the magnetic precession [16].

Similar to the ST-FMR experiment carried out in a spin valve or MTJ, we can also excite magnetic dynamics using the spin current generated by the SHE. By making a NM/FM bilayer and applying an oscillating charge current through the bilayer film, a transverse spin current will be generated inside the NM if there is a SHE and the spin current can be further injected into the adjacent FM [Fig. 5.2(a)], thereby exerting an oscillating spin torque (ST) on the FM that induces magnetization precession. Similar to the case of spin valves or MTJs where the resistance oscillates due to the GMR or TMR, there will also be an oscillation in the resistance of the bilayer sample because of the existence of anisotropic magnetoresistance (AMR). The mixing of the RF current and the RF resistance will give rise to a DC voltage, from which we can make a direct quantitative measurement of the SHE.

5.2 Theoretical derivation

In this section, I will make the mathematical preparations for the analysis of the FMR signal. In 5.2.1, I will derive the FMR amplitude under field torque or spin torque. And in 5.2.2, I will calculate the DC voltage that we can measure in the FMR experiment.

5.2.1 FMR amplitude under spin torque and field induced torque

In the presence of both RF magnetic field and RF spin current, the dynamics of magnetic moment $\hat{m}$ can be described by the Landau-Lifshitz-Gilbert equation containing the ST term [17]:

$$\frac{d\hat{m}}{dt} = -\gamma \hat{m} \times \vec{H}_{eff} + \alpha \hat{m} \times \frac{d\hat{m}}{dt} + \gamma \frac{\hbar}{2e\mu_0 M_S t} J_{S,RF} (\hat{m} \times \hat{\sigma} \times \hat{m}) - \gamma \hat{m} \times \vec{H}_{RF} . \quad (5.1)$$

Here γ is the gyromagnetic ratio, α is the Gilbert damping coefficient, μ_0 is the permeability in vacuum, M_S is the saturation magnetization of magnetic material, t is the thickness of the magnet, $J_{S,RF}\hbar/2e$ represents the oscillating spin current density, H_{RF} is the Oersted field, H_{eff} is the effective magnetic field exerted on $\hat{m}$ and it contains the applied DC field and the out-of-plane demagnetization field. The third term on the right hand side represents the spin torque influence τ_{ST} while the fourth term is the magnetic field torque τ_H. We assume that the equilibrium position for $\hat{m}$ is aligned along the $\hat{y}$ axis (Fig 5.1), the injected spins $\hat{\sigma}$ and the RF magnetic field are both in the *xy* plane. Our discussion will be limited to the thin film limit and assume that the *z* axis is the direction normal to the plane. Therefore, the demagnetization field can be written as $\vec{H}_{demag} = -m_z\hat{z}$. For simplicity, we will only focus on the small angle precession case, that is, the *y* component of the magnetization $m_y \approx 1$ and the *x* and *z* component $m_x, m_z \ll m_y$. From Equation 5.1, we can calculate that under this assumption, the corresponding spin torque τ_{ST} is mainly along the *x* direction while the RF field torque τ_H is in the *z* direction. In the following, to make the calculation more general, we will use τ_x and τ_z to represent the spin torque and RF magnetic field torque so that we can deal with the cases where $\hat{\sigma}$ or H_{RF} is not perfectly aligned along the *x* or *z* axis. In addition, we will assume that the external field is applied along the *y* direction and other fields like the anisotropy field due to the shape or due to the crystalline anisotropy are negligible.

Equation 5.1 can be now written in the scalar form:

$$\frac{dm_x}{dt} = \gamma M_{eff} m_z + m_z H_{ext} + \alpha \frac{dm_z}{dt} + \tau_x, \tag{5.2}$$

$$\frac{dm_z}{dt} = -\gamma m_x H_{ext} - \alpha \frac{dm_x}{dt} + \tau_z . \tag{5.3}$$

Note that we used the small angle approximation here, $m_y \approx 1$ and $dm_y / dt = 0$. From Equation (5.2) and (5.3), we can get the second derivative:

$$\frac{d^2 m_x}{dt^2} = \gamma M_{eff} \frac{dm_z}{dt} + \gamma H_{ext} \frac{dm_z}{dt} + \alpha \frac{d^2 m_z}{dt^2} + \frac{d\tau_x}{dt} , \tag{5.4}$$

$$\frac{d^2 m_z}{dt^2} = -\gamma H_{ext} \frac{dm_x}{dt} - \alpha \frac{d^2 m_x}{dt^2} + \frac{d\tau_z}{dt} \tag{5.5}$$

Substitute Equation (5.3) and (5.5) into (5.4), we get:

$$(1+\alpha^2)\frac{d^2 m_x}{dt^2} = -\gamma\alpha M_{eff} \frac{dm_x}{dt} - \gamma^2 (M_{eff} + H_{ext}) H_{ext} m_x + \gamma (M_{eff} + H_{ext})\tau_z + \alpha \frac{d\tau_z}{dt} + \frac{d\tau_x}{dt} \tag{5.6}$$

For most cases, we have $\alpha \ll 1$, so we can ignore the α^2 term and the $\alpha d\tau_z / dt$ term. Let's assume that the driving torques have the form: $\tau_x = \tau_{x0} e^{iwt}$, $\tau_z = \tau_{z0} e^{iwt}$ and m_x is in the form $m_x = m_{x0} e^{iwt}$. Here we assumed that τ_x and τ_z are in phase with each other. We should be alert about this assumption because under some experimental circumstances, this may not apply. Now, Equation (5.6) becomes:

$$-\omega^2 m_{x0} = -\gamma^2 (M_{eff} + H_{ext}) H_{ext} m_{x0} - i\omega\alpha\gamma M_{eff} \frac{dm_x}{dt} + \gamma (M_{eff} + H_{ext})\tau_{z0} + i\omega\tau_{x0} \tag{5.7}$$

From Equation (5.7), it is easy to see that the resonance condition is $\omega = \omega_0 = \gamma[(M_{eff} + H_{ext})H_{ext}]^{1/2}$. And we can also solve m_{x0}, that is:

$$m_{x0} = \frac{\omega}{\omega^2 - \omega_0^2 - i2\omega\Delta\omega}\left[\frac{\gamma(M_{eff} + H_{ext})}{\omega}\tau_{z0} + i\tau_{x0}\right]. \tag{5.8}$$

Here $\Delta\omega$ is defined as $\Delta\omega = 0.5\alpha\gamma M_{eff}$. Close to the resonant point, we have $w \approx w_0$. Equation (5.8) can be further simplified to:

$$m_{x0} = \frac{0.5}{\omega - \omega_0 - i\Delta\omega}\left[\frac{\gamma(M_{eff} + H_{ext})}{\omega}\tau_{z0} + i\tau_{x0}\right]. \tag{5.9}$$

Remembering that only the real part of m_{x0} has physical meaning, we can get Re(m_{x0}) as:

$$m_{x0} = \frac{0.5(\omega - \omega_0)}{(\omega - \omega_0)^2 - \Delta\omega^2}\frac{\gamma(M_{eff} + H_{ext})}{\omega}\tau_{z0} - \frac{0.5\Delta\omega}{(\omega - \omega_0)^2 - \Delta\omega^2}\tau_{x0}. \tag{5.10}$$

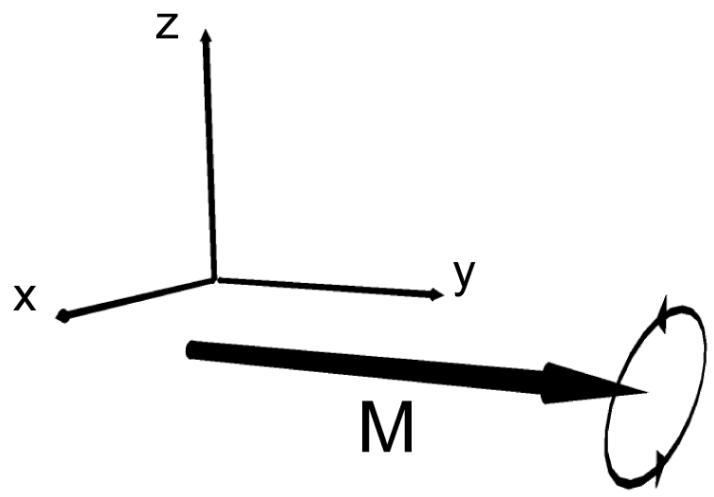

Figure 5.1 Precession orbit of magnetic moment. The equilibrium position is along the *y* axis.

So far we have obtained the precession amplitude of the magnetic moment.

5.2.2 Calculation of the mixed voltage

In experiment, the signal is obtained from the DC voltage, which comes from the mixture of the RF current and RF resistance. No matter whether the resistance change is caused by GMR, TMR or the AMR effect, the RF resistance can always be written as $\delta R = dR/d\theta\delta\theta$. For small angle precession around the *y* axis, we have $\delta\theta \approx m_x = m_{x0}\sin\omega t$. Since the RF current is given by $\delta I = I_{RF}\sin\omega t$, therefore, the mixed voltage is:

$$V_{DC} = -\frac{1}{4} I_{RF} \frac{dR}{d\theta}\left[\frac{(\omega-\omega_0)}{(\omega-\omega_0)^2-\Delta\omega^2}\frac{\gamma(M_{eff}+H_{ext})}{\omega}\tau_{z0} - \frac{\Delta\omega}{(\omega-\omega_0)^2-\Delta\omega^2}\tau_{x0}\right]. \quad (5.11)$$

So far we have obtained the formula for the mixed voltage in the FMR experiment. Note here that τ_x and τ_z can be arbitrary RF torques, for example, in-plane spin torque, out-of plane spin torque or RF magnetic field torque.

In some experiments, instead of sweeping the frequency to get the FMR signal, one can sweep the magnetic field, so in this kind of situation it is more convenient to re-write Equation (5.11) using the field *H* as the variable. Close to the resonance condition, we have $\omega - \omega_0 = d\omega / dH\big|_{H=H_0} (H - H_0)$. So, Equation (5.11) can be transformed into:

$$V_{DC} = -\frac{1}{4}\frac{I_{RF}}{\Delta H\,(2\pi df / dH)\big|_{H=H_0}}\frac{dR}{d\theta}\left[\frac{\Delta H(H-H_0)}{(H-H_0)^2-\Delta H^2}(1+M_{eff}/H)^{1/2}\tau_{z0}\right.$$
$$\left.-\frac{\Delta H^2}{(H-H_0)^2-\Delta H^2}\tau_{x0}\right], \qquad (5.12)$$

where $\Delta H = (2\pi f / \gamma)\alpha$ is the linewidth for the field sweeping case. It is easy to check that the first term in the bracket has the lineshape of an antisymmetric Lorentzian function, and the second term corresponds to a symmetric Lorentzian function. Therefore, torques in the different directions will give rise to resonance peaks having different symmetries. This can be used to separate the contributions from difference sources.

For the SHE induced ST-FMR, we have the spin torque $\tau_{ST} = \gamma(\hbar / 2e\mu_0 M_S t) J_{S,RF}(\hat{m} \times \hat{\sigma} \times \hat{m})$, where $J_{S,RF}$ is the spin current injected into FM layer from the SHE. As is shown in Fig. 5.2 (a), when the angle between the equilibrium position of M and the charge current is θ, the spin torque can be simplified as: $\tau_{ST} = \gamma(\hbar / 2e\mu_0 M_S t) J_{S,RF} \cos\theta$, and its direction is in the film plane. If there is an in-plane RF magnetic field in addition to this spin torque, the torque due to the magnetic field will also exist and has the form $\tau_H = -\gamma \hat{m} \times \vec{H}_{RF}$. In the geometry shown in Fig 5.2 (a), this can be written as $\tau_H = -\gamma H_{RF} \cos\theta$ and its direction is perpendicular to plane. Therefore, τ_{x0} and τ_{z0} are given by τ_{ST} and τ_H separately in this case.

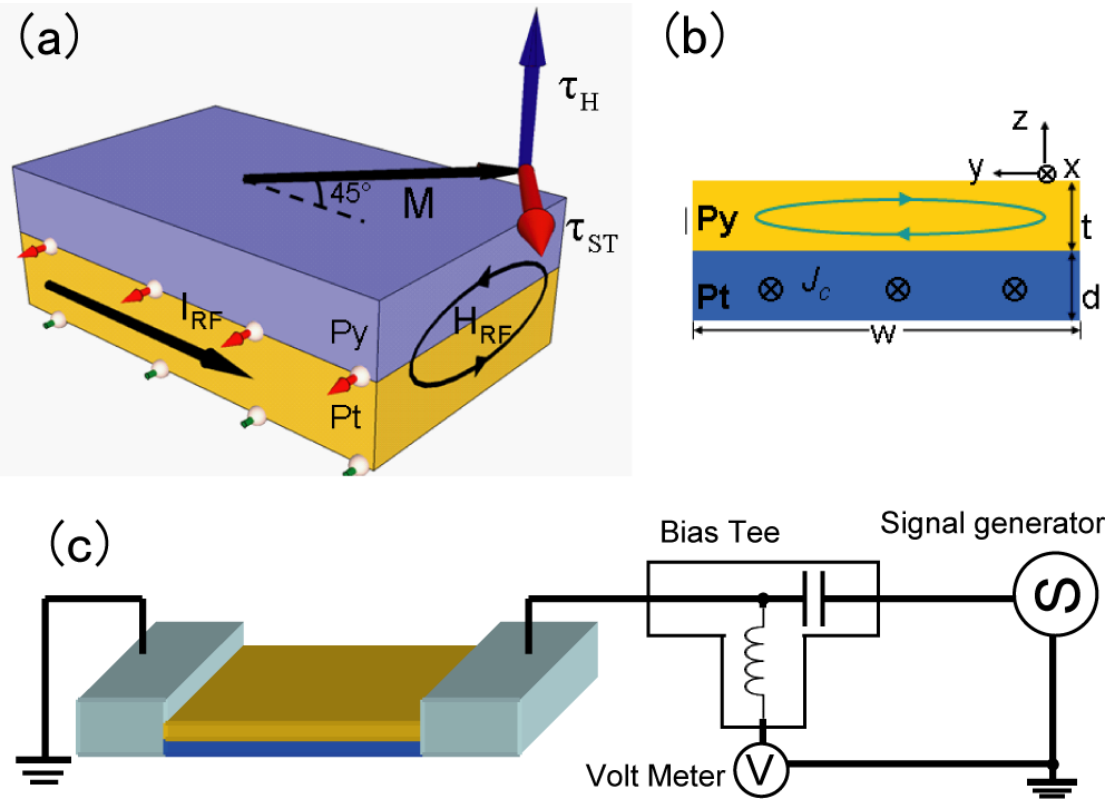

Figure 5.2 Schematic illustration of the sample used for the ST-FMR experiment. (a) Schematic of a Pt/Py bilayer thin film illustrating the spin transfer torque τ_{STT} and the field torque τ_H induced by the Oersted field H_{RF}. The angle between the external field and the current flowing direction is fixed at $\theta = 45°$. (b) Left side view of the Pt/Py system, with the solid line showing the Oersted field generated by the current flowing just in the Py layer, which should produce no net effect on the Py AMR. (c) Schematic circuit for the ST-FMR measurement.

In the sample shown as in Fig. 5.2 (a), the Oersted field H_{RF} can be calculated from the geometry of the sample. Since the microwave skin depth is much greater than the FM thickness (only a few nanometers) the current density in the FM should be spatially uniform, and in this case the Oersted field from the charge current in the FM itself should produce no net torque on the FM moment [Fig. 5.2(b)]. The Oersted field can therefore be calculated entirely from the current density $J_{C,RF}$ in the NM layer. The microstrip width is much larger than the NM thickness, so the sample can be

approximated as an infinitely wide conducting plate and the Oersted field is determined by Ampère's law, $H_{RF} = J_{C,RF} d / 2$, where d is the NM thickness. We checked H_{RF} by numerical integration and the difference is less than 0.1% from the infinite plate approximation. Since both the spin torque and torque due to the Oersted field can be calculated analytically, using Equation (5.12) we can now reach the ratio between the symmetric peak and antisymmetric peak:

$$\frac{S}{A} = \frac{\tau_{x0}}{(1 + M_{eff} / H)^{1/2} \tau_{z0}} = \frac{(\hbar / 2e\mu_0 M_S t) J_{S,RF}}{(1 + M_{eff} / H)^{1/2} H_{RF}}. \tag{5.13}$$

Or equivalently,

$$\frac{J_{S,RF}}{J_{C,RF}} = \frac{S}{A} \frac{e\mu_0 M_S t d}{\hbar} (1 + M_{eff} / H_{ext})^{1/2} \tag{5.14}$$

All of the parameters entering Equation (5.14) are either fundamental constants or quantities that can be measured directly, so this expression allows a measurement of $J_{S,RF} / J_{C,RF}$ from the lineshape of the resonance curves. The measurement is self-calibrated in the sense that the strength of the torque from the spin current is measured relative to the torque from H_{RF}, which can be calculated easily from the geometry of the sample.

5.3 Experiment

5.3.1 Results of Pt/Py bilayer samples

The first system that we studied using the ST-FMR technique was the Pt/Py bilayer film. We studied Pt because it was one of the most extensively studied SHE material, and it is also believed that Pt has a relatively large magnitude of SHE compared with the other metals. In this experiment, Pt/Py bilayer was grown by DC magnetron sputter deposition. The individual layer thicknesses were 4~15 nm, with specific values stated below. The starting material for the Pt was 99.95% pure. Highly

resistive Ta (1 nm) was employed as the capping layer to prevent oxidation of the Py. The bilayers were subsequently patterned into microstrips using photolithography and ion milling. The samples' widths ranged from 1 to 20 μm and the lengths from 3 to 250 μm. The final sample geometry is shown in Fig. 5.2 (a) and the driving forces for the ST-FMR: the spin torque τ_{ST} and the Oersted field torque τ_H are labeled in the figure, respectively. By using a bias tee, we were able to apply a microwave current to our sample and at the same time measure the DC voltage [Fig. 5.2(c)]. A sweeping magnetic field H_{ext} was applied in the film plane, with the angle θ between H_{ext} and microstrip kept at 45° unless otherwise indicated. The output power of the microwave signal generator was varied from 0 to 20 dBm and the measured DC voltage was proportional to the applied power, indicating that the induced precession was in the small angle regime. All the measurements we present were performed at room temperature with a power of 10 dBm.

In the sample geometry shown in Fig. 5.2, another possible effect that will influence the final result is the spin pumping + inverse spin Hall effect (ISHE). When the magnetic moment precesses around the equilibrium position, there will be DC spin current injected into the NM from the FM layer due to the spin pumping effect [18-19]. This injected spin current will be converted into a DC charge current due to the inverse SHE in the Pt layer [10]. And experimentally the DC voltage generated from the ISHE will have the same form with the mixed voltage due to spin torque, i.e., they will both have symmetric Lorentzian lineshape. However, this effect is second order in θ_{SH} in our geometry and it can be calculated to contribute a negligible voltage, about two orders of magnitude smaller than the signals shown below.

Figure 5.3(a) shows the ST-FMR signals measured on a Pt(6)/Py(4) (thicknesses in nanometers) sample for f = 5-10 GHz. As expected from Equation 5.12, the resonance peak shapes can be very well fit by the sum of symmetric and antisymmetric Lorentzian curves with the same linewidth for a given f [fits are shown as lines in Fig. 5.3(a)]. The fact that the symmetric peak changes its sign when H_{ext} is reversed [inset of Fig. 5.3(a)] agrees with the form of spin torque $\vec{\tau}_{ST} \propto \hat{m} \times \hat{\sigma} \times \hat{m}$ given in Equation 5.1, and excludes the possibility that the signal is due to an unbalanced perpendicular Oersted field torque, in direction $\hat{m} \times \hat{H}_{RF}^{\perp}$, which would yield symmetric peaks with the same sign for opposite H_{ext}. The resonant peak positions are summarized in Fig. 5.3(b), and agree well with the Kittel formula $f = (\mu_0 \gamma / 2\pi)[H_0(H_0 + M_{eff})]^{1/2}$. From a one-parameter fit to the resonance frequencies we determine that the demagnetization field $\mu_0 M_{eff} = 0.8050 \pm 0.050$ Tesla for the Pt(6)/Py(4) bilayers. We have also measured the saturation magnetization M_S = 640 emu/cm^3 in test samples [20].

To verify the SHE origin of field-symmetric components of the FMR signals, We studied control samples with the layers Cu(6)/Py(4) and 4 nm of Py alone, with results as shown in Fig. 5.4. The Cu/Py bilayer sample gives a purely antisymmetric signal, indicating that only the Oersted-field contribution is present, as expected because of the very small SHE in Cu in comparison to that in Pt. For the Py(4) sample, we would expect no resonance signal at all, since there is no SHE and as noted above if the current density in the Py is uniform there should also be no net effect of the Oersted field on the Py dynamics. However, we do observe a very small, purely antisymmetric signal in the 4 nm Py sample. We suspect that this may arise from an Oersted field due to non-uniform current flow at the ends of the Py due to the electrode contacts. The lack of field-symmetric components in the resonance curves

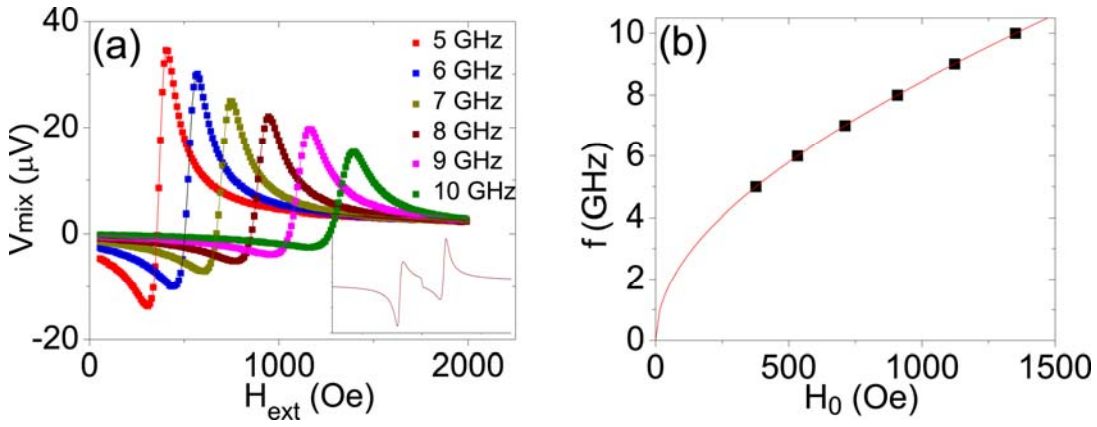

Figure 5.3 ST-FMR spectra obtained from from a Pt(6)/Py(4) sample. (a) Mixed voltage measured under frequencies of 5-10 GHz. The sample dimension is 20 μm wide × 110 μm long. Inset: ST-FMR spectrum of 8 GHz for both positive and negative H_{ext}. (b) Resonance frequency f as a function of the resonant field H_0. The solid curve represents a fit to the Kittel formula.

for the control samples provides strong support that the symmetric component we observe in Pt(6)/Py(4) does indeed arise from the SHE in the Pt.

With M_{eff} and M_S determined , we can use Equation (5.14) and the measured values of *S/A* to calculate $J_{S,RF} / J_{C,RF}$. The results are shown in Fig. 5.5 (a) for the resonance curves spanning 5-10 GHz shown in Fig. 5.3 (a). We find $J_{S,RF} / J_{C,RF}$ = 0.056 ± 0.005 for Pt(6)/Py(4). We measured more than ten Pt(6)/Py(4) samples with different lateral dimensions and the total variation of $J_{S,RF} / J_{C,RF}$ was < 15%. The dominant experimental uncertainty [and the small variation with H_{ext} visible in Fig. 5.5(a)] may be associated with Oersted fields from non-uniform currents at the sample ends, as noted above for the single-layer Py sample. Note that according to Equation 5.13 *S/A* should not depend upon the angle of the applied DC field, as confirmed by the results shown in Fig. 5.5 (b). The lack of an angle dependence is also distinct from

the spin pumping/AMR experiment where the ratio of S/A is shown to be a function of the angle [21].

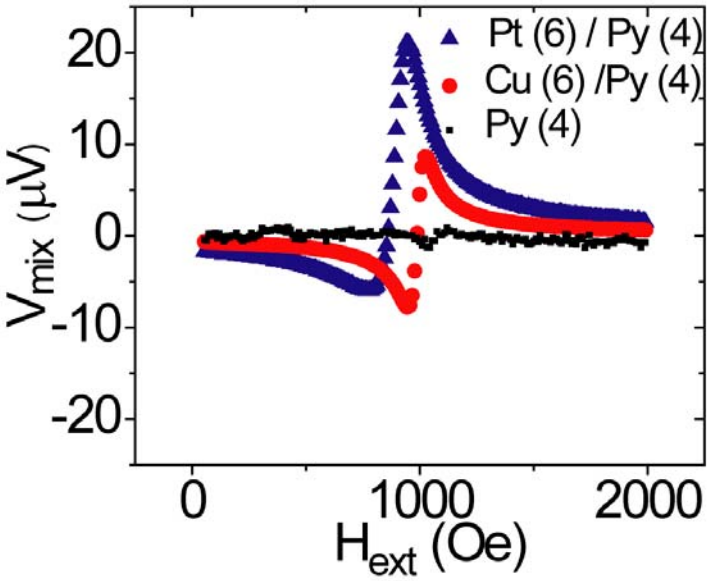

Figure 5.4 FMR spectra on the Pt/Py sample and control samples. The Pt (6)/Py (4) sample is represented by the blue triangles, while the Cu(6)/Py(4) and Py (4) control samples are shown by the red circles and black squares, separately.

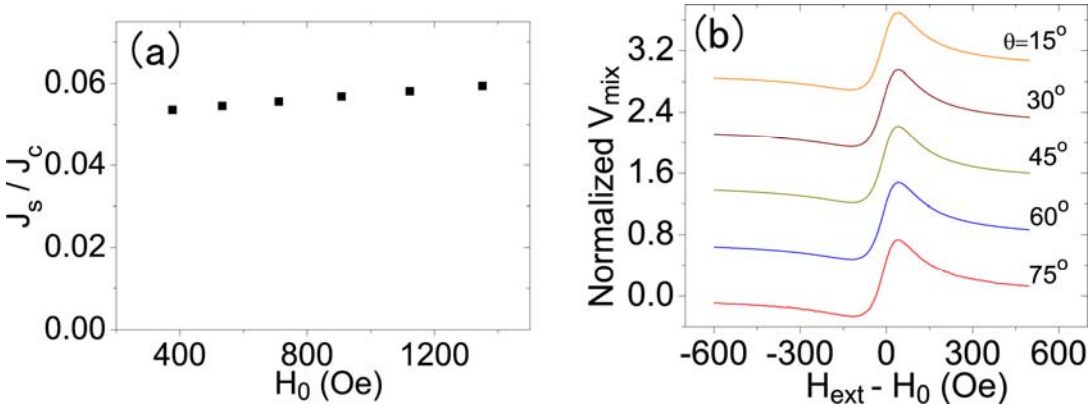

Figure 5.5 J_S/J_C obtained on the Pt/Py sample. (a) J_S/J_C values determined from the FMR analysis at different *f*. (b) FMR signals measured for different external field angles θ (f = 8 GHz). The mixing voltages V_{mix} are normalized and offset to enable comparison of the lineshapes.

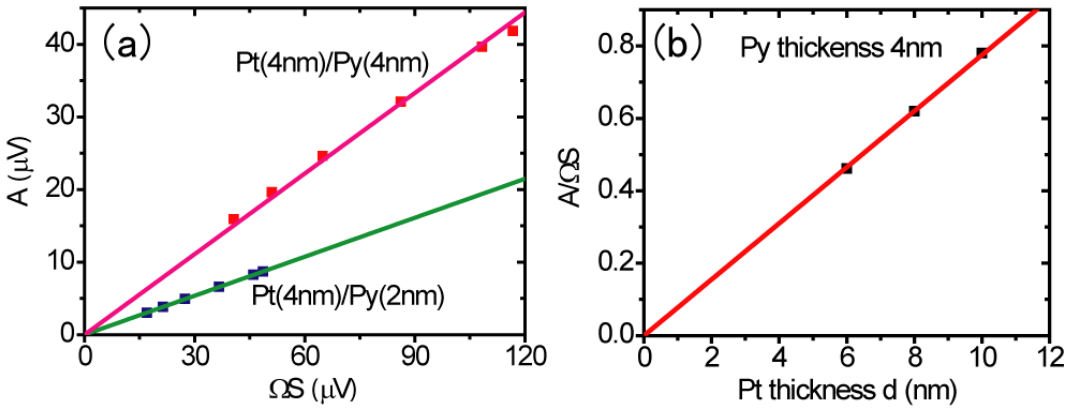

Figure 5.6 Amplitude of symmetric and antisymmetric peaks under different Pt and Py thicknesses. (a) A versus ΩS for two types of Pt/Py samples where the thickness of the Pt is held constant at 4nm while the Py thickness is varied between 2 and 4 nm. (b) A/ ΩS for Pt(d)/Py(4) samples for which the thickness of Pt d is varied between 6 and 10 nm.

The validity of the analysis that we utilized above can be further checked by varying the Py and Pt thicknesses in the sample. From Equation 5.14, the ratio between the antisymmetric and symmetric peak A/S should be proportional to the product of the Py thickness t and Pt thickness d, i.e., $A/\Omega S \propto td$, where Ω is the coefficient to account for the different efficiencies in causing resonance for torques in x and z direction and from Equation 5.14, we have $\Omega = (1 + M_{eff} / H)^{1/2}$. First of all, we can keep the Pt thickness d constant and vary the thickness of Py t. As is shown in Fig. 5.6 (a), two samples of Pt(4)/Py(2) and Pt(4)/Py(4) are compared. The values of $A/\Omega S$ for the Pt(4)/Py(4) and the Pt(4)/Py(2) sample are measured to be 0.355 and 0.179. So $A/\Omega S$ for the Pt(4)/Py(4) sample is twice as large as that for the Pt(4)/Py(2) sample, reflecting the interfacial nature of the spin torque. This is because the spin torque is an interfacial effect while the Oersted field works on the bulk of the FM layer, therefore, if we double the thickness of the FM layer, the A/S ratio should also double. Secondly, we can also vary the thickness of Pt layer while keeping the Py

thickness constant. Rigorously speaking, $A/\Omega S$ is not a simple linear function of d. The reason for this is that the spin current injected into the FM layer is influenced by the spin diffusion length of the Pt film λ_{sf}. Only when d >> λ_{sf}, the spin current injection efficiency can be treated as unchanged. As we will show in Section 5.3.3, λ_{sf} can be determined to be ~1.4 nm for Pt. Therefore, for d thickness larger than 6 nm, we can see a linear increase in $A/\Omega S$ when d goes up [Fig. 5.6 (b)].

5.3.2 Modulating the FMR linewidth using the spin Hall effect

The spin current density absorbed by the Py layer can be independently checked by an alternative method, that is, measuring the FMR linewidth Δ as a function of DC current, similar to the technique introduced in Ref. [8]. According to the theory of ST, a DC spin current $I_{S,DC}$ will increase or decrease the effective magnetic damping, or equivalently, the resonance linewidth: [22]

$$\Delta = \frac{2\pi f}{\gamma}\left(\alpha + \frac{\sin\theta}{(H_{ext} + 0.5M_{eff})\mu_0 M_S t}\frac{\hbar J_S}{2e}\right) \tag{5.15}$$

Our results obtained with a Pt(6)/Py(4) sample ~1 μm wide are shown in Fig. 5.7. The measured damping coefficient at zero current ($\alpha \approx 0.028$) is significantly higher than that measured in a spin valve nanopillar sample having a 4 nm Py free layer ($\alpha \approx 0.01$) [23]. This can be explained by the spin pumping effect previously observed in the Py/Pt system [18-19]. For a negative applied field (H_{ext} applied -135° from the current direction in the microstrip), the linewidth is broadened when I_{DC} ramps from -0.7 mA to 0.7 mA; while for a positive field (H_{ext} applied 45° from the current direction), the trend is the opposite. By fitting the data shown in Fig. 5.7, and calculating the charge current density in the Pt using the measured resistivities $\rho_{Pt} = 20\mu\Omega cm$ and $\rho_{Py} = 45\mu\Omega cm$, the damping coefficient change can be calculated

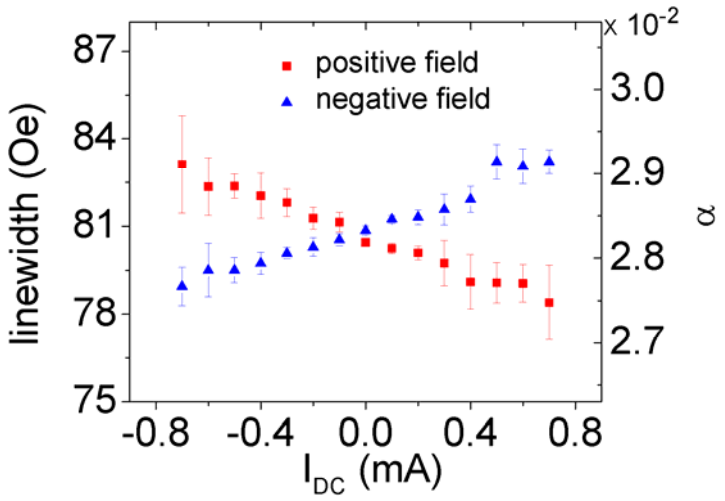

Figure 5.7 SHE induced damping change. The change of the FMR linewidth (left y axis) and Gilbert damping coefficient (right y axis) as a function of I_{DC} for two orientations of the Py magnetization relative to the current direction. The data are taken at $f = 8$ GHz.

to be $\Delta\alpha / J_c = (0.9 \pm 0.012) \times 10^{-10}$ $(\mathrm{A/cm^2})^{-1}$. With Equation 5.15, this yields $J_s / J_c = 0.048 \pm 0.007$ for Pt(6)/Py(4), which agrees well with the value 0.056 ± 0.005 determined from the FMR lineshape.

5.3.3 Determination of the spin diffusion length of Pt using ST-FMR

The results for J_S/J_C that we obtained above reflect the ratio between the spin current density that is injected into the Py layer and the charge current density in the Pt layer. This number is equal to the spin Hall angle only when the Pt film thickness is much larger than the spin diffusion length λ_{sf} and Pt/Py interface is perfectly transparent. But usually, these conditions are not always fulfilled. So in order to know the intrinsic spin Hall angle of Pt we need to determine λ_{sf}. The procedure we used to measure λ_{sf} is as follows. A series of Pt(t_{Pt})/Py(4 nm) thin film samples [$\sigma_{Pt} = 5 \times 10^6$ $(\Omega\mathrm{m})^{-1}$] were grown and patterned into microstrip lines as is described above, with Pt thicknesses t_{Pt} varying from 1.5 nm to 10 nm, widths 1 - 20 μm, and lengths 5 - 200 μm. (The results for θ_{SH} were consistent, independent of width and

length for a given layer structure.) The final result for the ratio of J_S/J_e as a function of Pt thickness is plotted in Fig. 5.8 (a). We observe that J_S/J_e is approximately constant for large Pt thicknesses and decreases abruptly with decreasing t_{Pt} for small values.

This dependence of the spin current on the Pt thickness has the form that is expected within a drift-diffusion analysis [24] of the spin flow that incorporates the spin Hall effect. If one assumes that no spin current can penetrate out through the bottom surface of the Pt layer, there must arise a vertical gradient in the spin-dependent electron chemical potentials adjacent to the bottom surface (within a length scale given by the spin diffusion length λ_{sf}) that produces a counterflowing spin current to cancel the spin-Hall-generated spin current near the bottom surface. This reduces the magnitude of the spin-Hall spin current in films whose thickness is comparable to λ_{sf}. In the limit of a transparent interface between the Pt and the permalloy (so that the spin current density transmitted into the permalloy is equal to the spin current density incident on the interface from the Pt side, for spins perpendicular to the permalloy magnetic moment) within the drift-diffusion analysis the spin current density should have the thickness dependence

$$\frac{J_S(t_{Pt})}{J_S(\infty)} = 1 - \mathrm{sech}\left(\frac{t_{Pt}}{\lambda_{sf}}\right). \qquad (5.16)$$

We find excellent agreement between the data in Fig. 5.8(a) and a one-parameter fit to this expression, with $\lambda_{sf} = 1.4 \pm 0.3$ nm. We have also analyzed the data in Fig. 5.8(a) using a generalization of Equation 5.16 that allows for a reflection coefficient *R* at the Pt/permalloy interface. For non-zero values of *R*, the fits to the data in Fig. 5.8(a) correspond to values of λ_{sf} even smaller than 1.4 nm, ranging down to 1.0 nm for $R = 0.9$.

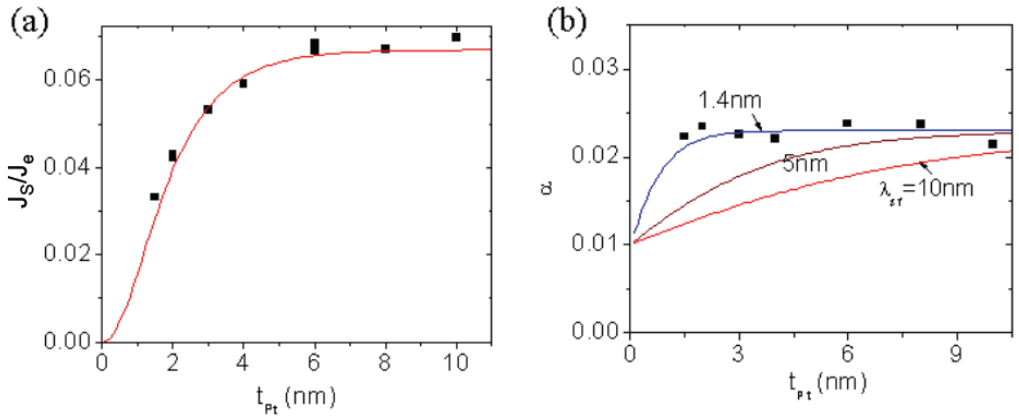

Figure 5.8 Determination of the spin diffusion length of Pt. (a) Squares: Results from ST-FMR measurements for the spin current density transmitted from Pt to the permalloy layer, divided by the charge current density in the Pt, as a function of the Pt thickness. Red line: Fit to Equation 5.16 that determines the value $\lambda_{sf} = 1.4 \pm 0.3$ nm. (b) Squares: The dependence of the damping coefficient α on t_{Pt} as measured by the ST-FMR experiment. Curves: predictions of Equation (5.17) for different values of λ_{sf}.

As an independent check, we can also analyze the dependence of the Gilbert damping coefficient α on the Pt thickness [Fig. 5.8(b)]. For each set of samples, we determined α from the linewidth of the FMR resonance ΔH, according to $\alpha = \gamma \Delta H / (2\pi f)$. As seen in Fig. 5.8(b), we measure only a very weak dependence of α on t_{Pt} in the range $t_{Pt} \geq 1.5$ nm. Within the theory of spin pumping [19], the presence of the Pt should increase the damping coefficient of the permalloy layer by an amount $\alpha(t_{Pt}) - \alpha(t_{Pt} = 0)$ above the intrinsic value, and this increase should depend on the ratio t_{Pt} / λ_{sf} in the form:

$$\frac{\alpha(t_{Pt}) - \alpha(t_{Pt} = 0)}{\alpha(t_{Pt} = \infty) - \alpha(t_{Pt} = 0)} = \frac{1 + [\sqrt{\varepsilon}]^{-1}}{1 + [\sqrt{\varepsilon}\tanh(t_{Pt} / \lambda_{sf})]^{-1}} \quad . \qquad (5.17).$$

This equation follows from Equation (21) of ref. [19]. The intrinsic damping coefficient in our permalloy films with no coupling to a Pt layer has the value $\alpha(t_{Pt} = 0) \approx 0.01$, while the quantity $\varepsilon = \tau_{el} / \tau_{sf}$, the spin-flip probability at each scattering, is for Pt believed to be > 0.1 [19]. The red, brown and blue curves in Fig.

5.8(b) show the form of Equation 5.17 for ε = 0.1 and λ_{sf} = 10 nm, 5 nm, and 1.4 nm, respectively. The curves are only weakly dependent on the value assumed for ε; our conclusions hold for any ε in the range 0.1~1. The result of comparing the data in Fig. 5.8(b) to Equation 5.17 is that the weak dependence of $\Delta\alpha$ on t_{Pt} implies a value of $\lambda_{sf} < 2$ nm, fully consistent with the value we determined above from the dependence of the spin current density on t_{Pt}. A related measurement of magnetic damping as a function of the thickness of a sputtered Pt film was performed previously by Mizukami *et al*. for a Cu/permalloy/Cu/Pt/Cu multilayer structure (Fig. 4 of ref. [25]), from which one can draw a similar conclusion, that $\lambda_{sf} \approx 1$ nm at room temperature for Pt.

Returning to the results of the ST-FMR measurement, the data in Fig. 5.8(a) provide the means to extrapolate to large Pt thicknesses using our measurements of the quantity J_S / J_e, the spin current density penetrating from Pt into the permalloy divided by the charge current density within the Pt. The best fit using the full set of samples is $J_S(\infty) / J_e = 0.068 \pm 0.005$. If the Pt/permalloy interface is transparent for spin transport, we can therefore conclude also that $\theta_{SH} = 0.068 \pm 0.005$ and. If there is any lack of transparency at the interface, these values represent lower bounds on the true values of θ_{SH} within the Pt sample.

5.3.4 Results for Ta/CoFeB bilayer samples

Materials with large spin Hall angle are needed for the efficient manipulation of magnetic moment using the SHE. So, after the determination of the spin Hall angle inside Pt, it is natural to keep on looking for materials that may have even larger spin Hall angles. Large spin Hall angles ($J_S/J_C > 0.10$) have been reported previously in different alloys, FePt [26] or CuIr [27]. However, because of the relatively longer spin

diffusion lengths in those materials, thicker films would be needed to ensure an efficient spin injection (the SHE will be fully exhibited only when the NM thickness is thicker than the spin diffusion length), which will further require a large current. In the meantime, ab initio calculations [28] predicted that highly resistive Ta may have a large spin Hall angle, comparable to or greater than that of Pt, and with the opposite sign in comparison to Pt or Au. In contrast, a non-local spin valve measurement [29] reported a very low value for the Ta spin Hall angle, 0.0037 (albeit with the predicted sign). However, as we discussed in Chapter 4, this measurement technique can greatly underestimate the spin Hall angle, particularly in highly resistive spin Hall materials such as Ta.

We used the ST-FMR technique to determine the spin Hall angle in β–Ta. The samples consisted of $Co_{40}Fe_{40}B_{20}$(4)/Ta(8) (thickness in nm) bilayers sputter-deposited onto oxidized Si substrates and patterned into 10 μm wide strips. It is known that high resistivity β–Ta will be produced when Ta is sputter deposited or evaporated onto amorphous surfaces such as, for example, oxidized Si [30] or CoFeB. Measurements of the bilayer resistance as a function of varying Ta thickness determined that the Ta resistivity was $\rho_{Ta} \approx 190$ μΩ-cm, confirming the β–Ta phase. The CoFeB resistivity was $\rho_{CoFeB} \approx 170$ μΩ-cm and for a 4-nm thick film the magnetic moment was oriented in-plane. We applied an oscillating current I_{RF} along the strips in the current-in-plane configuration, with an external magnetic field B_{ext} in the film plane at a 45° angle with respect to the current direction (Fig. 5.9a). Note here that compared with Fig. 5.2a, the sequence of the film stack is reversed, the FM layer is now on the bottom of the film stack instead of on top. What's more, the spin orientations generated by the SHE is also opposite in Fig. 5.9 and Fig. 5.2, reflecting opposite signs in the spin Hall angle

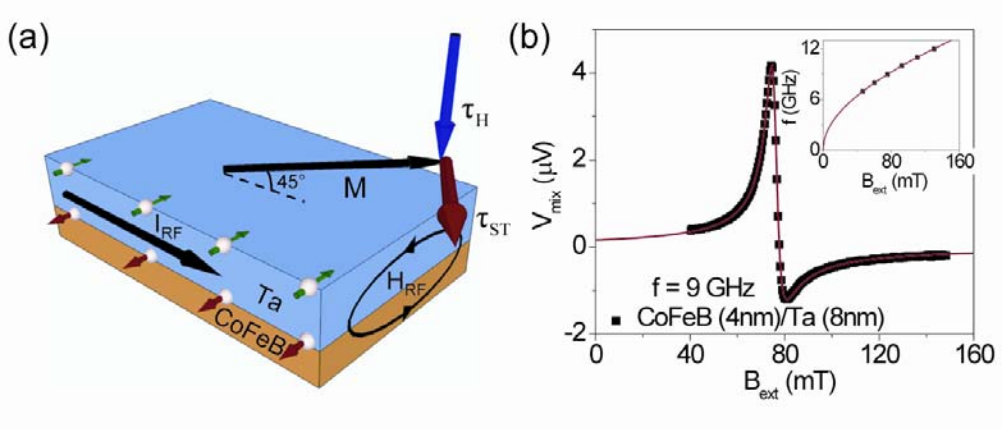

Figure 5.9 SHE induced ST-FMR in the CoFeB/Ta sample. (a) Sample geometry for the ST-FMR measurement. I_{RF} and H_{RF} represent the applied RF current and corresponding Oersted field. τ_H is the torque on the magnetization due to the Oersted field and τ_{ST} is the spin transfer torque from the spin Hall effect. (b) Resonant lineshapes of the ST-FMR signals under a driving frequency f = 9 GHz for CoFeB(4 nm)/Ta(8 nm) sample. The squares represent experimental data while the lines are fits to a sum of symmetric and antisymmetric Lorentzians. Inset to (b): Dependence of the frequency f on the resonance magnetic field, in agreement with the Kittel formula (solid curve).

in Pt and Ta. A typical resonance signal is shown in Fig. 5.9b, where the resonance peak is fitted by the sum of a symmetric Lorentzian and an antisymmetric Lorentzian. We measured the resonant signal for different applied frequencies and found that the positions of the resonant peaks agree well with the Kittel formula $f = (\gamma / 2\pi)[B(B + \mu_0 M_{eff})]^{1/2}$ [Fig. 5.9 (b), inset], where $\gamma = 1.76 \times 10^{11}$ HzT^{-1} is the gyromagnetic ratio and M_{eff} is the effective demagnetization field and $\mu_0 M_{eff}$ is determined to be 1.3 T from the fit.

The magnitude of the SHE was determined using the ratio of the symmetric peak amplitude S to the antisymmetric peak A. Independent of the frequency employed, we found the consistent result that $J_S / J_e = 0.15 \pm 0.03$ in our 8 nm Ta films. If λ_{sf}^{Ta} is comparable to or larger than the film thickness, then the bulk value of

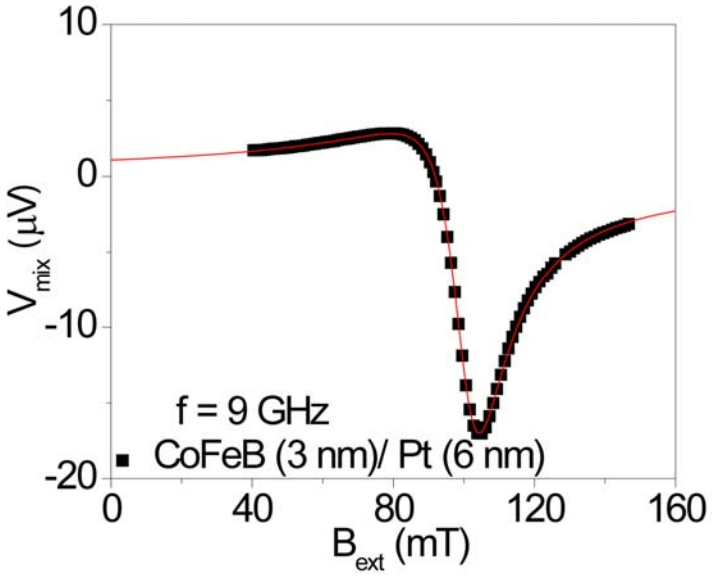

Figure 5.10 SHE induced ST-FMR in the CoFeB/Pt sample. From the ratio of the symmetric and antisymmeteric peak components, the J_S/J_e ratio for Pt can be determined to be ~0.07, consistent with the result obtained from Pt/Py sample in previous section.

θ_{SH} is even larger than 0.15 ± 0.03.

To compare the SHE in Ta with that of Pt, a different sample with the stack structure: substrate/CoFeB(3)/Pt(6) (thicknesses in nm) was made and measured, with the result shown in Fig. 5.10. Comparing the resonant signals of CoFeB/Ta and CoFeB/Pt in Fig. 5.9 and 5.10, we see that the antisymmetric peaks of the two samples have the same sign, as expected from their common origin. The symmetric peaks in the two cases are opposite in sign, which directly shows that the SHE in Ta is opposite to that in Pt, in agreement with the prediction [28] and the previous measurement [29]. We can also note here that the antisymmetric and symmetric peaks shown in Fig 5.10 for the CoFeB/Pt sample are opposite to what was illustrated in Fig. 5.3, for a substrate/Pt/Permalloy sample. This is because the relative order of the FM/NM layers was reversed in that case.

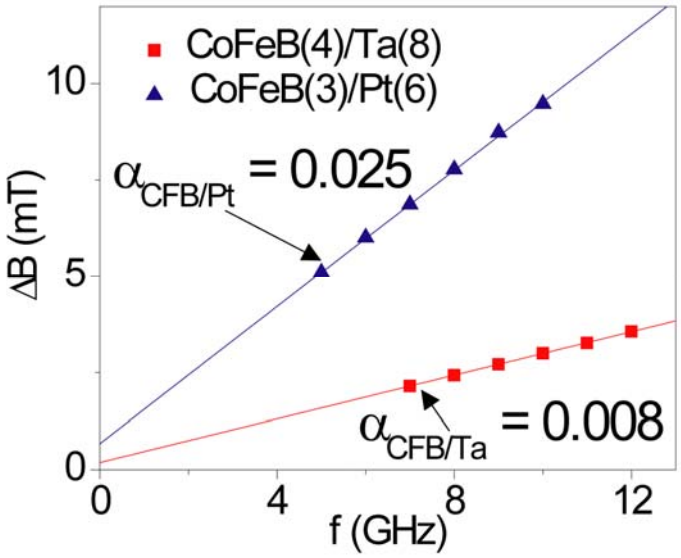

Figure 5.11 Resonance linewidths as determined from ST-FMR signals. The Gilbert damping coefficients α for Ta and Pt are calculated from the linear fits to these linewidth data.

If the spin torque from the SHE is to be utilized for switching nanomagnets by the conventional anti-damping ST switching mechanism [31], it is important that the nonmagnetic layer does not substantially increase the effective magnetic damping of the adjacent FM by the spin pumping effect [18, 32]. The ST-FMR measurements discussed above allow a determination of the Gilbert damping coefficient α from the linewidth ΔB (half width at half maximum) of the FMR peak, using the relationship $\alpha = (\gamma / 2\pi f)\Delta B$. The results shown in Fig. 5.11 indicate that $\alpha = 0.008$ for the CoFeB(4)/Ta(8) bilayer film, close to the intrinsic value expected for a 4 nm thick CoFeB layer [33], and much smaller than the corresponding $\alpha \approx 0.025$, for the CoFeB(3)/Pt(6) sample. This is consistent with ref. [18] in which damping caused by spin pumping was determined to be much stronger in FM/Pt bilayers than in FM/Ta, although the phase of Ta studied in [18] was not reported. The observation of a strong spin Hall effect in β–Ta is not in conflict with the weakness of the spin pumping effect

in Ta films, because the strength of the spin pumping depends not just on the strength of spin-orbit coupling, but also on the ratio of the elastic scattering time to the spin flip scattering time and the value of the spin mixing conductance [32], either or both of which might be smaller in β–Ta than Pt.

5.4 Conclusion

In summary, in this chapter I showed that spin current generated by the SHE in a Pt or Ta film can be used to excite spin-torque FMR in an adjacent metallic ferromagnet (Py or CoFeB) thin film. This technique also allows a determination of the efficiency of spin current generation, J_s/J_c (the spin current density absorbed by the Py divided by the charge current density in the Pt). Different from previous reports, we measured much larger J_s/J_c values, indicating that the SHE in Pt and Ta can be efficient enough for applications that utilize the SHE to manipulate ferromagnet dynamics. And in the following chapters I will demonstrate how the SHE can be used to realize those kind of functions.

REFERENCE

1. J. E. Hirsch, Spin Hall effect, *Phys. Rev. Lett.* **83**, 1834 (1999).
2. S. F. Zhang, Spin Hall effect in the presence of spin diffusion, *Phys. Rev. Lett.* **85**, 393 (2000).
3. J. Sinova, D. Culcer, Q. Niu, N. A. Sinitsyn, T. Jungwirth and A. H. MacDonald, Universal intrinsic spin Hall effect, *Phys. Rev. Lett.* **92**, 126603 (2004).
4. S. Murakami, N. Nagaosa and S. C. Zhang, Dissipationless quantum spin current at room temperature, *Science* **301**, 1348 (2003).
5. Y. K. Kato, R. C. Myers, A. C. Gossard and D. D. Awschalom, Observation of the spin hall effect in semiconductors, *Science* **306**, 1910 (2004).
6. S. O. Valenzuela and M. Tinkham, Direct electronic measurement of the spin Hall effect, *Nature* **442**, 176 (2006).
7. E. Saitoh, M. Ueda, H. Miyajima and G. Tatara, Conversion of spin current into charge current at room temperature: Inverse spin-Hall effect, *Appl. Phys. Lett.* **88**, 182509 (2006).
8. K. Ando, S. Takahashi, K. Harii, K. Sasage, J. Ieda, S. Maekawa and E. Saitoh, Electric manipulation of spin relaxation using the spin Hall effect, *Phys. Rev. Lett.* **101**, 036601 (2008).
9. T. Kimura, Y. Otani, T. Sato, S. Takahashi and S. Maekawa, Room-temperature reversible spin Hall effect (vol 98, art no 156601, 2007), *Phys Rev Lett* **98**, 156601 (2007).
10. O. Mosendz, J. E. Pearson, F. Y. Fradin, G. E. W. Bauer, S. D. Bader and A. Hoffmann, Quantifying Spin Hall Angles from Spin Pumping: Experiments and Theory, *Phys Rev Lett* **104**, 046601 (2010).
11. A. A. Tulapurkar, Y. Suzuki, A. Fukushima, H. Kubota, H. Maehara, K. Tsunekawa, D. D. Djayaprawira, N. Watanabe and S. Yuasa, Spin-torque diode effect in magnetic tunnel junctions, *Nature* **438**, 339 (2005).
12. J. C. Sankey, P. M. Braganca, A. G. F. Garcia, I. N. Krivorotov, R. A. Buhrman and D. C. Ralph, Spin-transfer-driven ferromagnetic resonance of individual nanomagnets, *Phys. Rev. Lett.* **96**, 227601 (2006).
13. J. C. Sankey, Y. T. Cui, J. Z. Sun, J. C. Slonczewski, R. A. Buhrman and D. C. Ralph, Measurement of the spin-transfer-torque vector in magnetic tunnel junctions, *Nature Phys.* **4**, 67 (2008).
14. H. Kubota, et al., Quantitative measurement of voltage dependence of spin-transfer torque in MgO-based magnetic tunnel junctions, *Nature Phys.* **4**, 37 (2008).
15. C. Wang, Y. T. Cui, J. A. Katine, R. A. Buhrman and D. C. Ralph, Time-resolved measurement of spin-transfer-driven ferromagnetic resonance and spin torque in magnetic tunnel junctions, *Nature Phys.* **7**, 496 (2011).
16. Y. T. Cui, Cornell University thesis, (2012).
17. J. C. Slonczewski, Current-driven excitation of magnetic multilayers, *J. Magn. Magn. Mater.* **159**, L1 (1996).

18. S. Mizukami, Y. Ando and T. Miyazaki, Ferromagnetic resonance linewidth for NM/80NiFe/NM films (NM = Cu, Ta, Pd and Pt), *J. Magn. Magn. Mater.* **226**, 1640 (2001).
19. Y. Tserkovnyak, A. Brataas and G. E. W. Bauer, Spin pumping and magnetization dynamics in metallic multilayers, *Phys. Rev. B* **66**, 224403 (2002).
20. I. N. Krivorotov, N. C. Emley, J. C. Sankey, S. I. Kiselev, D. C. Ralph and R. A. Buhrman, Time-domain measurements of nanomagnet dynamics driven by spin-transfer torques, *Science* **307**, 228 (2005).
21. A. Azevedo, L. H. Vilela-Leao, R. L. Rodriguez-Suarez, A. F. L. Santos and S. M. Rezende, Spin pumping and anisotropic magnetoresistance voltages in magnetic bilayers: Theory and experiment, *Phys. Rev. B* **83**, 144402 (2011).
22. S. Petit, C. Baraduc, C. Thirion, U. Ebels, Y. Liu, M. Li, P. Wang and B. Dieny, Spin-torque influence on the high-frequency magnetization fluctuations in magnetic tunnel junctions, *Phys. Rev. Lett.* **98**, 077203 (2007).
23. G. D. Fuchs, et al., Spin-torque ferromagnetic resonance measurements of damping in nanomagnets, *Appl. Phys. Lett.* **91**, 062507 (2007).
24. P. C. Vanson, H. Vankempen and P. Wyder, Boundary Resistance of the Ferromagnetic-Nonferromagnetic Metal Interface, *Phys. Rev. Lett.* **58**, 2271 (1987).
25. S. Mizukami, Y. Ando and T. Miyazaki, Effect of spin diffusion on Gilbert damping for a very thin permalloy layer in Cu/permalloy/Cu/Pt films, *Phys. Rev. B* **66**, 104413 (2002).
26. T. Seki, Y. Hasegawa, S. Mitani, S. Takahashi, H. Imamura, S. Maekawa, J. Nitta and K. Takanashi, Giant spin Hall effect in perpendicularly spin-polarized FePt/Au devices, *Nature Mat.* **7**, 125 (2008).
27. Y. Niimi, M. Morota, D. H. Wei, C. Deranlot, M. Basletic, A. Hamzic, A. Fert and Y. Otani, Extrinsic Spin Hall Effect Induced by Iridium Impurities in Copper, *Phys. Rev. Lett.* **106**, 126601 (2011).
28. T. Tanaka, H. Kontani, M. Naito, T. Naito, D. S. Hirashima, K. Yamada and J. Inoue, Intrinsic spin Hall effect and orbital Hall effect in 4d and 5d transition metals, *Phys. Rev. B* **77**, 165117 (2008).
29. M. Morota, Y. Niimi, K. Ohnishi, D. H. Wei, T. Tanaka, H. Kontani, T. Kimura and Y. Otani, Indication of intrinsic spin Hall effect in 4d and 5d transition metals, *Phys. Rev. B* **83**, 174405 (2011).
30. R. Hoogeveen, M. Moske, H. Geisler and K. Samwer, Texture and phase transformation of sputter-deposited metastable Ta films and Ta/Cu multilayers, *Thin Solid Films* **275**, 203 (1996).
31. D. C. Ralph and M. D. Stiles, Spin transfer torques, *J. Magn. Magn. Mater.* **320**, 1190 (2008).
32. Y. Tserkovnyak, A. Brataas and G. E. W. Bauer, Enhanced Gilber damping in thin ferromagnetic films, *Phys. Rev. Lett.* **88**, 117601 (2002).
33. H. Lee, L. Wen, M. Pathak, P. Janssen, P. LeClair, C. Alexander, C. K. A. Mewes and T. Mewes, Spin pumping in Co(56)Fe(24)B(20) multilayer systems, *J. Phys. D: Appl. Phys.* **41**, 215001 (2008).

CHAPTER 6

SPIN HALL EFFECT INDUCED SWITCHING IN PERPENDICULARLY MAGNETIZED FILMS

6.1 Introduction

In the previous chapter, we have already shown that the spin Hall effect [1-6] (SHE) inside heavy metals like Pt and Ta can be strong. Especially by utilizing the spin torque FMR technique, we illustrated that a large spin current density can be injected from the SHE materials into the adjacent ferromagnetic materials. Compared with conventional spin valve or MTJ geometries, the SHE configuration can be more efficient. Consider a thin film geometry such as shown in Fig. 6.1, where the charge current flows through a small in-plane area *a* and the spin current can act through a much larger perpendicular area *A*, the ratio of the total spin current to the total charge current $I_S / I_e = J_S A / (J_e a)$ can be much greater than one, meaning that for every electron charge passing through the device many $\hbar / 2$ units of angular momentum can flow perpendicular to the film to apply a spin transfer torque to an adjacent magnetic layer. Therefore it would be of great advantage if we could utilize the spin current generated by this efficient process to induce magnetic dynamics and switch magnetic moments.

Generally speaking, there are two approaches to switch a magnetic moment using the spin torque: anti-damping switching [7-8] and ballistic switching [9-10]. In anti-damping switching, the orientations of the injected spins σ are antiparallel with the equilibrium position of the local magnetic moment *m*. Therefore, the spin torque $\tau_{ST} \propto J_S m \times (\sigma \times m)$ is collinear with the damping torque $\tau_{damp} = \alpha \gamma m \times (H \times m)$,

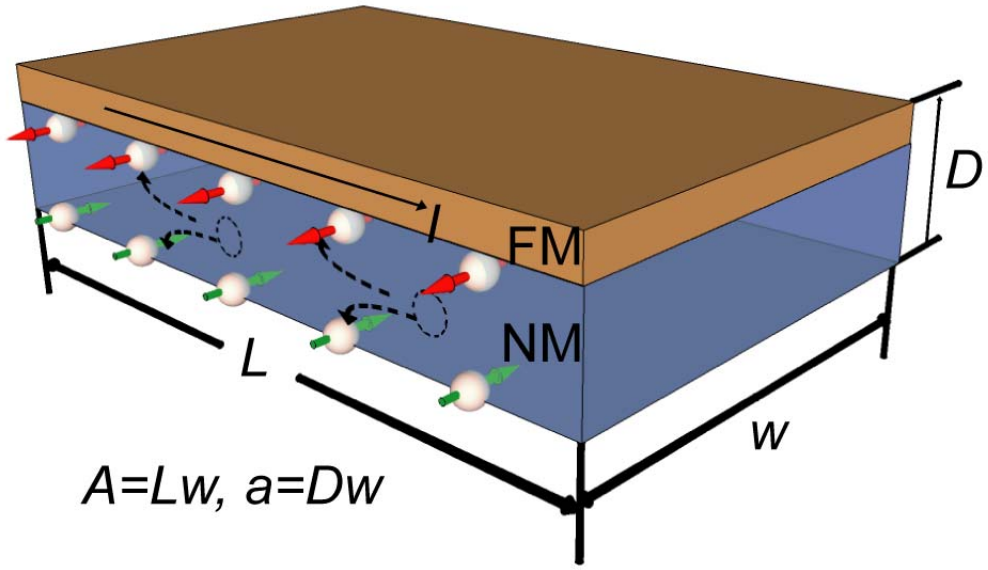

Figure 6.1 Schematic illustration of the spin current injected into FM layer due to the SHE. The red and green arrows represent spins accumulated at the top and bottom surface of the normal metal (NM) layer. The cross section for the charge current and the spin current are given by *a* and *A*, separately.

where H represents the effective magnetic field. τ_{ST} acts like a negative damping, and switching happens when the net effective damping is reduced to zero. In this case the critical current for switching is proportional to the damping coefficient α. However, as we have shown in Chapter 5, for materials like Pt, the spin pumping mechanism will bring in an extra damping to the ferromagnetic layer, and make the switching difficult. On the other hand, in ballistic switching, the injected spins are orthogonal to *m*. In this configuration, instead of fighting against the damping term, the spin torque is balanced with the torque provided by the effective magnetic field. And the critical current for switching is given by the anisotropy field H_{an}. So the critical current for switching is no longer influenced by the damping of the FM layer and it can be easier to realize the SHE induced magnetic switching in this configuration for materials with strong spin pumping.

The ballistic switching mechanism was first proposed theoretically because it can provide a very fast switching speed compared with the conventional antidamping switching [9]. To achieve this, the polarizer layer is usually magnetized perpendicular to plane and the free layer lies within the film plane, so that the injected spins and the local magnetic moment are orthogonal to each other. In this chapter we will see that ballistic switching can also happen within the system where the free layer is magnetized out of plane and the injected spins are in-plane oriented. Especially we will talk about two systems: Pt/Co and Ta/CoFeB, where a perpendicular anisotropy can be easily obtained and the spin Hall angle is large (see Chapter 5). In-plane current induced switching for perpendicularly magnetized FM films was first observed by Miron *et al*. in ref. [12]. However, Miron et al. argued that the spin Hall effect was not strong enough to explain their measurements, asserting instead that a Rashba mechanism was dominant. In the rest of this chapter I will show, by modeling and measurement, that the SHE can account for the switching quantitatively and the Rashba effect does not make a contribution in the observed switching. We will also see that in those systems the SHE torque is capable of driving switching in magnetic memory devices using switching currents that are comparable to conventional spin-transfer-torque magnetic tunnel junctions [11], so that SHE-torque switching could be highly effective in technological applications.

6.2 Modeling and simulation

6.2.1 Macrospin model for SHE switching

Let's first solve a simple zero-temperature macrospin model to illustrate the types of behavior that can be generated by a SHE torque acting on a magnetic layer with perpendicular anisotropy. We assume the magnetic layer has thickness t, constant magnetization magnitude M_S, and magnetic orientation $\hat{m}$ and lies on top of the SHE

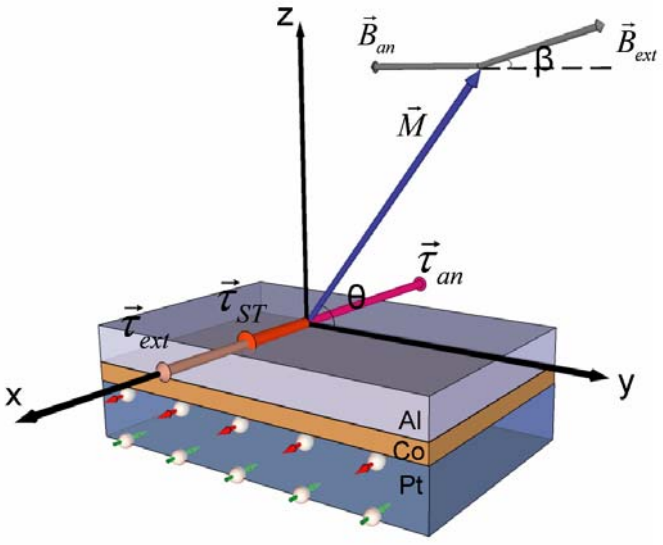

Figure 6.2 Schematic illustration of the fields and torques exerted on the magnetization. Here, the spin torque is assumed to be small so that $|\tau_{ST}^0| < 0.5 B_{an}^0$ and *M* lies in the yz plane. The external field $\vec{B}_{ext}$ is applied in the yz plane and forms an angle β with the y axis. $\vec{\tau}_{ext}$ and $\vec{\tau}_{an}$ represent the torques generated by $\vec{B}_{ext}$ and the anisotropy field $\vec{B}_{an}$. $\vec{\tau}_{ST}$ is the spin torque due to the SHE when electrons flow in the -y direction.

metal of thickness *d* (for simplicity, we will take Pt/Co system as an example in the following discussion). We consider the geometry shown in Fig. 6.2, with the sample in the *xy* plane and with an applied magnetic field $\vec{B}_{ext} = 0\hat{x} + B_y\hat{y} + B_z\hat{z}$ (the model is generalizable for other field directions). Let's assume that the magnetic layer has perpendicular anisotropy, i.e., the equilibrium position of $\hat{m}$ is along $\pm z$ direction. Positive current (electrons flowing in the $-\hat{y}$ direction) induces a spin Hall current within the Pt layer such that spin moments pointing in the $\hat{\sigma} = \hat{x}$ direction (spin angular momentum pointing in $-\hat{x}$) flow upward, in the $\hat{z}$ direction. When this spin current reaches the Pt/ferromagnet interface, the spin component perpendicular to $\hat{m}$ can be absorbed by the ferromagnet, imparting a spin-transfer "torque" per unit moment $\vec{\tau}_{ST} = \tau_{ST}^0(\hat{m}\times\hat{\sigma}\times\hat{m}) = \dfrac{\hbar}{2e\mu_0 M_S t} J_S(\hat{m}\times\hat{\sigma}\times\hat{m})$. Taking into account also the

torques (per unit moment) due to the external magnetic field, $\vec{\tau}_{ext} = -\hat{m} \times \vec{B}_{ext}$, and due to the anisotropy field, $\vec{\tau}_{an} = -\hat{m} \times \vec{B}_{an} = -\hat{m} \times \left[-B_{an}^{0} (\hat{m} - m_z \hat{z}) \right] = -B_{an}^{0} m_z (\hat{m} \times \hat{z})$, the equilibrium orientations of $\hat{m}$ satisfy the condition $\vec{\tau}_{tot} = \vec{\tau}_{ST} + \vec{\tau}_{ext} + \vec{\tau}_{an} = 0$. We use macrospin simulations of the equation of motion $\left(1/|\gamma|\right) d\hat{m}/dt = \vec{\tau}_{tot} + \left(\alpha/|\gamma|\right) \hat{m} \times (d\hat{m}/dt)$ with α > 0 to distinguish stable from unstable equilibria.

Within this model, we calculate how the orientation of $\hat{m}$ depends on τ_{ST}^{0} and $\vec{B}_{ext}$. For currents corresponding to small to moderate values of spin torque, $|\tau_{ST}^{0}| < 0.5 B_{an}^{0}$, $\hat{m}$ can remain within the *yz* plane as long as $B_x = 0$. In this case all three torques ($\vec{\tau}_{ST}, \vec{\tau}_{ext}, \vec{\tau}_{an}$) are collinear in the $\hat{x}$ direction and the torque balance equation that determines the magnetization angle θ takes a simple scalar form,

$$\tau_{tot} \equiv \hat{x} \cdot \left(\vec{\tau}_{ST} + \vec{\tau}_{ext} + \vec{\tau}_{an} \right) = \tau_{ST}^{0} + B_{ext} \sin\left(\theta - \beta\right) - B_{an}^{0} \sin\theta \cos\theta = 0. \qquad (6.1)$$

θ and the applied field angle β are defined as in Fig. 6.2 with $-\pi/2 < \beta \leq \pi/2$. As the current is ramped from zero for fixed values of B_{ext} and β, initially the dominant effect of $\vec{\tau}_{ST}$ is not to provide an anti-damping torque as it would if the Co was magnetized in-plane, but rather to rotate $\hat{m}$ within the *yz* plane, thereby shifting θ continuously, until, for sufficiently large currents, Equation 6.1 predicts abrupt hysteretic switching. In Figure 6.3 (a), we show magnetic hysteresis curves predicted by this macrospin model for representative fixed values of the in-plane magnetic field. We can see that an important feature associated with the SHE switching is that the switching polarity is not only determined by the sign of the applied current but also by the applied in-plane field. The sign of the hysteresis reverses when the in-plane field component is reversed. The reason for this reversal is that although an in-plane magnetic field does not favor either magnetic orientation by itself, an in-plane field breaks the symmetry in the response to the SHE torque [Fig. 6.3 (b)]. With a magnetic field component in

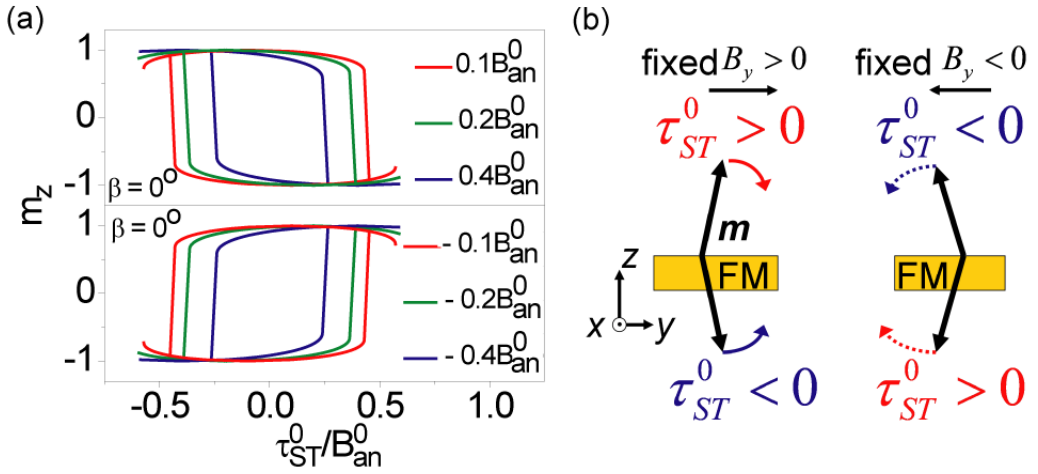

Figure 6.3 Macrospin modeling for SHE induced switching. (a) Predictions for current-induced magnetic switching within the macrospin model. The red, green and blue curves correspond to in-plane magnetic fields $B_y = \pm 0.1\, B^0_{an}$, $\pm 0.2\, B^0_{an}$ and $\pm 0.4\, B^0_{an}$, respectively, and the direction of switching reverses when B_y changes sign. (b) Schematic illustration of the magnetization vectors for the two tilted magnetic states which are stable in the absence of current when a fixed in-plane magnetic field $B_y > 0$ (left) or $B_y < 0$ (right) is applied. (The angle of the tilt from vertical is exaggerated) The directions of current-induced switching depend on the sign of τ^0_{ST} as shown.

the in-plane $\hat{y}$ direction, the barrier against clockwise rotation of $\hat{m}$ from the $m_z > 0$ state to the $m_z < 0$ is different than for clockwise rotation from the $m_z < 0$ to the $m_z > 0$ state, with the result that the direction of the in-plane field determines which out-of-plane magnetic orientation will be favored by a given sign of τ_{ST}.

For very large spin torques, $\left|\tau^0_{ST}\right| > B^0_{an}/2$, the SHE torque is greater than the maximum value of the restoring torque from the magnetic anisotropy, $\left|\vec{\tau}_{an}\right|$, and for sufficiently small values of $\left|B_{ext}\right|$ there is no solution of Equation 6.1. This means that $\hat{m}$ cannot remain in the *yz* plane. By solving the full vector equation $\vec{\tau}_{tot} = 0$, we find that for large $\left|\tau^0_{ST}\right|$ there is a current-stabilized state in which $\hat{m}$ develops a component in the $+\hat{x}$ direction for positive τ^0_{ST} and $\hat{m}$ tilts toward $-\hat{x}$ for negative τ^0_{ST}.

6.2.2 Determining the phase diagram in the macrospin model

As is discussed in the previous section, the magnetic moment *m* can be oriented within the *yz* plane or out of the *yz* plane, depending upon the magnitude of the spin torque and the applied field. The full phase diagram in the macrospin model for $\hat{m}(\tau_{ST}^0, B_y, B_z)$ which contains both of those two cases can be calculated using the equations that we gave out in the previous section.

For simplicity, let's assume that there is no applied magnetic field component in the *x* direction as in Fig. 6.2. We will determine the magnetic orientations $\hat{m}(\tau_{ST}^0, B_y, B_z)$ that satisfy the torque balance equation $\vec{\tau}_{tot} \equiv \vec{\tau}_{ST} + \vec{\tau}_{ext} + \vec{\tau}_{an} = 0$, where

$$\vec{\tau}_{ST} = \tau_{ST}^0 (\hat{m} \times \hat{x} \times \hat{m}) \tag{6.2}$$

$$\vec{\tau}_{ext} = -\hat{m} \times \vec{B}_{ext} \tag{6.3}$$

$$\vec{\tau}_{an} = -\hat{m} \times \vec{B}_{an} = -\hat{m} \times \left[-B_{an}^0 \left(\hat{m} - m_z \hat{z} \right) \right] = -B_{an}^0 m_z (\hat{m} \times \hat{z}) . \tag{6.4}$$

By defining the *x*, *y*, *z* axes as in Fig. 6.2, we can evaluate each of these torques in Cartesian coordinates, using $\hat{m} = \left(m_x, m_y, m_z \right)$ with $m_x^2 + m_y^2 + m_z^2 = 1$ and $\vec{B}_{ext} = \left(B_x, B_y, B_z \right)$.

$$\vec{\tau}_{tot} = 0 = \begin{array}{c} \hat{x}\left[\tau_{ST}^0 \left(m_y^2 + m_z^2 \right) - B_z m_y + B_y m_z - B_{an}^0 m_y m_z \right] \\ + \hat{y}\left[-\tau_{ST}^0 m_x m_y + B_z m_x - B_x m_z + B_{an}^0 m_x m_{zz} \right] \\ + \hat{z}\left[-\tau_{ST}^0 m_x m_z - B_y m_x + B_x m_y \right] \end{array} \tag{6.5}$$

By construction, all of the torques are perpendicular to $\hat{m}$, so it is convenient to consider just the two components within the plane perpendicular to $\hat{m}$ by taking projections along the directions

$$\hat{x} \times \hat{m} = -m_z \hat{y} + m_y \hat{z} \tag{6.6}$$

$$\text{and} \quad \hat{m} \times \hat{x} \times \hat{m} = \left(m_y^2 + m_z^2 \right) \hat{x} - m_x m_y \hat{y} - m_x m_z \hat{z} . \tag{6.7}$$

It is reasonable to perform these projections for all cases except when $\hat{m} = \hat{x}$ (in which case both vectors are zero). This case can be ignored because $\hat{m} = \hat{x}$ is not a stable

solution of Equation 6.5 for any interesting physical case with $B_x = 0$. These two projections give the results

$$\left(\hat{x} \times \hat{m}\right) \cdot \vec{\tau}_{tot} = 0 = B_x \left(m_y^2 + m_z^2\right) - B_y m_x m_y - B_z m_x m_z - B_{an}^0 m_x m_z^2 \tag{6.8}$$

$$\left(\hat{m} \times \hat{x} \times \hat{m}\right) \cdot \vec{\tau}_{tot} = 0 = \tau_{ST}^0 \left(m_y^2 + m_z^2\right) + B_y m_z - B_z m_y - B_{an}^0 m_y m_z \,. \tag{6.9}$$

If we consider only cases in which $B_x = 0$, we have

$$0 = m_x \left(B_y m_y + B_z m_z + B_{an}^0 m_z^2\right) \tag{6.10}$$

$$0 = \tau_{ST}^0 \left(m_y^2 + m_z^2\right) + B_y m_z - B_z m_y - B_{an}^0 m_y m_z \,. \tag{6.11}$$

Given the form of Equation 6.10, the solutions for the case $B_x = 0$ break up into two classes, either $m_x = 0$ or $B_y m_y + B_z m_z + B_{an}^0 m_z^2 = 0$, corresponding to different phases in which the magnetization remains in the *yz* plane (at small values of τ_{ST}^0) or in which it is forced to tilt out of this plane (at larger values of τ_{ST}^0). We will consider these two phases separately.

6.2.2.1 Solutions for $B_x = 0$ with $m_x = 0$

In this case, we have $m_y^2 + m_z^2 = 1$ and Equation 6.11 becomes

$$0 = \tau_{ST}^0 + B_y m_z - B_z m_y - B_{an}^0 m_y m_z \,. \tag{6.12}$$

This is identical to Equation 6.1 with the identifications that for $m_x = 0$ then $m_y = \cos\theta$, $m_z = \sin\theta$, $B_y = B_{ext} \cos\beta$, and $B_z = B_{ext} \sin\beta$. Equation 6.12 can be solved numerically. The stable and unstable equilibrium states can be distinguished by simulating the LLG equation with positive damping coefficient.

For convenience in determining the limits of stability for the $m_x = 0$ states (analogous to the Stoner-Wohlfarth astroid), we can rewrite Equation 6.12 in the form

$$0 = \tau_{tot}^x \equiv \tau_{ST}^0 + B_y \sin\theta - B_z \cos\theta - B_{an}^0 \sin\theta\cos\theta \,. \tag{6.13}$$

Within a zero-temperature macrospin model, the switching conditions for which an $m_x = 0$ solution becomes unstable are determined by equation 6.13 together with

the condition:

$$d\tau_{tot}^{x} / d\theta = 0 = B_y \cos\theta + B_z \sin\theta + B_{an}^{0} \left(\sin^2\theta - \cos^2\theta\right). \tag{6.14}$$

We can reach a symmetric form for the switching conditions by combining Equations 6.13 and 6.14 to eliminate first B_z and then B_y. To eliminate B_z, we multiply Equation 6.13 by $\sin\theta$ and Equation 6.14 by $\cos\theta$ and then add, to give

$$B_y + \tau_{ST}^{0} \sin\theta = B_{an}^{0} \cos^3\theta. \tag{6.15}$$

To eliminate B_y, we multiply Equation 6.13 by $-\cos\theta$ and Equation 6.14 by $\sin\theta$ and then add, to give

$$B_z - \tau_{ST}^{0} \cos\theta = -B_{an}^{0} \sin^3\theta. \tag{6.16}$$

6.2.2.2 Solutions for $B_x = 0$ with $m_x \neq 0$ but with $B_y m_y + B_z m_z + B_{an}^{0} m_z^2 = 0$

From Equation 6.10 we have

$$m_y = -\frac{B_z m_z + B_{an}^{0} m_z^2}{B_y}. \tag{6.17}$$

Substituting this into Equation 6.11 and factoring the result, we find

$$0 = m_z \left(\tau_{ST}^{0} m_z + B_y\right) \left[\frac{\left(B_{an}^{0}\right)^2}{B_y^2} m_z^2 + \frac{2 B_z B_{an}^{0}}{B_y^2} m_z + \frac{B_z^2}{B_y^2} + 1 \right]. \tag{6.18}$$

There is no allowed physical solution for which the quadratic equation in the square brackets is equal to zero (the discriminant is negative). There is an apparent solution with $m_z = 0$, ($m_x = 1$, $m_y = 0$, $m_z = 0$), but this arises as an artifact of our choice to project along the axes $\hat{x} \times \hat{m}$ and $\hat{m} \times \hat{x} \times \hat{m}$ -- these vectors are both trivially zero if $\hat{m} = \hat{x}$. By substituting directly into the starting equation, Equation 6.5, one can see that is not actually a solution of the starting equation. Therefore the only allowed solution in this class is

$$m_z = -\frac{B_y}{\tau_{ST}^{0}} \tag{6.19}$$

$$m_y = -\frac{B_{an}^{0} B_y}{\left(\tau_{ST}^{0}\right)^2} + \frac{B_z}{\tau_{ST}^{0}} \tag{6.20}$$

$$m_x = \pm\sqrt{1-(m_y)^2-(m_z)^2} = \pm\sqrt{1-\left(\frac{B_y}{\tau_{ST}^0}\right)^2-\left(-\frac{B_{an}^0 B_y}{(\tau_{ST}^0)^2}+\frac{B_z}{\tau_{ST}^0}\right)^2}\ . \qquad (6.21)$$

Only one sign of m_x will be a stable equilibrium. We determine which one is stable by simulating the equation of motion $\left(1/|\gamma|\right)d\hat{m}/dt = \vec{\tau}_{tot} + \left(\alpha/|\gamma|\right)\hat{m}\times(d\hat{m}/dt)$ with α > 0.

We have verified these two different classes of analytical solutions ($m_x = 0$ and $m_x \neq 0$) as well by numerical solution of the macrospin Landau-Lifshitz-Gilbert equation with the spin Hall torque included. There are no dynamical states that can be excited by a constant spin Hall torque within this model for a magnetic film with perpendicular anisotropy and for $B_x = 0$.

Equations 6.15, 6.16 and 6.21 allow a numerical solution for the value of the SHE torque needed to achieve switching for any fixed values of B_y and B_z.The full phase diagram can therefore be calculated. We show particular sections through the phase diagram in Fig. 6.4 (a) and (b), which correspond to the case of $B_z = 0$ and $B_y = 0.2\,B_{an}^0$, seperately. In the central areas of Fig. 6.4 (a) and (b) (labeled $m_z = \uparrow / \downarrow$, $m_x = 0$) $\hat{m}$ is bistable between the ($m_z > 0$, $m_x = 0$) and ($m_z < 0$, $m_x = 0$) states. The solid lines are boundaries at which one of these $m_x = 0$ states is destabilized, producing a hysteretic transition. These switching boundaries are calculated from Equation (6.15) and (6.16), which as we discussed above, give the solution under the constraint of $m_x = 0$.

The distinct high current states for which the SHE torque tilts the magnetic orientation out of the *yz* plane are labeled in Fig. 6.4 by $m_x > 0$ and $m_x < 0$. When $\left|\tau_{ST}^0\right| > B_{an}^0/2$, from Equations 6.15 and 6.16 it can be seen that these $m_x \neq 0$ states are the only allowed solutions for small $\left|B_{ext}\right|$. Once formed, the $m_x \neq 0$ states can remain

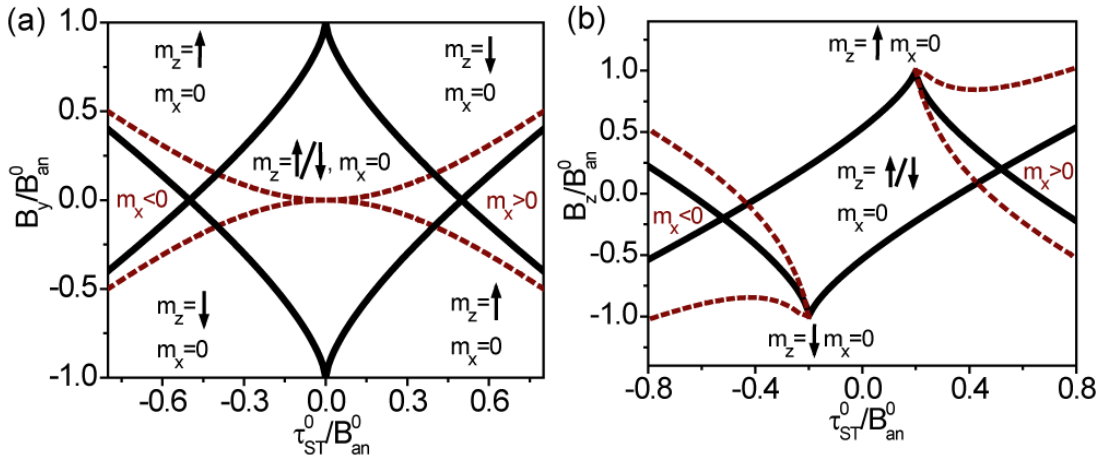

Figure 6.4 Calculated switching phase diagram (SPD). The switching boundaries are obtained by using the zero-temperature macrospin model. (a) B_{ext} is applied along the y axis. (b) B_y is fixed at 0.2 B^0_{an} and B_z is varied continuously. The solid lines represent switching boundaries for the ($m_z = \uparrow/\downarrow$, $m_x = 0$) states while the dashed lines show the limits of stability for the $m_x \neq 0$ states. The symbol $\uparrow$ means $m_z > 0$ and $\downarrow$ means $m_z < 0$, not $m_z = \pm 1$.

stable even for a range of smaller $\left|\tau^0_{ST}\right|$. The limits of stability for these high-current $m_x \neq 0$ solution are determined by the condition that the quantity under the square root in Equation 6.21 changes from positive to negative. The dashed lines in Fig 6.4 represent the boundaries at which the $m_x \neq 0$ states become locally unstable.

6.3 Experiment

6.3.1 Sample and measurement setup

6.3.1.1 Sample description

The first type of samples that we studied consist of Pt(20)/Co(6)/Al(16) (thicknesses in Å) multilayer (Fig. 6.2). The films were deposited by sputtering onto thermally oxidized Si wafers at a base pressure lower than 2×10^{-8} torr. The growth rate was controlled to be less than 0.5 Å/s in order to achieve a highly oriented texture.

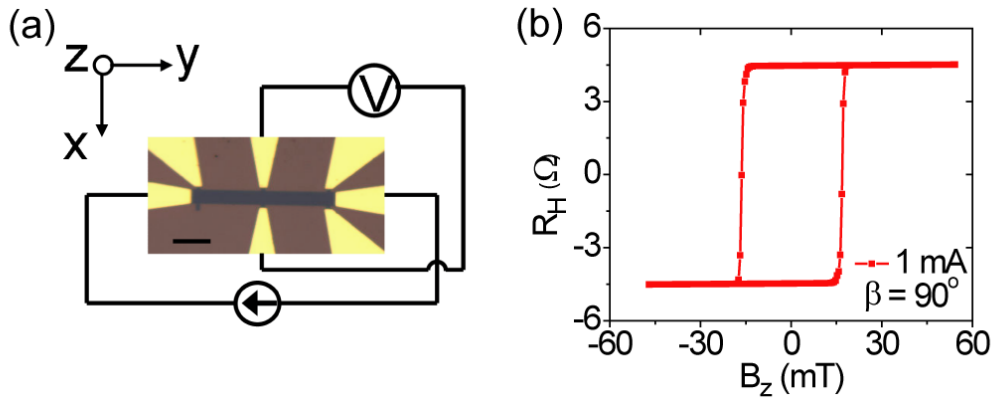

Figure 6.5 Measurement of the anomalous Hall effect. (a) Top view of the sample (50 μm scale bar). (b) The anomalous Hall resistance R_H as a function of external field B_{ext} when B_{ext} is applied perpendicular to the sample plane.

The Al capping layer was oxidized by exposure to the atmosphere; no plasma oxidation was employed. The Pt/Co/Al sample was annealed under ultra-high vacuum at 350 °C for 1 hr, which improved the squareness of magnetic hysteresis loops as a function of magnetic field swept in the *z* direction. The films were patterned into Hall bar geometries using photolithography and ion milling [Fig. 6.5 (a)]. Ti/Au electrodes were evaporated to provide electrical connection. The Hall bar has a total resistance ~ 2000 Ω. We measure the anomalous Hall resistance, R_H, which is proportional to the average vertical component of the Co magnetization M_z [13]. Measurements as a function of vertical magnetic field near zero current establish the existence of perpendicular magnetic anisotropy [Fig. 6.5(b)].

6.3.1.2 Calibration of the angles for the sample holder

For our Hall resistance measurements, the sample chip was installed onto a rotary stage which provided a 360° rotation range and 0.02° rotation precision. The accuracy of the angle between the sample plane and the magnetic field (as is defined by β in Fig. 6.2) is crucial for our measurement of the spin torque. In order to

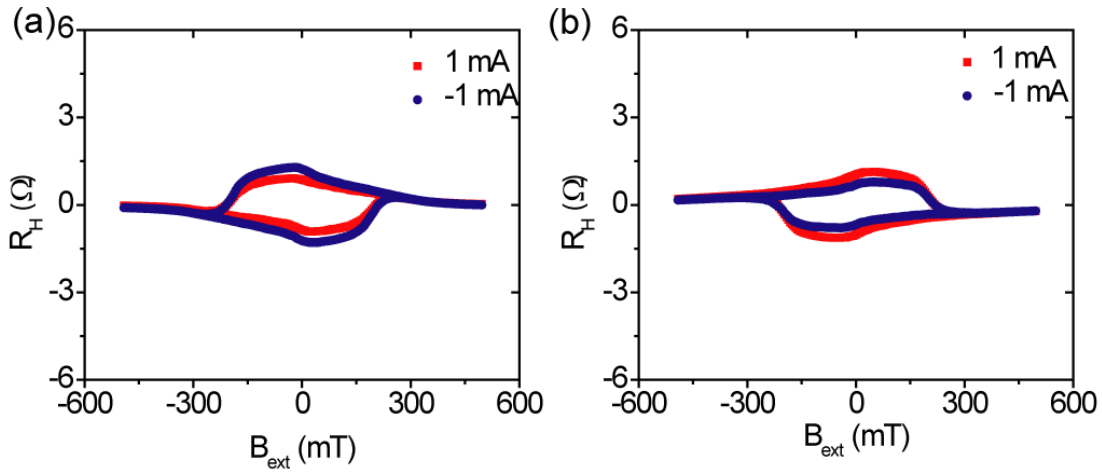

Figure 6.6. Hysteresis loops used to determine the zero point for the angle β. The curves shown in (a) and (b) correspond to a small positive and negative β, respectively.

determine the zero point for the angle β we recorded magnetization curves (R_H vs. B_{ext}) for different fixed values of the field angle β. Small currents (I = 1 mA) were utilized for those measurements in order to minimize the effect of spin torque on the magnetization. The curves shown in Fig. 6.6 (a) and (b) were obtained near $\beta \approx 0$ with a difference in β of less than 1°. It can be seen that the sign of R_H is opposite between the R_H vs. B_{ext} curves of these two plots, indicating that the z components of B_{ext} for those two angles are positive and negative, separately. We are therefore able to determine that the angle corresponding to $\beta = 0$ is bounded by the two positions. The accuracy of the angle read from the stage is limited by the uncertainty of the zero point, and is within $\pm 1°$.

6.3.2 Current induced switching

The current induced switching obtained from the Pt/Co/Al sample is plotted in Fig. 6.7. In Fig. 6.7 (a) we apply a small constant in-plane magnetic field (along the current direction $\hat{y}$ as shown in Fig. 6.2, *i.e.* $\beta = 0°$) that tilts the average moment by approximately 2° from vertical, but does not provide any preference for either the up

or down magnetic state in the absence of current. A quasi-static in-plane current then generates hysteretic magnetic switching between the $M_z > 0$ and $M_z < 0$ magnetic states, with positive current favoring $M_z < 0$ [Fig. 6.7(a)]. If the small constant in-plane magnetic field is reversed, the current-driven transitions invert, with positive current now favoring $M_z > 0$, despite the fact that the in-plane field still does not favor either magnetic state in the absence of current [Fig. 6.7(b)]. The Oersted magnetic field generated by the quasistatic current cannot explain this remarkable result, as it is oriented in plane. We have observed the same switching phenomenon in Hall bars with widths varying from 1 to 20 μm, with at least five samples studied for each type.

6.3.3 Quantitative measurement of the spin torque

Current induced switching for a perpendicularly magnetized Co layer was previously reported by Miron et al.[12], who argued that the mechanism was primarily a current-generated Rashba field associated with having different materials below (Pt) and above (AlO_x) the Co layer. In order to determine whether the observed switching is due to the spin Hall effect or due to the Rashba field, we need to determine the amplitude of those two effects quantitatively in the studied system and compare them with the results obtained elsewhere.

Because the switching shown in Fig. 6.7 happens in the multi-domain regime, non-uniform switching mechanisms like domain wall nucleation and domain wall motion can influence the switching current significantly. Therefore, it is difficult to extract the magnitude of the spin Hall effect or the Rashba field directly from the switching data. Instead, we can focus on the regime where magnetic moments in different domains rotate coherently. By analyzing the direction and magnitude of current-induced rotation we can measure the SHE torque, and distinguish the SHE

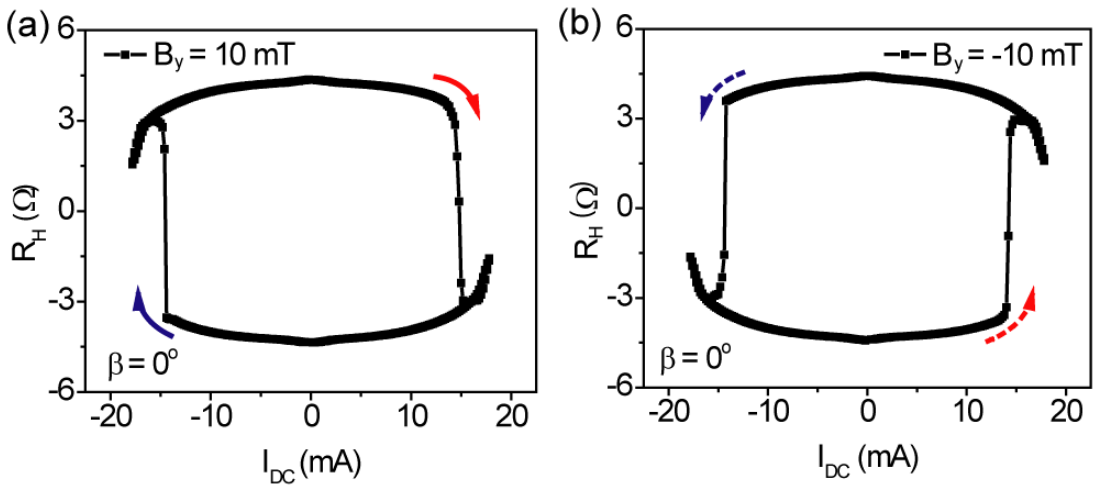

Figure 6.7 Current-induced switching in a Pt/Co/AlO$_x$ sample. The measurement was taken at room temperature in the presence of a small, fixed in-plane magnetic field B_y with (a) B_y = 10 mT and (b) B_y = -10 mT.

torque from an in-plane Rashba field [12].

We first apply $\vec{B}_{ext}$ in the *yz* plane with a small angle $\beta = 4°$ relative to the *y* axis (Fig. 6.2). In this case the field-induced torque is parallel to $\hat{x}$ so it adds to or subtracts from the SHE torque, depending on the sign of *I*. The nonzero angle β suppresses domain formation so that the magnetization rotates coherently, and the macrospin model applies. We compare field sweeps for the same magnitude of current, positive and negative [$I = \pm 12$ mA in Fig. 6.8 (a)], so that Ohmic heating should be identical. We define $B_+(\theta)$ as the value of B_{ext} required to produce a given value of θ when *I* is positive and $B_-(\theta)$ as the corresponding quantity for *I* negative. From Equation 6.1, $B_{+/-}(\theta) = [B_{an}^0 \sin\theta\cos\theta \mp \tau_{ST}^0]/\sin(\theta-\beta)$, so that $B_-(\theta) - B_+(\theta) = 2\tau_{ST}^0/\sin(\theta-\beta)$. The angle β is known for our apparatus with an accuracy of $\pm 1°$ and $\sin\theta$ can be determined accurately from R_H. Therefore, by taking the difference of the two experimental B_{ext} versus R_H curves (for $\pm I$) [Fig. 6.8 (b)] and performing a one-parameter fit, we can determine $\tau_{ST}^0 = 4.0 \pm 0.7$ mT for $I =$

12 mA, or $\tau_{ST}^0 / I = 0.33 \pm 0.06$ mT/mA. We find that τ_{ST}^0 / I is approximately independent of *I* [Fig. 6.8(c)]. A current of 12 mA corresponds to a charge current density $J_e = 2.3 \times 10^7$ A/cm^2, assuming for simplicity that the current density is uniform throughout the Pt/Co bilayer and the Al is fully oxidized. Using $\tau_{ST}^0 = \hbar J_S / (2eM_S t)$ with the measured value $M_S \approx 1.0 \times 10^6$ A/m, our value of τ_{ST}^0 at 12 mA corresponds to $J_S \approx 7 \times 10^5$ A/cm^2, or $J_S(d = 2 \text{ nm}) / J_e = 0.03 \pm 0.01$. According to our discussion in section 5.3.3, the spin current injected into the FM layer would be reduced from its bulk value when the Pt film thickness is smaller or comparable to the spin diffusion length: $J_S(d) / J_S(\infty) = 1 - \text{sech}(d / \lambda_{sf})$. Using the spin diffusion length of $\lambda_{sf} = 1.4$ nm that we determined in section 5.3.3, the measurement of $J_S(d = 2 \text{ nm}) / J_e = 0.03 \pm 0.01$ corresponds to a corrected bulk value $J_S(d = \infty) / J_e = 0.06 \pm 0.02$. This agrees quantitatively with measurements for in-plane-polarized Pt/permalloy bilayers in Chapter 5. A similar analysis of $B_+(\theta) + B_-(\theta)$ allows a determination of B_{an}^0 as a function of $|I|$: $B_{an}^0 = 280$ mT near $I = 0$ and decreases significantly as a function of increasing $|I|$, reflecting heating. B_{an}^0 measured under different $|I|$ are summarized in Fig. 6.9 (a). It can be seen that there is a strong decrease in B_{an}^0 as a function of $|I|$, also presumably due to Ohmic heating.

Next we describe a similar experiment with $\vec{B}_{ext} = B_x \hat{x}$. If there is any current-induced Rashba field, it should be primarily in the $\hat{x}$ direction [14-17], therefore yielding current-induced shifts in R_H vs. B_x curves. Fig. 6.8 (d) shows representative data for $I = \pm 10$ mA, corresponding to a current density of 1.9×10^7 A/cm^2. We observe no measurable shift between the two curves for any value of $|I|$, from which we conclude that any Rashba field in our sample has a magnitude that is less than our sensitivity, $|B_{Rashba}| / J_e < 1.3 \times 10^{-7}$ mT /(A/cm^2). This result is in striking contrast to ref. [18] , where an $\hat{x}$-oriented Rashba field 75 times larger than our upper bound was

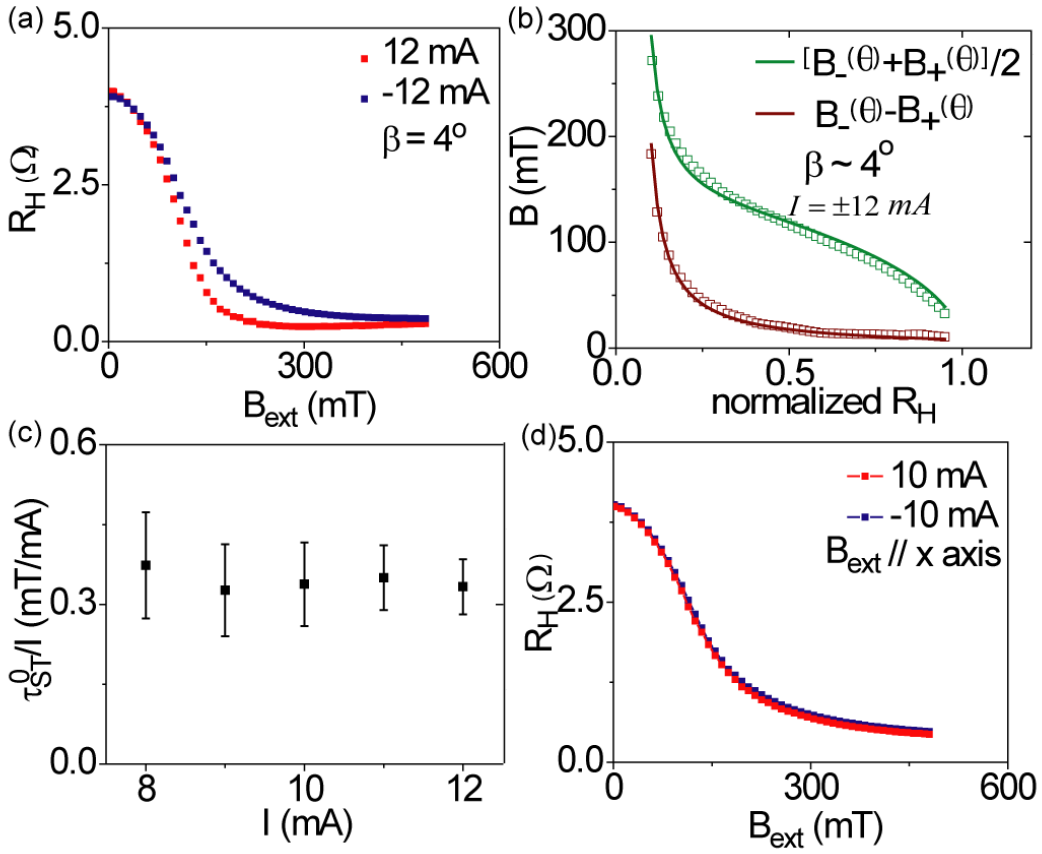

Figure 6.8 Determination of the magnitude of spin torque. (a) R_H vs. B_{ext}, measured during coherent rotation for I = ±12 mA, when the magnetic field is in the *yz* plane at β = 4°. (b) Points: Measured values of $B_-(\theta) - B_+(\theta)$ and $[B_-(\theta) + B_+(\theta)]/2$ as defined in the text, determined from the data in (a). Lines: fits to the macrospin model to determine $\tau_{ST}^0(I)$ and $B_{an}^0(I)$. (c) τ_{ST}^0 / I measured for different values of I. (d) R_H as a function of applied field when B_{ext} is applied along the x direction, for $I = \pm$ 10 mA. The curves are indistinguishable, allowing us to set a limit on the in-plane Rashba field.

reported for similar Pt(30)/Co(6)/AlO_x samples. (The $\hat{x}$-oriented Oersted field, which is $\left|B_{Oersted}\right| / J_e = \mu_0 d / 2 = 1.3\times10^{-8}$ mT /(A/cm^2) by Ampere's law, is less than our measurement sensitivity.) Therefore the Rashba effects proposed by Miron et al.[12, 18] do not make a measurable contribution to the magnetic orientation in our samples.

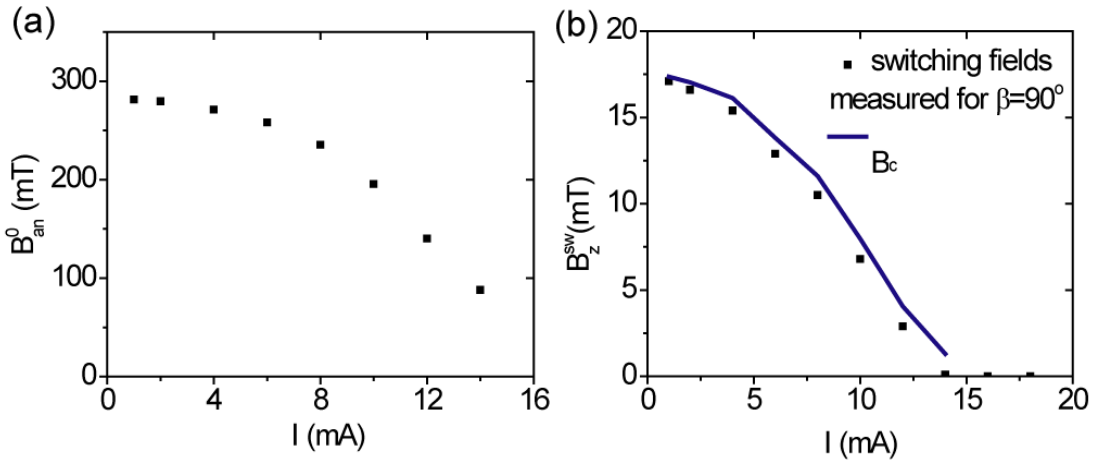

Figure 6.9. The current dependence of the perpendicular anisotropy field and the intrinsic coercive field. (a), B^0_{an} as a function of the applied current $|I|$ measured as explained in Section 6.3.3. (b), Square points: Measured switching fields B^{sw}_z for field sweeps perpendicular to the sample plane. Solid line: The intrinsic coercive field $B_c(|I|)$ after correcting for the effects of the spin Hall torque as explained in Section 6.3.4.

6.3.4 Experimental switching phase diagram

To compare with the switching phase diagrams (SPDs) predicted within the macrospin model (Fig. 6.4), we measured switching curves under different current and field combinations and summarized the results in Fig. 6.10. Qualitatively, these SPDs have shapes and symmetries very similar to the stability boundaries in the macrospin model (Fig. 6.4), supporting our assertion that the switching can be explained by the SHE torque. However, to analyze the effects of the SHE torque quantitatively, it is not appropriate to use a zero-temperature macrospin model for two reasons: (i) current-induced heating can be significant and (ii) magnetic switching occurs by means of a spatially non-uniform reversal process. Nonuniform switching is evident even for $I = 0$, in that the easy axis switching field [$B_c =$ 17 mT, see Fig. 6.5 (b)] is much less than the value $B_c = B^0_{an}$ expected within the macrospin model ($B^0_{an} = 280$ mT near $I = 0$, determined in section 6.3.3). Nevertheless, we can achieve a reasonable

quantitative modeling of the SPDs by including the effects of the SHE torque within a modified Stoner-Wohlfarth model [19] that accounts approximately for the reduced switching threshold for fields in the *z* direction by substituting a reduced perpendicular coercive field $B_c\left(|I|\right)$ in place of B_{an}^0 in Equation 6.16. Now Equations 6.15 and 6.16 become:

$$\frac{B_y}{B_{an}^0}+\frac{\tau_{ST}^0}{B_{an}^0}\sin\theta=\cos^3\theta \tag{6.22}$$

$$\frac{B_z}{B_C}-\frac{\tau_{ST}^0}{B_C}\cos\theta=-\sin^3\theta \tag{6.23}$$

In Equations 6.22 and 6.23, the parameter $B_c\left(|I|\right)$ can be determined experimentally by measuring the switching field as a function of *I* for $\vec{B}_{ext}$ perpendicular to the sample plane, the angle for which spin torque effects are weakest. Fig. 6.9 (b) illustrates the switching fields B_z^{sw} that we measured under different applied current. The coercive field $B_c\left(|I|\right)$ can be then extracted from the measured switching fields by solving the equation sets formed by Equations 6.22 and 6.23 with $B_y=0$ ($\beta=90°$) and $B_{an}^0\left(|I|\right)$ determined from Fig. 6.9 (a). $B_c\left(|I|\right)$ is shown as the solid curve in Fig. 6.9 (b). As expected for $\beta=90^\circ$, the intrinsic coercive field $B_c\left(|I|\right)$ is only slightly larger than the measured switching fields $B_z^{sw}\left(|I|\right)$. We can also see from Fig. 6.9 (b) that $B_c\left(|I|\right)$, like $B_{an}^0\left(|I|\right)$, has a strong current dependence that we likewise attribute to heating.

With $B_c\left(|I|\right)$ determined, the only other parameters in the model are the SHE torque strength $\tau_{ST}^0(I)=(0.33\text{ mT/mA})I$ and $B_{an}^0\left(|I|\right)$ as determined in Fig. 6.9 (a). With these inputs, switching currents can be calculated in the modified Stoner-Wohlfarth model for all field values and compared to the experiment with no adjustment of fitting parameters [solid lines in Figs. 6.10]. We find remarkable agreement

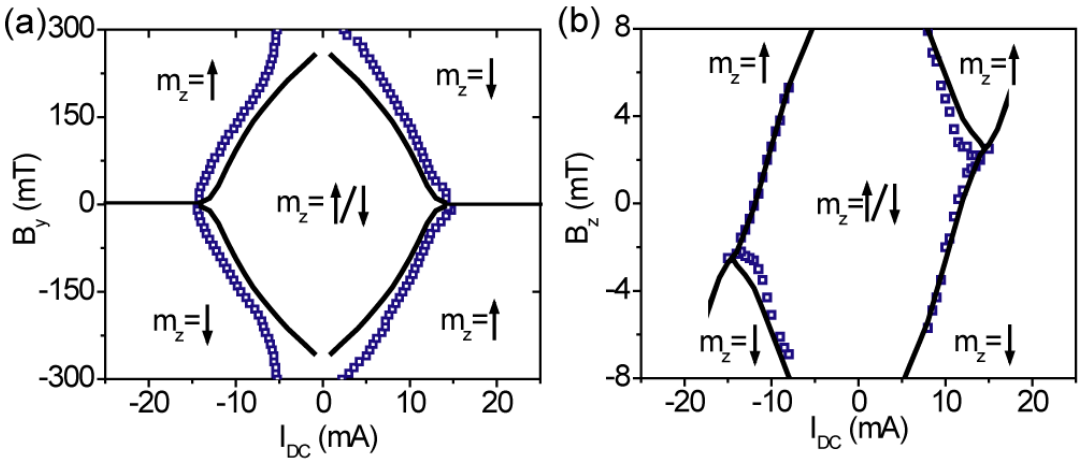

Figure 6.10 Experimental switching phase diagrams. The blue squares represent switching points measured experimentally while the solid lines represent switching boundaries calculated using the modified Stoner-Wohlfarth model. In (a) the switching current is determined by sweeping I and keeping B_{ext} fixed along the y axis. In (b) the switching field B_z is obtained by fixing the current and sweeping B_z, we also applied a constant field $B_y = 40$ mT. In all panels, the symbol ↑ means $m_z > 0$ and ↓ means $m_z < 0$, not $m_z = \pm 1$.

considering the simplicity of the model. In particular, the skewed shape of the hysteretic region in Fig. 6.10 (b) is reproduced with no fitting parameters. We conclude that the SHE torque in combination with heating provides a quantitative description for the current-driven switching. Heating alone cannot explain the data, since heating depends on $|I|$ and we measure opposite signs of switching for opposite signs of I.

6.3.5 Experiment on the Ta/CoFeB/MgO system

In Chapter 5 by using the ST-FMR technique we showed that compared with Pt, Ta has an even stronger SHE and the spin Hall angle of those two materials are opposite in sign. So it is natural to expect that the same type of switching for perpendicular magnetized films could be realized by using Ta as the SHE material.

For this measurement we deposited a thin film stack with the structure: substrate/Ta(4)/$Co_{40}Fe_{40}B_{20}$(1)/MgO(1.6)/Ta(1) (thicknesses in nm) and patterned it into Hall bars 2.5-20 μm wide and 3-200 μm long. MgO was used as a capping layer because previous studies [20] have shown that for a sufficiently thin CoFeB layer, the Ta/CoFeB/MgO structure has a strong perpendicular magnetic anisotropy; this was confirmed by our measurements [Fig. 6.11 (a)]. (The top Ta layer served merely to protect the MgO from exposure to atmosphere.) Similar to our measurement for the Pt/Co/AlO_x sample, we recorded the anomalous Hall resistance to monitor the z component of the CoFeB magnetization. Fig 6.11 (b) shows an example of the abrupt current-induced switching caused by the SHE-ST, as measured for a 2.5 μm wide sample with $\beta = 0°$ and $B_{ext} = \pm 10$ mT. The switching curves shown are obtained under the same bias conditions as in Fig. 6.7. Comparison between the two reveals that the switching direction caused by the in-plane current in Fig. 6.11 (b) is opposite to that in the Pt/Co/AlO_x system. We made additional control samples from a Pt/CoFeB/MgO multilayer and found that the switching direction is the same as with Pt/Co/AlO_x, demonstrating that the sign reversal comes from the difference between the sign of the SHE in Pt and Ta, and not from any differences between the FM/oxide interfaces or between Co and CoFeB.

To quantitatively determine the magnitude of the spin Hall angle from the response of perpendicularly magnetized Ta/CoFeB/MgO samples, we swept the magnetic field keeping its direction fixed at a small field angle $\beta \approx 2°$. As we mentioned in Section 6.3.3, the vertical component of the external magnetic field $B_z = B_{ext} \sin\beta$ under non-zero β will cause the magnetization of the Hall bar structure to remain uniformly magnetized as long as the current is well below the switching point, so that the magnetization rotates coherently with field and current [Fig. 6.11 (c)]. For

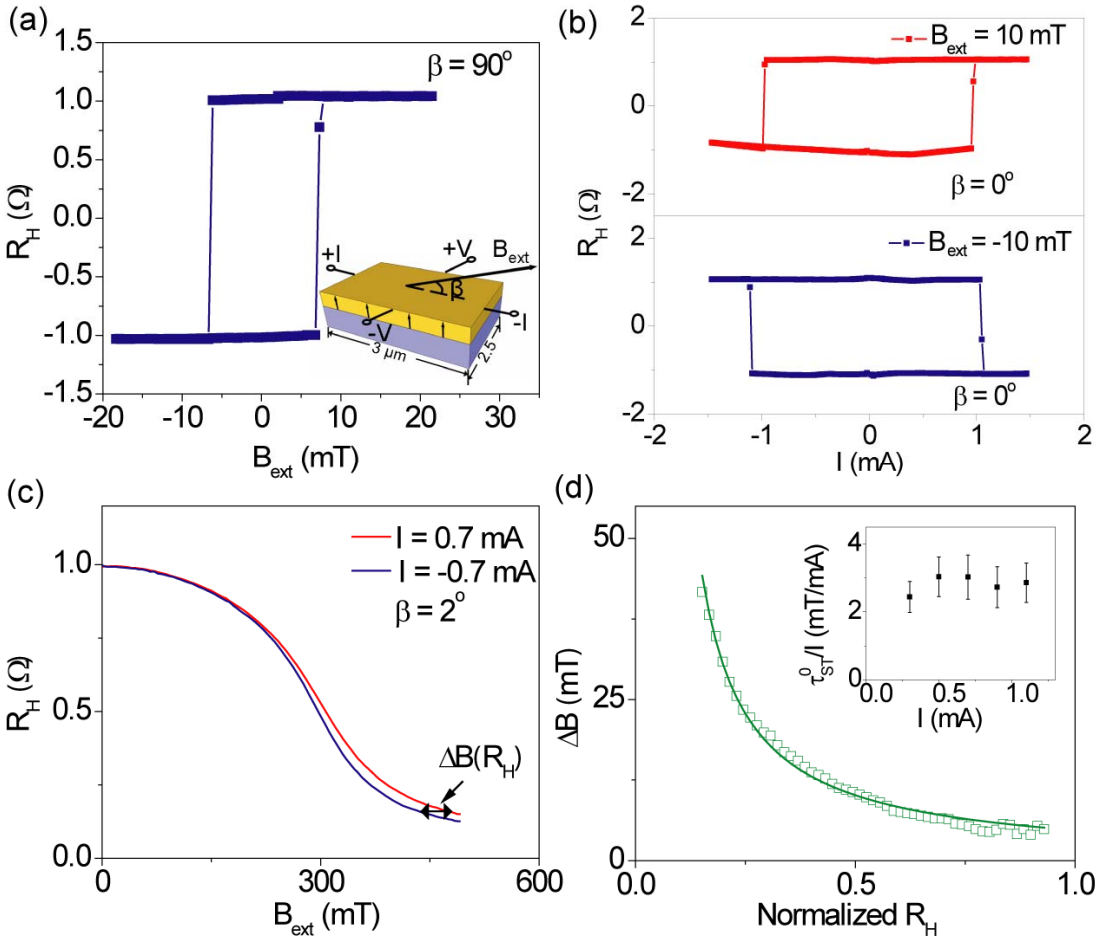

Figure 6.11. Spin Hall effect induced switching in a Ta/CoFeB/MgO/Ta film. (a) The anomalous Hall resistance R_H as a function of magnetic field when B_{ext} is applied along the easy axis (perpendicular to the film plane). Inset: device geometry used for the measurement. B_{ext} is applied in the plane defined by the direction of current flow and the normal vector to the sample plane. β is the angle between the direction of B_{ext} and the applied current. (b) Current-induced switching when B_{ext} is parallel (top panel) or antiparallel (bottom panel) to the current direction defined as in (a) inset. In both panels, β = 0°. (c) R_H vs B_{ext} determined experimentally when the field is applied at the angle β = 2°. Constant currents of ±0.7 mA were applied to the sample while sweeping the field. (d) $\Delta B(R_H)$ as determined from the difference of the two data sets in (c). The line is a fit to the macrospin model. Inset: The values of τ_{ST}^0 / I determined at different bias currents.

convenience in the data analysis, we will treat B_{ext} as function of R_H instead of the reverse. Similar to what we did in Fig. 6.8 (b), by subtracting the two data sets in Fig. 6.11 (c) we can get the difference in the applied external fields $\Delta B[R_H(\theta)] = B_+(\theta) - B_-(\theta)$ for the same tilted angle under positive and negative biasing current [Fig. 6.11 (d)]. Using a one-parameter fit to the equation $\Delta B[R_H(\theta)] = 2\tau_{ST}^0 / \sin(\theta - \beta)$, the magnitude of the spin torque can be determined to be $\tau_{ST}^0 \approx 2.1$ mT for $|I| = 0.7$ mA. The τ_{ST}^0 / I ratios obtained for different values of applied current are summarized in the inset of Fig 6.11 (d), and on average we find $\tau_{ST}^0 / I \approx 2.8 \pm 0.6$ mT/mA. By using the formula $J_S = 2eM_S t\tau_{ST}^0 / \hbar$ with saturation magnetization $M_S = (1.1 \pm 0.2) \times 10^6$ A/m and CoFeB film thickness $t = 1.0 \pm 0.1$ nm, we obtain $J_S / J_e = 0.12 \pm 0.03$ for the 4 nm Ta layer, consistent with the value $J_S / J_e = 0.15 \pm 0.03$ from the ST-FMR study for an 8 nm Ta layer in Chapter 5. Here we assume a uniform current density throughout both the Ta and CoFeB layers because their resistivities are similar, $\rho_{Ta} \approx 190$ μΩ-cm and $\rho_{CoFeB} \approx 170$ μΩ-cm.

6.4 Discussion

6.4.1 Spin Hall effect versus Rashba field

Miron *et al.*[12] measured similar current induced switching in Pt/Co/AlO_x samples. And they believed it is the Rashba field in the $\pm z$ direction which give rise to this switching. Additionally, in the Supplementary Information of ref. [12], the authors made two arguments why they believe that the current-induced switching they measured cannot be explained by a spin Hall torque.

The first argument concerns the slopes of the switching boundaries in data like Fig. 6.10 (b), which allow comparison between the relative strength of the current and the $\hat{z}$-component of magnetic field in giving rise to switching transitions. Using an in-

plane field of 100 mT (in the $\hat{y}$ direction by our convention) and sweeping B_z, Miron et al. [12] observed slopes corresponding to $\left|dB_z / dJ_e\right| \approx$ 7-9 $\times$ 10^{-10} T/(A/cm^2). They argued that this was too strong a shift to be explained by the spin Hall torque, which they estimated to have a maximum possible value $d\tau_{ST}^0 / dJ_e = 1.6 \times 10^{-10}$ T/(A/cm^2). Indeed, we calculate that in a simple zero-temperature macroscopin model one should have $\left|dB_z / d\tau_{ST}^0\right| = \left|dB_z / dJ_e\right| / \left|d\tau_{ST}^0 / dJ_e\right| \approx 2$ when $B_y \ll B_{an}^0$ (see Fig 6.4), so that if heating can be neglected then $\left|dB_z / dJ_e\right|$ should be no more than a factor of two greater than $d\tau_{ST}^0 / dJ_e$.

We observe a similar, large difference between the measured slopes of the switching boundaries in our data and our measurement of τ_{ST}^0. The slopes in Fig. 6.10 (b) correspond to $\left|dB_z / dI\right| \approx 1.3$ mT/mA or $\left|dB_z / dJ_e\right| \approx 7 \times 10^{-10}$ T/(A/cm^2). Like the result in ref. [12], this is more than a factor of two greater than the value of the spin Hall torque that we measure independently from the magnetic moment rotation, $d\tau_{ST}^0 / dI = 0.33$ mT/mA or $d\tau_{ST}^0 / dJ_e = 1.7 \times 10^{-10}$ T/(A/cm^2). Nevertheless, as we show in Fig. 6.10, the switching boundaries that we measure are still in quantitative agreement with the predictions of our modified Stoner-Wohlfarth model. The reason why the modified Stoner-Wohlfarth model agrees with the data while the zero-temperature macrospin model does not is that the modified Stoner-Wohlfarth model takes into account, at least approximately, the effects of heating and spatially incoherent magnetization reversal, in addition to the spin Hall torque. The consequences of heating, to reduce B_{an}^0 and B_c with increasing $|I|$, make the current increasingly effective in contributing to switching as $|I|$ is increased, and therefore shift the slopes of the switching boundaries $\left|dB_z / dJ_e\right|$ to larger values. We should note, to be clear, that heating alone cannot explain the measured current-induced switching phenomena in the absence of a spin Hall torque, since heating alone cannot

explain the strong dependence of the switching direction on the sign of the current seen in Fig. 6.7.

The second argument of Miron *et al.* against the spin Hall torque mechanism was based on measurements of three sets of Pt/Co/AlO_x layers formed by oxidizing Al layers with different thicknesses. Samples made with thicker Al layers, so that they were less oxidized, exhibited lower values of $B_{an}^{0}(I=0)$ and $B_c(I=0)$, but higher critical currents for switching. Miron *et al.* argued that if the spin Hall torque were the mechanism for switching and if the strength of the spin Hall torque were the same in the different samples, then the samples with the lower values of $B_{an}^{0}(I=0)$ and $B_c(I=0)$ must have lower critical currents, in conflict with the data. We find this argument unpersuasive. First, the different samples are unlikely to have the same strength of the spin Hall torque. The thicker, less-oxidized samples will have either partially unoxidized metallic aluminum or less oxidation of the Co layer (or both) compared to the thinner, more oxidized samples, with the result that in the less-oxidized samples a smaller share of the applied current will flow through the Pt layer, due to shunting through the Co or Al. This will decrease the current density in the Pt and hence the strength of the spin Hall torque in the thicker samples and therefore increase the total critical current needed for switching. Second, the amount of heating in these samples is substantial. The thicker, less-oxidized samples will have lower resistances and therefore somewhat less heating. Since B_{an}^{0} and B_c are temperature dependent, this means that $B_{an}^{0}(I=I_c)$ and/or $B_c(I=I_c)$ may be greater in the less-oxidized samples than in the more-oxidized samples even if the reverse is true for $I=0$. This factor could also contribute to larger critical currents for the less-oxidized samples. Finally, different extents of formation of antiferromagnetic Co oxide at the Co/Al interface and the fluctuating exchange biasing [21] might affect how readily a

current promotes the nucleation and motion of magnetic domain walls during the magnetic reversal process and therefore alter the values of critical currents.

Since our measurements of both magnetization rotation and switching in Section 6.3.2 ~ 6.3.4 are explained quantitatively by the same value of J_S / J_e, and this number is in agreement with previous experiments, we believe that the SHE torque mechanism fully explains the current-induced switching, and there is no evidence for the out-of-plane ($\pm\hat{z}$) Rashba effect proposed in ref. [12]. Theoretical calculations indicate that any Rashba field in the $\pm\hat{z}$ direction should be accompanied by an even larger Rashba field along $\pm\hat{x}$ [14-17], so the lack of a measurable $\pm\hat{x}$ Rashba field in our rotation experiments of Section 6.3.3 gives additional reason to question the existence of a large $\pm\hat{z}$ Rashba field.

To further verify that the driving force for the switching come from the Pt layer instead of from the ferromagnet or the ferromagnet/oxide interface as is suggested in ref. [12], we have also measured current-induced switching in Pt(30)/Co(5)/Ni(10)/Ta(10) (Fig. 6.12), Pt(30)/Co(5)/Ni(10)/Au(10) and Pt(30)/CoFeB(10)/MgO(16) samples (thicknesses in Å). This shows that the switching does not depend on the presence of an oxide capping layer, and occurs for ferromagnet thicknesses up to 15 Å and for ferromagnets with different chemical compositions. These observations suggest strongly that it is the Pt film which drives switching, rather than a Rashba field within the ferromagnet.

6.4.2 Approaches for optimizing the switching current

Understanding that the SHE torque explains current-induced switching of perpendicularly-polarized magnetic layers enables quantitative estimates for how to

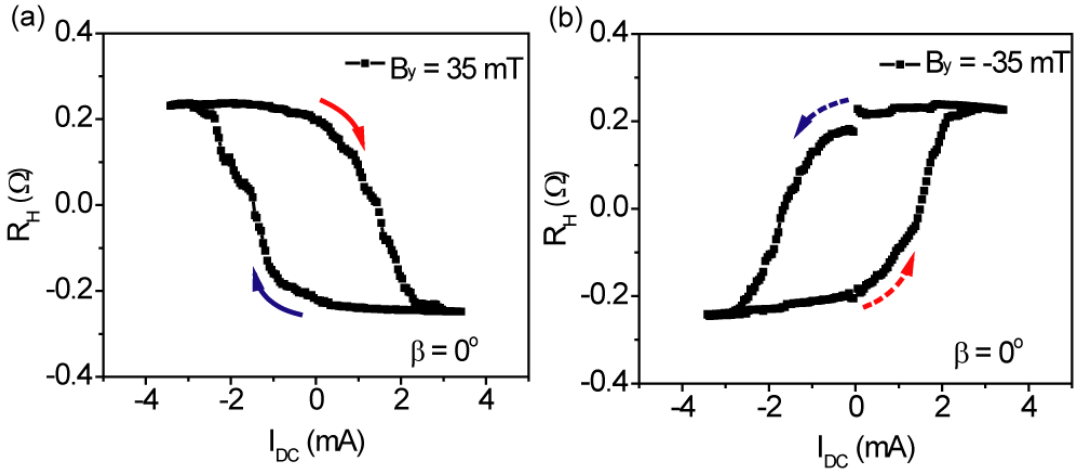

Figure 6.12. Current induced switching in a Pt/Co/Ni/Ta sample. SHE switching was measured in a Pt(30)/Co(5)/Ni(10)/Ta(10) device (thicknesses in Å) 3 μm wide and 3 μm long, with an in-plane magnetic field (a) B_y = 35 mT and (b) B_y = -35 mT. The current-induced switching is gradual, rather than abrupt, consistent with the easy axis magnetization curves of this sample for which the field-driven switching is gradual, as well.

optimize the effect. For a sufficiently small sample, the macrospin model should apply. We assume a magnetic layer of length L, width w, and thickness t for which the perpendicular anisotropy field is optimized to provide an energy barrier of 40 k_BT (where k_B is Boltzmann's constant and T = 300 K), corresponding to a retention time of 10 years [22]. The small, fixed, symmetry-breaking in-plane magnetic field needed to set the direction of the spin-Hall switching can be applied easily by the dipole field from a nearby magnetic layer.

Within this macrospin model, both the critical current for switching and the energy barrier for reversal depend on B_y. We therefore first consider how to set B_y to minimize the critical current for a given fixed value of the energy barrier. For a thin

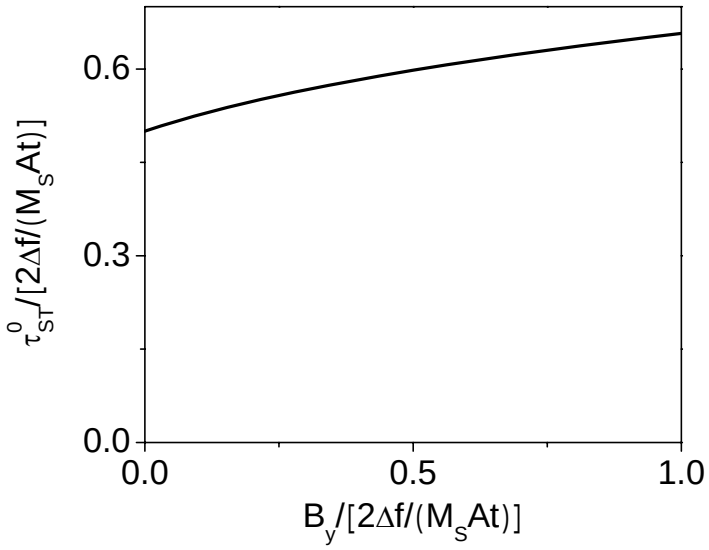

Figure 6.13. The dependence of spin torque required for switching on B_y. In this calculation, the energy barrier against thermal fluctuations is kept constat and B^0_{an} is adjusted as a function of B_y to keep the energy barrier constant.

film magnet with uniaxial anisotropy, the free energy has the form $f(B_y,\theta) = M_S At\left[(B^0_{an}\cos^2\theta)/2 - B_y\cos\theta\right]$ and the equilibrium orientation is $\theta_0 = \cos^{-1}\left(B_y / B^0_{an}\right)$ (θ is defined as in Fig 6.2). Here M_S is the saturation magnetization, A is sample area, and t the thickness of the ferromagnetic layer. Therefore the energy barrier is

$$\Delta f(B_y) = f(B_y,\theta=\theta_0) - f(B_y,\theta=0) = M_S AtB^0_{an}[1-(B_y / B^0_{an})]^2/2. \qquad (6.24)$$

In order to determine the switching current as a function of B_y for a given energy barrier, for each value of B_y we scale the parameter B^0_{an} in Equations 6.15 and 6.16 so that the energy barrier is constant, and then use Equations 6.15 and 6.16 to calculate the switching current. Our result for the switching current as a function of B_y for a constant energy barrier is shown in Fig. 6.13. In this macrospin model the most efficient critical current is obtained for B_y close to (but not equal to) zero, for which the spin torque required for switching is $\tau^0_{ST} \approx B^0_{an}\left(\left|I_c\right|\right)/2$. Only a few mT of B_y is

enough to define a clear switching direction, making the switching deterministic (see Fig. 6.7). In practical device geometries, this small, fixed, in-plane magnetic field can be easily applied by the magnetic dipole field of a nearby magnetic layer. The energy barrier against thermal reversal for the switching layer is then approximately $\Delta f_0 = AtM_S\left(I=0\right)B_{an}^0\left(I=0\right)/2$, which we will set equal to 40 k_BT.

To complete the calculation of an optimum critical current for a thermally stable magnetic element we use the following relationships, applicable for the sample geometry we are considering.

$$\tau_{ST}^0 = \frac{\hbar J_S}{2e\mu_0 M_S t} \tag{6.25}$$

$$J_S = J_e\left(\frac{J_S(d=\infty)}{J_e}\right)\left[1-\text{sech}(d/\lambda_{sf})\right] \quad \text{(spin diffusion length effect)} \tag{6.26}$$

$$\frac{J_{e,Pt}}{\sigma_{Pt}} = \frac{J_{e,F}}{\sigma_F} \tag{6.27}$$

$$I = J_{e,Pt}wd + J_{e,F}wt\,. \tag{6.28}$$

Here d is the thickness of the Pt layer, w is the sample width (in the $\hat{x}$ direction, perpendicular to the current) and we will use that L is the sample length (in the $\hat{y}$ direction, parallel to the current). We have taken into account that the electrical conductivities of the Pt (σ_{Pt}) and the ferromagnetic layer (σ_F) may be different, so the charge current densities in the two layers, $J_{e,Pt}$ and $J_{e,F}$, may also differ. Assembling these equations, the condition $\tau_{ST}^0 \approx B_{an}^0\left(\left|I_c\right|\right)/2$ is equivalent to

$$I_c = \frac{2e\left(40\ k_BT\right)\left[d+\left(\sigma_F/\sigma_{Pt}\right)t\right]}{\hbar L\left(J_S(d=\infty)/J_{e,Pt}\right)\left[1-\text{sech}(d/\lambda_{sf})\right]}\frac{M_S\left(\left|I_c\right|\right)B_{an}^0\left(\left|I_c\right|\right)}{M_S\left(I=0\right)B_{an}^0\left(I=0\right)}. \tag{6.29}$$

We assume t = 0.6 nm, d = 2.0 nm, L = 200 nm, $J_S(d=\infty)/J_{e,Pt} = 0.07$ and λ_{sf} = 1.4 nm for Pt, according to our measurement in Chapter 5. We also assume for simplicity that $\sigma_{Pt} = \sigma_F$. The energy barrier of 40 k_BT corresponds, *e.g.*, to a perpendicular anisotropy field $B_{an}^0(I=0) \approx 28$ mT for a sample with $M_S = 1.0\times10^6$ A/m, L = 200 nm, w = 100 nm. If we ignore the effects of heating, so that $M_S(|I_c|)B_{an}^0(|I_c|)/\left[M_S(I=0)B_{an}^0(I=0)\right]=1$, then based on Equation 6.29 we estimate a critical current $I_c \sim 170$ μA with no thermal assistance for Pt. We have assumed that the energy barrier scales with the sample area, so the dependence of I_c on 1/L in Equation 6.29 reflects a dependence on the aspect ratio of the device; I_c can be reduced further by increasing L beyond 200 nm while reducing w to keep $A = Lw$ constant, as long as the magnetization dynamics can still be described in the macrospin approximation. I_c is also likely to be decreased further if there is any heating, due to the reduction of the ratio $M_S(|I_c|)B_{an}^0(|I_c|)/\left[M_S(I=0)B_{an}^0(I=0)\right]$. Heating need not compromise the energy barrier for thermal stability, since stability is required only when I = 0. Even further reductions of the switching current might be achieved by taking advantage of non-macrospin dynamics during the switching process. Materials with even larger $J_S(d=\infty)/J_e$ compared to pure Pt will, of course, further reduce the critical current. Take Ta that we studied in Section 6.3.5 as an example. Using $J_S/Je = 0.12$ for Ta and assuming that $\lambda_{Ta} << d_{Ta}$, we can get a critical current of ~ 40 μA for the same device we discussed above. We therefore conclude that spin Hall torque switching of an optimized perpendicularly magnetized memory element should be possible with currents competitive with the optimum currents required for switching driven by conventional spin transfer torque in magnetic tunnel junctions [20, 22-23]. Compared to conventional MTJs, spin-Hall switched devices have an advantage that charge currents do not need to flow through tunnel barriers that are sensitive to electrical breakdown.

REFERENCE

1. J. E. Hirsch, Spin Hall effect, *Phys. Rev. Lett.* **83**, 1834 (1999).
2. S. F. Zhang, Spin Hall effect in the presence of spin diffusion, *Phys. Rev. Lett.* **85**, 393 (2000).
3. J. Sinova, D. Culcer, Q. Niu, N. A. Sinitsyn, T. Jungwirth and A. H. MacDonald, Universal intrinsic spin Hall effect, *Phys. Rev. Lett.* **92**, 126603 (2004).
4. S. Murakami, N. Nagaosa and S. C. Zhang, Dissipationless quantum spin current at room temperature, *Science* **301**, 1348 (2003).
5. S. O. Valenzuela and M. Tinkham, Direct electronic measurement of the spin Hall effect, *Nature* **442**, 176 (2006).
6. T. Kimura, Y. Otani, T. Sato, S. Takahashi and S. Maekawa, Room-temperature reversible spin Hall effect, *Phys. Rev. Lett.* **98**, 156601 (2007).
7. J. C. Slonczewski, Current-driven excitation of magnetic multilayers, *J. Magn. Magn. Mater.* **159**, L1 (1996).
8. J. A. Katine, F. J. Albert, R. A. Buhrman, E. B. Myers and D. C. Ralph, Current-driven magnetization reversal and spin-wave excitations in Co/Cu/Co pillars, *Phys. Rev. Lett.* **84**, 3149 (2000).
9. A. D. Kent, B. Ozyilmaz and E. del Barco, Spin-transfer-induced precessional magnetization reversal, *Appl. Phys. Lett.* **84**, 3897 (2004).
10. O. J. Lee, V. S. Pribiag, P. M. Braganca, P. G. Gowtham, D. C. Ralph and R. A. Buhrman, Ultrafast switching of a nanomagnet by a combined out-of-plane and in-plane polarized spin current pulse, *Appl. Phys. Lett.* **95**, 012506 (2009).
11. D. C. Ralph and J. Z. Sun, Magnetoresistance and spin-transfer torque in magnetic tunnel junctions, *J. Magn. Magn. Mater.* **320**, 1227 (2008).
12. I. M. Miron, et al., Perpendicular switching of a single ferromagnetic layer induced by in-plane current injection, *Nature* **476**, 189 (2011).
13. N. Nagaosa, J. Sinova, S. Onoda, A. H. MacDonald and N. P. Ong, Anomalous Hall effect, *Reviews of Modern Physics* **82**, 1539 (2010).
14. A. Manchon and S. Zhang, Theory of nonequilibrium intrinsic spin torque in a single nanomagnet, *Phys. Rev. B* **78**, 212405 (2008).
15. K.-W. Kim, S.-M. Sea, J. Ryu, K.-J. Lee and H.-W. Lee, arXiv:1111.3422, (2012).
16. X. Wang and A. Manchon, arXiv:1111.5466, (2012).
17. D. A. Pesin and A. H. MacDonald, arXiv:1201.0990, (2012).
18. I. M. Miron, G. Gaudin, S. Auffret, B. Rodmacq, A. Schuhl, S. Pizzini, J. Vogel and P. Gambardella, Current-driven spin torque induced by the Rashba effect in a ferromagnetic metal layer, *Nature Mat.* **9**, 230 (2010).
19. A. L. Ribeiro, Characterization of Soft-Magnetic Materials Using a Modified Stoner-Wohlfarth Model, *J. Magn. Magn. Mater.* **133**, 97 (1994).
20. S. Ikeda, et al., A perpendicular-anisotropy CoFeB-MgO magnetic tunnel junction, *Nature Mat.* **9**, 721 (2010).

21. O. Ozatay, et al., Sidewall oxide effects on spin-torque- and magnetic-field-induced reversal characteristics of thin-film nanomagnets, *Nature Mat.* **7**, 567 (2008).
22. J. Z. Sun, Spin-current interaction with a monodomain magnetic body: A model study, *Phys. Rev. B* **62**, 570 (2000).
23. T. Kishi, H. Yoda, T. Kai, T. Nagase, E. Kitagawa, M. Yoshikawa and K. Nishiyama, Lower-current and Fast switching of A Perpendicular TMR for High Speed and High density Spin-Transfer-Torque MRAM. In Proc. IEDM 2008, San Francisco, CA, 15–17 December 2008. New York, NY: IEEE. (doi:10.1109/IEDM.2008.4796680).

CHAPTER 7

SPIN HALL EFFECT INDUCED SWITCHING IN IN-PLANE MAGNETIZED NANOMAGNET

7.1 Introduction

The most standard way to induce magnetic switching using spin torque is through the "anti-damping" approach [1]. Under this configuration, the orientation of the injected spins is antiparallel with the local magnetic moment, and the effect of the spin torque is equivalent to a negative damping term. When the net effective damping becomes zero, magnetic switching will happen. In this anti-damping ST switching, the critical current density for switching in the absence of thermal fluctuations is given by [2-3]

$$J_{C0} \approx \frac{2e}{\hbar}\mu_0 M_S t\alpha (H_C + M_{eff}/2)/(J_S/J_e), \tag{7.1}$$

where M_S, t and H_C represent the saturation magnetization, the thickness and the coercive field of the FM nanomagnet, respectively. M_{eff} corresponds to the effective demagnetization field. Therefore, in order to get an efficient anti-damping switching, we want the spin current as large as possible and the damping coefficient as small as possible.

As we have already measured in Chapter 5 and 6, the SHE in Ta is large, meaning we could expect to inject enough spin current into an adjacent nanomagnet to produce switching. In the meantime, Ta has negligible effect on the damping of adjacent magnetic layers (Fig. 5.11). Both of those two effects make Ta an excellent material for effecting ST switching of an in-plane magnetized nanomagnet. Unlike the perpendicularly magnetized samples, where the orientation of the magnetic moment

can be easily determined using the anomalous Hall effect, we have to use an additional spin valve or MTJ to read out the state of the magnet electrically. To do this, a three terminal device is needed, where the DC switching current flows in the current-in-plane (CIP) configuration and the AC resistance is read across the MTJ. In section 7.2, I will describe the fabrication details of this type of three terminal devices. And In section 7.3 I will discuss how we did the measurement.

7.2 Sample fabrication

The three-terminal devices were made out of multilayer stacks consisting of: substrate/Ta(6.2)/CoFeB(1.6)/MgO(1.6)/ CoFeB(3.8)/Ta(5)/Ru(5) (units in nm). The films were sputtered on thermally oxidized Si substrates in 2 mTorr Ar in a chamber with base pressure < 2×10^{-8} Torr. The full stack was then patterned into the geometry shown in Fig. 7.1. The Ta bottom layer was patterned into a 1 μm wide and 5 μm long strip (with resistance 3 kΩ) and the rest of the layers were etched to form a magnetic tunnel junction (MTJ) on top of the Ta with lateral dimensions ~ 100 × 350 nm^2, and with the long axis of the nanopillar perpendicular to the long axis of the Ta microstrip.

In this device, both the 1μm-wide Ta microstrip and the MTJ nanopillar were defined by e-beam lithography, therefore two aligned e-beam lithography steps were needed. The alignment accuracy needs to be better than 200 nm, so it is necessary to define the alignment marks using the e-beam lithography instead of photolithography. In the experiment, it turned out that better alignment could be achieved (with less than 50 nm error) by using chip alignment marks rather than global alignment. Fig. 7.2a gives an illustration of a set of the alignment marks. The two big green asteroid marks are for the following photolithography. The pair of crosses in red are the global alignment marks for e-beam lithography. For each die, there are four small cross

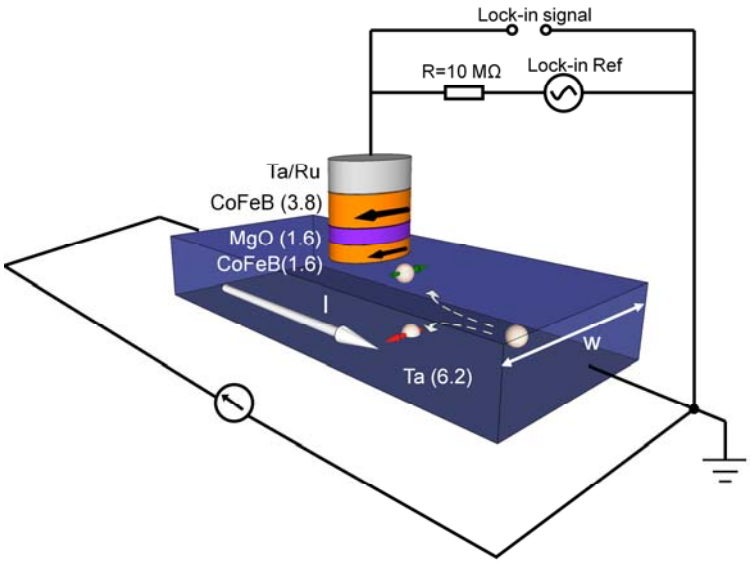

Figure7.1 Schematic of a three-terminal SHE device. The current flowing direction for positive sign is labeled in the figure. The orientations of the magnetic moment in the figure correspond to the equilibrium positions under a large positive external field.

alignment marks at the corners, represented by the blue crosses. In this step, thick PMMA was used as the e-beam resist and long time ion milling was employed to make the trenches used as alignment marks.

In the second step, PMMA was used again as the e-beam resist to define the microstrip. As is shown in Fig. 7.2b, two windows (blue squares) were defined with e-beam lithography. The gap between them defines the width of the microstrip. Ion milling was then employed to transfer the pattern into the metallic films. We use photolithography to further isolate the microstrip as well as the contact pads (the yellow pattern in Fig. 7.2b). The rest of the fabrication procedure is very similar to that of the ordinary two terminal devices described in Chapter 2. Table 7.1 gives a summary of the fabrication procedure. Detailed parameters were shown for the steps that are different from the conventional spin valves or MTJs. At the end of the steps,

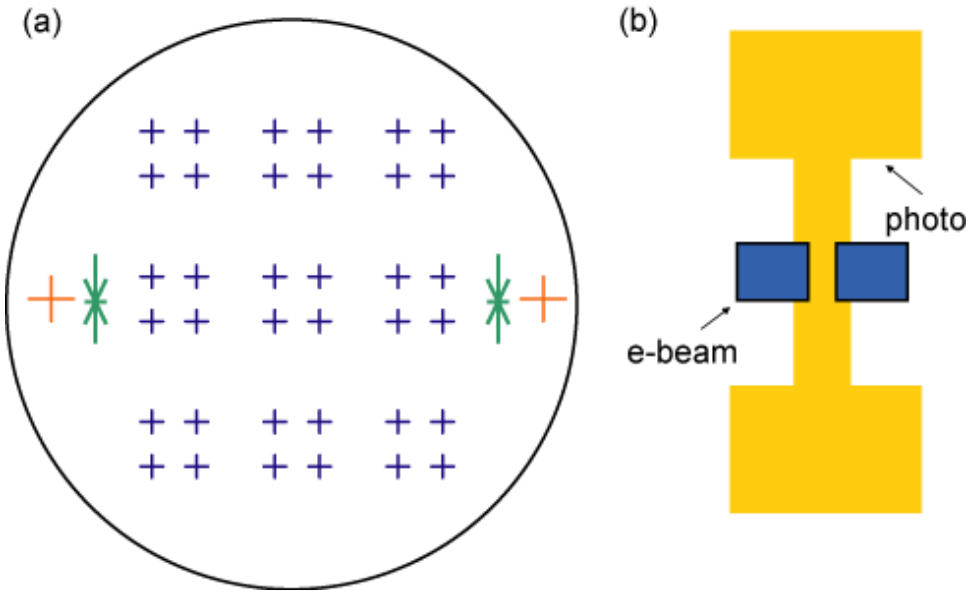

Figure7.2 Schematic of the E-beam lithography pattern. (a) Alignment marks for photolithography and e-beam lithography. (b) Illustration of the e-beam and photolithography steps used for defining the Ta microstrip.

the completed device was annealed at 280°C in vacuum for one hour before measuring to enhance the tunneling magnetoresistance. This annealing was not sufficient to diffuse the B out of the CoFeB and thus did not result in fully-crystallized CoFe.

7.3 Measurement

7.3.1 Field and current induced switching

Using the circuit shown in Fig. 7.1, we can measure the resistance of the MTJ. The magnetoresistance response of one of the MTJs is illustrated in Fig. 7.3 (a), which indicates a coercive field $B_C \approx 4$ mT, a zero bias MTJ resistance $R_{MTJ} \approx 65$ kΩ, and a tunneling magnetoresistance (TMR) ≈ 50%. During subsequent magnetic switching measurements we applied a -3.5 mT in-plane magnetic field along the long axis of the MTJ to cancel the dipole field from the top layer of the MTJ acting on the bottom

Table 7.1 Fabrication procedures for three terminal SHE device

Step 1: define alignment marks	Resist: PMMA 495 K 8% Spin: 1000 rpm Bake: 170°C for 10 min Do the spining twice to get a total thickness of 2 μm Expose: 1000 μm/cm^2 Develop: MIBK:IPA = 1:1, 2 min
Step 2: Ion mill alignment mark	Time: 90 min
Step 3: Strip PMMA	Soak in Remover PG to remove PMMA + Etch in oxygen plasma to remove any residual
Step 4: define microstrip	Resist: PMMA 495 K 8% Spin: 3000 rpm thickness ~500 nm Bake: 170°C for 10 min Expose: 1000 μm/cm^2 Develop: MIBK:IPA = 1:1, 1 min Descum: O2 plasma, 5 sec.
Step 5: Ion mill	
Step 6: Strip resist	Remover PG + oxygen plasma
Step 7: Define the contact pads	
Step 8: define nanopillar	Omnicoat + PMMA + HSQ
Step 9: Evaporate SiO_2	
Step 10: Strip e-beam resist	
Step 11: Open the window above the pads	CF_4 etch, 2 min
Step 12: Top leads deposition	

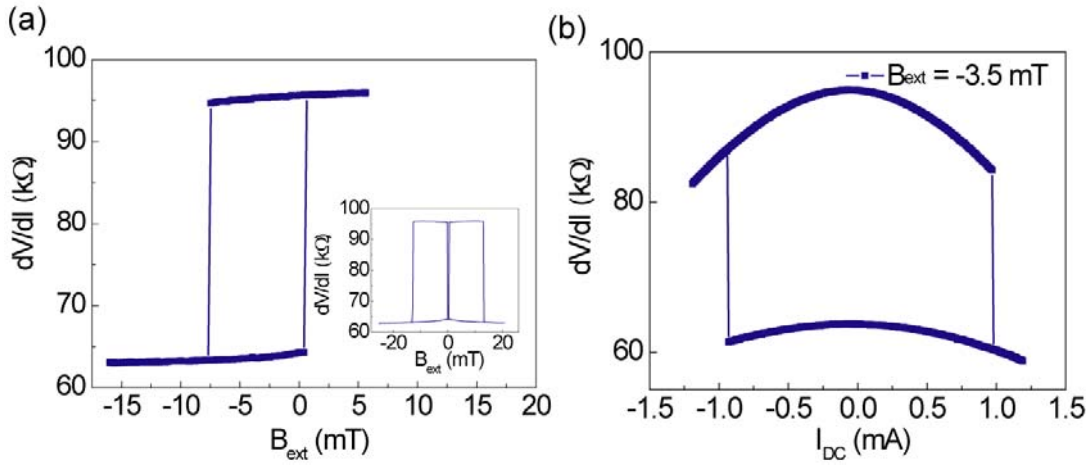

Figure7.3 Field and current induced switching. (a) TMR minor loop of the magnetic tunnel junction as a function of the external applied field B_{ext} applied in-plane along the long axis of the sample. Inset: TMR major loop of the device. (b) TMR of the device as a function of applied DC current I_{DC}. An in-plane external field of -3.5 mT is applied to set the device at the center of the minor loop.

layer, and thus biased the junction at the midpoint of its minor magnetoresistance loop. We then applied a DC current I_{Ta} to the Ta microstrip while monitoring the differential resistance *dV/dI* of the MTJ. Since we connected a large resistor (Fig. 7.1) in series with the MTJ, only a negligible amount of I_{Ta} could flow through the MTJ. And correspondingly, the bias voltage across the MTJ should be very small. Fig. 7.3 (b) shows that abrupt hysteretic switching of the MTJ resistance occurred when I_{Ta} was swept through 1 mA, which resulted in antiparallel to parallel (AP-P) switching, and then this switching was reversed (P-AP switching) when the current was swept back past -1 mA.

7.3.2 Determination of the SHE magnitude from the switching critical current

Since all of our measurements were carried out at room temperature, the switching current is influenced by thermal fluctuation. To account for the thermal

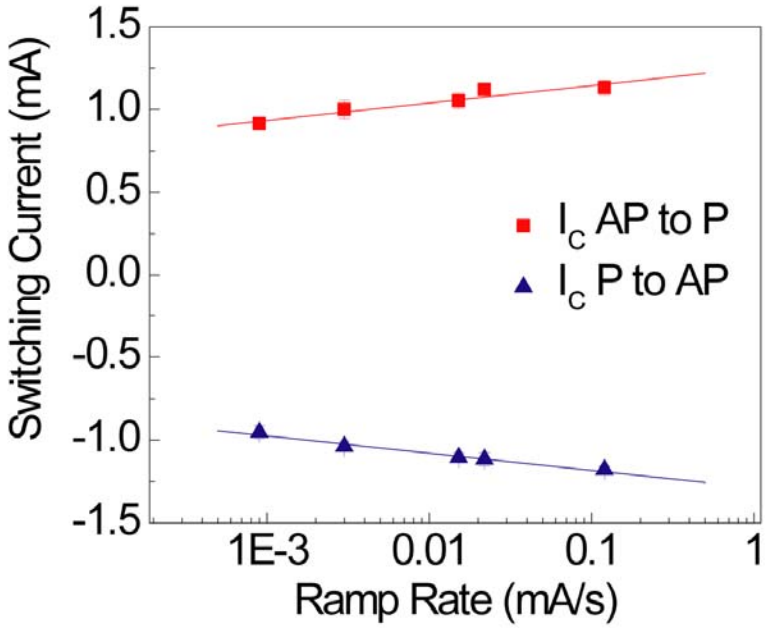

Figure7.4 Ramp rate measurement of the SHE induced switching. The red squares indicate switching from AP to P and the blue triangles indicate switching from P to AP.

effect and to determine the non-thermally assisted critical current, a ramp rate measurement was employed. Fig. 7.4 gives the relationship between the switching current and the ramp rate. Using the standard model for thermally-activated ST switching [4], we determined both the zero-thermal-fluctuation ST critical currents and the energy barriers for the thermally activated AP-P and P-AP transitions. We found the two critical currents to be essentially the same, $|I_{c0}| = 2.0 \pm 0.1$ mA, and similarly for the energy barriers $U = 45.7 \pm 0.5\ k_BT$. The latter is not surprising but the former, while consistent with a SHE origin, is distinctly different from the case for ST switching by the spin polarized current generated by spin filtering within a spin valve or MTJ, where in general, $|I_{c0.P\text{-}AP}| \neq |I_{c0.AP\text{-}P}|$ due to, respectively, spin accumulation in the spin valve and the MTJ magnetoresistance behavior. The equivalence of the two critical currents for a SHE-ST switching device could be a significant technical

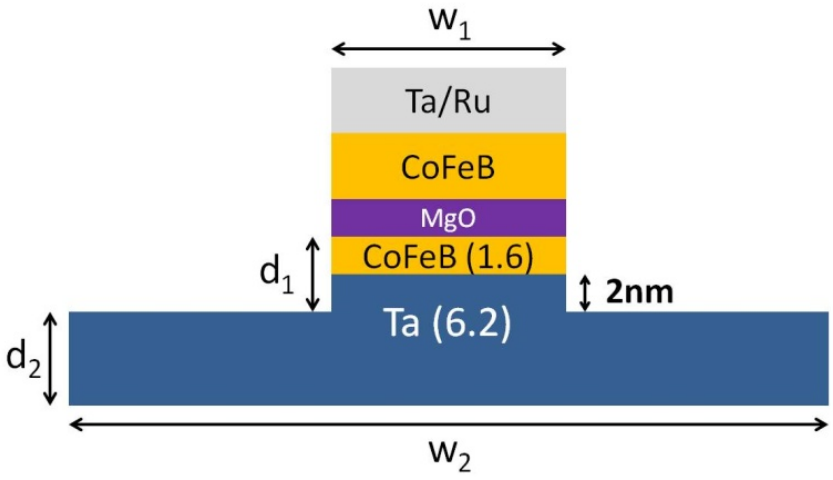

Figure 7.5 Cross section of the three-terminal device. The widths w_1 and w_2 are in the direction perpendicular to the current flow. d_1 is the thickness of CoFeB free layer plus the over-etched Ta thickness. d_2 is the thickness of the remaining Ta bottom layer. w_1 is the length of the long axis of MTJ pillar. w_2 is the width of Ta bottom layer.

advantage.

For a given value of the zero-temperature critical current I_{c0}, we can estimate the critical current density in the Ta layer required for spin torque switching as

$$J_{C0} = I_{c0} / \left(w_1 d_1 + w_2 d_2 \right), \tag{7.2}$$

where w_1, d_1, w_2, and d_2 are defined as in Fig. 7.5. This equation assumes that the current flows uniformly in the CoFeB and Ta layers. This is a reasonable approximation since we determined the resistivities of the CoFeB and Ta from thicker thin-film samples in separate measurements and obtained values that are quite similar for the two materials: $\rho_{Ta} \approx 190$ μΩ-cm and $\rho_{CoFeB} \approx 170$ μΩ-cm. Using $d_1 = 3.6$ nm, $d_2 = 4.2$ nm, $w_1 = 350$ nm, $w_2 = 1000$ nm and $I_{c0} = 2$ mA, we obtained $J_{C0} = 3.7 \times 10^7$ A/cm^2.

From Equation 7.1, it can be seen that in order to determine J_S/J_C from the calculated current density, we should also know the value of the demagnetization field M_{eff} and the damping coefficient α. The demagnetization field can be determined using the anomalous Hall effect. We patterned Ta(6.2nm)/CoFeB(1.6nm)/MgO(1.6nm)/Ru(3.3nm) multilayers into Hall bar microstrips using photolithography and ion milling, and then annealed the devices in vacuum at 280°C for one hour. By applying the magnetic field perpendicular to the sample plane, we can tilt the magnetic moment out of plane. Results of anomalous Hall resistance measurements are shown in Fig. 7.6, for microstrips with lateral dimensions of 20 μm × 200 μm and 2.5 μm × 2.5 μm. From Fig. 7.6, it can be extracted that the demagnetization field ≈ 0.76 T at room temperature for both samples. The demagnetization field is reduced compared with the one calculated using the saturation magnetization of CoFeB, $B_{demag} = \mu_0 M_S \sim 1.3$ T. This is due to the interfacial perpendicular anisotropy at the CoFeB/MgO interface [5]. We will talk about this effect in more details in Chapter 9. We also measured the damping coefficient α of the 1.6 nm thick CoFeB film from Ta(6.2)/CoFeB(1.6)/MgO(1.6)/Ru(3.3) (thickness in nm) multilayers using the ST-FMR technique as described in Chapter 5. From the linewidth of the resonance peaks at different frequencies, α is determined to be 0.021 ± 0.003, which is significantly larger than the damping coefficient of 4 nm thick CoFeB films in Chapter 5. This difference is consistent with previous work [5], which showed that the damping coefficient for CoFeB has a strong thickness dependence when CoFeB is sandwiched between Ta and MgO and its thickness is reduced below 5 nm. With these values, we can estimate the J_S/J_e ratio from Equation 7.1. Using $\alpha = 0.021$, t =1.6 nm, $\mu_0 H_C = 4$ mT, $\mu_0 M_{eff} = 0.76$ T and $M_S = 1.1 \times 10^6$ A/m (measured by magnetometry on large-area films), we find $J_S/J_e = 0.12 \pm 0.04$. Note that this number is consistent with the

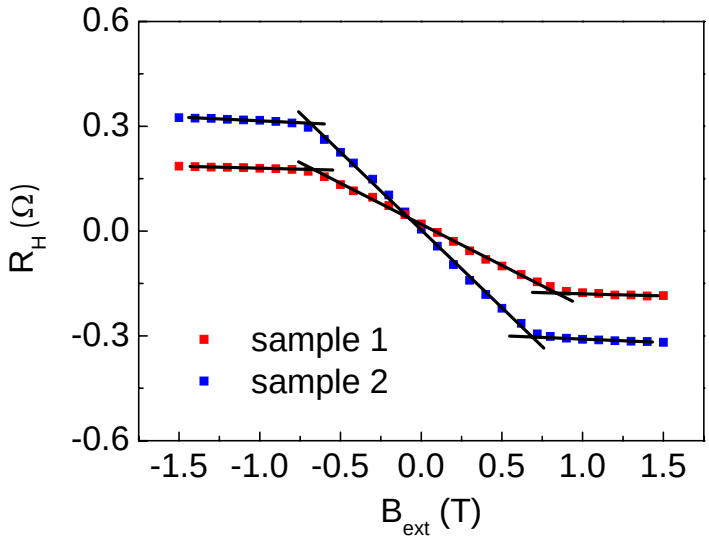

Figure 7.6 Determination of the demagnetization field. Anomalous Hall resistance was measured as a function of applied magnetic field for two different Ta(6.2 nm)/CoFeB(1.6 nm)/MgO(1.6 nm)/Ru(3.3 nm) samples. The magnetic field B_{ext} is applied perpendicular to the film plane. Sample 1 and sample 2 have lateral dimensions 20 μm × 200 μm and 2.5 μm × 2.5 μm, respectively. The solid lines represent linear fits to the magnetization curves and the demagnetization field is given by the saturation field.

results obtained in Chapter 5 and Chapter 6.

7.3.3 Exclusion of the field effect

It can be checked that in the geometry shown in Fig. 7.1 the Oersted field generated by the current inside the Ta strip will be oriented in the film plane at the location of the free layer. So, it is very important to exclude the contribution from the current induced field.

The Oersted field generated by the current can be ruled out as the switching mechanism because it has the polarity to *oppose* the switching that we observe. We employed a Gauss meter to determine the direction of the external field (B_{ext}) and used Ampere's Law (right hand rule) to determine the direction of the Oersted field

generated by current flow in the Ta microstrip. We determined that a positive (negative) current flowing through the Ta strip corresponded to an Oersted field that was aligned with the positive (negative) field direction as defined by B_{ext} in Fig. 7.3 (a). Therefore the minor TMR loop shown in Fig. 7.3 (a) shows that an Oersted field generated by a positive current in the Ta microstrip will tend to switch the free layer into the high resistance state, just as a sufficiently strong positive B_{ext} does. This is opposite to what we observed in Fig. 7.3 (b), where a sufficiently strong positive current acts to switch the free layer into the low resistance states. Therefore we can conclude that the Orested field generated by the current flow in the Ta acts to oppose the switching driven by the spin torque arising from the SHE.

As an independent check on the direction of the Oersted field, we measured the TMR major loop under positive and negative currents flowing through the Ta microstrip. Since the fixed layer is only influenced by the Oersted field and not by the spin torque, we can determine the direction of the Oersted field from the current dependence of the fixed layer switching field in the major TMR loop. Because the fixed layer and the free layer are located on the same side of the microstrip, the Oersted field exerted on them should have the same direction. Fig. 7.7 (a) and Fig. 7.7 (b) show that the fixed layer switching fields shift negatively (positively) due to a positive (negative) current, which is in agreement with the results that we obtained above, *i.e*. the positive (negative) current generates an Oersted field in the positive (negative) direction. Note that the shifts of the free layer switching in Fig. 7.7 differ from those of the fixed layer because the SHE-ST shifts the switching fields of the free layer more strongly than does the Oersted field.

As a further independent check, we measured the switching phase diagram of our three-terminal devices as the function of current and externally applied magnetic

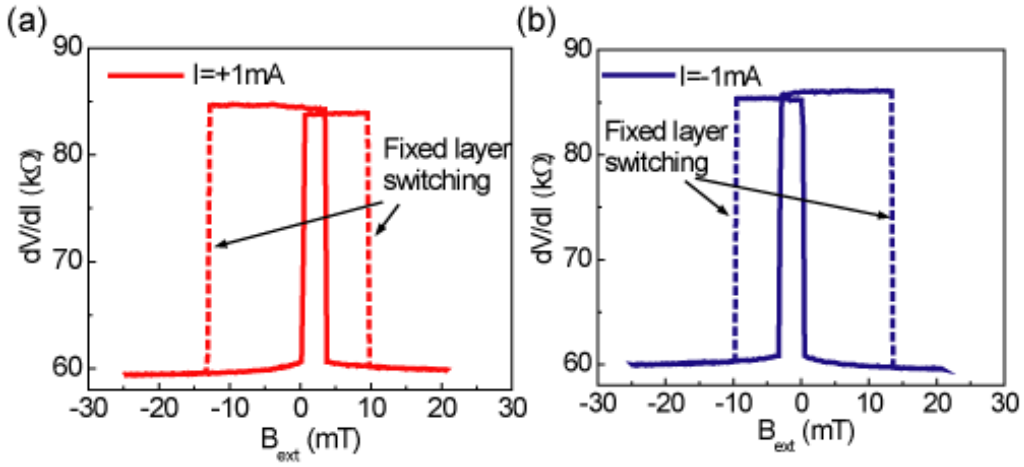

Figure 7.7 TMR major loop with applied current. (a) major loop under I_{DC} = +1 mA. (b) major loop under I_{DC} = -1 mA. The switching transitions for the fixed layer are labeled by dashed lines.

field. Figure 7.8 shows the switching phase diagram determined for a three-terminal MTJ device with lateral dimensions of 50 nm × 180 nm, formed on a 1 μm wide Ta microstrip. The smaller coercive field and lower switching currents of this MTJ device, in comparison to the one in Fig. 7.3, allowed a wider range of current to be applied without electrically damaging the device. The rhombohedral shape of the phase diagram (*i.e.*, with a shape that is closed on the top and bottom) is typical of that obtained from switching by a thermally-assisted spin torque mechanism [4], [6], but cannot be explained by switching by an effective magnetic field. For a mechanism based on an in-plane effective field transverse to the current, the switching boundaries on this type of B_{ext} vs. current graph would simply be two straight lines that do not meet on top and bottom.

7.4 Conclusion

Improvements to this initial three-terminal SHE device can be very reasonably expected to result in significant reductions in the switching currents for thermally

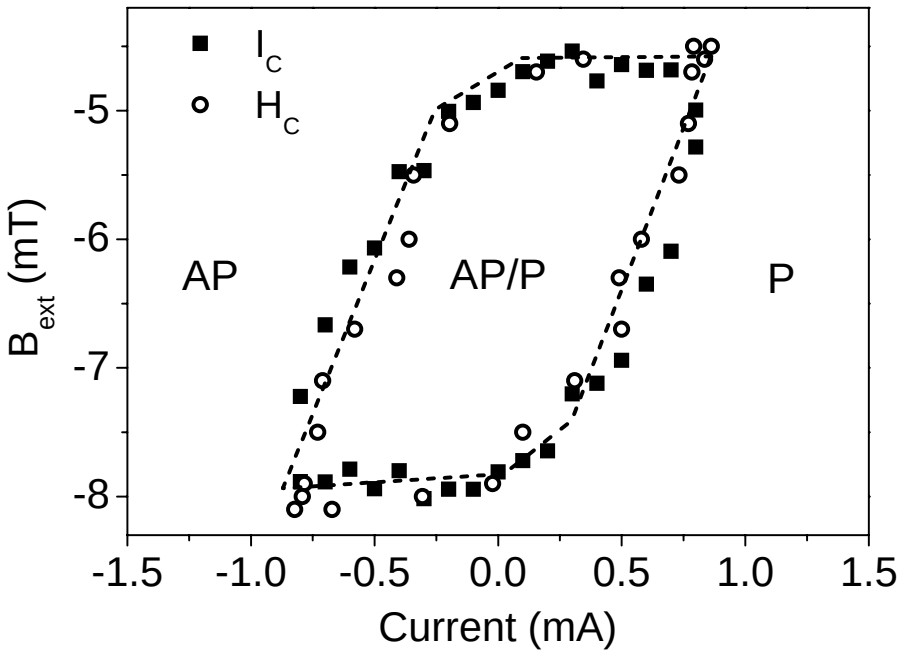

Figure 7.8. Phase diagram of the SHE induced switching. The boundaries for switching transitions between parallel (P), antiparallel (AP) and bistable (AP/P) states are shown. The solid squares represent switching fields obtained from field scans at fixed current and the hollow circles represent switching currents obtained from current scans at fixed field. The dashed lines serve as a guide to eye. The dipole field from the fixed layer is ~ 6.3 mT. The rhombehedral shape of the bistable region is a signature of anti-damping switching by a spin transfer torque. In contrast, the boundaries for switching caused by a current-induced in-plane effective field would simply be straight lines on this type of B_{ext} vs. current plot.

stable nanomagnets. Straightforward changes in the fabrication process that reduce the width of the Ta microstrip close to the length of the long axis of the nanopillar would of course reduce I_{c0} by a factor of 3 without affecting thermal stability. A further reduction in I_{c0} could be achieved by reducing the demagnetization field of the FM free layer from 700 mT to ≤ 100 mT (see Chapter 3 and ref [7]). With such improvements I_{c0} could be reduced to < 100 μA, at which point the three-terminal SHE devices would be competitive with the efficiency of conventional ST switching in

optimized MTJs [3, 5, 8], while providing the added advantage of a separation between the low impedance switching (write) process and high impedance sensing (read) process. This separation solves the reliability challenges that presently limit applications based on conventional two-terminal MTJs while also giving improved output signals. Of course the discovery of materials with even larger values of the spin Hall angle than in β-Ta could also add to the competitiveness of SHE-ST.

In summary we have demonstrated an in-plane-polarized three-terminal SHE-ST device that is particularly promising for applications: compared to conventional MTJ structures it offers highly competitive spin torque efficiency together with isolation between the writing current and the reading current (allowing for a fully reliable write operation and a large signal read operation), while compared to previous three-terminal approaches [9-10] it can provide better spin-torque efficiency and is much easier to fabricate. Finally, just like in a transistor, the third terminal can be used to provide extra controls over the device, for example, the magnetic properties of the free magnetic layer can be tuned by the electric field applied across the third terminal. Therefore the device can be utilized for logic applications. This point will be further discussed in Chapter 9.

REFERENCE

1. J. C. Slonczewski, Current-driven excitation of magnetic multilayers, *J. Magn. Magn. Mater.* **159**, L1 (1996).
2. J. A. Katine, F. J. Albert, R. A. Buhrman, E. B. Myers and D. C. Ralph, Current-driven magnetization reversal and spin-wave excitations in Co/Cu/Co pillars, *Phys. Rev. Lett.* **84**, 3149 (2000).
3. J. Z. Sun, Spin-current interaction with a monodomain magnetic body: A model study, *Phys. Rev. B* **62**, 570 (2000).
4. E. B. Myers, F. J. Albert, J. C. Sankey, E. Bonet, R. A. Buhrman and D. C. Ralph, Thermally activated magnetic reversal induced by a spin-polarized current, *Phys. Rev. Lett.* **89**, 196801 (2002).
5. S. Ikeda, et al., A perpendicular-anisotropy CoFeB-MgO magnetic tunnel junction, *Nature Mat.* **9**, 721 (2010).
6. I. N. Krivorotov, N. C. Emley, A. G. F. Garcia, J. C. Sankey, S. I. Kiselev, D. C. Ralph and R. A. Buhrman, Temperature dependence of spin-transfer-induced switching of nanomagnets, *Phys. Rev. Lett.* **93**, 166603 (2004).
7. T. Moriyama, T. J. Gudmundsen, P. Y. Huang, L. Q. Liu, D. A. Muller, D. C. Ralph and R. A. Buhrman, Tunnel magnetoresistance and spin torque switching in MgO-based magnetic tunnel junctions with a Co/Ni multilayer electrode, *Appl. Phys. Lett.* **97**, 072513 (2010).
8. T. Kishi, H. Yoda, T. Kai, T. Nagase, E. Kitagawa, M. Yoshikawa and K. Nishiyama, Lower-current and Fast switching of A Perpendicular TMR for High Speed and High density Spin-Transfer-Torque MRAM. In Proc. IEDM 2008, San Francisco, CA, 15–17 December 2008. New York, NY: IEEE. (doi:10.1109/IEDM.2008.4796680).
9. J. Z. Sun, et al., A three-terminal spin-torque-driven magnetic switch *Appl. Phys. Lett.* **95**, 109901 (2009).
10. P. M. Braganca, J. A. Katine, N. C. Emley, D. Mauri, J. R. Childress, P. M. Rice, E. Delenia, D. C. Ralph and R. A. Buhrman, A Three-Terminal Approach to Developing Spin-Torque Written Magnetic Random Access Memory Cells, *IEEE. Trans. Nanotech.* **8**, 190 (2009).

CHAPTER 8

PERSISTENT MAGNETIC OSCILLATIONS INDUCED BY THE SPIN HALL EFFECT

8.1 Introduction

As is discussed in Chapter 1, two types of magnetic dynamics can be realized using the spin transfer torque: transient dynamics as is observed in magnetic switching [1] and persistent dynamics as is in radio frequency magnetic moment oscillations [2]. Spin torque driven magnetic precession can be very useful as a microwave nano-oscillator because of its compact size and the good tunability. Conventionally, the spin current was usually obtained through the spin filtering effect of ferromagnetic electrodes in spin valves or magnetic tunnel junctions (MTJs). More recently, with the discovery of the spin Hall effect (SHE) [3-9], it was realized that the spin transfer torque could also be provided by the transverse spin current from non-magnetic materials. In Chapter 6 and Chapter 7 we have already seen that by injecting the spin current from the SHE into the adjacent magnetic layer, one could induce magnetic switching in ferromagnetic (FM) metals. Ref. [10] also shows that DC magnetic dynamics could be obtained in ferrimagnetic insulators with ultra low damping and very small saturation magnetization. Now a natural question is whether it is possible to excite DC dynamics in normal FM metals using the spin Hall effect. More importantly from the application perspective, it is also important to demonstrate that relatively large microwave oscillation signal could be electrically detected.

Compared with the traditional spin valve or MTJ, the SHE can be more efficient in terms of transfering the spin torque into the FM layer (see Chapter 6) and it

could also provide more versatile configurations for the spin torque device(as is shown in Chapter 7). In this chapter, we will show that persistent DC dynamics can be excited in a ferromagnetic metal using the SHE as the driving force. And by combining the SHE together with an MTJ, we can detect the magnetic oscillation electrically through the radio frequency (RF) output voltage across the MTJ. The observed magnetic oscillation provides an additional proof for the spin torque origin of the current induced switching in the Ta based system observed in Chapter 7. The separation between the driving current and the sensing current in this spin Hall device also allows additional controls over the frequency and amplitude of the output power.

8.2 Experiment

8.2.1 Device and experimental setup

We studied samples made from a Ta(6)/CoFeB(1.5)/MgO(1.2)/CoFeB(4)/Ta(5)/Ru(5) stack (units in nanometers), where the the CoFeB/MgO/CoFeB MTJ was milled into 50×180 nm^2 nanopillars and the bottom Ta layer was patterned into microstrips 1.2 μm wide. The thickness of the free CoFeB layer was chosen such that the perpendicular anisotropy from CoFeB/MgO interface was significant, therefore greatly reducing the demagnetization field and decreasing the onset current for dynamics, but meanwhile it was not strong enough to tilt the magnetic moment fully out of plane. The thickness of the MgO barrier was thinner compared with that in Chapter 7, to provide a better impedance match between the MTJ and the transmission cable. The MTJ was oriented such that the long axis was perpendicular to the direction of the Ta strip (the direction that the current flows) and the external field was applied along this easy axis. Therefore the spins injected into the CoFeB free layer from the SHE are either parallel or antiparallel with the equilibrium position of the free layer magnetic moment. The magnetic

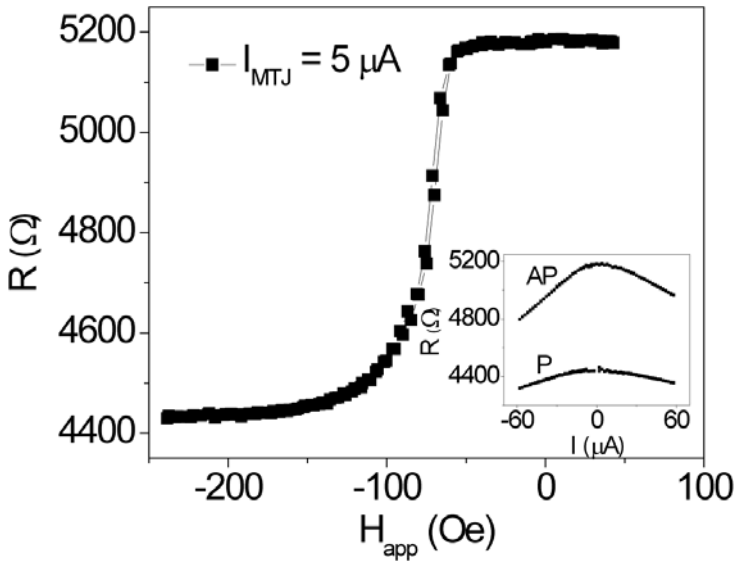

Figure 8.1 Magnetic minor loop of the MTJ. The lead resistance of 1.8 kΩ due to the Ta strip is already subtracted. Inset: the bias current dependence of the resistance of the MTJ in both the AP and P states.

response of the MTJ is shown in Fig. 8.1, from which we can see that the free layer is super-paramagnetic at room temperature and the magnetic moment is mainly oriented in the film plane under the applied in-plane field. The resistance of the Ta strip was measured independently to be ~ 3.6 kΩ. From the magnetic minor loop (the lead resistance from the Ta strip is already subtracted), the TMR of the MTJ can be determined to be ~ 17% under zero bias and RA product of the MTJ is ~ 40 Ω-μm^2. The bias current dependence of the resistance for both the P and AP states is summarized in the inset of Fig. 8.1, and we can see that the TMR decreases when a finite current is applied across the MTJ.

We used the circuit shown in Fig. 8.2 to excite and detect the magnetic dynamics in the device. Two DC current sources with common ground were employed to apply current across the Ta strip and the MTJ, separately. The current through the Ta strip I_{Ta} was used to inject spin current into the CoFeB free layer through the SHE

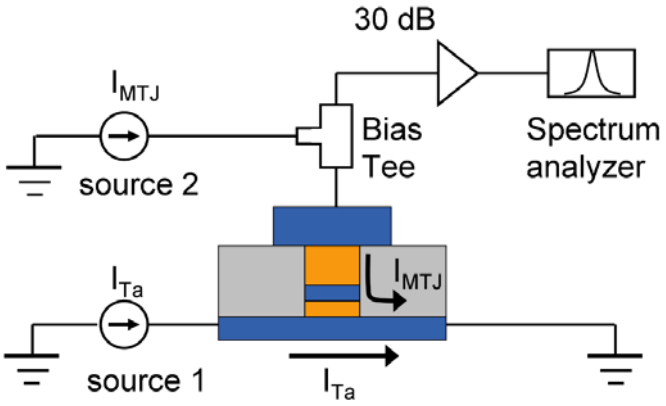

Figure 8.2 Schematic illustration of the circuit for the study of the magnetic oscillation. The black arrows denote the current distribution inside the three terminal SHE device. The currents I_{Ta} and I_{MTJ} come from current source 1 and current source 2, respectively and the positive direction for the currents are defined by the arrows.

and excite the magnetic dynamics therein, while the current across the MTJ I_{MTJ} was used to convert the oscillations in the MTJ resistance R_{rf} into an oscillating voltage V_{rf} = $I_{MTJ}R_{rf}$ so that the dynamics can be electrically detected. The output RF power was amplified and then detected using the spectrum analyzer. The amplification of the amplifier and the transmission coefficient caused by the impedance mismatch between the sample and the transmission cable ($1-\Gamma^2 = 1-[(R-50\Omega)/(R+50\Omega)]^2$) have been accounted for and corrected. So the microwave spectra shown in the rest of the work reflect the output power directly from the device. Since the internal resistances of the current sources and the DC impedance of the RF end of the bias tee can be regarded as infinitely large compared to the resistances of any other component in this circuit, the current flowing across the MTJ only comes from current source 2 and the current distribution inside the device is given exactly as in Fig. 8.2.

8.2.2 Microwave spectrum induced by the SHE

The spectra of the microwave power for I_{Ta} between -0.8 mA and 0.8 mA are shown in Fig. 8.3 (a). Here the applied external field is H_{app} = -160 Oe and the sensing current across the MTJ is kept at I_{MTJ} = 60 μA. Using the TMR of ~ 14 % under I_{MTJ} = 60 μA, this corresponds to a spin current density of 1.7×10^5 A/cm^2 , a value which is about ten times smaller than the spin current density generated by the SHE when I_{Ta} = ± 0.8 mA ($J_S \approx 1.6 \times 10^6$ A/cm^2 for $|I_{Ta}|$ = 0.8 mA when the measured value of J_S/J_C = 0.15 in Chapter 7 is used for Ta). From Fig. 8.3 (a), we can see that the magnetic dynamics are excited when I_{Ta} was negative, but no signal is observed when I_{Ta} is positive. As is known, persistent magnetic dynamics can be formed when the spin torque and the external field torque compete with each other. Since the applied field H_{app} = -160 Oe aligns the free layer into the P state, this implies that negative I_{Ta} tends to switch the magnetic moment into the AP state, which is consistent with the switching direction observed in Chapter 7. The fact that microwave signals was observed only for one current direction but not the other also excludes the possibility that the observed phenomenon comes from thermally excited magnetic resonance, because the thermal effect should be proportional to $|I_{Ta}|^2$. When the magnetic moment of the free layer undergoes small angle precessions around the equilibrium position in the collinear configuration, the resistance would oscillate at twice this frequency because $\Delta R \propto \cos\theta$ is an even function of the oscillation angle θ. Both the first and second harmonic peaks were observed in Fig. 8.3 (a) while the height of the second harmonic peak is much larger than the first one. This agrees with the parallel configuration and the small first harmonic peak may indicate that there is a small misalignment between the free layer and fixed layer under the applied field. The lineshape of the second harmonic peak can be fit using a Lorentzian function. As is shown in Fig. 8.3 (b), for I_{Ta} = - 0.8 mA the resonance frequency was determined to be $2f_0$ = 1.62 GHz and the linewidth was 104 MHz. The relationship between Δ ($2f$) and

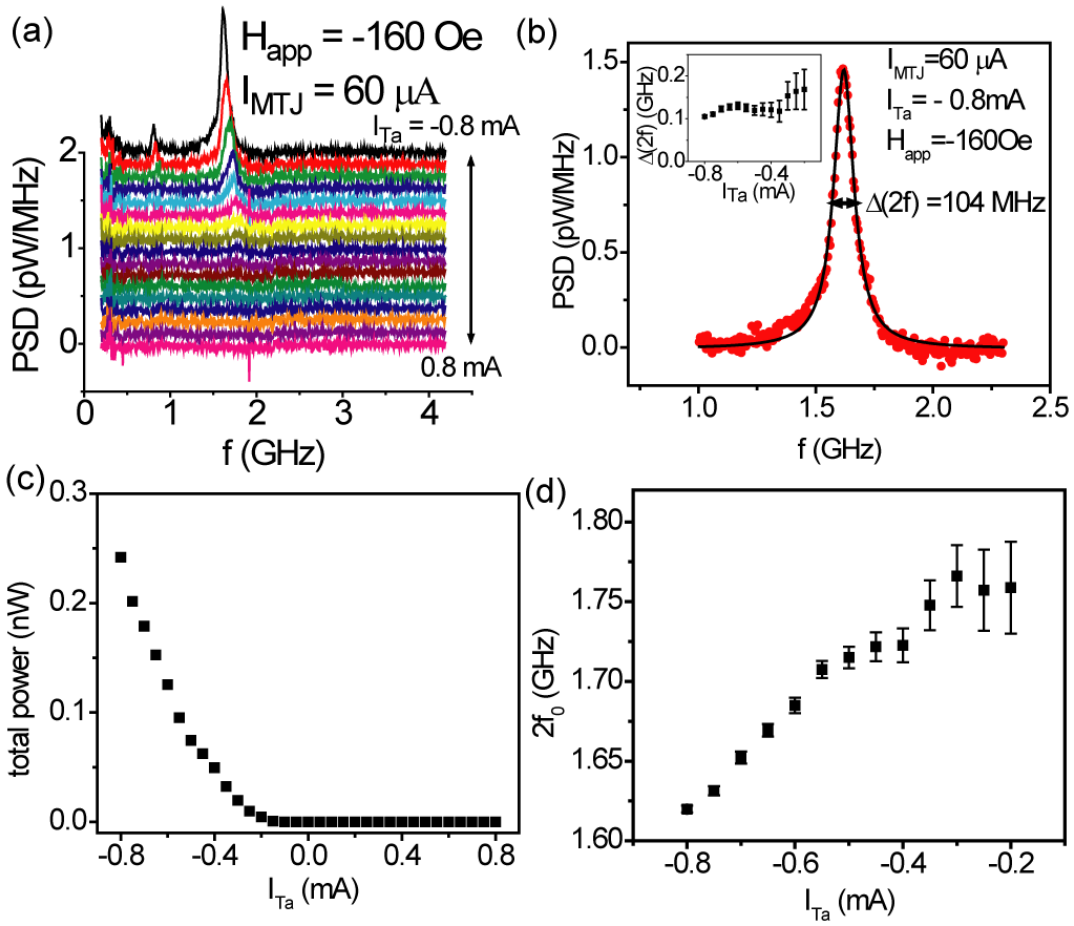

Figure 8.3 Microwave oscillations driven by the SHE. (a) Microwave spectra measured when the applied field H_{app} = -160 Oe, biasing current across the MTJ is fixed at I_{MTJ} = 60 μA and the Ta strip current is varied between I_{Ta} = -0.8 mA and +0.8 mA. The spectra under different currents are shifted vertically for the ease of comparison. The background signal when I_{MTJ} and I_{Ta} are both equal to zero is subtracted. (b) Microwave spectrum fitted using the Lorentzian function. The spectrum corresponds to the I_{Ta} = -0.8 mA case in (a). The linewidth of the second harmonic peak is determined to be 104MHz. Inset: the dependence of the linewidth of the second harmonic peaks on I_{Ta}. (c) Total microwave power for the second harmonic peaks shown in (a). (d) Central frequency of the second harmonic ($2f_0$) versus the applied Ta current.

I_{Ta} is illustrated in the inset of Fig. 8.3 (b). The integrated power under the second harmonic for different applied I_{Ta} is summarized in Fig. 8.3 (c), from which the onset current can be estimated to be around - 0.2 mA. Fig. 8.3 (d) shows the peak frequency

of $2f_0$ under different currenst. We can see that the oscillation frequency shifts lower (red shift) when the absolute value of the current I_{Ta} increases.

8.2.3 Influence of the tunneling current on the microwave spectra

In contrast to conventional spin valves or MTJs where the driving current to excite the dynamics and the sensing current to provide the output power are the same, these two currents are separable in the device that we studied, therefore allowing us to study the influences of those two parameters on the microwave signals independently. In Fig. 8.4 (a), we measured the microwave spectra under different I_{MTJ} while keeping I_{Ta} constant. Ideally, when the sensing current has no influence on the magnetic dynamics, we would expect that the output power P scales as I_{MTJ}^2. It can be seen from Fig. 8.4 (a) that as is expected, the measured power increases as $|I_{MTJ}|$ goes up and no signal was observed when $I_{MTJ} = 0$. In Fig. 8.4 (b) we plot the integrated power P (triangles) and the normalized power $P/(I_{MTJ}^2 T)$ (circles) *vs.* I_{MTJ} for the second harmonic peak, where $T(I_{MTJ})$ is the normalized bias-dependent TMR value of the MTJ: $T = \Delta R\,(I_{MTJ})/\Delta R\,(I_{MTJ} = 0)$. As expected the normalized power is roughly constant with bias apart from a slow decrease as I_{MTJ} increases from its greatest negative to its greatest positive value.

As illustrated in Fig. 8.4 (c), an important aspect of the behavior of this three-terminal STNO is a quite significant blue shift of the resonant frequency as I_{MTJ} is increased in the positive direction. Note that the frequency change is much larger for $\Delta I_{MTJ} = 120$ μA than it is for $\Delta I_{Ta} = 0.6$ mA in Fig. 8.3 (d). This large frequency shift is not reasonably attributable to the anti-damping spin torque of the tunneling current because of the low spin current density associated with I_{MTJ} compared to the spin current density from the SHE. Nor can the field-like torque exerted by I_{MTJ} explain this

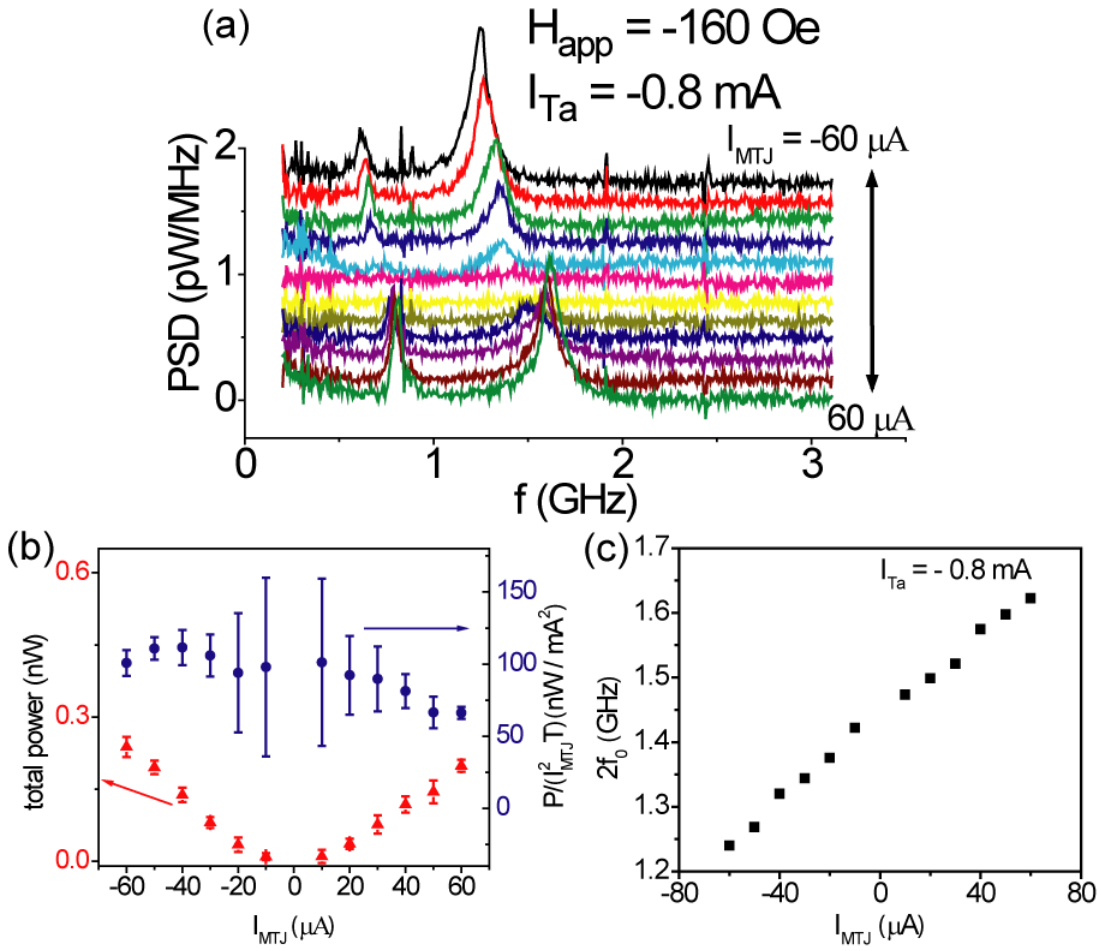

Figure 8.4 Tunneling current influence on the microwave spectra. (a) Microwave spectra measured when H_{app} = -160 Oe, I_{Ta} = -0.8 mA and I_{MTJ} is varied between -60 μA and 60 μA. (b) Red triangles: microwave power P of the second harmonic peaks shown in (a) versus the applied MTJ current. Blue circles: microwave power normalized by I^2_{MTJ} and the magnetoresistance T under the corresponding current. (c) Central frequencies of the second harmonic peaks in (a) versus the applied MTJ current.

frequency shift, since to the first order the field-like torque is an even function of I_{MTJ} [11-12]. The substantial frequency shift as the function of I_{MTJ} can however be quantitatively related to the perpendicular anisotropy change induced by the changes in the electric field across the MgO tunnel barrier as I_{MTJ} is varied. It has recently been reported that the electric field at a ferromagnetic/MgO interface can affect the

interfacial magnetic anisotropy energy [13-19] which in turn can substantially modify the free layer oscillation frequency. Within the single domain or macrospin model, f_0 for small angle oscillations should obey the Kittel formula:

$$f = \mu_0 \frac{\gamma}{2\pi} \sqrt{H_{ext}(H_{ext} + H_{demag}^{eff})} \,. \tag{8.1}$$

Here H_{ext} is the net external field, which contains both the applied field and the dipole field from the fixed layer and $H_{demag}^{eff} = M_S - 2K_u / (\mu_0 M_S)$ is the effective demagnetization field where M_S denotes the saturation magnetization and K_u is the uniaxial anisotropy energy coefficient. Thus, a change in K_u will finally cause a shift in oscillation frequency. The electric field induced ansitropy change can also account for the changes in the normalized power observed in Fig. 8.4 (b). An increased H_{demag}^{eff} will increase the onset current needed for exciting the DC dynamics and suppress the oscillation angle under the same driving current, which could further result in a reduced output microwave power. The in-plane spin torque from I_{MTJ} cannot explain the observed power variation since under positive I_{MTJ}, the resultant spin torque tends to facilitate instead of suppress the magnetic oscillations (Fig. 8.2), which is opposite to the trend in Fig. 8.4 (b).

8.2.4 Determination of electric field induced anisotropy change

To establish that the frequency shift comes from the anisotropy change, we measured the power spectra under different applied fields [Fig. 8.5 (a)] when the applied currents are kept constant at I_{Ta} = -0.8 mA and I_{MTJ} = 60 μA. The central frequencies of oscillation peaks are represented by the red triangles in Fig. 8.5 (b) (Note that the base frequency f_0 is used here). By fitting with Equation 8.1 [the red solid line in Fig. 8.5 (b)] and taking into account the small frequency shift caused by finite I_{Ta},, we can extract the value for the demagnetization field $H_{demag}^{eff} = 1100 \pm 60$ Oe for I_{MTJ} = 60 μA. This number is much smaller than the intrinsic demagnetization

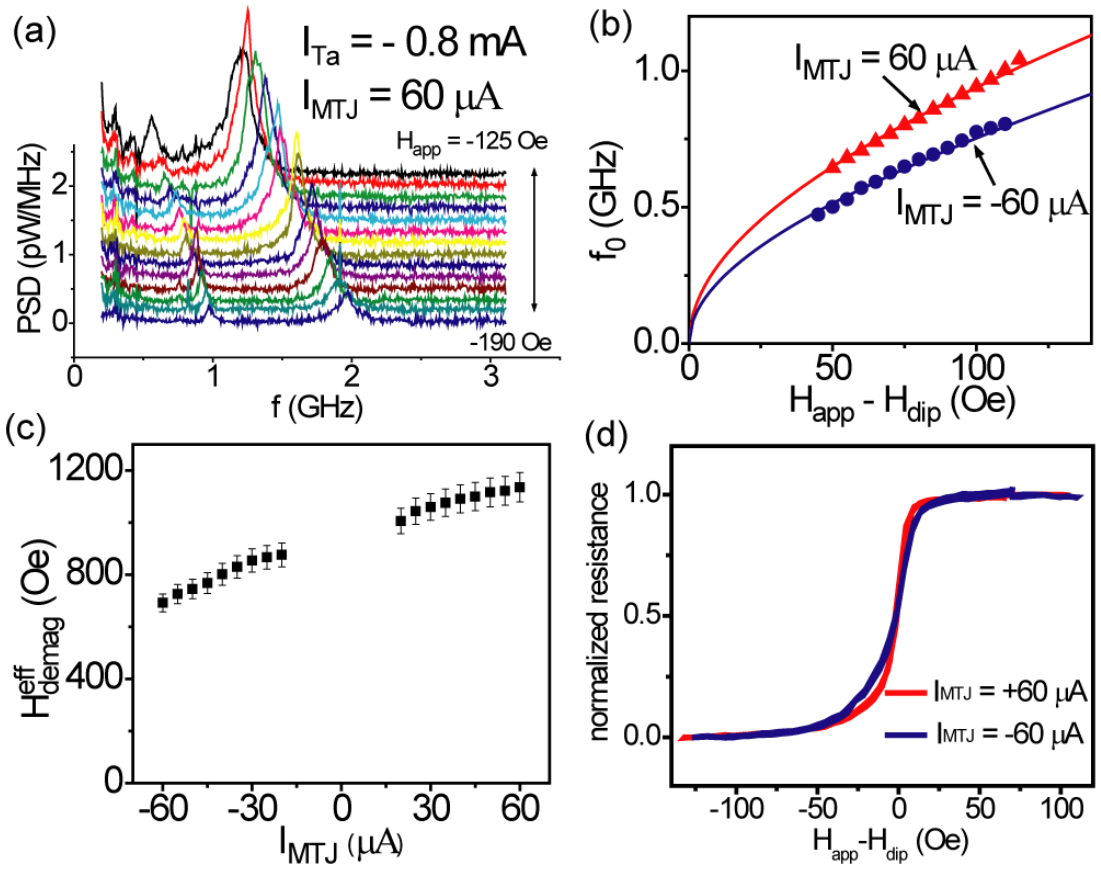

Figure 8.5. External magnetic field dependence of the spectra. (a) Microwave spectra measured when I_{Ta} = -0.8 mA, I_{MTJ} = 60 μA and H_{app} is applied between -125 Oe and -190 Oe. (b) Fundamental oscillation frequency f_0 versus the net external field $H_{app} - H_{dip}$. The red triangles are obtained from the data in (a) and the blue circles are from the spectra measured for I_{Ta} = -0.8 mA and I_{MTJ} = - 60 μA. The solid lines represent the fittings for both currents using the Kittel formula. (c) The dependence of the effective demagnetization field H_{demag}^{eff} on the applied MTJ current. H_{demag}^{eff} is determined from fittings similar to those shown in (b). (d) Magnetoresistance minor loops measured under + 60 μA (red) and – 60 μA (blue). The resistances are normalized with R_{AP}-R_P under each current to make the comparison easier.

field for CoFeB thin film ($4\pi M_S \approx 13000$ Gauss [20]), and is consistent with the large interfacial perpendicular anisotropy observed in the Ta/CoFeB/MgO system [21]. In Fig. 8.5 (b), we also plot oscillation frequencies *vs* external field for the I_{MTJ} = - 60 μA case (blue circles). The extracted effective demagnetization field is reduced to

$H_{demag}^{eff}(I_{MTJ} = 60\,\mu\text{A}) = 700 \pm 40$ Oe. With I_{Ta} fixed at - 0.8 mA, we measured the microwave spectra for different I_{MTJ} and H_{ext}. The effective demagnetization fields under each I_{MTJ} were plotted in Fig. 8.5 (c). We can see that there is almost a linear increase in the effective demagnetization field when I_{MTJ} is increased in the positive direction. The slope in Fig 8.5 (c) is 3.2 ± 0.4 Oe/μA, or 730 ± 90 Oe/V by using the resistance of the MTJ. Taking into account the thickness of CoFeB t_{CoFeB} = 1.5 nm, the thickness of MgO barrier t_{MgO} = 1.2 nm, $M_S = 1.1\times10^6$A/m and the interfacial anisotropy energy $E_{perp}t = 0.5\mu_0 M_S H_{an} t$, this leads to a change in $E_{perp}t$ of ~70 μJ/m^2 for applied electric field of 1V/nm, quite similar to values reported previously from different experiments, where the anisotropy change ranges from 30 to 140 μJ/m^2 (V/nm)$^{-1}$ [13-19]. The sign of the effect in our experiment is also consistent with previous reports [15, 17-18], that is, a positive electric field as in Fig. 8.2 leads to a decrease in K_u.

To further verify that the tunneling current through our MTJ can effect a significant change in the magnetic anisotropy of the free layer, we measured the magnetic minor loop under $I_{MTJ} = \pm 60$ μA [Fig. 8.5 (d)]. The switching curve under I_{MTJ} = + 60 μA is steeper compared with the one for I_{MTJ} = - 60 μA, indicating that the negative (positive) biasing current increases (decreases) the perpendicular anisotropy of the free layer, consistent with the frequency shift direction.

8.3 Conclusion

The three-terminal SHE device provides an ideal platform for studying how spin torque and electric field can influence magnetic dynamics in nanomagnets. A frequency shift has been previously observed in the DC current induced magnetic dynamics of multiple MTJs with thin free layers [22-23]. However, it has been very

difficult to differentiate the contribution from the two effects: the electric field and the spin torque, because both of those two effects exist and can be comparable to each other. Especially, it makes the determination of the field like torque complicated in this type of MTJs. In contrast, in the three terminal device, the spin torque for exciting the dynamics comes from the SHE instead of the tunneling current. So MTJs with high RA product can be used for the study and only a very small tunneling current is needed for the detection of the signal. Therefore, as is illustrated above, the three terminal device can give us better knowledge about the origins of the frequency change.

In conclusion, we have demonstrated that the spin Hall effect can be used to excite persistent magnetic oscillations in a metallic nanomagnet. Microwave power was electrically detected by integrating a MTJ with the SHE material. Compared with conventional MTJs, the SHE-based magnetic nano-oscillator provides independent control over the magnetic dynamics and the electric power, therefore allowing for a better tunability over the frequency and amplitude of the output microwave signal. We also quantitatively measured the electric field induced magnetic anisotropy change at the CoFeB/MgO interface using the three terminal device. We showed that compared to pure spin torque, the electric field can be used to tune the oscillation frequency over an even wider range.

REFERENCE

1. J. A. Katine, F. J. Albert, R. A. Buhrman, E. B. Myers and D. C. Ralph, Current-driven magnetization reversal and spin-wave excitations in Co/Cu/Co pillars, *Phys. Rev. Lett.* **84**, 3149 (2000).
2. S. I. Kiselev, J. C. Sankey, I. N. Krivorotov, N. C. Emley, R. J. Schoelkopf, R. A. Buhrman and D. C. Ralph, Microwave oscillations of a nanomagnet driven by a spin-polarized current, *Nature* **425**, 380 (2003).
3. M. I. Dyakonov and V. I. Perel, Current-Induced Spin Orientation of Electrons in Semiconductors, *Phys. Lett. A* **35**, 459 (1971).
4. J. E. Hirsch, Spin Hall effect, *Phys. Rev. Lett.* **83**, 1834 (1999).
5. S. F. Zhang, Spin Hall effect in the presence of spin diffusion, *Phys. Rev. Lett.* **85**, 393 (2000).
6. J. Sinova, D. Culcer, Q. Niu, N. A. Sinitsyn, T. Jungwirth and A. H. MacDonald, Universal intrinsic spin Hall effect, *Phys. Rev. Lett.* **92**, 126603 (2004).
7. S. Murakami, N. Nagaosa and S. C. Zhang, Dissipationless quantum spin current at room temperature, *Science* **301**, 1348 (2003).
8. Y. K. Kato, R. C. Myers, A. C. Gossard and D. D. Awschalom, Observation of the spin hall effect in semiconductors, *Science* **306**, 1910 (2004).
9. S. O. Valenzuela and M. Tinkham, Direct electronic measurement of the spin Hall effect, *Nature* **442**, 176 (2006).
10. Y. Kajiwara, et al., Transmission of electrical signals by spin-wave interconversion in a magnetic insulator, *Nature* **464**, 262 (2010).
11. J. C. Sankey, Y. T. Cui, J. Z. Sun, J. C. Slonczewski, R. A. Buhrman and D. C. Ralph, Measurement of the spin-transfer-torque vector in magnetic tunnel junctions, *Nature Phys.* **4**, 67 (2008).
12. C. Wang, Y. T. Cui, J. A. Katine, R. A. Buhrman and D. C. Ralph, Time-resolved measurement of spin-transfer-driven ferromagnetic resonance and spin torque in magnetic tunnel junctions, *Nature Phys.* **7**, 496 (2011).
13. T. Maruyama, et al., Large voltage-induced magnetic anisotropy change in a few atomic layers of iron, *Nature Nanotech.* **4**, 158 (2009).
14. S. S. Ha, N. H. Kim, S. Lee, C. Y. You, Y. Shiota, T. Maruyama, T. Nozaki and Y. Suzuki, Voltage induced magnetic anisotropy change in ultrathin Fe(80)Co(20)/MgO junctions with Brillouin light scattering, *Appl. Phys. Lett.* **96**, 142512 (2010).
15. T. Nozaki, Y. Shiota, M. Shiraishi, T. Shinjo and Y. Suzuki, Voltage-induced perpendicular magnetic anisotropy change in magnetic tunnel junctions, *Appl. Phys. Lett.* **96**, 022506 (2010).
16. M. Endo, S. Kanai, S. Ikeda, F. Matsukura and H. Ohno, Electric-field effects on thickness dependent magnetic anisotropy of sputtered MgO/Co(40)Fe(40)B(20)/Ta structures, *Appl. Phys. Lett.* **96**, 212503 (2010).
17. W. G. Wang, M. G. Li, S. Hageman and C. L. Chien, Electric-field-assisted switching in magnetic tunnel junctions, *Nature Mat.* **11**, 64 (2012).

18. Y. Shiota, T. Nozaki, F. Bonell, S. Murakami, T. Shinjo and Y. Suzuki, Induction of coherent magnetization switching in a few atomic layers of FeCo using voltage pulses, *Nature Mat.* **11**, 39 (2012).
19. J. Zhu, et al., Voltage-Induced Ferromagnetic Resonance in Magnetic Tunnel Junctions, *Phys. Rev. Lett.* **108**, 197203 (2012).
20. L. Q. Liu, Pai, C.-F., Li, Y., Tseng, H. W., Ralph, D. C. & Buhrman, R. A, Spin torque switching with the giant spin Hall effect of tantalum, *Science* **336**, 555 (2012).
21. S. Ikeda, et al., A perpendicular-anisotropy CoFeB-MgO magnetic tunnel junction, *Nature Mat.* **9**, 721 (2010).
22. A. M. Deac, et al., Bias-driven high-power microwave emission from MgO-based tunnel magnetoresistance devices, *Nature Phys.* **4**, 803 (2008).
23. S. Petit, N. de Mestier, C. Baraduc, C. Thirion, Y. Liu, M. Li, P. Wang and B. Dieny, Influence of spin-transfer torque on thermally activated ferromagnetic resonance excitations in magnetic tunnel junctions, *Phys. Rev. B* **78**, 184420 (2008).

CHAPTER 9

ELECTRIC FIELD MODULATED SPIN HALL SWITCHING

9.1 Introduction

The magnetic properties of ferromagnetic films can be electrically manipulated either by using a current [1-2] or using an electric field [3-5]. As is discussed in most of the chapters in this dissertation, the spin current can change the effective magnetic damping through the spin transfer torque mechanism [6-8], and therefore has long been studied as an efficient way to achieve bi-polar magnetic switching. In the meantime, an electric field was recently shown to be able to modify the anisotropy of magnetic films [3-5, 9-14]. Compared with the current induced magnetic switching, electric-field-based manipulation has the potential for lower energy consumption and therefore attracts quite a lot of interest.

Electric field control of magnetic properties has been experimentally verified using different approaches. Ohno *et al.*[3] first demonstrated that by applying a DC gate voltage across a magnetic semiconductor, one could modify the Curie temperature (T_C) of the semiconductor. It is known that the magnetism is mediated by the holes through a RKKY like exchange mechanism in (In,Mn)As. The application of the electric field can change the hole concentration inside the semiconductor, therefore modifying the magnetic properties of the film. By measuring the anomalous Hall resistance under a temperature close to T_C, Ohno *et al.* showed that (In,Mn)As can be switched between the ferromagnetic and paramagnetic states reversibly through the application of a positive (negative) electric field. Field modulated ferromagnetism can also be realized through the use of special multiferroic materials [10-11]. In

multiferroic materials, ferroelectricity and ferromagnetism (or antiferromagnetism) ordering exist simultaneously and are coupled together. So it is possible to change the magnetic structure by applying an electric field.

More recently it was shown that the magnetic anisotropy can be modified via direct control over the electronic structure at the ferromagnetic metal surface [4-5]. This was first demonstrated in FePt and FePd films that were immersed in an electrolyte [4]. By using the FM metal as an electrode and applying a voltage to the electrolyte, Weisheit *et al.* [4] showed that the coercive field of FePt and FePd can be modified by a few percent. The perpendicular anisotropy of the ferromagnetic films is changed because under electric field ions will adhere onto the FM electrode and shift the occupation of *d* orbitals. In 2009, Maruyama *et al.* [5]showed that a similar phenomenon could happen by applying voltage at the interface between 3d transition metal and an insulator like MgO. The electric field can influence the filling of the *d* band at the Fermi surface, which can further induce an anisotropy change [13-14]. So far, people have demonstrated efficient voltage control on magnetic anisotropy with different ferromagnetic electrodes including Fe, CoFe or CoFeB [5, 12, 15-17]. Several strategies have even been developed in order to achieve a bi-stable switching using these anisotropy changes [18-19].

In the previous chapters, I have shown that the spin Hall effect (SHE) can be an efficient way to generate spin current, to induce magnetization oscillation (chapter 8) and cause magnetic switching (chapter 6 and 7). Especially in chapter 7, in order to realize magnetic switching for in-plane magnetized films, we fabricated a three terminal magnetic device which used the spin Hall effect to switch the magnetic moment and used a magnetic tunnel junction (MTJ) to read out the information.

Compared with conventional two terminal MTJs, this design not only provides a split between the reading and writing operations, but also allows additional control on the magnetic properties of the free layer through the third terminal. Especially, it is possible to apply an electric field across the MTJ and use the field to modulate the properties of the free magnetic layer. In this chapter, I will show that by utilizing a three terminal magnetic device we can switch the magnetic orientation of the free layer by the spin torque from the spin Hall effect and at the same time tune the magnetic anisotropy independently through the gate voltage. The critical current for spin torque switching can be adjusted significantly through the variation of the gate electric field. The realization of gate modulated spin torque switching can enable simpler architectures for magnetic memories and it also opens up new strategies for non-volatile spin logic applications.

9.2 Experiment

9.2.1 Measurement Setup

As is shown in Fig. 9.1, the full stack of substrate/Ta(6)/CoFeB(1.5)/MgO(1.2)/CoFeB(4)/Ta(5)/Ru(5) (units in nanometers) was deposited and patterned into the three terminal magnetic device as is described in Chapter 7. The bottom Ta microstrip is 1 μm wide and 6 μm long and the MTJ is patterned into nanopillars with the area 100×350 nm^2, with the long axis aligned perpendicular to the Ta strip orientation. The thickness of the free layer CoFeB is chosen such that the perpendicular anisotropy from the CoFeB/MgO interface is significant so it greatly reduces the effective demagnetization field of the CoFeB film. But meanwhile it is not strong enough to tilt the magnetic moment fully out of plane. No annealing was employed to avoid further change in the anisotropy of the system.

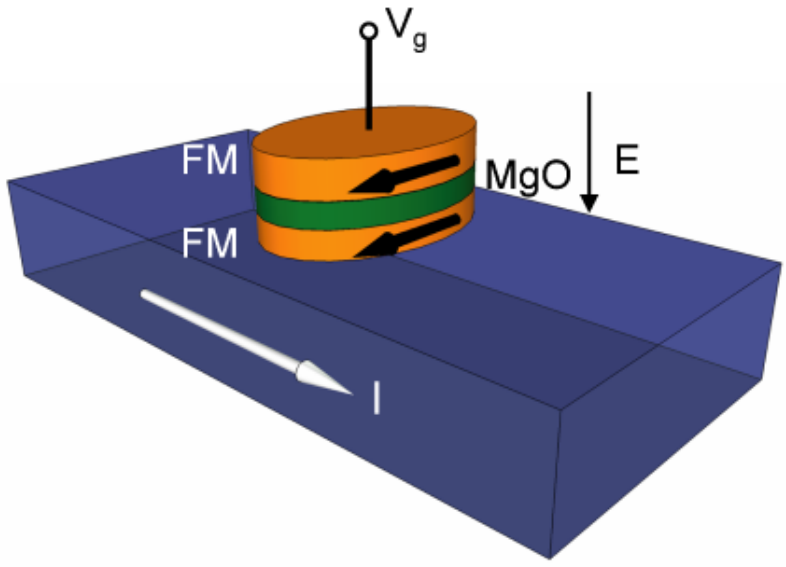

Figure 9.1 Schematic illustration of the field modulated SHE device. *I* is the switching current flowing through the Ta strip, and *E* represents the electric field applied across the MgO barrier.

The resistances of the Ta strip and the MTJ are measured to be around 4 kΩ and 1 kΩ, separately. More than ten devices were checked and consistent behaviors were obtained. The data shown below came from the same device and all of the measurements were carried out at room temperature.

In order to study the SHE induced switching, current pulses were applied through the Ta microstrip and the MTJ, simultaneously. As is shown in the circuit diagram of Fig. 9.2 (a), pulses of equal lengths were injected into the Ta strip and the MTJ from the two channels of the pulse generator. Large resistors of 20 kΩ and 10 MΩ were connected in series with Channel 2 and the lock-in amplifier oscillator respectively, to prevent the current of Channel 1 pulse from flowing across the MTJ. The differential resistance of the MTJ *dV/dI* was measured after each pulse to monitor the resistance state of the device. When voltages are applied both through the Ta strip

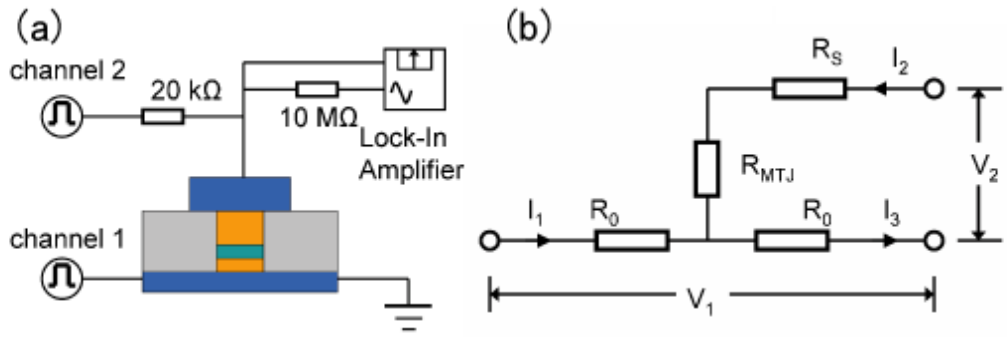

Figure 9.2 Circuit used to apply voltage pulses to the SHE device. (a) Schematic illustration of the device and the circuit used to apply voltage and measure the resistance. (b) Equivalent circuit of the device shown in (a). R_0 is half of the Ta strip resistance, R_{MTJ} represents the resistance of the MTJ. R_S = 20 kΩ, is the standard resistance connected in series with the MTJ. V_1 and V_2 are the voltages applied from Channel 1 and channel 2 of the pulse generator. The circuit for the Lock-In amplifier part is not shown.

and across the MTJ, the current and voltage distribution inside the device is not obvious. As is shown in the equivalent circuit of Fig. 9.2 (b), the resistances of the Ta microstrip and the MTJ are $2R_0$ and R_{MTJ}, separately. Since the MTJ is located in the middle of the Ta strip, the left and right halves of the Ta strip each has resistance of R_0. The standard resistor in series with the MTJ is R_S. During measurement, voltages of V_1 and V_2 are applied between different pairs of terminals as is shown in the figure. I_1, I_2 and I_3 represent the current flowing through the left part of the Ta strip, the MTJ and the right part of the Ta strip. According to Kirchhoff's circuit laws, we have:

$$I_1 + I_2 = I_3 \tag{9.1}$$

$$I_1 R_0 + I_3 R_0 = V_1 \tag{9.2}$$

$$I_2 (R_S + R_{MTJ}) + I_3 R_0 = V_2 \tag{9.3}$$

By solving the Equations 9.1~9.3, we can get $I_2 = (V_2 - 0.5V_1)/(R_S + R_{MTJ} + 0.5R_0)$, and $I_1 = V_1/(2R_0) - 0.5I_2$, $I_3 = V_1/(2R_0) + 0.5I_2$. In the device that we studied, we have $R_{MTJ} \approx 1000\ \Omega$, $2R_0 \approx 4000\ \Omega$ and the standard resistance $R_S = 20000\ \Omega$. First of all,

let's look at the case where the bias voltage from Channel 2 is set at 0. Under this condition, the current flowing across the MTJ is $I_2 = -0.5V_1/(R_S + R_{MTJ} + 0.5R_0)$. For the largest voltage that we applied $V_1 \approx 3$ V, this corresponds to a current of 70 μA, or a current density of 2×10^5 A/cm^2, therefore, the corresponding spin transfer torque from the MTJ can be neglected in this case. Secondly, the voltage across the MTJ can be written as $V_{MTJ} = I_2 R_{MTJ} = R_{MTJ}(V_2 - 0.5V_1)/(R_S + R_{MTJ} + 0.5R_0)$. It can be verified that so long as V_{MTJ} is kept moderate or large ($V_{MTJ} \geq 100$ mV), the voltage that we applied through channel 2 V_2 will be much larger than the largest voltage that we applied through channel 1, and V_1 can therefore be neglected in the calculation of I_2 and V_{MTJ}. So for most values of the applied V_2, the voltage across the MTJ can roughly calculated as $V_{MTJ} \approx V_2 \bullet R_{MTJ}/(R_S + R_{MTJ} + 0.5R_0)$. Thirdly, since $I_{1,3} = V_1/(2R_0) \mp 0.5I_2$, half of the current through the MTJ flows rightwards and the other half flows leftwards. This indicates that for Ta located directly under the MTJ, current I_2 does not make extra contribution to the spin Hall effect because the right-going and left-going current cancel out with each other. So, when calculating the spin torque from the spin Hall effect, we only need to consider the current generated by V_1, i.e., $I_{SHE} = V_1/(2R_0)$.

9.2.2 Data and analysis

The magnetic field response of the MTJ is shown in Fig. 9.3 (a). The tunneling magnetoresistance (TMR) can be calculated to be ~17% at zero bias voltage (after subtracting the resistance contribution from the Ta strip) and the RA product of the MTJ is 35 Ω-μm^2. In a system where the the demagnetization energy was partially cancelled by the perpendicular interfacial energy, the total static magnetic energy can be written as: $E_{tot} = 0.5\mu_0 H_{demag}^{eff} M_S$. Here M_S represents the saturation magnetization,

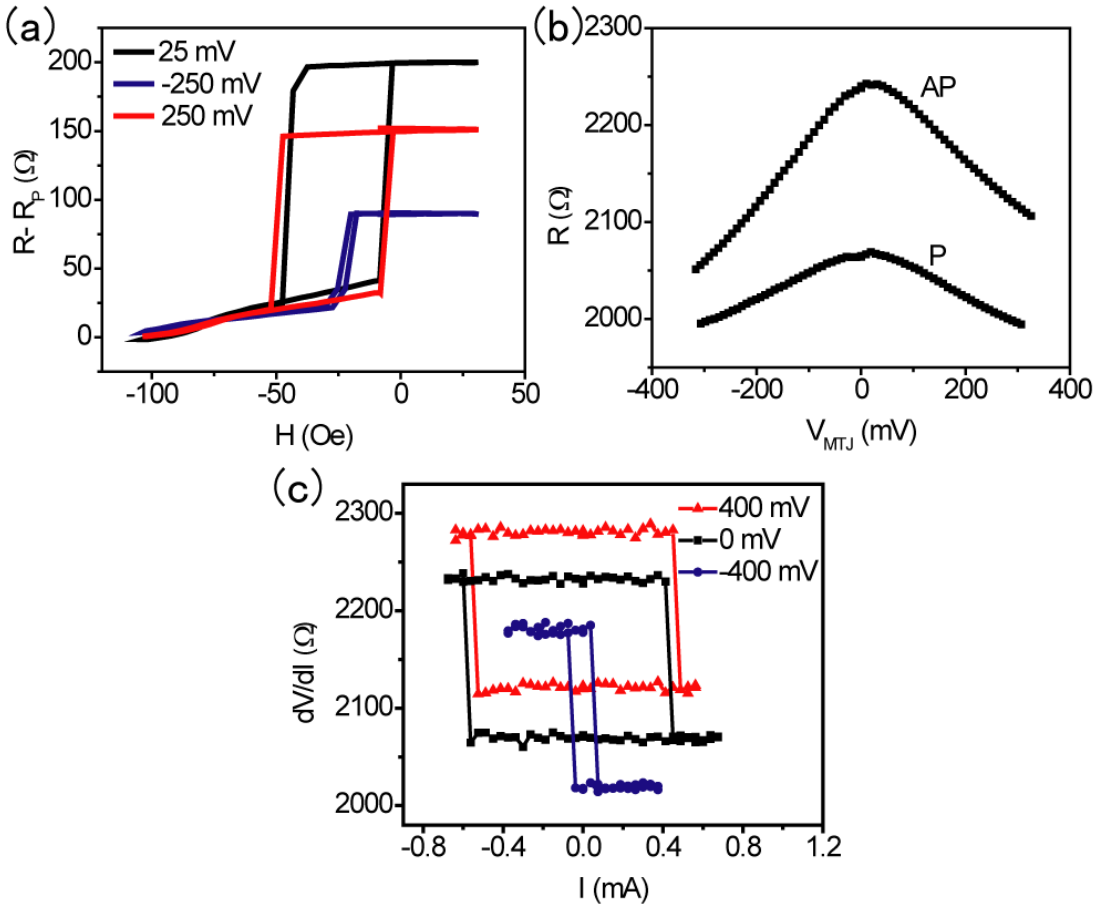

Figure 9.3 Field and current induced switching. (a) Magnetic minor loop of the MTJ under bias voltages of V_{MTJ} = 25 mV and ± 250 mV. Here, V_{MTJ} represent the voltage drop only across the MgO barrier. The voltage contribution from the bottom lead resistance is excluded. (b) Voltage dependence of the MTJ resistance. The resistance includes the lead resistance of Ta of ~ 1 kΩ. (c) SHE induced switching when V_{MTJ} is set at 0 mV and ± 400mV. The pulse lengths for both channels are set at 10 milliseconds.

H_{demag}^{eff} is the effective demagnetization field and is equal to $M_S - H_K$, where M_S is the intrinsic demagnetization field and $H_K = 2K_u/(\mu_0 M_S)$ is the perpendicular anisotropy field. By applying a voltage across the MTJ, the perpendicular anisotropy field is expected to vary from H_K to $H_K + \Delta H_K$ from the electric field effect. To check the effect of the electric field on the magnetic properties of the MTJ, DC voltages of ± 250 mV were applied across the MgO barrier [Fig. 9.3 (a)]. It can be

seen that the TMR is reduced significantly compared with the zero biased case, reflecting the voltage dependence of the magnetoresistance [Fig. 9.3 (b)]. The coercive field H_C respond differently to the applied voltage, depending on the sign. For negative applied E field (the sign of the E field is the defined as in Fig. 9.1), the coercive field decreases significantly, corresponding to an increased H_K case, while for positive applied E field, the coercive field is slightly increased (H_K is reduced). This trend on the voltage induced anisotropy change has the same sign with the previous reports [16, 18-19], where most of the systems studied are magnetized out-of plane.

The black curve in Fig. 9.3 (c) shows the data for magnetic switching induced by 10 millisecond current pulses flowing inside the Ta strip. We can see that the magnetic moment of the free layer can be switched between the P and AP states reversibly at around ± 0.5 mA. To test the influence of the electric field on the switching currents, additional voltage pulses were applied across the MTJ simultaneously with the biasing current through the Ta strip. The red and blue data points in Fig. 9.3 (c) represent the cases when the biasing voltages across the MTJ are ± 400 mV, from which we can see that when negatively biased the switching current decreases significantly, by more than 5 times, while the positive bias voltage does not change the switching current much. This cannot be explained by a pure heating effect, since the heating should scale with I^2, and therefore would have the same influence for the positive and negative MTJ bias voltages. The spin torque from the tunneling current across the MTJ cannot explain the observed phenomena either. The spin current generated from the bias voltage across the MTJ can be calculated using the TMR ratio. Using the Julliere's model [20] $\Delta R / R_P = 2P_L P_R /(1 - P_L P_R)$ and assuming that the spin polarization for the left electrode P_L and right electrode P_R are equal, we can calculate spin polarization to be ~ 0.3. This corresponds to a spin current density

of around 3×10^5 A/cm^2 for $|V_{MTJ}| = 400$ mV. As for the spin current due to the spin Hall effect, the average switching critical current at zero gate voltage is ~ 0.5 mA for 10 millisecond pulses. This corresponds to a current density of ~ 8.3×10^6 A/cm^2. Using the J_S/J_C value of 0.15 we determined for Ta from the previous experiment, we can get the spin current density of 1.2×10^6 A/cm^2. Therefore, the spin current density flowing across the MTJ due to the applied gate voltage is about 4 times smaller than the spin current density generated by the spin Hall effect. What's more, the net effect of spin torque from the tunneling current would be to add to or subtract from the spin torque from the spin Hall effect and hence would shift the switching curve as a whole to the left or the right, which is not consistent with the behavior in Fig. 9.3 (c).

The switching currents for different gate voltages were measured and summarized in Fig. 9.4 (a). For each data point, the critical current was averaged from ten scans. It can be seen that there is a large reduction in the critical current I_C with the increase of $|V_{MTJ}|$ when $V_{MTJ} < 0$ and there is only a very small change in I_C when $V_{MTJ} > 0$. Under zero temperature, the critical current density for spin torque switching should have the form [1, 21]:

$$J_{C0} = \frac{2e\mu_0 M_S t\alpha}{\hbar |\cos\theta|}(H_C + 0.5H_{demag}^{eff})/(J_S / J_C), \qquad (9.4)$$

where μ_0 denotes the permeability in vacuum, t, M_S and α represent the thickness, the saturation magnetization and the Gilbert damping coefficient of the free magnetic layer, θ is defined as the angle between the injected spin and the equilibrium position of the free layer magnetic moment, J_S/J_C represents the efficiency for the generation of the spin current. We can see that the critical current density is roughly proportional to the effective demagnetization field H_{demag}^{eff} when H_{demag}^{eff} is much larger than the coercive field H_C. At finite temperature, the spin torque switching can be assisted by thermal agitations, and the critical current will be reduced. Generally, the critical

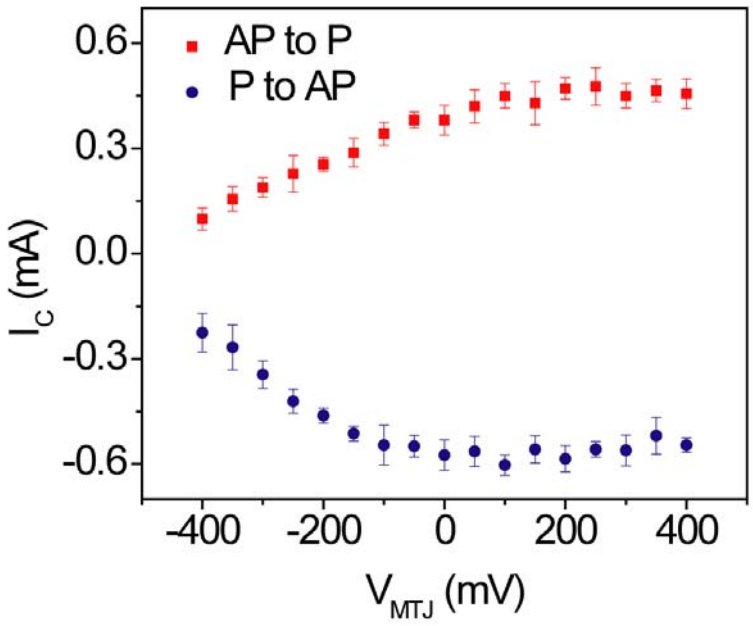

Figure 9.4 Bias voltage dependence of the SHE critical current. Pulse lengths for I_{Ta} and V_{MTJ} were set at 10 milliseconds. The red squares and blue circles represent AP to P and P to AP switching, separately.

current density for thermally-assist switching can be written as [22]:

$$J_C = J_{C0}[1-(k_B T/E)\ln(\tau/\tau_0)], \tag{9.5}$$

where E is the energy barrier, τ and τ_0 represent the applied pulse length and the inverse of the attempt frequency. Therefore, the electric field can have a two-fold effects on the switching current at ambient temperature: first, the electric field can modulate the perpendicular anisotropy field and H_{demag}^{eff}, which according to Equation 9.4 will influence the non-thermal assisted critical current J_{C0} correspondingly. Secondly, under the applied electric field, the change in H_{demag}^{eff} can further influence the coercive field H_C and the energy barrier E, as is observed in Fig. 9.3 (a). The change in E will also lead to modifications of J_C.

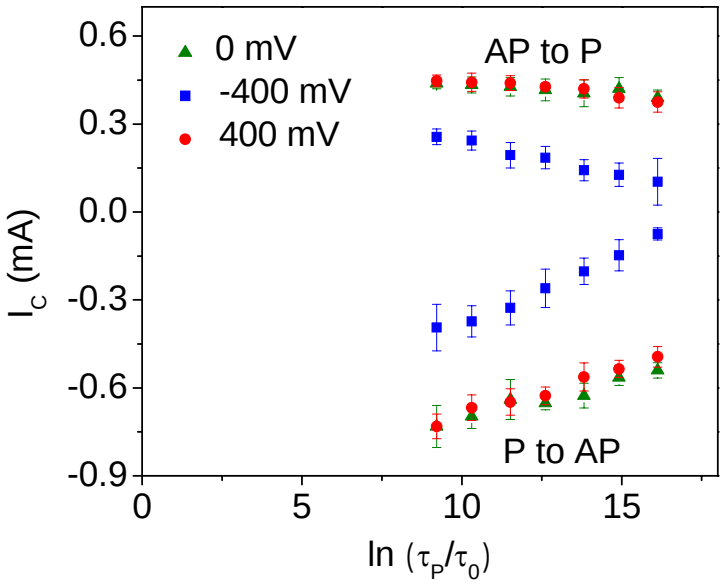

Figure 9.5 Spin Hall critical current under different pulse lengths. The pulse length τ_P is varied from 10 microseconds to 10 milliseconds. The red, green and blue data points stand for the cases when V_{MTJ} = 400 mV, 0 mV and -400 mV.

To get the voltage dependence of the demagnetization field and energy barrier, we measured the switching curves with different pulse lengths for I_{Ta} and V_{MTJ}. V_{MTJ} was set at ± 400 mV and 0 mV. As is shown in Fig. 9.5, the pulse length for channel 1 and channel 2 was varied from 10 milliseconds to 10 microseconds. By fitting the data in Fig 9.5 to Equation 9.5, we can obtain the values of I_{C0} and the ratio of E/k_BT under different bias voltages. The result is summarized in Table 9.1. First of all, it can be noted that there is a large asymmetry between the $|I_{C0}|$ for P to AP switching and AP to P switching and we have $I_{C0}^{P\to AP} > I_{C0}^{AP\to P}$ under all of the applied gate voltages. This is different from our previous observation in Chapter 7, where the critical current for both switching directions were measured to be about the same. This may result from the fact that in the device that we studied, the P state is not a perfectly parallel state when biased in the middle of the magnetic minor loop using an external field. As is

Table 9.1. Non-thermal assistant critical current I_{c0} and energy barrier E. The data are determined from fittings of Fig. 9.5.

	AP to P		P to AP	
	I_{C0} (mA)	E/k_BT	I_{C0} (mA)	E/k_BT
-400 mV	0.43±0.03	18	0.87±0.03	18
0 mV	0.51±0.02	72	0.97±0.04	37
400 mV	0.55±0.02	53	1.03±0.03	31

revealed from the magnetic major loop (Fig. 9.6), under an external field of – 25 Oe, the resistance of the P state does not reach the lowest value, indicating that there is an angle θ between the equilibrium position of the magnetization of the free layer and the orientation of the injected spins. From Equation 9.4, the efficiency of the spin torque switching scales as $1/\cos\theta$, so a non-zero θ value would lead to a larger critical current. The fact that the magnetization of the free layer at the P state is not perfectly aligned along the long axis can also result in the relatively lower energy barrier, as is observed from Table 9.1. From Table 9.1, it can be seen that when biased with the negative voltage, the energy barrier is heavily reduced, which is consistent with the decrease of H_C in Fig. 9.3 (a). Positive voltages also reduce the E/k_BT value slightly, and this may come from the Joule heating. Finally, from Table 9.1, we can extract the change in I_{C0} when V_{MTJ} is varied between ± 400 mV, and 0n average this corresponds to $|\Delta I_{c0}| \approx 0.14$ mA. Assuming that the switching obeys the macrospin model, we can calculate the voltage induced demagnetzaiton field change using Equation 9.4, $\Delta H_{demag}^{eff} \approx 530$ Oe. Here we utilized the previously measured values of M_S = 1.1×10^6A/m, α = 0.021 and J_S/J_C = 0.15 from Chapter 7. The change of perpendicular anisotropy energy per unit area can be estimated to be $\Delta E_{perp} t = 0.5\mu_0 M_S \Delta H_{an} t \approx 45$ μJ/m^2 for ΔV_{MTJ} of 800 mV, or 67 μJ/m^2 (V/nm)$^{-1}$. This is consistent with the results obtained in Chapter 8 and the previous reports [5, 16-18], where the energy change was determined to be in the range of $30 \sim 90$ μJ/m^2 (V/nm)$^{-1}$ for different

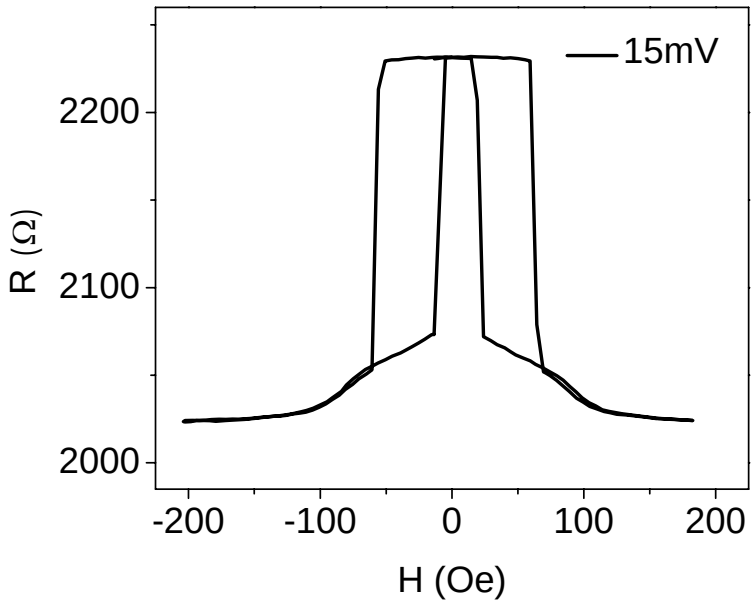

Figure 9.6. Magnetic major loop of the MTJ. The slope in the P state indicates that the equilibrium position for the free layer magnetization is not collinear with the fixed layer under small external *H* field.

ferromagnetic/oxide systems.

Because of the stochastic nature of the spin torque switching at room temperature, it is important to have the switching events under different applied voltages well separated from each other for the purpose of practical application. We studied the SHE induced switching probability for V_{MTJ} = 0 and -400 mV and the results are shown in Fig. 9.7 (a) and (b). The pulse lengths were set at 10 microseconds and the switching probability for each applied current is obtained by averaging over 50 attempts. From the figures, we can see that for each switching direction, there are windows where the switching probability is 100 % for $V_{MTJ} = -400$ mV and 0 % for $V_{MTJ} = 0$, implying that by working in those regions, it is possible to use V_{MTJ} as a gate to determine whether the switching will happen or not

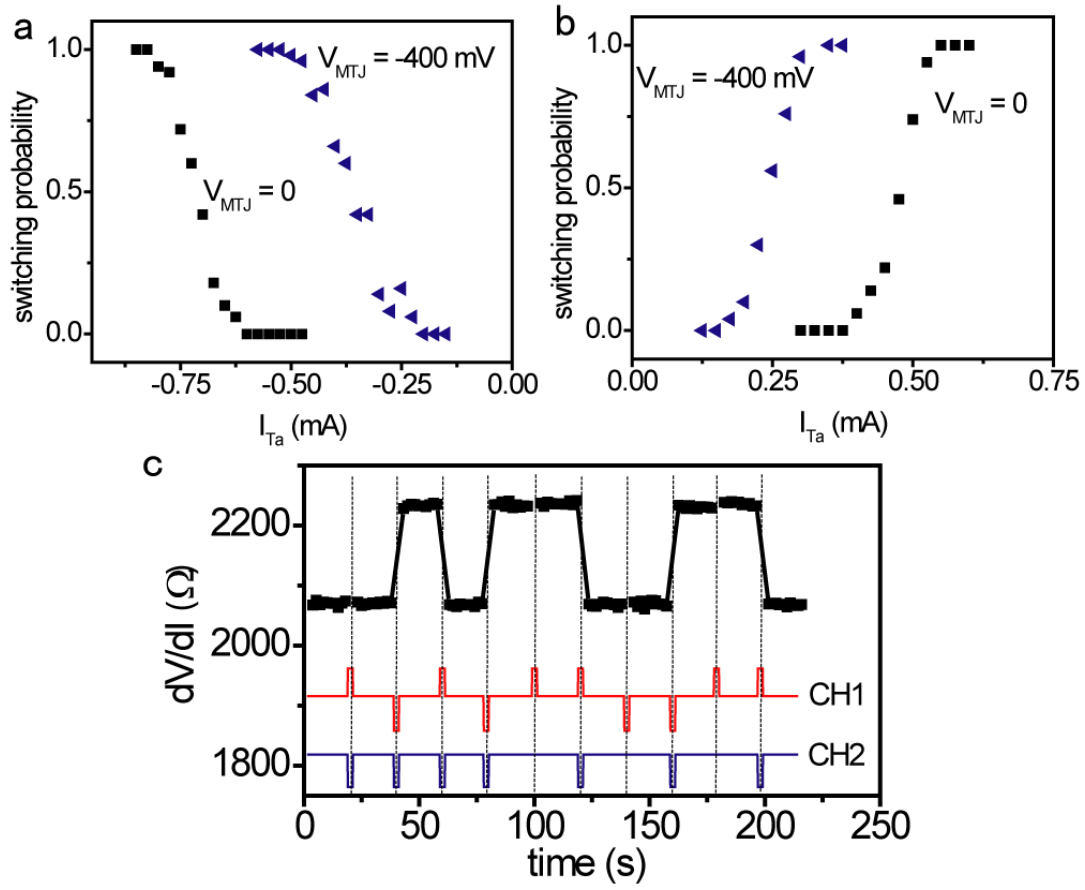

Figure 9.7. Spin Hall switching with different combinations of I_{Ta} and V_{MTJ}. (a) and (b), the switching probability with the bias voltage V_{MTJ} = 0 mV (black squares) and -400 mV (blue triangles) for (a) P to AP switching and (b) AP to P switching. The pulse lengths are 10 microseconds. (c), gate modulated SHE switching under a series of 10 microseconds pulses. Here, the voltage output from channel 2 is chosen to be V_{MTJ} = 0 mV and -400 mV. And channel 1 is applied such that the current I_{Ta} falls within the window shown in a and b.

for the same Ta current. As is shown in Fig. 9.7 (c), we applied different combinations of pulses through channel 1 and channel 2. When the device was set in the ON state ($V_{MTJ} = -400$ mV), bipolar switching was achieved by the applied current through the tantalumn. And no switching happened when the device was set in the OFF stae ($V_{MTJ} = 0$) for the same amount of I_{Ta}.

9.3 Conclusion and outlook

The electric field induced critical current change can be further optimized by adjusting the perpendicular anisotropy of the FM film. By choosing an appropriate thickness for the FM layer, it is possible to achieve an effective demagnetization field of ~1000 Oe. Then by applying a moderate electric field of ~ - 0.7 V/nm, one could achieve ~ - 500 Oe in ΔH_{demag} using the parameters that we determined in this work. This could lead to a reduction of ~ 50% in I_{C0}. The large modulation on I_{C0} predicted here will make sure that the device can have also good performance in the short pulse regime (~ nanosecond), where the electric field induced energy barrier change is no longer efficient in tuning the switching current. Note that although our demonstration here is based upon devices with in-plane magnetized FM layers, the same strategy should be applicable to perpendicularly magnetized devices. As is shown in Chapter 6, the spin Hall effect can also be used as the switching source for magnetic moment that are magnetized fully out-of-plane, and the critical current would be proportional to H_{an} in this case. Therefore, similar or even better performance can be achieved for out of plane devices, where a higher storage density is predicted.

The realization of electric field modulation on the critical current can have significant influence on the architecture of magnetic memory and on the development of spin logic devices. As is illustrated in this chapter, we have already shown some basic logic operation. More complicated operations may be realized using more than one device or by incorporating this three terminal device with other type of magnetic or semiconductor logic cells. The fact that the voltage can be used as the gate to switch the device between ON and OFF state also provides the possibility to simplify the geometries of current magnetic memories. The gate voltage can be used to determine which MTJ cell is selected for writing. Together with special strategies for reading

operation [23], this could reduce the basic cell of magnetic memory from one MTJ one transistor to N MTJs one transistor, which will greatly increase the storage density and reduce the cost for fabrication.

REFERENCE

1. J. A. Katine, F. J. Albert, R. A. Buhrman, E. B. Myers and D. C. Ralph, Current-driven magnetization reversal and spin-wave excitations in Co/Cu/Co pillars, *Phys. Rev. Lett.* **84**, 3149 (2000).
2. S. I. Kiselev, J. C. Sankey, I. N. Krivorotov, N. C. Emley, R. J. Schoelkopf, R. A. Buhrman and D. C. Ralph, Microwave oscillations of a nanomagnet driven by a spin-polarized current, *Nature* **425**, 380 (2003).
3. H. Ohno, D. Chiba, F. Matsukura, T. Omiya, E. Abe, T. Dietl, Y. Ohno and K. Ohtani, Electric-field control of ferromagnetism, *Nature* **408**, 944 (2000).
4. M. Weisheit, S. Fahler, A. Marty, Y. Souche, C. Poinsignon and D. Givord, Electric field-induced modification of magnetism in thin-film ferromagnets, *Science* **315**, 349 (2007).
5. T. Maruyama, et al., Large voltage-induced magnetic anisotropy change in a few atomic layers of iron, *Nature Nanotech.* **4**, 158 (2009).
6. J. C. Slonczewski, Current-driven excitation of magnetic multilayers, *J. Magn. Magn. Mater.* **159**, L1 (1996).
7. L. Berger, Emission of spin waves by a magnetic multilayer traversed by a current, *Phys. Rev. B* **54**, 9353 (1996).
8. D. C. Ralph and M. D. Stiles, Spin transfer torques, *J. Magn. Magn. Mater.* **320**, 1190 (2008).
9. J. W. Lee, S. C. Shin and S. K. Kim, Spin engineering of CoPd alloy films via the inverse piezoelectric effect, *Appl. Phys. Lett.* **82**, 2458 (2003).
10. W. Eerenstein, N. D. Mathur and J. F. Scott, Multiferroic and magnetoelectric materials, *Nature* **442**, 759 (2006).
11. Y. H. Chu, et al., Electric-field control of local ferromagnetism using a magnetoelectric multiferroic, *Nature Mat.* **7**, 478 (2008).
12. Y. Shiota, T. Maruyama, T. Nozaki, T. Shinjo, M. Shiraishi and Y. Suzuki, Voltage-Assisted Magnetization Switching in Ultrathin Fe(80)Co(20) Alloy Layers, *Appl. Phys. Express* **2**, 063001 (2009).
13. C. G. Duan, J. P. Velev, R. F. Sabirianov, Z. Q. Zhu, J. H. Chu, S. S. Jaswal and E. Y. Tsymbal, Surface magnetoelectric effect in ferromagnetic metal films, *Phys. Rev. Lett.* **101**, 137201 (2008).
14. G. H. O. Daalderop, P. J. Kelly and M. F. H. Schuurmans, Magnetocrystalline Anisotropy and Orbital Moments in Transition-Metal Compounds, *Phys. Rev. B* **44**, 12054 (1991).
15. S. S. Ha, N. H. Kim, S. Lee, C. Y. You, Y. Shiota, T. Maruyama, T. Nozaki and Y. Suzuki, Voltage induced magnetic anisotropy change in ultrathin Fe(80)Co(20)/MgO junctions with Brillouin light scattering, *Appl. Phys. Lett.* **96**, 142512 (2010).
16. T. Nozaki, Y. Shiota, M. Shiraishi, T. Shinjo and Y. Suzuki, Voltage-induced perpendicular magnetic anisotropy change in magnetic tunnel junctions, *Appl. Phys. Lett.* **96**, 022506 (2010).

17. M. Endo, S. Kanai, S. Ikeda, F. Matsukura and H. Ohno, Electric-field effects on thickness dependent magnetic anisotropy of sputtered MgO/Co(40)Fe(40)B(20)/Ta structures, *Appl. Phys. Lett.* **96**, 212503 (2010).
18. W. G. Wang, M. G. Li, S. Hageman and C. L. Chien, Electric-field-assisted switching in magnetic tunnel junctions, *Nature Mat.* **11**, 64 (2012).
19. Y. Shiota, T. Nozaki, F. Bonell, S. Murakami, T. Shinjo and Y. Suzuki, Induction of coherent magnetization switching in a few atomic layers of FeCo using voltage pulses, *Nature Mat.* **11**, 39 (2012).
20. M. Julliere, Tunneling between Ferromagnetic-Films, *Phys. Lett. A* **54**, 225 (1975).
21. J. Z. Sun, Spin-current interaction with a monodomain magnetic body: A model study, *Phys. Rev. B* **62**, 570 (2000).
22. R. H. Koch, J. A. Katine and J. Z. Sun, Time-resolved reversal of spin-transfer switching in a nanomagnet, *Phys. Rev. Lett.* **92**, 088302 (2004).
23. W. Zhao, S. Chaudhuri, C. Accoto, J.-O. Klein, C. Chappert and P. Mazoyer, Cross-point architecture for spin transfer torque magnetic random access memory, *arXiv*, 1202.1782 (2012).